University of Zagreb
Faculty of Science

Tomislav Vuletić

COLLECTIVE ELECTRONIC STATES OF THE NEW QUASI-ONE-DIMENSIONAL MATERIALS

Dissertation

Zagreb, 2004.

University of Zagreb
Faculty of Science

Tomislav Vuletić

COLLECTIVE ELECTRONIC STATES OF THE NEW QUASI-ONE-DIMENSIONAL MATERIALS

Dissertation

Supervisor: Silvia Tomić

Thesis committee:

A. Hamzić (chairman)
S. Barišić
M. Dressel
D. Jérome
S. Tomić
A. Bjeliš
B. Korin-Hamzić

Zagreb, 2004.

Sveučilište u Zagrebu
Prirodoslovno-matematički fakultet

Tomislav Vuletić

Kolektivna elektronska stanja novih kvazijednodimenzionalnih materijala

Disertacija
predložena Fizičkom odsjeku
Prirodoslovno-matematičkog fakulteta
Sveučilišta u Zagrebu
radi stjecanja akademskog stupnja

doktora prirodnih znanosti

Mentor: Silvia Tomić

Povjerenstvo za obranu:

A. Hamzić (predsjednik)
S. Barišić
M. Dressel
D. Jérome
S. Tomić
A. Bjeliš
B. Korin-Hamzić

Zagreb, 2004.

Acknowledgment

I began this journey into one-dimensional world already with my B.Sc. Thesis, starting in 1997. Since I was a novice in the laboratory, the first years I concentrated on the technical aspects of an experimental venture into physics. It was very exciting for me to find that I indeed managed to grasp how to use all this equipment. I have to confess, only later I got interested in the broader physical picture. Now, the more I explore it, the more I learn about the physics, the more I find it exciting to investigate and to try to understand the importance of my experimental results. In the end, I even started to venture into higher dimensions... Now, the years have passed, and although the time elapsed might seem long just for obtaining a single degree, I now find that it is indeed very short, compared to a life of learning which awaits.

My enlightenment could not have been better assisted, but with the supervision of my Mentor, dr. Silvia Tomić. I am grateful to her for the never ceasing support, and for the optimistic attitude, which resulted in my career never experiencing any setback.

What I learned in the lab in Zagreb was very much extended thanks to my very productive visits to the group of dr. D. Jérome at Laboratoire de Physique des Solides, Orsay. I am grateful to Denis Jérome and members of his group, dr. P. Auban-Senzier and dr. C. Pasquier for broadening my perspectives.

I would not find myself on this track if it were not for prof. S. Barišić and his advice at the very beginning of my career, for which I am grateful. And I am also thankful to him for recent encouragements and guidance towards understanding what can be learned from my experiments. I am indebted to his assistant, dr. I. Mrkonjić, who did a great deal of work taking me through the vast expanses of theory, and I would not benefit so much from prof. Barišić expertise if she did not work out the basics with me.

In particular, I acknowledge the opportunity to discuss, work and publish with prof. M. Dressel and dr. B. Gorshunov from 1. Physikalisches Institut, Universität Stuttgart, Germany.

This is also an opportunity to thank prof. A. Hamzić, for his assistance and understanding throughout the final preparation stages of my Thesis.

Always somewhere nearby during my career was prof. K. Maki, giving me the opportunity to discuss with him, and allowing me to take part in a fine example of cooperation between theory and experiment. Dr. B. Korin-Hamzić offered me irreplaceable support in the lab and I thank her for the perfect example of teamwork we performed. For all imaginable complications one can encounter during experiments and with all the equipment, throughout the years I had support from my colleagues dr. M. Pinterić, dr. N. Biškup, dr. M. Basletić, dr. M. Prester, dr. Đ. Drobac and dr. J. Ivkov.

Recollecting, I find that it is not easy to recall all the occasions at which I was given invaluable support, advice and criticism. Among others I wish to thank: dr. P. Monceau, prof. A. Bjeliš, dr. K. Biljaković, dr. O. Milat, dr. A. Smontara, dr. E. Tutiš, dr. A. Šiber, mr. O. Barišić. I have been greatly supported by all my colleagues, researchers from the Institute of physics in Zagreb and all the technical staff, especially by M. Vukelić, K. Drvodelić and M. Marukić. My thanks are due to Lj. Vukić and L. Hamberger who improved the English of my Thesis considerably. I also thank my colleagues from LPS, Orsay, dr. J. Moser and dr. P. Wzietek who introduced me with the international character of a career in physics. My stay in Orsay was a pleasant one thanks to H. Albouze and my hosts F. and Y. Gonthier.

A person living a life in science may on many occasions be very unbearable to the closest ones. I thank all my friends who accept me as I am. I thank my Ana for understanding and forgiving me. I find myself very happy that I found someone who can live with somebody like me. I thank my mother Marija, my father Nikola and my brother Marko for being calm when I was tense. I wish them all the joy, and I congratulate Marko on managing his Thesis within the corporate environment.

Tomislav Vuletić
Zagreb, August 2004.

Contents

1 Investigated quasi-one-dimensional materials

1.1 q1D Bechgaard salt $(TMTSF)_2PF_6$ - still a new material

A common feature of many strongly correlated electron systems is a proximity of a superconducting state to some kind of magnetically ordered insulating state. Examples include low-dimensional organic materials, [1, 2], heavy fermion superconductors [3], and layered high-T_c copper oxide superconductors (HTSC), [4]. Particularly, the close proximity of antiferromagnetic (AF) or spin-density wave (SDW) phases with the onset of organic superconductivity (SC) in the temperature and pressure phase diagram of organic compounds, indicated at an early stage, that the apparent difficulty to describe both phenomena emerges from their mutual interaction, [5]. It needs to be pointed out that the proximity of the two phases poses the question whether the two order parameters interact (support each other) or compete (repulse each other), Fig. 1.1.

An AF – SC coexistence region has been observed recently in the layered organic κ-$(BEDT\text{-}TTF)_2X$ compounds under well controlled pressure [2, 6]. Even better characterised system featuring the coexistence of AF (or SDW) and SC (or normal state) is formed in the quasi-one dimensional organic superconductors, *i.e.* the Bechgaard-Fabre salts. This family of materials features a unified phase diagram, Fig. 1.1, lower right panel. Different members of the family are positioned at different points in the diagram, as indicated by arrows. Applying enough pressure stabilizes any of the ground states found to the right of the arrow which denotes respective material. A recent observation of the whole spectrum of states from this diagram for $(TMTTF)_2PF_6$, where SC was reached at 43.5 kbar, confirmed this, [7]. Even after 25 years of investigation the nature of the transition from magnetism, *i.e.* SDW to superconductivity, and the respective part of the unified phase diagram has

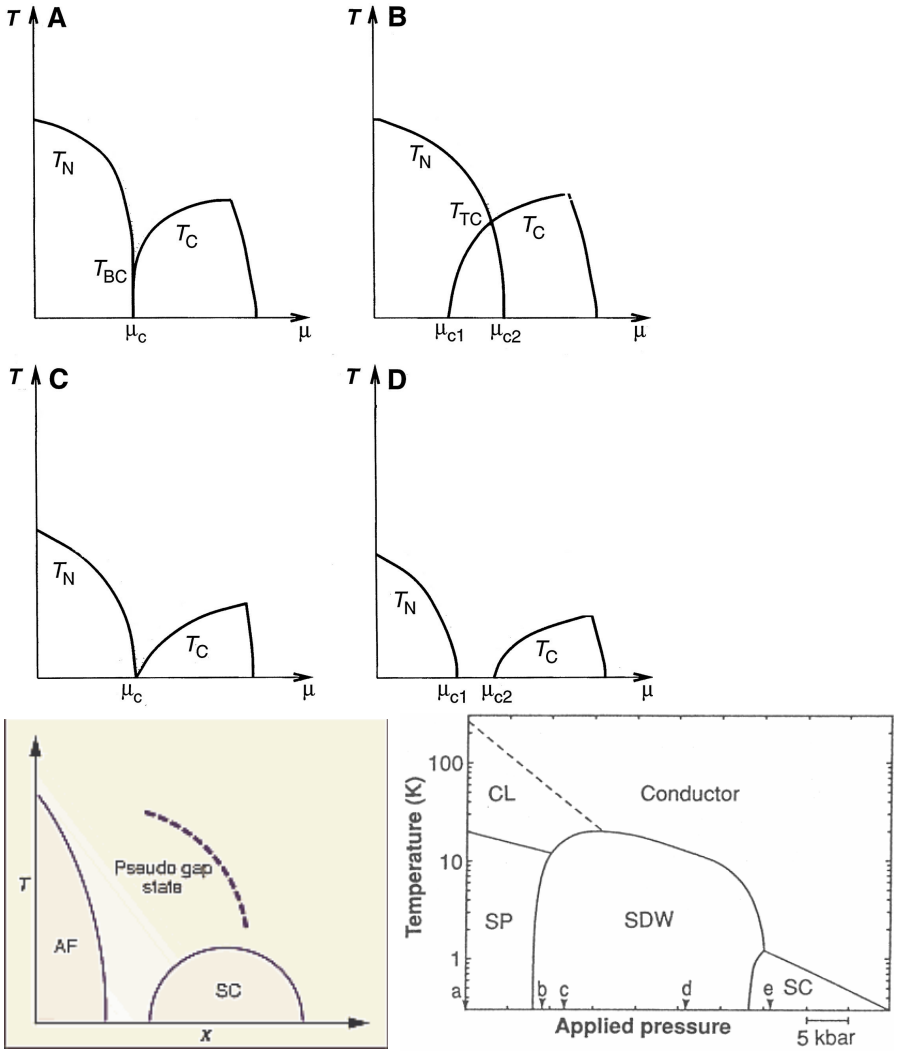

Figure 1.1: Upper panel: Theoretically possible phase diagrams for the case of proximity between the magnetic (AF or SDW) and SC ground states. T_N and T_c are the respective transition temperatures. There are four possible types of transitions from the magnetic to SC state, [8]. (A) a direct first-order transition terminating at a bicritical point T_{bc}. (B) two second-order phase transitions with an intermediate phase. The second-order lines merge at a tetracritical point T_{tc}. (C) a single second-order phase transition at a quantum critical point. (D) two second-order quantum phase transitions with an intermediate quantum-disordered phase. These possibilities may be compared to the well known experimental phase diagrams: Lower left panel, HTSC layered cuprates. At low doping x, an AF ordering is established. At higher doping, a SC phase is created with the pseudo gap state above it, [9]. Lower right panel, the Bechgaard-Fabre salts. The SC state has a common boundary with the SDW state. The ambient pressure locations in the generalized phase diagram for $(TMTTF)_2PF_6$(a), $(TMDTDSF)_2PF_6$(b), $(TMTTF)_2Br$(c), $(TMTSF)_2PF_6$(d), $(TMTSF)_2ClO_4$(e) is indicated. The dashed line delimits the charge-localized (CL) behavior. SP refers to spin-Peierls state, [10].

remained unclear, [10, 17, 19, 20]. In particular, the prototype and most studied compound, $(TMTSF)_2PF_6$, has an ideal position in this phase diagram and an improved experimental setup now allows for investigation of this transition. This justifies for the title of this Section- $(TMTSF)_2PF_6$ is still a new material worth investigating due to its rich (especially when magnetic field is introduced as a third axis) and still not completely explored phase diagram [10, 18]. This phase diagram, in the low temperature region, features all known electronic transport mechanisms. Besides metallic conductivity and superconductivity (observed 25 years ago, [21]), the other two, theoretically dissipationless transport mechanisms, occur in the spin-density wave phase and the quantum Hall effect (QHE) state, [11, 12, 16, 17, 18]. Finally, it may be noted that the role of Bechgaard-Fabre salts, as the most explored q1D systems, is also very well appreciated. The Thesis also benefits from this, since any work on other q1D materials is much more instructive if compared to the results obtained on $(TMTSF)_2PF_6$, the principal compound of the family.

1.1.1 Structure

All members of Bechgaard, $(TMTSF)_2X$ and Fabre salts $(TMTTF)_2X$, in general TM_2X, are isostructural compounds. TMTSF/TMTTF, tetramethyltetra(selena /thia) fulvalene is a derivative of an organic molecule, fulvalene, where four carbon atoms are substituted by four selenium /sulphur atoms, and four methyl (CH_3) groups have been added. Fulvalene (pentafulvalene) structure is basically two pentafulvene (derivative of cyclopentadiene) molecules joined by a double bond between two ring carbons, Fig. 1.2. The double-bonds within and between the rings make the fulvalene a planar molecule, [13]. TMTSF/TMTTF form salts with inorganic anions, where the charge is transferred from the fulvalene molecules to the inorganic anions. There are many possible anions: X = PF_6, AsF_6, SbF_6, BF_4, ClO_4, Re_4, NO_3... The anions are placed into centrosymmetrical cavities delimited by methyl groups. Therefore, the most important property of these anions is their symmetry, *i.e.* , the compounds with the centrosymmetric anions have very similar experimental properties, which are quite different from those with noncentrosymmetric ones, where a substantial disorder is introduced, and anion ordering plays a role. The selenium based salts were first synthetized in 1979., by the electrochemical method, by Bechgaard *et al.* [14], Fig. 1.2. The crystal structure was obtained by X-ray diffraction (XRD) and found to be triclinic, [15]. The parameters of the unit cell are a=3.65 Å, b=7.711 Å, c=13.522 Å, α=83.39^o, β=86.27^o and γ=71.01^o. The planar shape of TMTSF/TMTTF molecules and their respective stack-

ing (in a somewhat zig-zag pattern) along crystal a-axis are responsible for the highly anisotropic electronic structure of TM_2X. In b-direction (interstack) TMTSF/TMTTF molecules are separated by a slightly larger distance than in a-direction (intrastack). Adding to the anisotropy, TMTSF/TMTTF stacks are in the c-direction separated by the anions X, Fig. 1.2. A tendency towards dimerization between the molecules in the stack is observed, especially for sulphur based compounds.

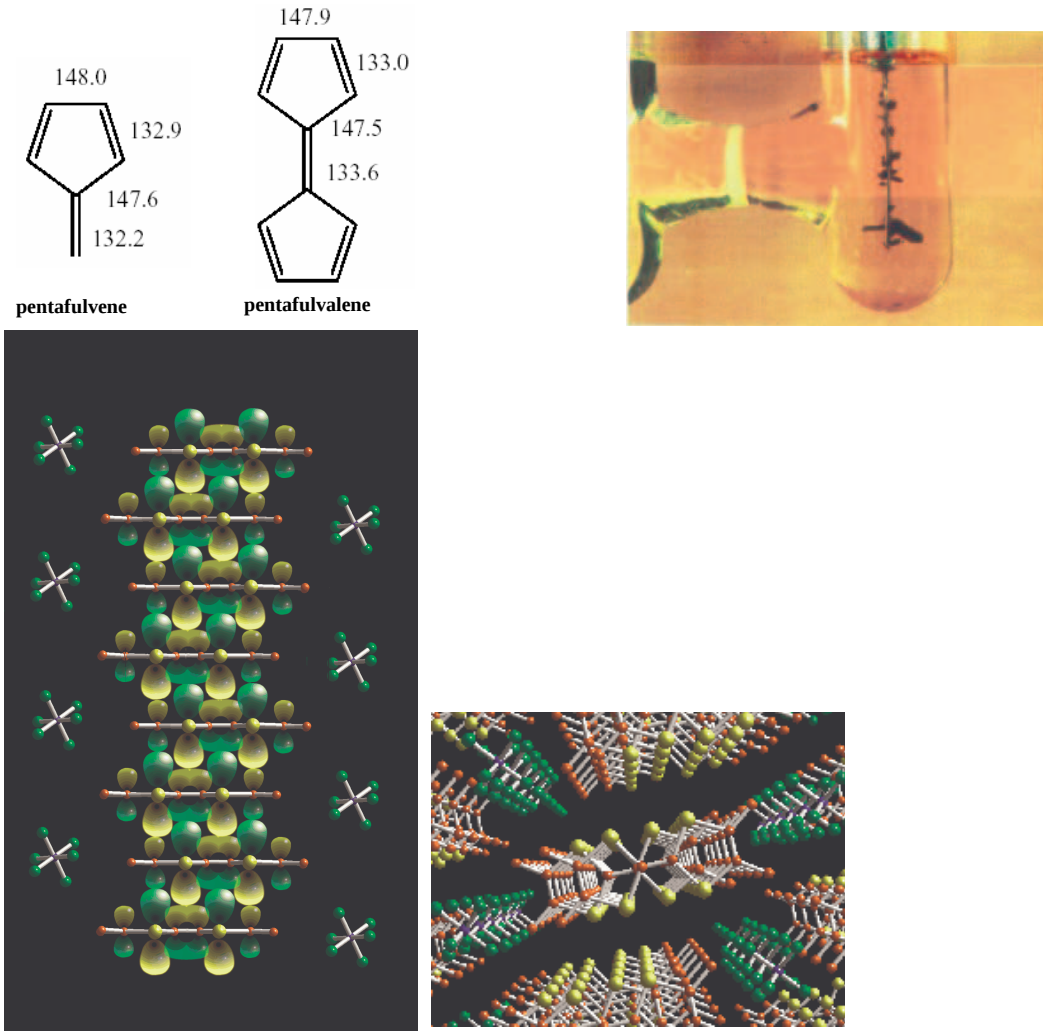

Figure 1.2: Upper left: Hartree-Fock geometries of fulvene and fulvalene molecules. Bond lengths in picometers. Upper right: The elongated, black crystals of $(TMTSF)_2PF_6$ grow on the electrodes during an electrochemical synthesis. Lower left: The structure of $(TMTSF)_2PF_6$ can be generated by stacking TMTSF molecules in a somewhat zig-zag pattern along the a-axis (the view is along the b-axis). The p-orbitals of the atoms within TMTSF molecule are shown. Lower right: Along the c-axis stacks are separated by PF_6 anions (the view is along the a-axis). yellow - Se, red - C, blue - P, green - F. Model: Institut des Materiaux Jean Rouxel.

1.1.2 Electronic structure and transport properties in metallic regime of $TMTSF_2X$

The charge transfer results in the excess of holes within the TMTSF stacks. A quarter filled tight-binding band (1 electron transferred per two molecules) is formed within the first Brillouin zone, leading to metallic properties. This band may be altered in case of dimerization, but this review concentrates on TMTSF compounds where this is not crucial. The band formation is due to the superposition of the p-orbitals of the selenium atoms of the neighbouring TMTSF molecules, Fig. 1.2, right picture. The overlap, characterized with the transfer integrals t_i, is by far the largest along the stacking direction a- and quite smaller along b-direction. Along c-, due to the anions inbetween TMTSF molecules, it is almost negligible. The transfer integrals t_i for $TMTSF_2X$ materials, were calculated within the tight binding approximation to be $t_a \approx 0.2\text{e}V : t_b \approx 0.02\text{e}V : t_c < 0.001\text{e}V$, [22], Fig. 1.3. These theoretical values are also in good agreement with the RT optical and magnetic measurements, [23, 24].

Experimentally, the electronic structure anisotropy reflects in room temperature (RT) conductivity anisotropy for $(TMTSF)_2PF_6$, $\sigma_a : \sigma_b : \sigma_c \sim 300 : 1 : 0.03$. Therefore, this and other materials from the family, are regarded as quasi-one-dimensional conductors. The RT conductivity is high $\sigma_a(300\text{K}) \approx 600\Omega^{-1}\text{c}m^{-1}$ [25], and metallic properties are observed in the electronic transport down to very low temperatures, [27]. The longitudinal resistance decrease follows a power law $T^{1.5}$ down to ≈ 100 K, [26]. Below 35 K, resistivity follows the residual resistivity law $\rho_{res} + AT^2$ down to metal-to-insulator transition, Fig. 1.4. The ratio RR between the room temperature and the minimum resistance just above the metal-to-insulator is very sample dependent, ranging from 30 to 1000 for the highest quality samples. For high quality samples, the residual resistivity ρ_{res} appears to be 0, [27], suggesting that the inelastic electron scattering term AT^2 is dominant in the conducting state at low temperature. Conductivity anisotropy seems to be temperature independent, [25] down to ≈ 25 K, with the values confirming the theoretical prediction $\frac{\sigma_a}{\sigma_b} \approx \frac{t_a^2 a}{t_b^2 b}$.

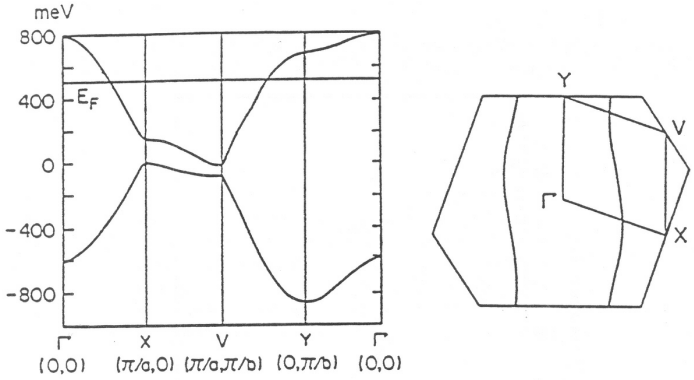

Figure 1.3: The calculated band structure for $(TMTSF)_2X$ materials. From Ref. [22]

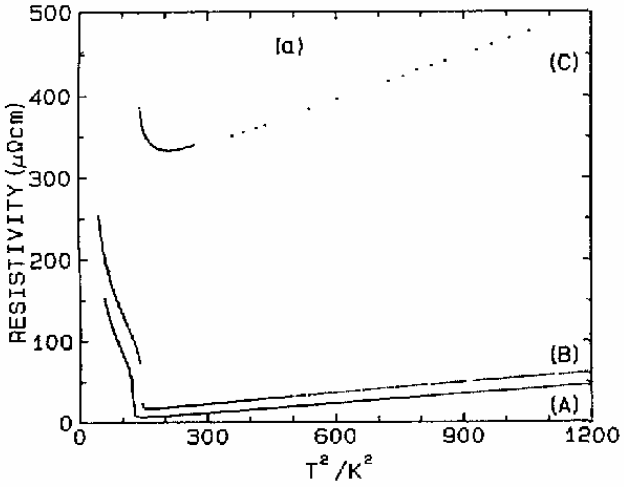

Figure 1.4: Resistivity *vs.* temperature squared for $(TMTSF)_2PF_6$ below 35 K behaves according to the residual resistivity law $\rho_{res} + AT^2$ down to metal-to-insulator transition. Samples from different batches show different residual resistivities, ρ_{res}, which even attains zero value for the batch A. A sharp rise of resistance is the onset of the metal-to-insulator transition (12 K for the high quality batch A). From Ref. [27]

1.1.3 SDW phase transition in $(TMTSF)_2PF_6$

A very sharp metal-to-insulator transition corresponds to the occurence of the spin-desity wave (SDW) ground state at $T_{\mathrm{SDW}} = 12$ K. The low field susceptibility of the SDW phase behaves very much like the susceptibility of a regular antiferromagnet, Fig. 1.5. These results for the analogous compound $(TMTSF)_2AsF_6$ show that the easy axis is aligned along b- and that a spin-flip transition arises around 5 kOe, [28]. The magnetic nature of the ground state has also been confirmed by the observation of AF resonance [30] and the measurement of a local field by NMR and μSR [31]. A sinusoidal SDW modulation of wave vector $\mathbf{Q}_{\mathrm{SDW}}$ =(0.5, 0.20-0.24,-0.06±0.20) and of amplitude 0.08 μ_B was suggested by two independent proton NMR experiments [24, 29]. A two component charge modulation (of the electronic system, not the lattice), was observed by X-ray diffuse scattering. One was characterized by a similar wave vector $\mathbf{Q}_1$ =(0.5±0.05, 0.25±0.05,0.25±0.20) as in the magnetic sector, the other had $\mathbf{Q}_2 = 2\mathbf{Q}_1$. The amplitude of the charge modulation was 0.1 electron per TMTSF molecule, *i.e.* , it was comparable to the amplitude of the SDW, [33, 34].

The transition to the SDW phase is driven by a specific *nesting* property of the Fermi surface (FS) of $(TMTSF)_2PF_6$, and of some other materials from the family, which have centrosymmetric anions. The characteristic vector of the spin modulation is defined by this FS property, indeed. The FS of an ideal 1D conductor would be composed of two flat opposing sheets. In Bechgaard salts, especially $(TMTSF)_2PF_6$, due to finite t_b FS is formed of two warped opposing sheets, Fig. 1.6, characterized by a feeble modulation along the b-axis, and negligible one along the c-axis, see Sec. 1.1.4. These two opposing FS sheets fit one onto another under a translation in the reciprocal space for a nesting vector $\mathbf{Q} \approx (2k_F, \frac{\pi}{b})$. This vector links the occupied orbitals close to one FS sheet to the unoccupied orbitals close to the other FS sheet. Since very many orbitals with very little energy difference, $E(\mathbf{k}) = E(\mathbf{k}+\mathbf{Q})$, are linked when the nesting is good, this leads to a logarithmic divergence in the spin susceptibility function $\chi_0(\mathbf{q} \approx \mathbf{Q})$ as $T \to 0$, and eventually to a transition to a spin-modulated ground state: spin-density wave (SDW). Spin density modulation is characterized with $\mathbf{Q}$ wave vector: $S(x) = S_0 \cos(\mathbf{Q}\mathbf{x}+\varphi(x)) = S_0 \cos(2k_F x+\varphi(x))$. This $2k_F$ SDW was observed experimentally, as already mentioned above [24, 29].

A long time ago Overhauser, [32] suggested that such a spin-density modulation may be understood as a combination of two electronic CDWs of opposite spin:

$$\delta\rho_\uparrow = \rho_0 \cos(2k_F x + \varphi(x))$$

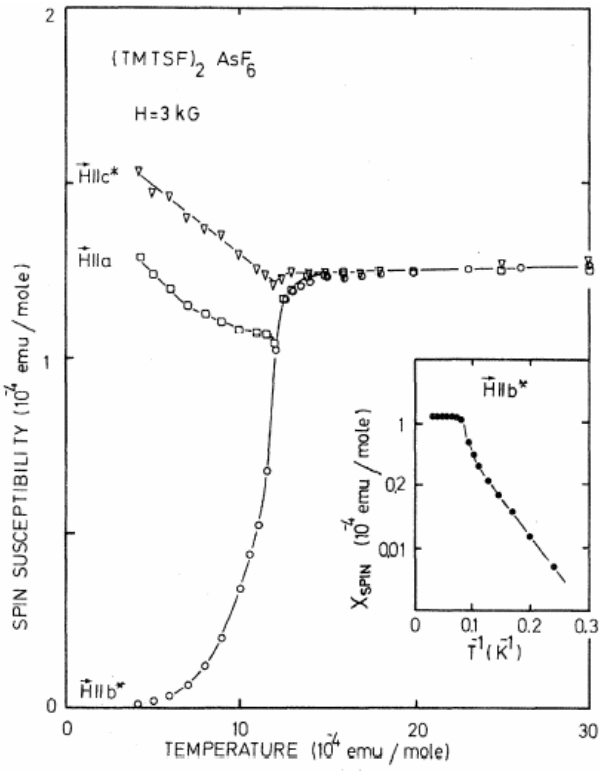

Figure 1.5: Spin-susceptibility of $(TMTSF)_2AsF_6$as deduced from static measurements with magnetic field along the respective crystal axes. The magnetic field 3 kG, is lower than critical spin-flip field. From Ref. [28].

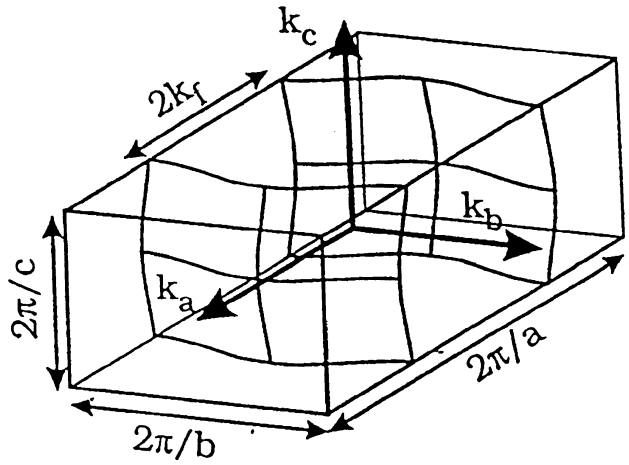

Figure 1.6: Fermi-surface for q1D materials. A good nesting between the two sheets leads to transition to the spin density wave phase. Warping in the b- direction is much stronger than the one in the c-direction, which is neglected and the nesting is considered to be perfect, with the nesting vector $\mathbf{Q} \approx (2k_F, \frac{\pi}{b})$. See Sec. 1.1.4.

$$\delta\rho_\downarrow = \rho_0 \cos(2k_F x + \varphi(x) + \theta) \tag{1.1}$$

For $\theta = \pi$ the pure SDW appears, while for $0 < \theta < \pi$ a mixed $2k_F$ CDW-$2k_F$ SDW state occurs, as observed by Pouget *et al.* and Kagoshima *et al.* [33, 34, 36]. The mechanism which stabilizes it is unknown.

The development of SDW opens a gap 2Δ at Fermi surface, leading to the metal-to-insulator transition, [37]. In the SDW phase resistance shows the Arrhenius behaviour, $R = R_0 e^{\Delta/T}$, Fig. 1.7. For high quality samples $\Delta \approx$ 21 K, and it has to be noted that the mean-field BCS relation $2\Delta = 3.52 T_{\mathrm{SDW}}$, is well satisfied for $(\mathrm{TMTSF})_2\mathrm{PF}_6$ and AsF_6 materials, [27]. This was also confirmed recently by the direct observation of SDW gap in $(\mathrm{TMTSF})_2$-PF_6, Fig. 1.7, by means of the electron tunnelling spectroscopy, using low temperature STM [35].

A mean-field treatment of the Hubbard hamiltonian for a 1D interacting electron gas model of $(\mathrm{TMTSF})_2\mathrm{PF}_6$, leads to the exponential dependence of the $2\Delta_{\mathrm{SDW}}$ gap on the interaction U. The following illustrates that T_{SDW} also shows the same dependence. The BCS relation $2\Delta = 3.52 T_{\mathrm{SDW}}$ is satisfied in this 1D interacting electron gas model, as well as in the experiment.

Firstly, the magnetic susceptibility for a noninteracting electron gas featuring dispersion $E(\mathbf{k})$, is given by Lindhard response function

$$\chi_0(\mathbf{q}) \propto \sum_{\mathbf{k}} \frac{f_{\mathbf{k}} - f_{\mathbf{k}+\mathbf{q}}}{E_{\mathbf{k}+\mathbf{q}} - E_{\mathbf{k}}} \tag{1.2}$$

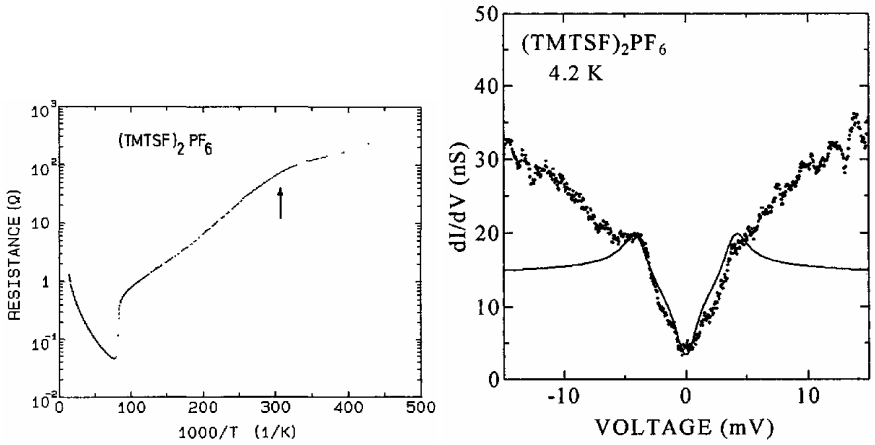

Figure 1.7: Left panel: Logarithm of resistance *vs.* inverse temperature for $(TMTSF)_2PF_6$. Activation energy Δ_{SDW} is 21 K below $T_{SDW} = 12$ K. Note a break in the slope at 3.2 K, indicating a crossover within the SDW phase. From Ref. [27]. Right panel: Direct observation of the gap with STM: Dots represent tunnelling differential conductance at 4.2 K. Solid line represents the calculation from which $2\Delta_{SDW} = 35$ K is obtained. From Ref. [35].

where $f_{\mathbf{k}}$ is Fermi-Dirac statistics at temperature T

$$f_{\mathbf{k}} = \frac{1}{exp\left[\frac{E_{\mathbf{k}}-E_F}{k_BT}\right]+1} \tag{1.3}$$

By numerical integration of Eq. 1.2, for the perfect nesting case of 1D dispersion given by Eq. 1.7 (where $t'_\perp$ is neglected), it can be demonstrated that the spin susceptibility diverges logarithmically, $\chi_0(\mathbf{Q},T) \propto \ln(1/T)$. Introduction of interaction U into this noninteracting electron gas enhances the susceptibility:

$$\chi(\mathbf{Q},T) = \frac{\chi_0(\mathbf{Q},T)}{(1-U\chi_0(\mathbf{Q},T))} \tag{1.4}$$

When the Stoner criterion $(1-U\chi_0(\mathbf{Q},T))$ is fulfilled the SDW ground state is expected below an ordering temperature $T_{SDW} \propto E_F \exp\left[-\frac{1}{N(E_F)U}\right]$. Below this temperature the electron system responds divergently at the $\mathbf{Q}$ vector, effectively *freezing* into a spin-modulated state, the spin-density wave.

A prominent feature of this phase is its response to dc and ac electric fields. The response to dc electric field is nonlinear due to SDW condensate sliding above a certain threshold electric field [38]. SDW condensate sliding is accompanied by a phenomenon of narrow band noise, [39]. The response

to ac field is characterized by the enormous dielectric constant of the order of 10^8-10^9 [45].

Finally, we would like to mention experiments indicating a complex nature and the possible existence of transition(s) inside the SDW phase of $(TMTSF)_2PF_6$, [44]. A calorimetric transition at 3.5 K with large hysteretic phenomena in the temperature range 2.5K - 4K caused by the sample history has been observed, [41]. In the electrical transport, a break in the slope of logarithm of resistance *vs.* inverse temperature curve for $(TMTSF)_2PF_6$ was observed at 3.2 K, indicating a crossover within the SDW phase, Fig. 1.7, [27]. Further, NMR measurements of the spin-lattice relaxation rate $(1/T_1)$, have shown a changeover at 3.5K from a temperature independent behaviour at higher temperatures to an activated behaviour at lower temperatures, with an activation energy much lower than the free carrier resistivity one. In addition, another anomaly in $1/T_1$ was detected at about 2K. Takahashi *et al.* [40] have suggested that the $1/T_1$ anomalies indicate the existence of successive transitions inside the SDW ground state, adding to the richness of $(TMTSF)_2PF_6$ phase diagram. Moreover, the X-ray diffuse scattering showed that SDW ground state is, indeed, mixed $2k_F$ CDW - $2k_F$ SDW ground state, (see above) [33, 34]. Other authors showed that CDW dissappears below 3-4 K, indicating a possible relation with the subphase structure of SDW in $(TMTSF)_2PF_6$, [36]. Additional magnetoresistance and Hall studies have also indicated changes inside SDW phase, [42, 43]. These authors have also interpreted that an unconventional SDW phase below $T^* = 4$ K is formed along SDW.

1.1.4 Phase transitions in $(TMTSF)_2PF_6$ under pressure

SDW supression under pressure

Here it is appropriate to relate the exposed band structure and corresponding spin susceptibility properties of $(TMTSF)_2PF_6$ to dependence of the SDW transition temperature T_{SDW} on pressure observed for $(TMTSF)_2PF_6$, in more detail. This dependence is presented within the schematic phase diagram of TM_2X family, Fig. 1.1. The data for this diagram were obtained in numerous electrical transport studies, [47, 12, 48] and also by an elaborate EPR experiment [46], Fig. 1.8. In order to discuss the stability of the SDW phase, it is essential to model the Fermi surface geometry, and the dispersion relation.

The description of the SDW transition and ground state as given in previous Section is based on a strictly one-dimensional model, with $\mathbf{Q} =$

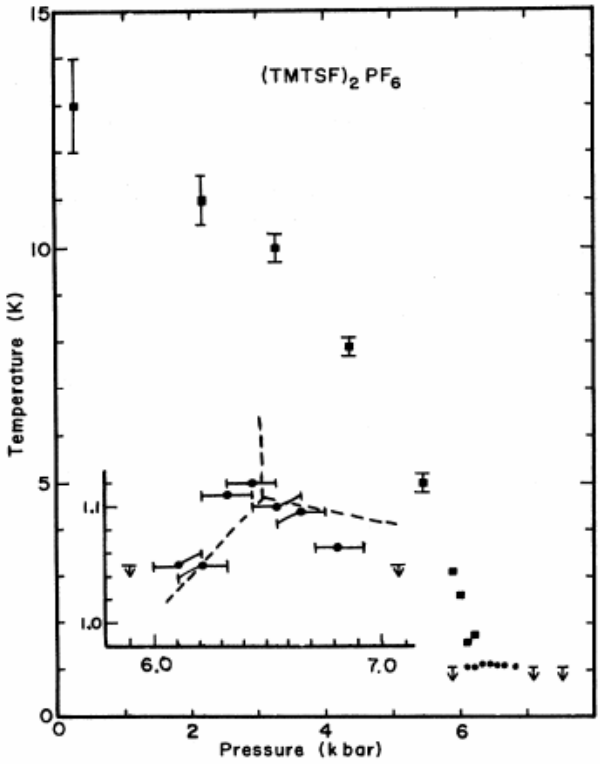

Figure 1.8: Temperature-pressure phase diagram showing metal-to-SDW transitions (squares) and superconducting transitions. The inset shows the details near the tricritical point. The data were obtained by electron-spin resonance in a single crystal at low magnetic fields. From Ref. [46]

$(2k_F, 0, 0)$, and it would also apply to the case of perfect nesting, $\mathbf{Q} \approx (2k_F, \frac{\pi}{b})$. However, as a realistic material, $(TMTSF)_2PF_6$is characterized by a certain degree of imperfect nesting. This concept is introduced as follows.

Although the symmetry of $(TMTSF)_2PF_6$ is triclinic, most physical features can be explained by taking an orthorombic symmetry (the deviations of the crystalline axes from the axes of the crystallographic coordinate system are neglected) with tight binding energy dispersion given as:

$$E(\mathbf{k}) = -2t_a \cos(k_x a/2) - 2t_b \cos(k_y b) - 2t_c \cos(k_z c) \tag{1.5}$$

Taking the origin of the energy at the Fermi energy $E_F = 0$, and staying close to the Fermi level ($k_B T < t_a$) this dispersion may be linearized without significant modifications in the physical properties of the model

$$E(\mathbf{k}) = E_0 - 2t_a \left(k_F a - |k_x|a\right) - 2t_b \cos(k_y b) - 2t_b^2/t_a \cos(k_y b) \tag{1.6}$$

Here $2at_a$ is Fermi velocity v_F. The band is quarter filled, $k_F = \pi/4a$. Only the highest occupied molecular orbital concentrated around Se atoms on the TMTSF molecule is taken into consideration. Commonly the dispersion Eq. 1.6 is written as

$$E(\mathbf{k}) = E_0 + v_F \left(|k_x| - k_F\right) - 2t_\perp \cos(k_y b) - 2t'_\perp \cos(k_y b) \tag{1.7}$$

where a nesting deviation parameter is defined as $t'_\perp = t_\perp^2/t_\parallel = t_b^2/t_a$. The dispersion along the c-direction is neglected. Thus, a Fermi surface of only slightly distorted sinusoidal shape is defined. If $t'_\perp$ is also neglected FS becomes perfectly sinusoidal and perfectly nested with the nesting vector $\mathbf{Q} = (2k_F, \frac{\pi}{b})$. But, for $(TMTSF)_2PF_6$ we have to note that the FS nesting is already imperfect at ambient pressure and $t'_\perp$ can not be neglected. That is, if transfer integral values calculated by Grant, [22], are taken into account, one gets $t'_\perp \approx 1 - 2$ meV, already at ambient pressure. This is comparable to the energy scale Δ_{SDW}, explaining why only a modest pressure of the order of 10 kbar is enough to suppress the SDW state, [12].

The role of pressure in this model is to increase $t'_\perp$ term in Eq. 1.7. Not surprisingly, the pressure is considered to increase the overlap between the p-orbitals, and respective transfer integrals. Thus $t'_\perp$ term becomes significant due to its quadratic dependence on t_b and the FS departs further from perfect nesting. $\chi_0(\mathbf{Q})$ no longer presents a logarithmic divergence, but only a relative maximum (nondivergent as $T \to 0$) at a slightly different nesting vector. Then there exists a critical value $t'_\perp = t_\perp^{**}$ above which SDW ground state is suppressed and a non-distorted q1D conductor is stabilized at low temperature, Fig. 1.9.

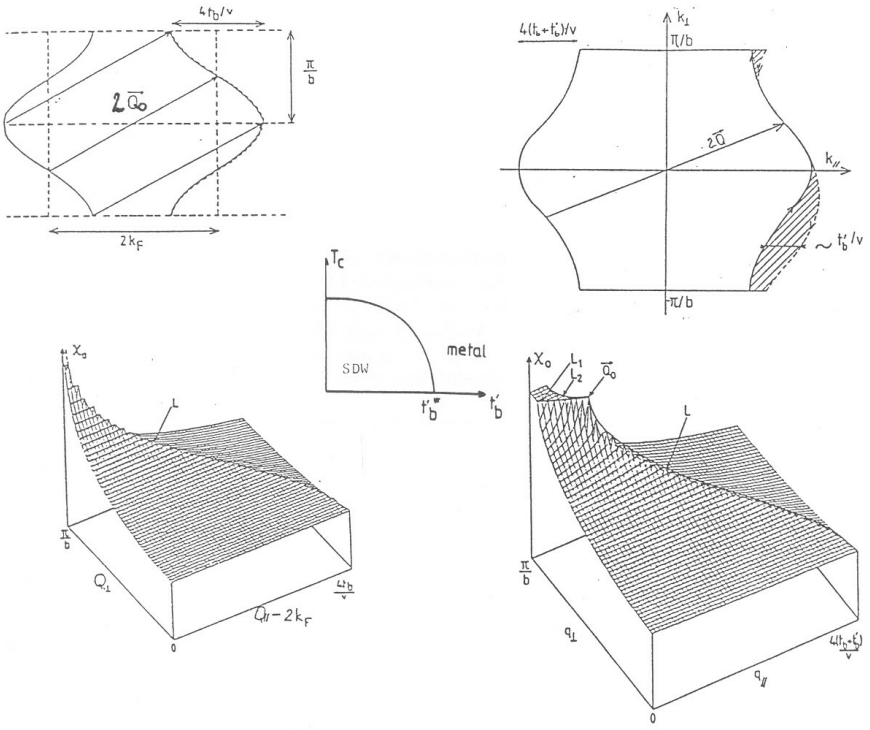

Figure 1.9: Lower left diagram: a logarithmically divergent $\chi_{(\mathbf{Q}=2k_F,\pi/b)}$ appears for perfect nesting case (upper left diagram), when $t'_b = 0$. Lower right diagram: $\chi_{(\mathbf{q})}$ is no longer divergent for $t'_b \neq 0$. Just a local maximum appears (non-perfect nesting) at a slightly different nesting vector $\mathbf{Q}_0$. Nesting is not perfect, unnested pockets of FS appear (shaded area in the upper right diagram). Central diagram: the SDW ground state of $(TMTSF)_2X$ is stable as long as $t'_b < t^{**}_b$. Around and above t^{**}_b other instabilities may prevail. Note: $t_\perp = t_b$, see text. From Ref. [49].

SC transition in $(TMTSF)_2PF_6$ above 9-10 kbar

When pressure is applied, the nesting properties in $(TMTSF)_2PF_6$ are spoiled, which causes a decrease of the ordering temperature T_{SDW}, up to a critical pressure $p_c \approx 9 - 10$ kbar above which the metal-to-SDW transition temperature T_{SDW} is totally suppressed, Fig. 1.8. In an isobaric experiment in the pressure range above $p_c \approx 9 - 10$ kbar, decreasing temperature leads to the observation of a metal-to-SC transition below $T_{SC} \approx 1.2$ K [21]. The observation of the Meissner flux expulsion and of specific heat anomaly give the picture of bulk superconductivity, [54, 55].

The experimental temperature - pressure phase diagram of $(TMTSF)_2PF_6$, [47, 46], Fig. 1.1, 1.8 has SC in close proximity to the SDW phase, similar to the theoretical phase diagram for an interacting one-dimensional electron gas [50], where SDW lies adjacent to triplet superconductivity, see also Fig. 2.3. The strong sensitivity of T_{SC} to nonmagnetic impurities could point toward the existence of SC phase of p-wave symmetry, [52]. An absence of a coherence peak [53] and power-law behavior in the temperature dependent proton spin-lattice relaxation rate ($1/T_1 \propto T^3$) were argued [59] for some nodal structure on the Fermi surface indicative of non-s-wave symmetry. On the contrary, thermal measurements such as specific heat [55] and thermal conductivity [56] indicated a finite gap, rather than nodes, on the Fermi surface. None of the above experiments directly probe spin parity and they yield an ambiguous conclusion on the orbital symmetry. Much more attention has been refocused on the issue by upper critical field studies [57] showing that superconductivity persists up to more than 4 times the Pauli limit, a conventional limit for singlet superconductors [58], which strongly support a spin-triplet state. Recently, Lee *et al.* , [60] presented a pulsed NMR Knight shift study of ^{77}Se, measured in pressurized $(TMTSF)_2PF_6$. This study directly probes the spin susceptibility, which was observed to stay unchanged between the normal state and SC state, giving a strong support to a hypothesis of triplet, p-wave, superconductivity. The SC phase transition temperature is also suppressed by the application of pressure, at a rate of $\partial T_{SC}/\partial p \approx -0.07$ K/kbar, [51].

SDW - SC boundary region of the phase diagram

A salient feature of superconductivity in $(TMTSF)_2PF_6$ is the common boundary between SC and SDW phase. The region of the generalized pressure phase diagram, Fig. 1.1, where this boundary occurs is observed in $(TMTSF)_2PF_6$ at pressures around 9-10 kbar. It is not possible to observe SDW-to-SC transition directly in an isothermic, pressure changing experi-

ment, due to the experimental constraints, which impose isobaric measurements. However, in the first experimental reproduction of organic superconductivity under pressure [61], it was noticed that both metal-to-SDW and an SDW-to-SC transition, appear consecutively upon cooling if applied pressures are from a narrow pressure domain around the SDW - SC boundary. Such investigation of the phase diagram of analogous compound $(TMTSF)_2AsF_6$ by Brusetti *et al.* [47] has led to similar observations. Such a competition is also observed in $(TMTSF)_2ClO_4$ [62] where anion disorder is the driving parameter. Further, in $(TMTSF)_2PF_6$, using EPR at low field with helium gas pressure technique, Azevedo *et al.* [46], Fig. 1.8 also have reported a consecutive appearance of sharp metal-to-SDW and SDW-to-SC transitions on cooling in at least 200 bar wide pressure domain around the SC - SDW boundary.

Merging of SDW into the SC state around a critical pressure has been extensively studied, from a theoretical point of view. The precursory work of Schulz *et al.* [51], which studied the border between SDW and SC states in $(TMTSF)_2PF_6$ has suggested two possible scenarios, namely, the existence of a quantum critical point between SDW and SC or a first order transition line between the insulating and superconducting states, see also Fig.1.1, upper panel. It was also suggested by Yamaji that, at a pressure slightly lower than the critical pressure, a *semi-metallic* SDW phase is formed, with small pockets of unpaired charge carriers, because the SDW gap is not opened on the whole Fermi surface, [63]. In Fig. 1.9, upper right plot shows unnested area (shaded) of FS. These unnested parts of FS may be susceptible to opening of the SC gap. In a way, there is a coexistence of metallic and magnetic phases coming from different parts of the reciprocal space. The possibility of a microscopic coexistence of superconducting and SDW phases at lower temperature, was studied in details by Yamaji in the framework of a phenomenological mean-field theory of the competition between SDW and s-wave SC states in the Bechgaard salts, [64, 65, 66]. The conclusion was negative, because the density of states of the unpaired carrier pockets, left by the SDW ordering in the case of imperfect nesting, is strongly reduced compared to the density of states of the original metallic phase. Such reduction in effective FS size decreases the effective superconducting coupling $gN(0)$ drastically, which leads to an exponentially small critical temperature. In the case of such microscopical coexistence of phases, there is still the issue of, how could it be translated into the real space, *i.e.* how would the two phases organize in the bulk of the crystal. Would such a segregation be produced on a microscopic scale ($l \ll \xi$, where ξ is the correlation length), on a mesoscopic scale ($l \sim \xi$), or rather on a macroscopic scale ($l \gg \xi$), *i.e.* which would be more energetically favorable? Here it is appropriate to note that Machida

was the first to discuss a model of coexisting SC and SDW order parameters and suggested possible phase diagrams, although he did not refer to the real or reciprocal space separation of phases, [67].

Studies of the border between SDW and SC states in $(TMTSF)_2PF_6$ were limited, either due to the experimental constraints, or to the sample quality, while the theoretical studies lack any attempt on quantification of the relationship between the SC and SDW phases. This study was initiated in order to determine the qualitative and quantitative features of this phase space region of $(TMTSF)_2PF_6$. The aim was to give a good basis for succesful modelling of the observed coexistence, with a possible wider application in other systems characterized by proximity of SC and magnetic phases.

1.2 q1D cuprates (La, Sr, Ca)$_{14}$Cu$_{24}$O$_{41}$ - a complex system

Low-dimensional quantum spin systems, q1D cuprates of the formula $A_{14}Cu_{24}O_{41}$ (A=Sr, Ca, La, Y...) are composite materials. Spins and charges are arranged differently within chain and ladder structural elements. q1D cuprates are under intensive study experimentally, as well as theoretically, [68]. Two independent groups, Siegrist *et al.* and McCarron *et al.* synthetized single crystals in 1988. They also solved the structure, [70, 71]. Only the theoretical suggestions by Dagotto *et al.* [77] in 1992. led the experiment to concentrate on investigating this new family of materials. The studies intensified after the discovery of superconductivity in one of these materials, $Sr_{0.4}Ca_{13.6}Cu_{24}O_{41}$, under pressure [69]. Indeed, it was theoretically predicted [77, 72, 73] that compounds, possessing hole doped even-leg ladder structural elements, can produce superconductivity reminiscent of the superconductivity in the underdoped high-T_c cuprates; alternatively, they can undergo a charge-density-wave (CDW) transition.

These ideas seemed applicable to q1D cuprates which contain only the structural element of ladders. Extrinsic hole doping of the pure ladder materials like $SrCu_2O_3$ did not lead to the discovery of a collective state, [79]. Then, the composite q1D cuprates of (La, Sr, Ca)$_{14}$Cu$_{24}$O$_{41}$ family were investigated. (La, Sr, Ca)$_{14}$Cu$_{24}$O$_{41}$ structure contains interpenetrating subsystems of CuO_2 chains and Cu_2O_3 two-leg ladders with (Sr, Ca, La) atoms coordinated to the ladder layer [70, 71]. Here, the hole doping of the ladders is intrinsically provided by the chain subsystem [75, 76, 73]. These materials, entering either SC as in $Sr_{14-x}Ca_xCu_{24}O_{41}$, $10 \leq x \leq 13.6$ or CDW, as in $Sr_{14-x}Ca_xCu_{24}O_{41}$, $0 \leq x \leq 9$, [69, 78], proved to be an experimental realisation of a theoretical concept .

We will describe the essence of knowledge on the structure and properties of these materials, at the beginning of our research. We will show (as in the case of $(TMTSF)_2PF_6$) how the design of an artificial structure is related to it's function. Before presenting the experimental framework, it is necessary to clarify the concepts of spin chains and ladders and hole doping.

1.2.1 Models of spin and charge arrangements applicable to cuprate structures

A copper site in cuprate materials is experimentally characterized either with a spin $S = \frac{1}{2}$ of the unpaired $3d^9$ electron of Cu^{2+} ion or with a *hole*: an effective Cu^{3+} site with spin $S = 0$. More appropriately, Cu^{3+} site exists due

to a hole located in the $2p$ orbitals of the four oxygens coordinated to a Cu^{2+} ion. A hole within the O2p orbitals of the CuO_4 square is strongly bound to Cu^{2+} ion, due to hybridization of the orbitals. Spin $S = 0$ is observed due to the combination of the spin $S = \frac{1}{2}$ of the hole with $S = \frac{1}{2}$ of the unpaired $3d^9$ electron in a *Zhang-Rice* singlet, see also Sec. 2.2.1, [74]. Zhang-Rice singlet effectively decouples spin and charge degrees of freedom for a hole. This leads to a complementarity between the spin and charge arrangements in cuprate structures.

HTSC cuprates parent insulator compounds, where the characteristic structural element is a CuO_2 layer, are the best examples of planar $S = \frac{1}{2}$ antiferromagnets with isotropic and predominantly nearest-neighbor coupling. They show simple long-range order (LRO) of AF character, in agreement with theory which predicts an ordered ground state for the Heisenberg $S = \frac{1}{2}$ AF model on a 2D square lattice, Fig. 1.10. This means that spin-spin correlations decay to a non-zero constant as mutual spin distance grows. This non-zero value indicates that there is a LRO in the spin system.

The spin-$\frac{1}{2}$ AF Heisenberg chain with the nearest-neighbor AF coupling is also well understood, Fig. 1.10. A famous exact solution, found by Bethe many years ago, showed that the quantum fluctuations are strong enough to prevent long-range order and that spin-spin correlations decay slowly to zero as a power law of distance. Still they remain dominant over finite length scales, and thus the spin chain is also of AF character. One structural element of q1D cuprates is the CuO_2 chain. When all copper sites carry spin they become examples of the Heisenberg $S = \frac{1}{2}$ chain with the nearest-neighbor AF coupling. In both one and two dimensional AF models there is no spin gap, *i.e.* there is no cost in energy to create a spin excitation with $S = 1$.

To make the transition from the quasi-LRO in a chain to the true LRO that occurs in a layer, one can assemble chains to make ladders, Fig. 1.10. Apparently, the ladder structures are somewhere inbetween the 1D and 2D case. But the crossover between the 1D and 2D case is not smooth at all. The theoretical investigations indicated that the Heisenberg model on two leg-ladder should show a *spin gap*. That is, a finite energy is necessary to create a spin excitation with $S = 1$, making the ladder systems qualitatively different from the chains and layers. The spin gap presence is relatively obvious in the *strong coupling* limit. In this limit coupling along the rung is stronger than along the leg of the ladder, $J_\perp > J_\parallel$. Thus, the ladder ground-state may be regarded as a product of spin singlets, one per rung, Fig. 1.10. The overall spin of the ladder in the ground-state is zero. It costs $J_\perp$ to create a triplet on the rung. If such excitations are created, they may propagate along the ladder, but their correlations decay exponentially, due to the finite spin-gap. Due to the purely short-range correlations this state is also referred

to as a *gapped spin-liquid*.

Final step is the concept of hole-doped ladders, Fig. 1.10. At low hole doping, and in the strong-coupling limit, the system prefers combining two holes in the same rung, in order to save the energy. Otherwise, two holes would break two singlets, producing substantial energy cost. After introducing this concept of pairs' formation, it is only natural to accept the possibility of establishing the superconducting state. Binding pairs of holes gives them a bosonic character, which is a necessary step on the way to superconductivity. However, this alone does not suffice because, in such a low dimensional system, another collective state competes, namely, a charge density wave. The balance between the two and the question which one dominates depends on the parameters of the model and, more generally, on residual interactions between hole pairs, all of which is hard to predict theoretically, [50, 80, 77]. The theoretical overwiev of the competition betweeen the possible ground states of q1D systems, as well as more detailed concept of ZR singlet and SC in doped ladders, are given in Chapter 2.

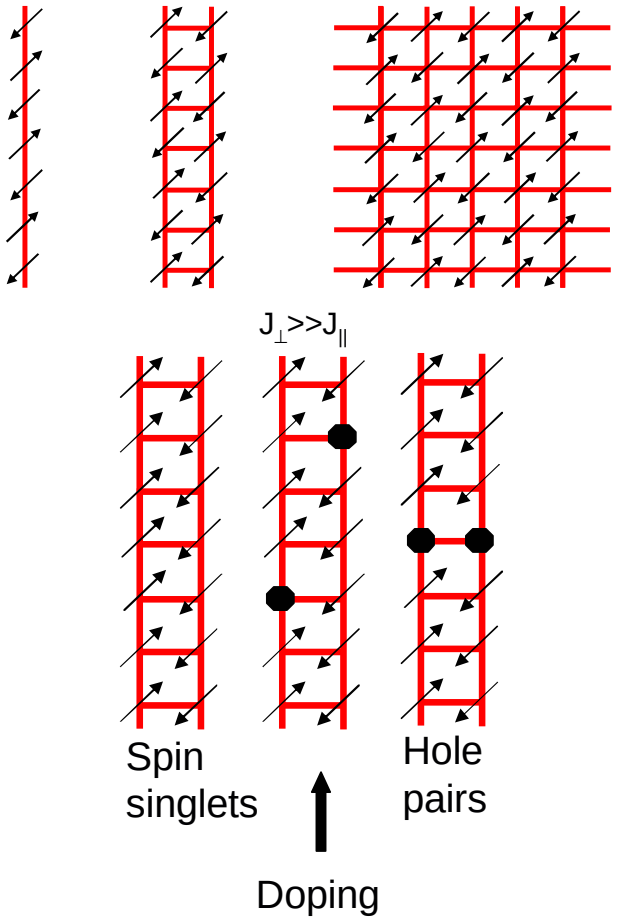

Figure 1.10: Upper panel: The Heisenberg $S = \frac{1}{2}$ antiferromagnetic model on chain, two-leg ladder and 2D square lattice. Lower panel: Suggested mechanism of hole-pairing in the two-leg ladders: When the coupling along the ladder rung $J_\perp > J_\parallel$ is stronger than along the ladder legs, the ground state is a direct product of spin singlets appearing on the rungs. Doping individual holes to the ladder leads to destroying the singlets, which is energetically unfavorable. Therefore, the holes tend to pair-up on the rungs, [68, 81].

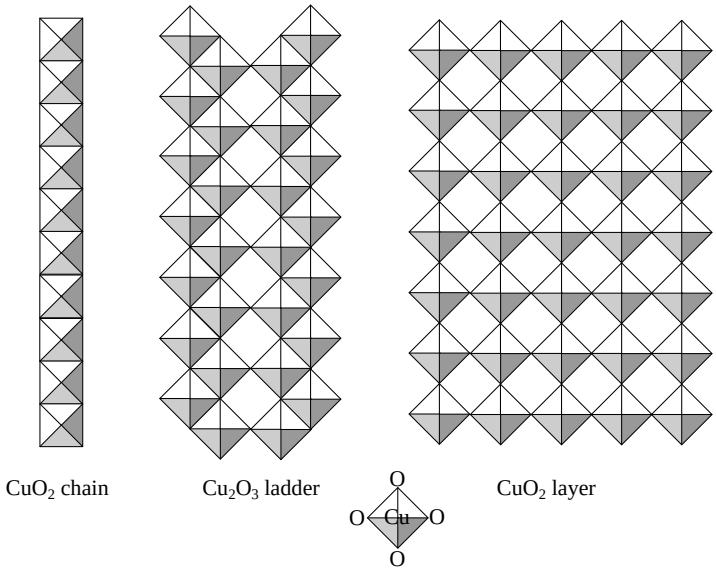

Figure 1.11: The basic building block of cuprate structures is a CuO_4 square. Corner and/or edge sharing arrangements of these squares produce different substructures like chains, ladders and layers.

1.2.2 Crystallographic structure of q1D cuprates $(La, Sr, Ca)_{14}Cu_{24}O_{41}$

Copper and oxygen form the functional structure of the q1D cuprates. They form two different substructures in these composite materials: CuO_2 chains and Cu_2O_3 two-leg ladders. Cu ions are coordinated to four oxygen ions - CuO_4 square is a basic building block, Fig. 1.11. The layer formed in HTSC cuprates is formed of solely corner sharing (oxygen sharing) CuO_4 squares. Chains may be regarded as strings of edge sharing CuO_4 squares. The two-leg ladders are arranged out of zig-zag chains composed of edge sharing CuO_4 squares, and the zig-zag chains touch at the corners of CuO_4 squares. The ladders are thus composed of both corner and edge sharing squares.

In Fig. 1.12 the formation of chains and ladders layers is shown, [70, 71]. Strings of (Sr, Ca, La) atoms enter between these layers. Strictly speaking, these atoms are coordinated to the ladder layer. They enter the spaces opened between the zig-zag chains. Thus, Sr, Ca, La atoms strings and the ladder layer form the ladder subsystem, while only CuO_2 chains in parallel arrangement form the chain subsystem. If the CuO_4 squares were ideal there would always be $1 : \sqrt{2}$ incommensurability along the chains and ladders subsystems (this is simply the ratio between a diagonal and a side of an ideal square). In the real q1D cuprate materials all the squares are distorted, but

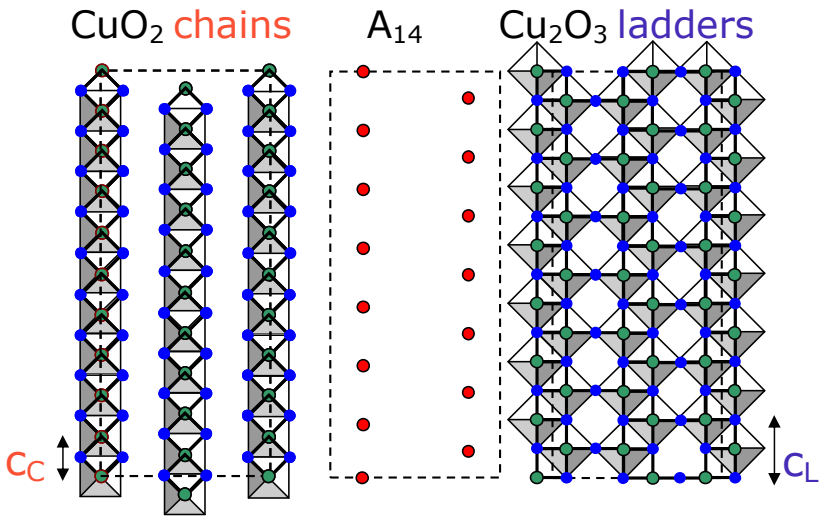

Figure 1.12: Inbetween every Cu_2O_3 ladder and CuO_2 chain layer (Cu - green, O - blue) enters a layer of strings of Sr, Ca, La atoms (red). These atoms are coordinated to the ladder layer. Thus two subsystems are formed. The c parameter differs and the subsystems are incommensurate: ladders c_L ≈3.9 Å, chains c_C ≈2.75 Å. Still, the subsystems are very close to commensurability at $10 \times c_C = 7 \times c_L$. Due to this and for practical reasons, an approximate superstructure cell with the parameter c'≈27.5 Å is then used, [70, 71]. This cell is outlined by a dashed line.

chain and ladder subsystems are still incommensurable. These distortions related to incommensurability lead to additional modulations of crystallographic positions, *i.e.* one subsystem is weakly modulated to adjust to the other and *vice versa*. These effects may be regarded as an intrinsic source of disorder, [82]. The unit cells in the $a-c$ plane of the two subsystems are different along c-axis: ladders c_L ≈3.9 Å, chains c_C ≈2.75 Å. For practical purposes, the fact that the subsystems are very close to commensurability at $10 \times c_C = 7 \times c_L$ leads to an approximate superstructure cell with the parameter c'≈27.5 Å. This cell in the $a-c$ plane is denoted in Fig. 1.12.

The orthorombic crystals of $(La, Sr, Ca)_{14}Cu_{24}O_{41}$ q1D cuprates are built by alternated stacking of chain and ladder subsystems along the b-axis, Fig. 1.13. Both b- and a- unit cell parameters are common to the subsystems and to the crystal as a whole. The composition of Sr, Ca, La strings dictates the unit cell parameter in b-direction.

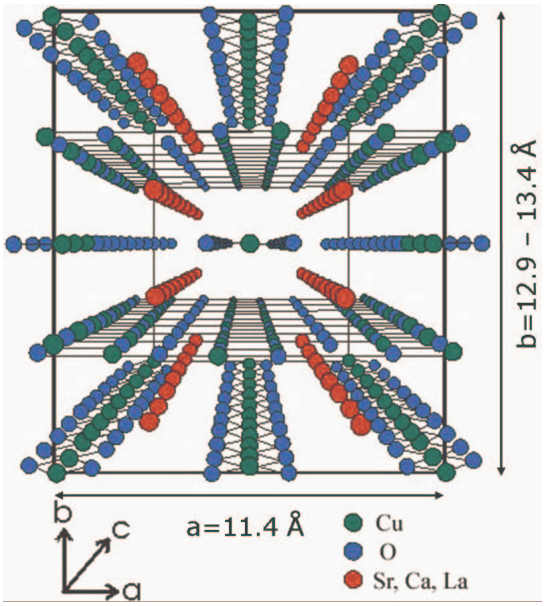

Figure 1.13: A stereo drawing of $(La, Sr, Ca)_{14}Cu_{24}O_{41}$ structure. The crystal system is orthorombic. The view is along the c-axis. The alternative stacking of CuO_2 chain and Cu_2O_3 ladder layers along with the included strings of Sr, Ca, La atoms (shown in red) is best understood in this view. Both chain and ladder subsystems and the crystal as a whole have the same a ≈11.5 Å and b ≈12.9 - 13.4 Å cell parameters. The b-parameter is the only one that is significantly dependent on the Sr, Ca, La composition. Subsystems are incommensurate along the direction of the c-axis, [70, 71].

1.2.3 Electronic structure of q1D cuprates (La, Sr, Ca)$_{14}$Cu$_{24}$O$_{41}$

The directions of Cu-O bonds characterize the dimensionality of the subsystems. These bonds are shown as lines which connect the atoms in Fig. 1.14. The chains are a structure of pronounced 1D nature where two neighbouring Cu^{2+} ions along the chain, are connected via two 90^o Cu-O-Cu exchange interaction links of ferromagnetic character. But one chain is completely decoupled from the other. In Fig. 1.12 the pattern of CuO_4 squares and interatomic bonds (black lines) seems to form a continuous ladder layer, of apparent 2D nature. The ladders, as a 1D structure, emerge from this picture as separate entities due to the following: strong antiferromagnetic 180^o Cu-O-Cu bonds make a ladder, while the interladder coupling is very weak both because of a very weak ferromagnetic 90^o Cu-O-Cu bond and triangular arrangement of Cu atoms between neighboring ladders, which results in frustration. Thus, the ladder layer may be recognized as composed of separate, decoupled ladders, denoted in Fig. 1.14.

180^o Cu-O-Cu bond forms due to the following: Cu^{2+} ion has a $3d^9$ configuration with the single hole occupying an antibonding orbital. This leads to an exceptionally strong ($J \approx 0.13$ eV) superexchange interaction of two neighboring Cu^{2+} ions through $dp\sigma$ overlap with the $2p$ orbital of the oxygen ion inbetween [73]. Here originates a planar structure of CuO_2 layers, composed of CuO_4 squares that are all corner sharing, Fig. 1.11. The 180^o Cu-O-Cu bonds are oriented equivalently along both directions within this layer. On the contrary, in the ladders, it should be noted that $J_{\parallel}$ along the ladder legs is larger than $J_{\perp}$ along the ladder rungs, thus further pronouncing one-dimensionality of this structure.

The electronic structure of parent compound $Sr_{14}Cu_{24}O_{41}$ was calculated *ab initio* by the linear-muffin-tin-orbital method, [83]. The calculations were performed on a small approximative unit cell containing one formula unit of $Sr_{14}Cu_{24}O_{41}$. However, this calculation was performed under the assumption that the system was metallic, and that led to finite density of states (DOS) at E_F, which contradicts the experimentally observed insulating behavior. The total and partial DOS is shown in Fig. 1.15, the Fermi energy is set at $E_F = 0$. Still, the total density of states for the valence band is compared with photoemission experiments with fairly good agreement. Around the Fermi energy there exist quasi-one-dimensional bands originating from the ladder and chain subsystems. The bands can be fitted by simple q1D tight-binding dispersions with only nearest-neighbor and next-nearest-neighbor hoppings along and between the ladders (or chains) considered. The nearest-neighbor interladder hoppings are estimated to be 5 - 20 % of the intraladder ones.

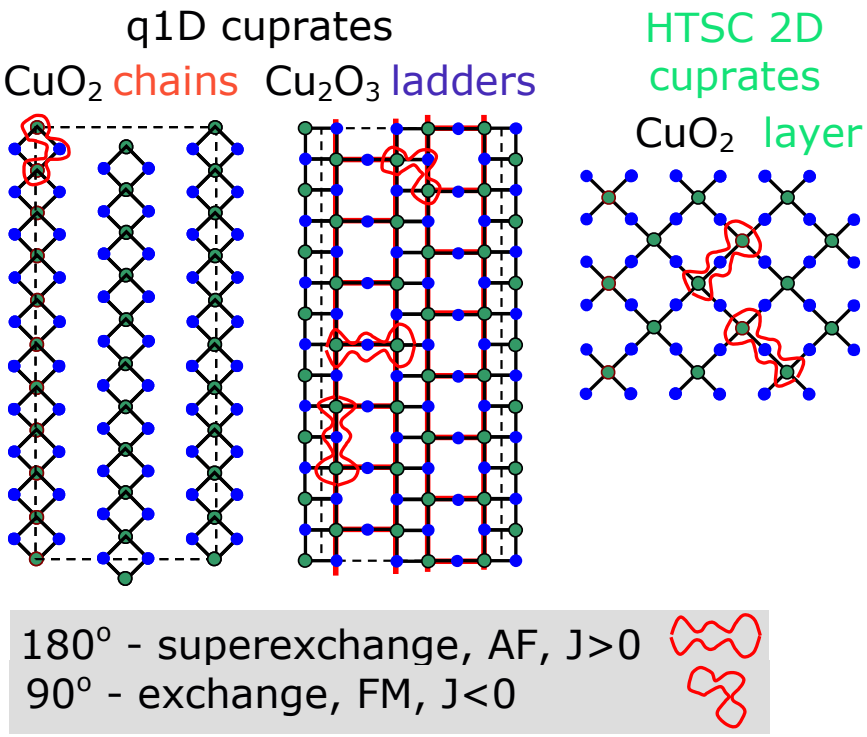

Figure 1.14: The direction of Cu-O bonds characterizes different cuprate structures: chains, ladders and planes. The 180^o Cu-O-Cu bonds are mutually orthogonally oriented within the square lattice layer, thus giving to HTSC cuprates their 2D nature. Chains and ladders also form layers, but the chains are mutually decoupled, which gives the chain subsystem it's 1D nature. The pattern of strong antiferromagnetic 180^o Cu-O-Cu bonds makes a ladder, and the interladder coupling is very weak both because of a very weak ferromagnetic 90^o Cu-O-Cu bond and triangular arrangement of Cu atoms between neighboring ladders, which results in frustration. Therefore, although ladders form layers, the ladder subsystem is also 1D in nature.

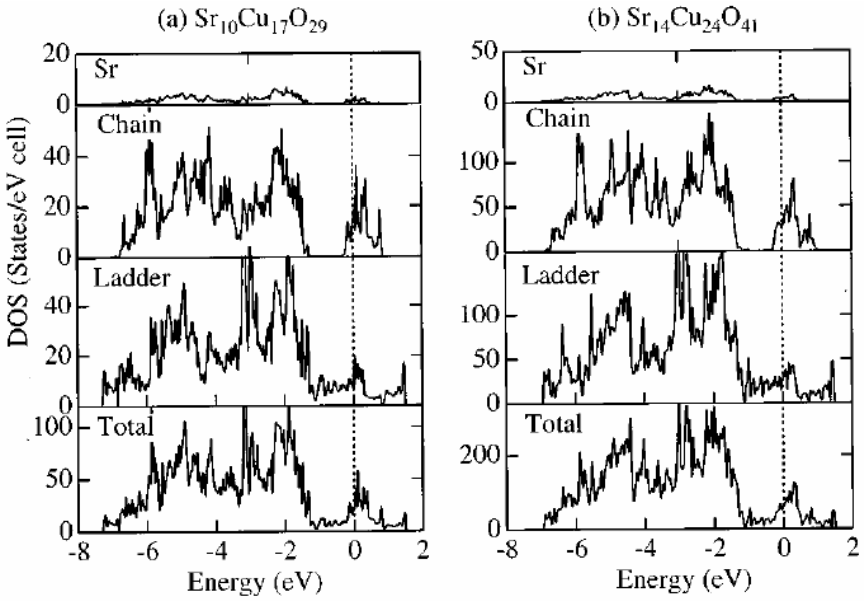

Figure 1.15: The total and partial density of states, of chains and of ladders, for a small approximative unit cell containing one formula unit of $Sr_{14}Cu_{24}O_{41}$.

The obtained interladder hopping seems non-negligible, contradicting the observed room temperature dc conductivity anisotropy, and despite that the strong correlation effects, such as hole-pairing are expected to increase the anisotropy on cooling. At RT these band anisotropy calculations seem to be consistent only with the optical absorption measurements, [84].

1.2.4 Hole distribution

The doping in composite (La, Sr, Ca)$_{14}$Cu$_{24}$O$_{41}$ materials is completely intrinsic, simple stoichiometry confirms this. In Sr$_{14-x}$Ca$_x$Cu$_{24}$O$_{41}$ materials there are 6 holes per formula unit, hole count $\delta_h = 6$. Nonisovalent substitution of Sr^{2+} or Ca^{2+} with La^{3+} (or Y^{3+}) reduces δ_h. There are 4 formula units per approximative superstructure cell as depicted in Fig. 1.13, so, for Sr$_{14-x}$Ca$_x$Cu$_{24}$O$_{41}$ materials there are 24 holes in this cell. This amounts to the hole density of $6 \times 10^{21}\text{cm}^{-3}$. The arrangement of these holes in a given subsystem is complementary with the spin arrangement, Fig. 1.16. Simple stoichiometric considerations lead to the arrangement as shown in this figure, where all the holes are found in the chains. Madelung energy calculations lead to the same conclusion for $x = 0$ material, but Sr-by-Ca substitution leads to the appearance of the hole transfer to the ladders [85]. The tendency of holes to move from chains to ladders is additionally proved by the calculation result for $x = 14$ (although, this material is not synthetized) where all holes are transferred to ladders. One of the basic assumptions of these calculations is the initial arrangement of the holes whose interactions and rearrangement to the lowest potential state are then calculated. In choosing these initial parameters lies a possibility that the results of these calculations do not refer to the experiment correctly. Still, they do confirm the concept of self-doped holes. This concept is also confirmed by bond-valence-sum (BVS) calculations by Kato *et al.* , [86] based on the crystallographic data for Cu-O bond lengths, [70, 71]. Kato *et al.* calculated, for $x = 6$ material, a slight increase in hole concetration in the ladder, when compared to $x = 0$ material.

Various experimentally observable properties of (La, Sr, Ca)$_{14}$-Cu$_{24}$O$_{41}$ materials are undoubtedly related to the redistribution of the holes and spins in the two subsystems. The parent compound Sr$_{14}$Cu$_{24}$O$_{41}$ has a rather high dc conductivity, which is believed to originate in ladders, along the legs of ladders, of about 300 $(\Omega\text{cm})^{-1}$ at 300 K, showing an anisotropy σ_c:σ_a:$\sigma_b \approx 1000$:100:1 [84]. However, starting from the 'simple' Sr$_{14}$Cu$_{24}$O$_{41}$, it is not clear what the mechanism of dc conductivity is. The basic question is where the holes at room temperature in Sr$_{14}$Cu$_{24}$O$_{41}$ are, and how are the holes redistributed between chains and ladders when temperature and Ca-content are changed.

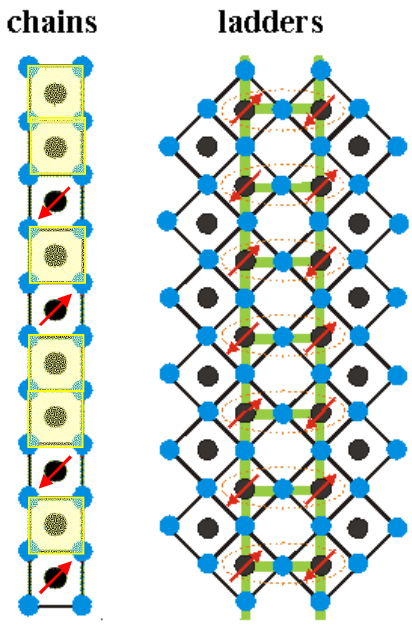

Figure 1.16: The complementary arrangement of holes and spins in the subsystems of $Sr_{14-x}Ca_xCu_{24}O_{41}$ (shown for one formula unit). Cu^{2+} ion of spin $S = \frac{1}{2}$ is denoted with red arrows, while the holes, which reside in the $2p$ orbitals of oxygens surrounding Cu^{2+} ions (whose spins form Zhang-Rice singlets with the spins of holes) are denoted by yellow squares. For $Sr_{14-x}Ca_x$-$Cu_{24}O_{41}$ materials, stoichiometrical considerations indicate that all 6 holes per formula unit reside in the chains. Madelung energy calculations denote the hole transfer upon Sr-by-Ca substitution (see text).

Evidence for stronger redistribution

The study of possible transfer of holes from chains to ladders was experimentally initiated in the work of Osafune *et al.* , [75]. They report RT optical conductivity $\sigma(\omega)$ measured along the ladder legs, $E||c$. Single crystals of materials $Sr_{14-x}Ca_xCu_{24}O_{41}$, $x = 0, 3, 6, 10, 11$ were studied. They also measured an Yttrium substituted material, $Y_3Sr_{11}Cu_{24}O_{41}$. Y^{3+} is nonisovalent to Ca^{2+} and Sr^{2+}, and thus this material has $\delta_h = 3$, lower than $\delta_h = 6$ of isovalent substituted $Sr_{14-x}Ca_xCu_{24}O_{41}$materials.

The optical conductivity spectrum of $Y_3Sr_{11}Cu_{24}O_{41}$ is typical of insulators, Fig. 1.17. The spectrum is characterized by a peak at 2.0 eV. The most possible origin of this peak is the charge-transfer excitation between Cu3d and O2p states which is also observed in the parent insulators of HTSC cuprates, [87]. The question for the composite material like $Y_3Sr_{11}Cu_{24}O_{41}$ is whether this peak has to be ascribed to the holes in the ladders or in the chains. Taking into account the Madelung energy and BVS calculations, the peak at around 3 eV for $Sr_{14-x}Ca_xCu_{24}O_{41}$ might be attributed to the holes in the chains.

The principal observation of Osafune *et al.* was that for $Sr_{14-x}Ca_x$-$Cu_{24}O_{41}$ materials Cu3d-O2p peak spectral-weight (SW) decreases and the conductivity in the low-frequency region below 1.2 eV increases with x. Such SW transfer is essentially the same as the transfer observed when the parent insulators of HTSC cuprates are doped with carriers. As the substitution of isovalent Ca does not change the hole count in $Sr_{14-x}Ca_xCu_{24}O_{41}$ material, the observed SW transfer should be attributed to a redistribution of holes between chains and ladders.

This transfer may also be quantified as presented in Fig. 1.18. The integrated conductivity N_{eff} is assumed to be proportional to the hole number; $\delta_h \propto N_{eff}(\omega) \propto \int_0^{\omega} \sigma(\omega')d\omega'$. Since the conductivity below 1.2 eV is attributed to the ladders, the values of $N_{eff}(\omega = 1.2eV)$ are regarded as proportional to the number of holes in the ladders. Here Osafune *et al.* assumed (correctly, as we will discuss later) that 5 holes reside in chains and one in ladders for $x = 0$. SW transfer increases with x and $N_{eff}(\omega = 1.2eV)$ reaches 0.20 for $x = 11$. This implies $\delta_h = 2.8$, *i.e.* almost half of the holes seem to be transferred in the ladders. Number of holes on the copper site in the ladders may be recalculated into the effective valence of copper. In the undoped ladder there are no holes and the average Cu valence is +2, thus coppers in the hole doped ladders have the average valence $+2 + N_{eff}(\omega = 1.2eV)$. From the ladder valence the basic stoichiometry gives the chain Cu valence. The respective dependence of Cu valence on Ca substitution is shown in the inset of Fig. 1.18.

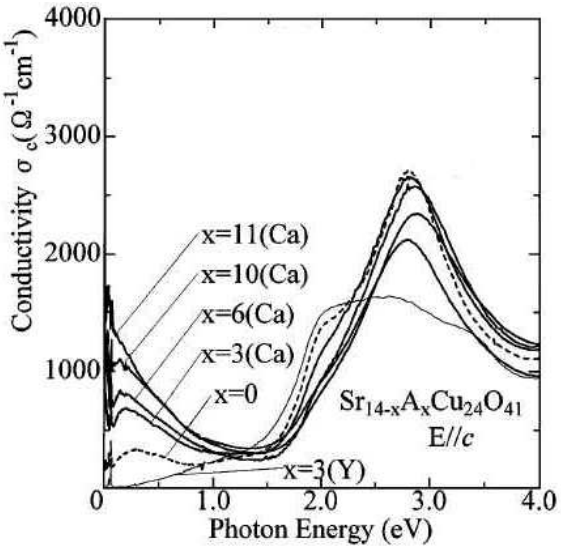

Figure 1.17: Optical conductivity *vs.* frequency, $\sigma(\omega)$, measured at room temperature along the ladder legs, $E||c$. Materials $x = 0, 3, 6, 10, 11$ were studied, as well as Y substituted $Y_3Sr_{11}Cu_{24}O_{41}$. The conductivity was obtained from the Kramers-Kronig transformation of the reflectivity spectra. From Ref. [75].

The conclusion from this analysis is that there is a redistribution of holes from chains to ladders, through the interpretation of the experimentally observed SW transfer process induced by the Ca substitution. However, this analysis provides only information on the relative change in the hole number. The absolute hole counts in the chains and ladders of $x \neq 0$ were based on the assumption for the hole counts in $x = 0$. An another important remark would be that the holes in the chains seem to be well localized, since the charge excitations attributed to the chains start only above 2.0 eV.

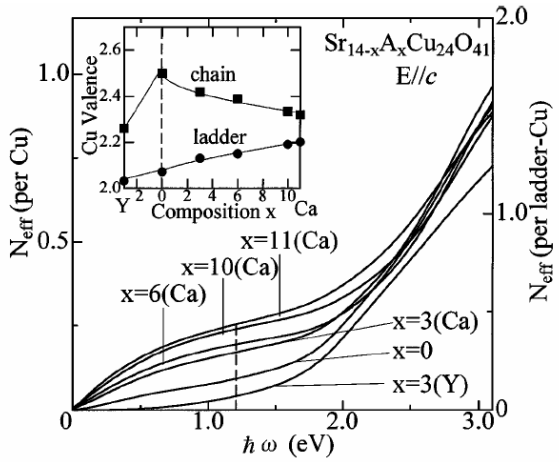

Figure 1.18: Effective electron number N_{eff} per Cu site (left-hand scale) from the conductivity sum is plotted as a function of energy for various compositions x. N_{eff} per ladder Cu site is indicated on the right-hand scale. The valences of both chain- and ladder-Cu estimated from $N_{eff}(\omega = 1.2eV)$ for each composition are plotted in the inset. From Ref. [75].

Evidence for weaker redistribution

The experiment which approached the hole distribution in (La, Sr, Ca)$_{14}$-Cu$_{24}$O$_{41}$ most directly is polarization-dependent near-edge x-ray absorption fine structure (NEXAFS), performed by Nücker *et al.* [76]. The excitation process in NEXAFS involves highly localized O1s core level. Orienting the electric field vector of the incident radiation, **E**, parallel to the crystallographic axes, allows one to investigate specifically the O2p orbitals oriented likewise, and thus gain site-specific information on the hole distribution. Three inequivalent oxygen sites appear in the NEXAFS measurements of O1s core levels spectra. With each of the inequivalent sites, a different Cu-O bond configuration is associated, Fig. 1.19. There is Cu-O-Cu interaction with 90^o geometry at the O(c) sites of the chains. There are straight bonds (180^o) connecting the Cu(l) sites in the two legs of a single ladder via the rung O(2) sites; and there is a different situation for the O(1) sites of the legs, which form bonds to each of the three neighboring Cu(l) atoms. Assuming that, analogous to the situation in HTSCs, only σ bonds formed between Cu3d and O2p states contribute to the spectral weight near the Fermi level, E_F, there are only five inequivalent O2p orbitals in the a, c plane which may contribute to spectral weight in O1s NEXAFS.

Nücker *et al.* investigated single crystals of various nonisovalently, (La/Y, Sr, Ca)$_{14}$Cu$_{24}$O$_{41}$, and isovalently, Sr$_{14-x}$Ca$_x$Cu$_{24}$O$_{41}$, x = 0, 5, 9, 11.5, 12, substituted materials. The nonisovalent materials have hole count δ_h of less than 6 (per formula unit). The observation that for La$_3$Sr$_3$Ca$_8$Cu$_{24}$O$_{41}$, $\delta_h = 3$, Y$_3$Sr$_{11}$Cu$_{24}$O$_{41}$, $\delta_h = 3$ and La$_2$Ca$_{12}$Cu$_{24}$O$_{41}$, $\delta_h = 4$, spectra can be attributed to only one type of O sites, which is furthermore almost symmetric within the a, c plane, is readily understood if the holes in the $\delta_h < 6$ materials occupy exclusively sites in the chains. In the materials $\delta_h = 6$, *i.e.* Sr$_{14-x}$Ca$_x$-Cu$_{24}$O$_{41}$, however, this symmetry is obviously broken. NEXAFS spectra unambiguously show that holes are found in all O sites and that distribution is no more symmetric between orbitals aligned along a and c axis.

The results are shown in Fig. 1.20. Number of holes refers to the total number of holes found in one of the subsystems in the orbitals oriented either along the a- or along c-, *i.e.* along the rungs and legs of ladders, respectively. This number changes with Ca substitution x. H1 denotes the spectra attributed to the chains subsystem, where distribution is still almost symmetric between a and c orientations, and the total number slightly changes from 5.2 to 4.9, that is, approximately 5 holes per formula unit are found in the chains of Sr$_{14-x}$Ca$_x$Cu$_{24}$O$_{41}$, independently of x. H2 denotes the spectra attributed to the ladders subsystem. Initially, for $x = 0$, holes are found in orbitals aligned along c, along the legs of the ladder, denoted H2 $E||c$. With

substitution x, they become transferred into the orbitals, aligned along a, of the rung oxygen, denoted H2 $E||a$. This transfer within the ladder seems more pronounced than the transfer between the chain and ladder systems.

NEXAFS experiment unambigously shows that there are holes in ladders already for $x = 0$. The number of holes increases from 0.8 for $x = 0$ to 1.1 for $x = 12$. This experiment confirms the assumption of Osafune *et al.* , that one hole resides in the ladders of $x = 0$. However, it is somewhat contradictory to their results, regarding the fact that the observed redistribution of holes from chains to ladders is lower. This experiment provides the absolute hole counts in the chains and ladders, while Osafune *et al.* provide only relative numbers. Therefore, we consider the NEXAFS results more reliable. That is, while the hole transfer unambigously occurs, this is probably not to the extent suggested by Osafune *et al.* .

In the presented outline of the hole distribution between the subsystems at RT, the question whether there is any redistribution at lower temperatures still remains. Studies of the hole/spin patterns within the subsystems provide an additional information on the hole distribution at RT, as well as at low temperatures. They will be presented in the following Sections.

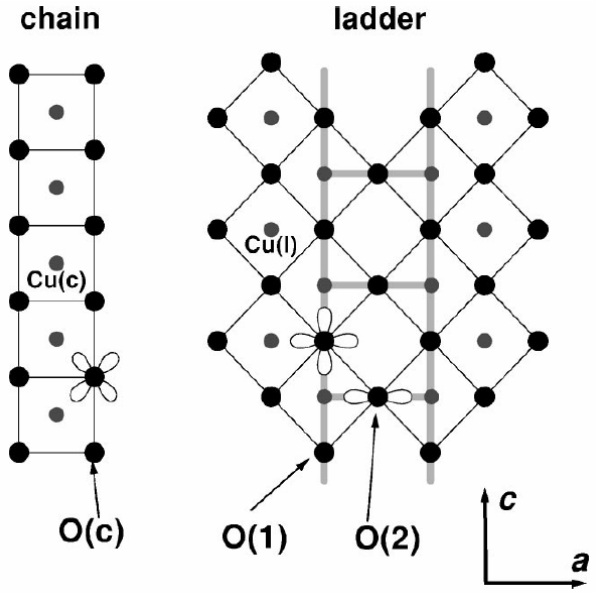

Figure 1.19: Three inequivalent oxygen sites appear in the NEXAFS measurements. A different Cu-O bond configuration is associated with each site . Chain oxygen orbitals O(c) take part in Cu-O-Cu interaction with about 90^o geometry. Ladder oxygens O(1,2) take part in the straight bonds (180^o), within the *legs* or within the *rungs*. Consequentially, orienting the electric field vector of the incident radiation, **E**, parallel to the crystallographic axes, allows one to investigate specifically the O2p orbitals oriented likewise, and thus gain site-specific information on the hole distribution. From Ref. [76].

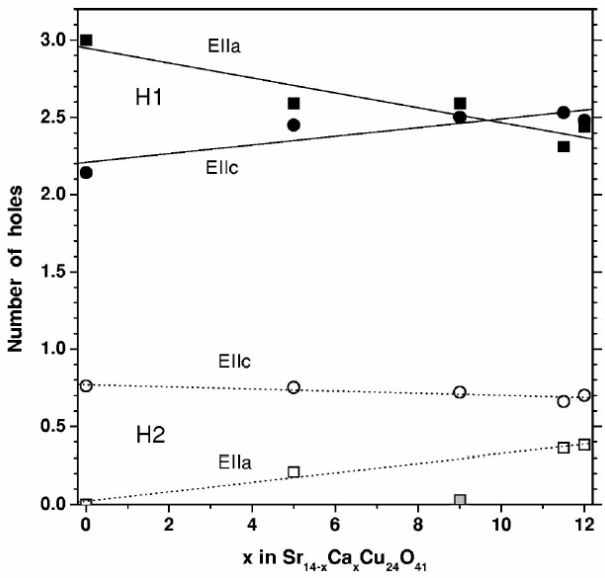

Figure 1.20: Hole count per formula unit as derived from renormalized spectral weights in NEXAFS for $Sr_{14-x}Ca_xCu_{24}O_{41}$. Contributions from O2$p$ orbitals oriented along the a- and c-axes in chain (H1) and ladder (H2) subsystems are shown. From Ref. [76].

1.2.5 Chains subsystem

Magnetic susceptibility

The magnetic susceptibility is a bulk technique which should not be able to discern between the subsystems. Still, the magnetic properties of (La, Sr, Ca)$_{14}$Cu$_{24}$O$_{41}$ have been studied by susceptibility, [88, 89, 84], and these results have lead to initial results on the arrangement of spins (and complementarily, the holes) in the chains.

In Fig. 1.21 the temperature dependence of susceptibility χ, measured by Motoyama *et al.* [84] is shown. Various single crystals of isovalently and nonisovalently substituted materials of different hole counts and different chain/ladder distributions were studied. The susceptibility for the pure two-leg ladder compound SrCu$_2$O$_3$ is shown for comparison. Carter *et al.* [89] argued that, for Cu$_2$O$_3$ ladders found in the composite compounds, the susceptibility should be negligibly small, if it can be approximated by the susceptibility of the isostructural SrCu$_2$O$_3$ that has a spin-gap of 420 K. This immediately leads to the conclusion that only spins in chains contribute to the susceptibility of the composite q1D cuprates, and that susceptibility measurements investigate the chain subsystem. Further, La$_6$Ca$_8$Cu$_{24}$O$_{41}$ material (hole count, $\delta_h = 0$) shows the susceptibility as expected for the Curie paramagnetism of the chain with uncorrelated, free spins on all the ten sites, $10 - \delta_h = 10$. Curie paramagnetism of lower magnitude is observed also for Y compounds, Y$_3$Sr$_{11}$Cu$_{24}$O$_{41}$, $\delta_h = 3$, $10 - \delta_h = 7$ free spins and Y$_1$Sr$_{13}$Cu$_{24}$O$_{41}$, $\delta_h = 5$, $10 - \delta_h = 5$ free spins (all the holes are found in the chains in nonisovalently substituted compounds, see previous Section).

Taking into account the results of Nücker *et al.* (previous Section) we note that isovalently substituted compounds Sr$_{14-x}$Ca$_x$Cu$_{24}$O$_{41}$, $\delta_h = 6$, have one hole transferred to the ladders. Thus, they have 5 spins (Cu^{3+} sites) for every ten chain sites. The susceptibility of these 5 spins deviates from the Curie behavior for free spins and shows a decrease in χ towards low temperatures. A strong decrease of susceptibility is most pronounced for the parent compound Sr$_{14}$Cu$_{24}$O$_{41}$ below 70 K. Thus, the susceptibility data indicate that the ground state of CuO$_2$ chains is also characterised with a spin gap. The question on the nature of ordering which leads to the spin-gapped state in the chains is still remaining.

Matsuda *et al.* [88] and Carter *et al.* [89] found that a simple AF dimer model gives a good fit to the low temperature part of χ. The AF dimer model is based on organizing spins along the chain into isolated antiferromagnetically coupled pairs. The solid line in Fig. 1.22 shows the result of the AF dimer model $\chi = 2N_D(g\mu_B)^2/kBT\left[3 + e^{(J/k_BT)}\right]$ with the number of

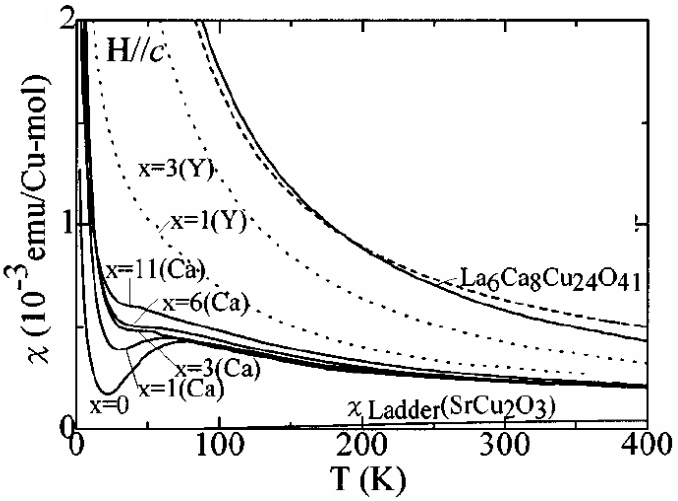

Figure 1.21: The temperature dependence of the magnetic susceptibility, χ, measured with magnetic field oriented along the c-axis. Various single crystals of isovalently and nonisovalently substituted materials of different hole counts and different chain/ladder distributions were studied. The dashed line is the expected Curie paramagnetism when all spins in the 10 chain Cu sites are free. From Ref. [84].

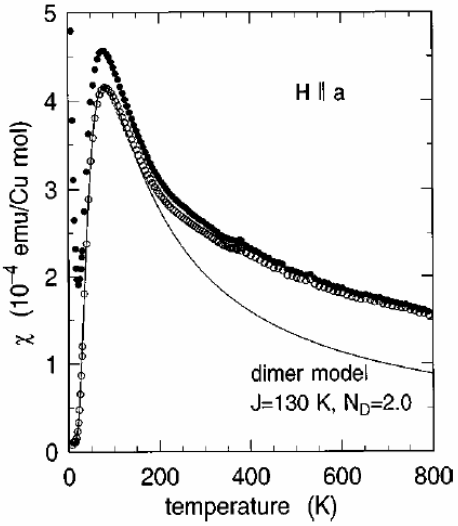

Figure 1.22: Comparison for $x = 0$, of the experimentally measured temperature dependence of the magnetic susceptibility, χ, represented by solid dots, Motoyama *et al.* [84], and the dimer model, $N_D = 2.0$ per formula unit, indicated by a line, as described in the text.

dimers $N_D = 2.0$ per formula unit ($g = 2.05$ along the a direction) and the intradimer exchange $J = 130$ K. The deviation of χ from the dimer model at high temperatures can be attributed to the contribution from the ladders. In the end, even the susceptibility method as a bulk measurement leads the way towards establishing the model of ordering in the chains.

Inelastic neutron scattering and X-ray diffraction

Early inelastic neutron scattering (INS) experiments by Matsuda *et al.* , [92] directly investigated spin ordering in the parent compound $Sr_{14}Cu_{24}O_{41}$, at low temperatures ($T = 8$ K). The observed spin excitations were interpreted by the authors with a model where two different types of antiferromagnetically coupled dimers exist, characterized by intradimer spin separation of two chain parameters and four chain parameters, $2c_C$ ad $4c_C$, respectively. Due to the complementarity of the spin and holes arrangements, in this model 6 holes appear for every 10 chain sites. The chain superstructural periodicity due to the complementary hole ordering, expected for this model, is equal to 10 c_C. More sensitive measurements of the same type, were performed also at the lowest temperatures, 5-20 K, by two independent groups of Eccleston *et al.* , [91] and Regnault *et al.* , [90]. These authors did not see any evidence of larger, $4c_C$ dimers in their results. Their interpretation was based on a model with only $2c_C$ AF dimers. Interdimer distance was found to be three chain parameters, $3c_C$, Fig. 1.23. Quantitatively, there is no difference to the previous model, since two dimers (as in the interpretation of the susceptibility results above) and 6 holes appear again for every 10 chain sites. The chain superstructure periodicity in this model is $5c_C$. Due to the low internal symmetry ($5c_C$=$2c_C$ intradimer+ 3 c_C interdimer) of such superstructural motif, energy gained from creating the superstructure would probably be smaller than the frustration due to the chain subsystem's interaction with the ladder subsytem. That is, the observation of such a superstructure in X-ray diffraction measurements is ascribed to the interactions between the subsystems and not to the charge-order in chains, [82, 93].

Still, direct observation of the lattice distortion due to the complementary charge-order is necessary to confirm the AF dimer model. Indeed, X-ray diffraction (XRD) results for $Sr_{14}Cu_{24}O_{41}$ directly point to structural change related to charge-order, Cox *et al.* [94]. These measurements were performed at 50 K. The observed periodicity was equal to 4 chain parameters. This observation is possible due to higher internal symmetry ($4c_C$=2 c_C intradimer+ 2 c_C interdimer) of such superstructural motif. This result leads to the choice of the model with the chain hole count 5, Fig. 1.23. In this model 2.5 AF dimers would appear per 10 Cu sites.

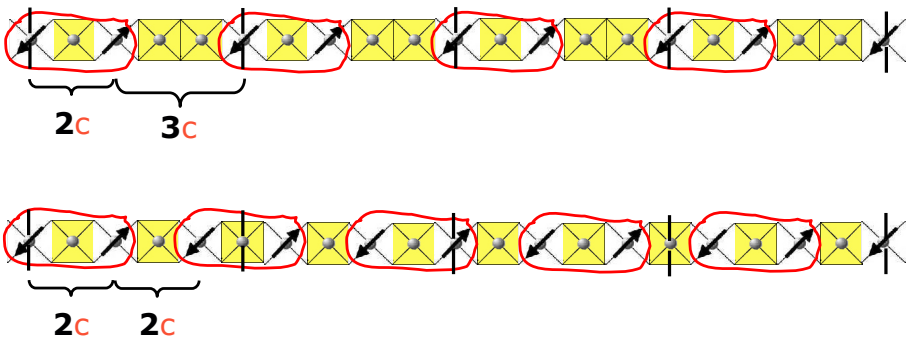

Figure 1.23: Spin (red arrows) arrangement into the AF dimer (encircled) patterns with the complementary charge-order of the holes (yellow squares) for $x = 0$ chains. The upper model, periodicity 5 c_C, chains hole count 6, is resulting from INS measurements at 5-20 K. The lower model, periodicity 4 c_C, chains hole count 5, is resulting from XRD measurements at 50 K.

We note the contradiction between the observed charge-order (by XRD) and spin ordering (by INS), *i.e.* chain hole counts of 5 and 6, respectively. However, the INS experiments were performed at lower temperatures than XRD. In order to resolve the contradiction we propose that the back-transfer of holes from the ladders to the chains occurs upon decrease in temperature below 50 K.

NMR

The AF dimer model interprets the appearance of the spin gap in chains of $Sr_{14-x}Ca_xCu_{24}O_{41}$ materials as observed in susceptibility measurements [84]. In the AF dimer model intradimer exchange, $J = 130$ K, may be related to the value of this gap [92]. NMR offers possibility of direct determination of the spin gap. ^{63}Cu NMR signals for the ladder site can be separated from those for the chain site, since nuclei of these sites possess different quadrupole coupling. The initial ^{63}Cu NMR measurements on polycrystalline samples by Kumagai *et al.* [95] addressed the issue of behavior of the spin-gap with increasing Ca-content x, for $Sr_{14-x}Ca_xCu_{24}O_{41}$, $x = 0$, 3, 6, 9. The spin-gap for the chains subsystem was found to be independent of x, with the value of 140 K. This value is well reproduced for $x = 0$ in other studies: susceptibility, [89, 84], inelastic neutron scattering [88, 92, 91] and NMR [98, 96]. The same value is also found for $x = 3.5$ by inelastic neutron scattering [97]. In Fig. 1.24, the temperature dependence of the spin-lattice relaxation rate $1/T_1$ for the chains is shown for different materials of the q1D

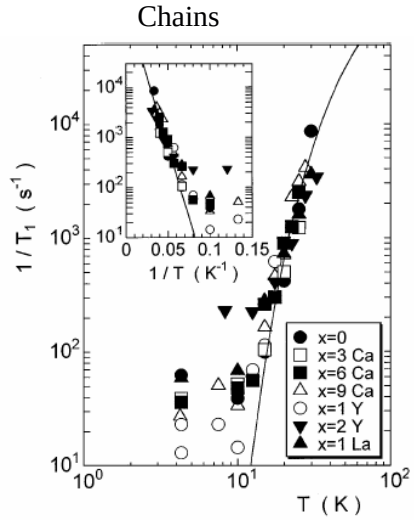

Figure 1.24: The temperature dependence of the spin-lattice relaxation rate $1/T_1$ for the chains is shown for different materials of the q1D cuprate family, and is most interesting for $Sr_{14-x}Ca_xCu_{24}O_{41}$, $x = 0$, 3, 6, 9. Full lines are fits to the activated behavior, established below 50 K. The activation energy is independent of x. From Ref. [95].

cuprate family [95]. From the activated behavior of $1/T_1$, it may be inferred that the spin-gap in the chains is fully opened below 50 K. Independence of x is also well documented.

The structure of NMR spectra also offers the possibility to analyze the temperature dependence of spin arrangement in chains. Takigawa *et al.* [98] performed ^{63,65}Cu NMR/NQR measurements on single crystals of $Sr_{14}Cu_{24}O_{41}$. Since holes (Cu^{3+} sites) and spins (Cu^{2+} sites) ordering is complementary, combination of methods sensitive to local magnetic fields and local electrical field gradients (EFG), seems to be well applied.

The first important result of Takigawa *et al.* , Fig. 1.25, left panel, is the observation of the chains ^{63}Cu NMR spectrum center line splitting below T^* of 200 K. Inequality of Cu sites inferred from this result again suggests that the AF dimer pattern is being established in chains. Temperature dependence of the line shift, equal to the susceptibility χ dependence, indicates that A sites are the AF dimer ones, *i.e.* Cu^{2+} sites. This is followed by the the clear site distinction observed at low temperatures in the NQR spectrum, Fig. 1.25, right panel and the splitting of the B line below 50 K. A possible scenario to explain this splitting is that the dimers are separated by at least two nonmagnetic sites, which is an exact reproduction of the INS observed spin-pattern which requires for all 6 holes to be in the chains at the lowest

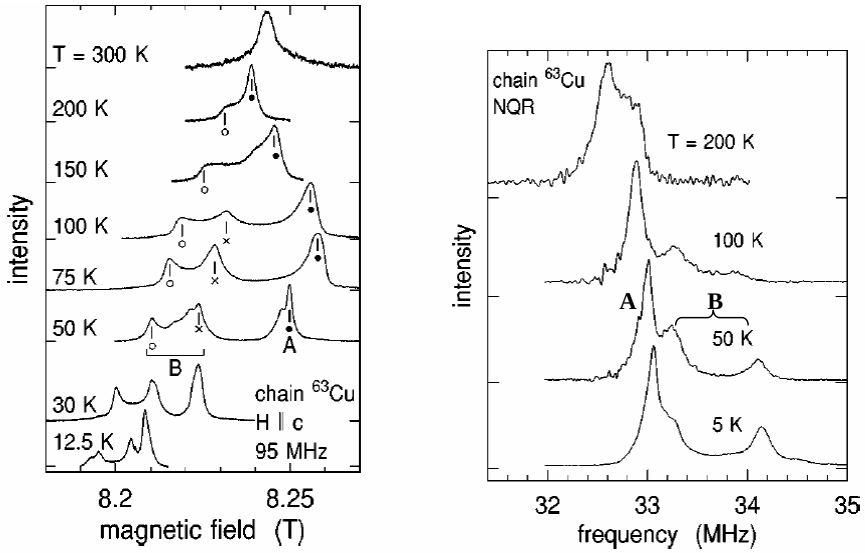

Figure 1.25: Left panel: Temperature variation of the center line NMR spectrum at the chain ^{63}Cu sites obtained at 95 MHz for $H||c$. Right panel: Temperature variation of the NQR spectrum at the chain ^{63}Cu sites. From Ref. [98].

temperatures, Fig. 1.23.

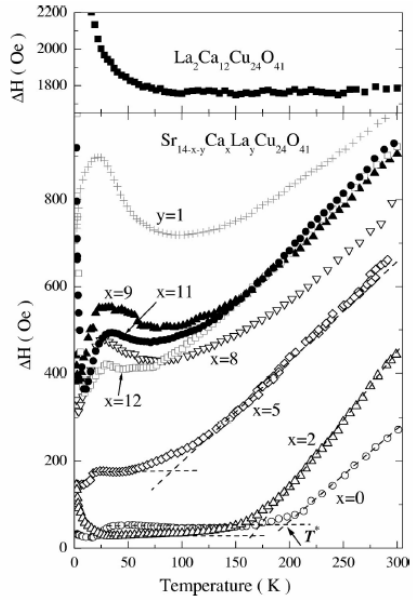

Figure 1.26: Bottom panel: temperature dependence of the ESR linewidth $\Delta H(T)$ of $Sr_{14-x}Ca_xCu_{24}O_{41}$ for various Ca contents, hole count $\delta_h = 6$. The topmost curve shows data for $La_1Sr_{13}Cu_{24}O_{41}$, $\delta_h = 5$. The magnetic field has been applied along the c axis of the crystals. The dashed lines denote the constant and linear contributions to $\Delta H(T)$. T^*, defined as the crossing point of the dashed lines, is identified with the onset of long-range charge order in the chains. Top panel: the same for $La_2Sr_{12}Cu_{24}O_{41}$, $\delta_h = 4$. T^* is not observed. From Ref. [99].

ESR

Kataev *et al.* [99] have studied the electron spin resonance (ESR) of the Cu^{2+} ions in the chains, and found that the Cu-spin relaxation is appreciably influenced by the charge dynamics in the chains, resulting in a strong temperature dependence of the ESR linewidth ΔH above a characteristic temperature T^*, Fig. 1.26. The crossover to a nearly temperature-independent line width ΔH_0 below T^* is identified with the onset of the long-range charge order associated with the AF dimer pattern order. With increasing Ca-content x this crossover shifts from about 200 K in $Sr_{14}Cu_{24}O_{41}$ to 80 K for $x = 5$, indicating a rapid destruction of this order. For x=8 the short-range order only remains, and persists shortly until for $x > 11$ it is replaced by an AF long-range order, below 3.5 K [102, 100, 101].

Conclusion: spin/charge arrangements in the chains

The analysis of the experimental results, as found in literature, regarding the chain subsystem of $Sr_{14-x}Ca_xCu_{24}O_{41}$ leads to the conclusion that 2D spin ordering (AF dimer pattern) occurs in the chains, *e.g.* below $T^* = 200$ K temperature for $x = 0$. The AF dimer pattern leads to the occurence of spin-gap for chains, which (gap) is independent of Ca-substitution in $Sr_{14-x}Ca_xCu_{24}O_{41}$ materials. The AF dimer pattern is accompanied by the complementary 2D charge-order of the holes present in the chains. Due to this charge-order, the holes are well localized in the chains. From the difference in the XRD and INS results it can be concluded that chains hole count increases from 5 to 6, at least for the parent compound, $x = 0$, in the temperature range below 50 K and down to 5-20 K. This corresponds to NMR observation according to which spin-gap in the chains is only established below 50 K and to the observation of the line splitting in the NQR spectrum below the same temperature. While T^* is 200 K, these observations indicate that long-range order in chains of $x = 0$ is fully established only below 50 K. Rapid destruction of long-range order occurs on Ca-substitution and for x=8 the short-range order only remains.

1.2.6 Ladders subsystem

Ladders spin-gap

While the chains subsystem showed somewhat unexpected gap in the spin excitation spectrum, the spin-gapped state of the ladder subsystem in $Sr_{14-x}Ca_xCu_{24}O_{41}$ was less unexpected. The theory predicted gapped spin-liquid state in the single ladder system. Indeed, such state was observed in the real materials, in the pure ladder compound $SrCu_2O_3$, as well as in the ladders subsystem of the composite compounds $(La, Sr, Ca)_{14}Cu_{24}O_{41}$.

Imai *et al.* [96] performed ^{17}O NMR measurements on $x = 0$ and 3 materials. They have observed a transition from paramagnetic into the spin-gapped ground state of the ladders, at $T^*(x = 0) \approx 200$ K and $T^*(x = 3) \approx 140$ K.

Takigawa *et al.* [98] performed $^{63,65}Cu$ NMR measurements on $x = 0$. The observed spectral lineshapes indicated a transition in the ladders at similar $T^*(x = 0) \approx 200$ K, Fig. 1.27. The center line attributed to the ladder sites shows a sharp single peak and no splitting, which occurs for chains due to charge-disproportionation. However, the satellite lines are broader and show temperature-dependent line shape below around 200 K.

The initial ^{63}Cu NMR measurements of the spin-lattice relaxation rate $1/T_1$ and of the Knight shift, on polycrystalline samples by Kumagai *et al.* [95], addressed the issue of behavior of the spin-gap with increasing Ca-content x, *i.e.* for $Sr_{14-x}Ca_xCu_{24}O_{41}$, $x = 0$, 3, 6, 9. The spin-lattice relaxation rate $1/T_1$ for the ladders shows x dependence. In Fig. 1.28 it is shown that the activated behavior of $1/T_1$ starts immediately below the room temperature and that different activation energies may be deduced for different x. Fig. 1.29 shows these results in comparison with the more recent NMR results for single crystals obtained by other groups [103, 98, 104]. The Ca-content dependence is qualitatively (and quantitatively for single crystals) the same in all studies. The gap decreases from 60 meV (≈ 600 K) for $x = 0$, 50 meV at $x = 2$, 35 meV at $x = 6$, 27 meV at $x = 8$. Above $x = 8$ it seems to saturate at 25-28 meV. On the contrary, the inelastic neutron scattering (INS) results, [97, 91, 105], do not indicate the Ca-content dependence. It is importatnt to note that the difference in the behavior of NMR and INS gaps is, effectively, a difference in the observed gap values for $x = 0$ and 2. The NMR results are obtained by fitting the data in temperature range from below 300 K down to 100 K, and INS results are obtained at temperatures below this range. Larger gaps for NMR than for INS for $0 \leq x \leq 2$ materials may correspond to this temperature range mismatch.

Still, it is important to note that the spin-gap in ladders does not get

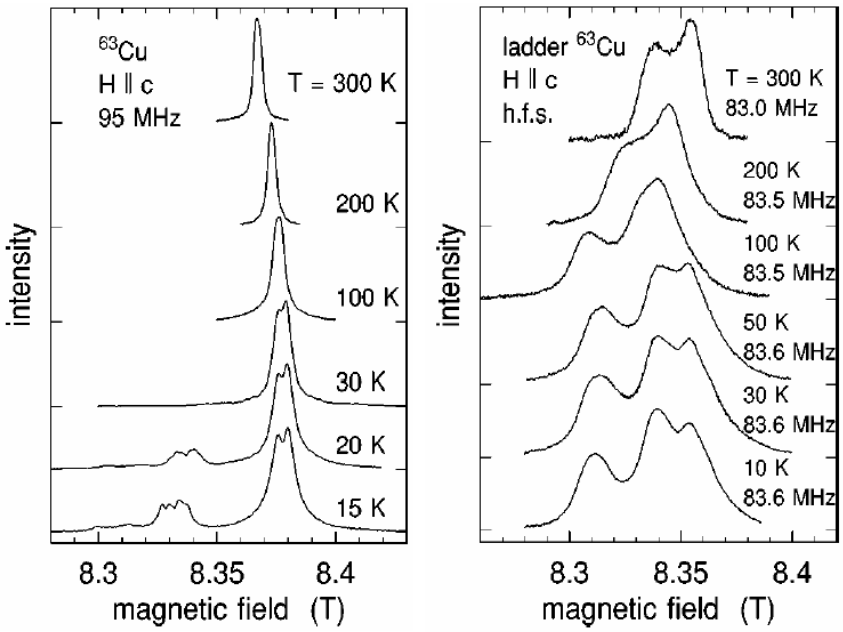

Figure 1.27: Temperature variation of the high-field NMR spectrum at the ladder ^{63}Cu sites of $Sr_{14}Cu_{24}O_{41}$with the magnetic field along the c-direction. Left panel: The center line of the ladder sites shows a sharp single peak. Right panel: The satellite lines are broader and show temperature-dependent line shape. From Ref. [98].

completely suppressed even for very high Ca-content, $x = 12$. This is noteworthy, since the presence of spin-gap is important in the mechanism which induces pairing of holes intrinsically doped into the ladders from the chains reservoir.

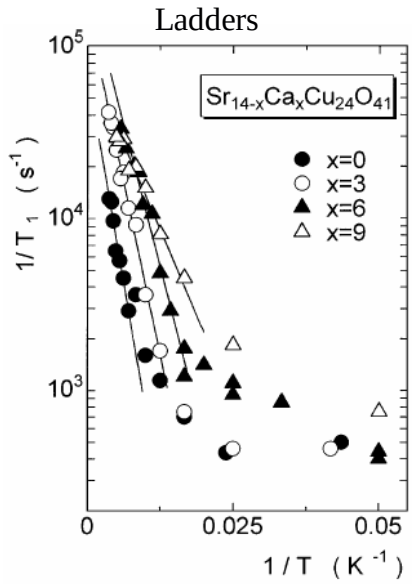

Figure 1.28: The temperature dependence of the spin-lattice relaxation rate $1/T_1$ for the ladders is shown for different materials of the q1D cuprate family, notably for $Sr_{14-x}Ca_xCu_{24}O_{41}$, $x = 0, 3, 6, 9$. Full lines are fits to the activated behavior. The activation energy decreases with x. From Ref. [95].

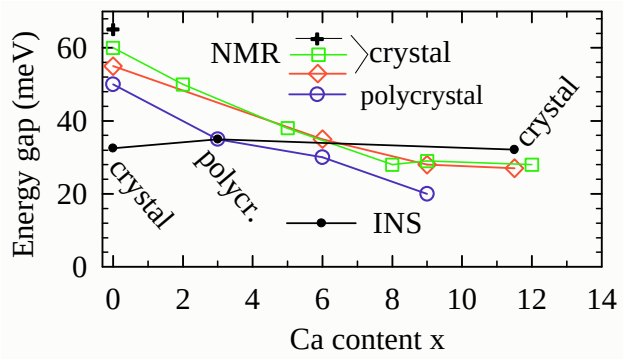

Figure 1.29: The dependence of the spin-gap in $Sr_{14-x}Ca_xCu_{24}O_{41}$ for various Ca-contents x. The results are obtained by different groups (see text) using NMR or INS techniques. Some groups used single crystals, some polycrystalline samples. The spin-gap remains finite up to the high Ca- contents $x = 12$.

Electrical transport in the ladders

As the holes in the reservoir in the chains seem to be well localized due to the spin AF dimer pattern and the complementary charge-order, the electrical transport paths must be found in the ladders. A comprehensive study of the anisotropic electrical resistivity on single crystals of $Sr_{14-x}Ca_xCu_{24}O_{41}$, $x = 0$, 3, 6, 11 was performed by Motoyama *et al.* [84]. In Fig. 1.30 $\ln \rho$ *vs.* $1/T$ plots are shown for the resistivity along the *c*- (parallel to the legs of ladders) and a axis (parallel to the rungs of ladders). All the compounds except $x = 11$, show a rapid increase in resistivity upon cooling - Arrhenius behavior of insulators. The value of a-axis resistivity, ρ_a, is larger than the *c*-axis resistivity, ρ_c, by one to two orders of magnitude. The anisotropic ratio, ρ_a/ρ_c , is not strongly dependent on x.

One should note that $Sr_{14}Cu_{24}O_{41}$ is not highly insulating if compared with the Y-substituted compounds. As exposed before, nonisovalently substituted compounds have hole counts of less than 6, and what is more important, all holes are found in the chains, where they become very localized. Henceforth their low conductivity already at the room temperature.

The room temperature conductivity $\approx 500\ \Omega^{-1}cm^{-1}$, seems to be close for various x, except that the conductivity increases slightly with Ca-substitution. This can not be quantitatively related to the ladders hole count results of Nücker *et al.* [76], *i.e.* with the fact that the hole count in this x range increases from 0.8 to 1.1 per ladder. Change in the activation energy, that is, its strong suppression is the most apparent in the resistivity results. In fact, $x = 11$ material appears to be metallic down to 100, or even 70 K (red line in Fig. 1.31). Only below these temperatures, weakly activated behavior of the resistivity reappears for $x = 11$.

Most interestingly, the application of pressure, at these Ca-substitution levels, suppresses the remains of the insulating behavior and superconductivity is observed, Fig. 1.31. Indeed, after the remarkable theoretical prediction of superconductivity for the ladder materials and the initial experimental findings of Uehara *et al.* [69] ($x = 13.6$, $T_c = 12$ K, $P_c = 3$ GPa) and Nagata *et al.* [107] ($x = 11.5$, $T_c = 6.5$ K, $P_c = 4.5$ GPa), the SC phase was observed for all Ca-substitutions $10 \leq x \leq 13.6$. A comprehensive presentation of development of the SC state under pressure for various x was given by Motoyama *et al.* [106], Fig. 1.32. They have also presented the suppression of the insulating state and establishment of the metallic behavior, for $Sr_{14}Cu_{24}O_{41}$ under pressure of 6.5 GPa, but, without occurence of SC. It is intriguing that metallic behavior is not observed for $x = 3, 6, 8$ at any pressure up to 8 GPa.

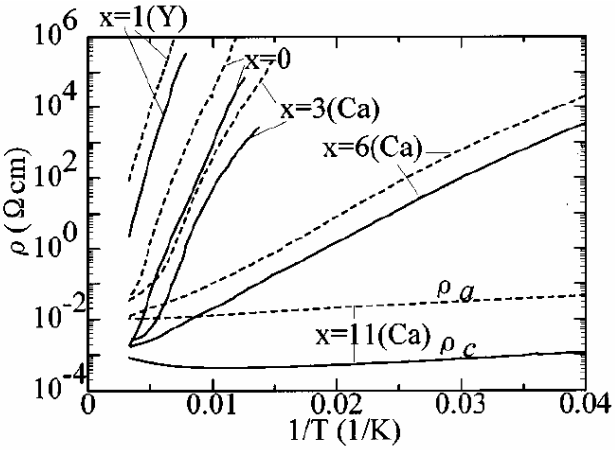

Figure 1.30: The Arrhenius plots of the dc resistivity for $Sr_{14-x}Ca_x$-$Cu_{24}O_{41}$ and $Y_1Sr_{13}Cu_{24}O_{41}$ along the c- and a-axis (solid and dashed curves, respectively). From Ref. [84].

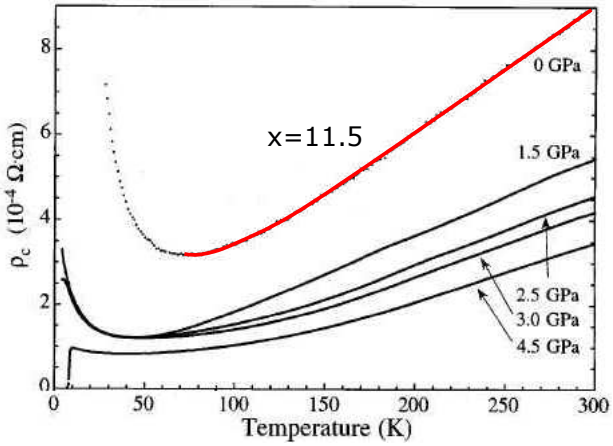

Figure 1.31: Temperature dependence of the dc resistivity along c-axis under various pressures in $x = 11.5$. From Ref. [107].

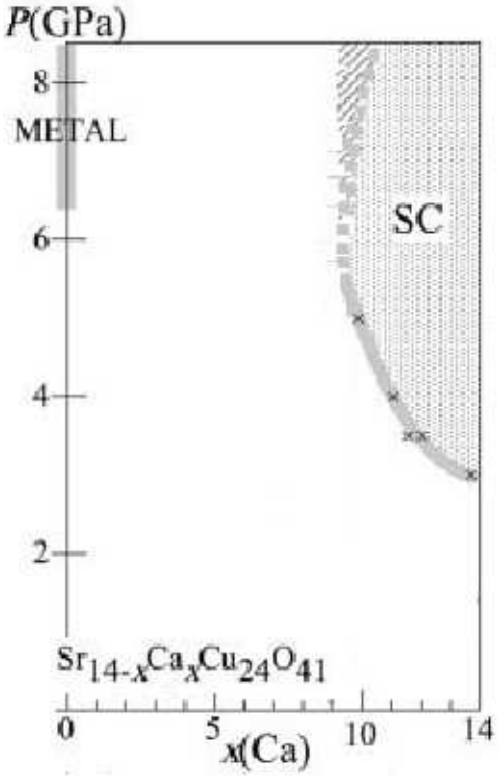

Figure 1.32: The $x-P$ phase diagram for $Sr_{14-x}Ca_xCu_{24}O_{41}$ by Motoyama *et al.* [106]. The SC phase is restricted at high pressures and for $10 \leq x \leq 13.6$ and experimentally determined critical pressure P_c is plotted as cross marks.

The relationship between the SC phase, and the spin-gap in the ladders

In this review we addressed the spin-gapped state of the ladders, as well as occurence of superconductivity. The superconductivity is established under pressure at substitution levels where finite spin gap is observed in the studies without pressure. The important question is whether the ladders' spin-gap is suppressed or remains finite when the pressure is applied and supraconductivity is established. Due to the experimental constraints this question has been studied on the local level by ^{63}Cu or ^{17}O NMR measurements by only two independent groups. First, Piskunov *et al.* [104] have performed experiments at pressure, $p = 3.2$ GPa $> p_c$, which stabilizes SC. It has to be noted that those measurements were not done in the SC phase, but above 10 K. They have shown that pressure decreases the gap in the magnon excitations and stabilizes low-lying spin excitations. For comparison, they also present that, in $x = 0$, high pressure decreases the gap but does not introduce excitations. The appearence of the low-lying spin excitations is inferred from the contribution to the spin-lattice relaxation rate T_1^{-1}, which is linear in temperature below 30-40 K (Korringa-like). They conclude that the condition for the observation of superconductivity is the existence of zero-frequency spin fluctuations within the magnon gap. This condition is met only above critical pressure in heavily substituted compounds ($10 \leq x \leq 13.6$).

Fujiwara *et al.* [108] also investigated $x = 12$ material by the same method at 3.5 GPa, but they reached temperatures as low as 1.4 K. They confirmed the SC transition by the ac-susceptibility-like measurements. They observed Hebel-Slichter peak at $T_{\rm SC}$ in the temperature dependence of the spin-lattice relaxation rate T_1^{-1} *vs.* T. They also identified two excitation modes in the normal state. One gives rise to the activation-type or gapped component in T_1^{-1}, the other T-linear (Korringa) component linking directly with the superconductivity. Besides confirming the experimental situation as described by Piskunov *et al.* , Fujiwara *et al.* interpreted that the gapless component likely arises from free motion of holon-spinon bound states appearing due to the hole doping, and the pairing of two spins within two holon-spinons likely causes the superconductivity, Fig.1.33. The Hebel-Slichter peak indicates that no nodes appear in the SC gap. In this picture, superconductivity has an s-wave-like character, but only in the sense that a finite gap exists in the quasiparticle excitation.

The nature of insulating phase, related to the nature of electrical transport in the ladders and its suppression is one of the principal issues left unanswered at the end of this review. Characterizing the insulating phase and the relationship between the insulating phase, the SC phase and the

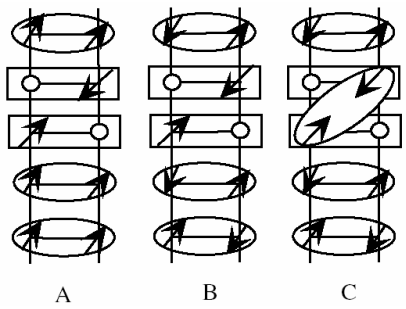

Figure 1.33: (A) Illustration of spin and charge configuration at high temperatures. Elipses show spin singlets on the rung. Some of them are in the triplet states at high temperatures. A rectangle implies the holon-spinon bound states. They move independently in the ladder. (B) Illustration at intermediate temperatures. A spin within the holon-spinon bound state is free and paramagnetic. All the spin pairs on the rungs are in the singlet state. (C) In the superconducting state. Two spins within the bound states form the pair. From Ref. [108]

spin-gap, that is, creating a phase diagram for the q1D cuprates is the focus of the research that will be presented in following chapters.

2 One-dimensional systems - theoretical overwiev

2.1 Phase diagram of weakly interacting 1D Fermi gas - the *g-ology* model

$(TMTSF)_2PF_6$ - q1D material, highly conducting at the ambient temperature and showing highly anisotropic metallic-like conductivity down to very low temperatures is almost ideal material for applying the 1D interacting Fermi gas model. The prerequisite for the formation of such a molecular conductor is the charge delocalization. In $(TMTSF)_2PF_6$ it occurs between the molecules on the TMTSF stack. The weak coupling limit is justified when the electron-electron interactions are smaller than the bandwidth $4t$, as occurs in TMTSF materials. The ground states (depending on the pressure) of $(TMTSF)_2PF_6$ have been identified as $2k_F$ SDW and triplet superconductivity.

Phase diagram and instabilities of 1D weakly interacting Fermi gas were successfully described by the *g-ology* model. This model contains the principal consequences of generalized, but weak, electron-electron interactions: the competition between the instabilities as well as 1D fluctuations, [50]. Depending on the coupling constants, *i.e.* wave vector of the interaction, various ground states may occur: singlet or triplet superconductivity and charge- and spin-density waves.

In a 1D system strong fluctuations, of either thermal or quantum origin, prevent long-range order at any temperature $T \geq 0$, [80, 1]. In the mean-field approximation these fluctuations are not taken into account, allowing for ordering at $T > 0$. In a real material, non-negligible interaction between the 1D structures will diminish the influence of the fluctuations and allow for ordering at $T > 0$. Therefore, the mean-field approach is usefull to show that the competition between the superconducting and density-wave orders is the basic issue in q1D materials.

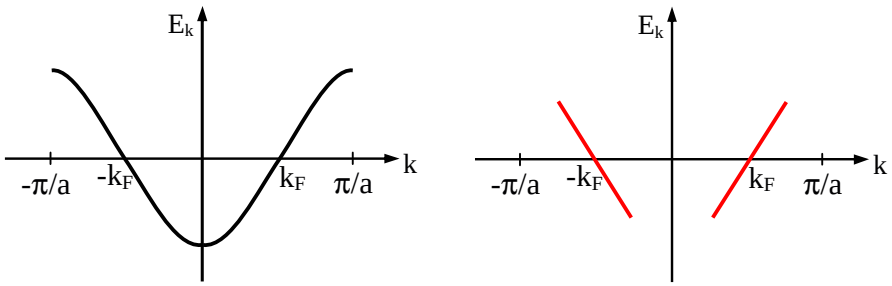

Figure 2.1: Upper panel: Dispersion relation of a 1D Fermi (noninteracting electron) gas, 1DEG. Fermi surface is reduced to two points, k_F, $-k_F$. Lower panel: Dispersion relation of a 1DEG linearized in the neighbourhood of Fermi points.

The *g-ology* draws it's name directly from the peculiarities of the perturbation theory in 1D. The model describes scattering processes, concerning states close to the FS, related by weak interactions and treated perturbatively, with respect to the Fermi liquid picture. Since the system of concern is 1D, FS is reduced to two points situated at $-k_F$ and k_F. There are only 4 possible scattering processes and the respective coupling constants are indexed as g_1, g_2, g_3 and g_4, hence the name for the model...

2.1.1 Noninteracting Hamiltonian

The Hamiltonian for the Fermi gas of non-interacting electrons is

$$H_0 = \sum_{\mathbf{k},\alpha} E_{\mathbf{k}} c^{\dagger}_{\mathbf{k},\alpha} c_{\mathbf{k},\alpha} \tag{2.1}$$

where $c^{\dagger}_{\mathbf{k},\alpha}(c_{\mathbf{k},\alpha})$ is creation (annihilation) operator of an electron with momentum $\mathbf{k}$ and spin α. The kinetic energy $E_{\mathbf{k}}$ is usually measured with respect to the Fermy energy. Considering Bloch states as the non-interacting ground states, the momentum representation is the most appropriate for the weakly interacting system. The corresponding dispersion relation is illustrated schematically in Fig. 2.1, left panel.

Since, only the electrons lying near the Fermi surface play an important role in physical processes, the dispersion may be linearized around FS, Fig. 2.1, right panel. We note that there are two well-defined branches of the electron dispersion. The creation (annihilation) operators for the electrons belonging to the negative k branch are indexed $b^{\dagger}_{\mathbf{k},\beta}(b_{\mathbf{k},\beta})$, while operators for the electrons belonging to the positive k branch are indexed $a^{\dagger}_{\mathbf{k},\alpha}(a_{\mathbf{k},\alpha})$,

respectively. The spins are indexed β (α) for b- and a-branches, respectively. In terms of these operators, the free Hamiltonian is given by

$$H_0 = \sum_{\mathbf{k},\alpha} v_F(k - k_F) a^\dagger_{\mathbf{k},\alpha} a_{\mathbf{k},\alpha} + \sum_{\mathbf{k},\beta} v_F(-k - k_F) b^\dagger_{\mathbf{k},\beta} b_{\mathbf{k},\beta} \tag{2.2}$$

2.1.2 Interacting part of the Hamiltonian

The interactions in this model system, in general, are the Coulomb or the phonon mediated electron-electron interactions. The interaction is introduced by adding H_{int} term to the Hamiltonian, Eq. 2.2.

$$H_{int} = \sum_{\mathbf{k},\mathbf{k'},\mathbf{q},\alpha,\alpha'} U_{\mathbf{q}} c^\dagger_{\mathbf{k}+\mathbf{q},\alpha} c^\dagger_{\mathbf{k'}-\mathbf{q},\alpha'} c_{\mathbf{k'},\alpha'} c_{\mathbf{k},\alpha} \tag{2.3}$$

Working in momentum space means that interaction can be represented by the Fourier sum, with different momentum transfers $\mathbf{q}$, separating local and long-range parts. As already mentioned, there are only 4 scattering processes and each contributes by a separate part H_i to the interaction Hamiltonian.

$$\begin{aligned} H &= H_0 + H_{int} \\ H_{int} &= H_1 + H_2 + H_3 + H_4 \end{aligned} \tag{2.4}$$

The diagrams of these processes are shown in Fig. 2.2. In the diagrams solid lines denote electrons from the right, a-branch, whose momenta are positive. The dashed lines refer to the electrons from the opposite branch.

The first process corresponds to backward scattering of electrons, where the momentum transfer is $q = 2k_F$, Fig. 2.2 (a). This component contains the contribution of the short-range, effectively on-site interactions. g_1 has a contribution from the Pauli principle or from the Coulomb repulsion U of two electrons found in the same orbital. The forward scattering component is characterized by momentum transfer $q = 0$, Fig. 2.2 (b), denoting long-range interactions. The diagram, Fig. 2.2 (c), corresponds to momentum transfer $4k_F$. It is not effective unless *Umklapp* occurs. Umklapp is active if the band is half-filled, since then the reciprocal lattice vector $\mathbf{G}$ is equal to $4k_F$ and thus cancells the scattering momentum transfer. This situation is realized in Fabre salts $(TMTTF)_2X$, where electron-electron umklapp scattering is generated by the small Coulomb potential of the X-anions, *i.e.* $g_3 \ll g_1, g_2$, [109]. In these materials this situation leads to the dimerization of TMTTF molecules within the stack. For TMTSF compounds this dimerization is small, thus g_3 is less important than in TMTTF compounds, [110]. In another possible

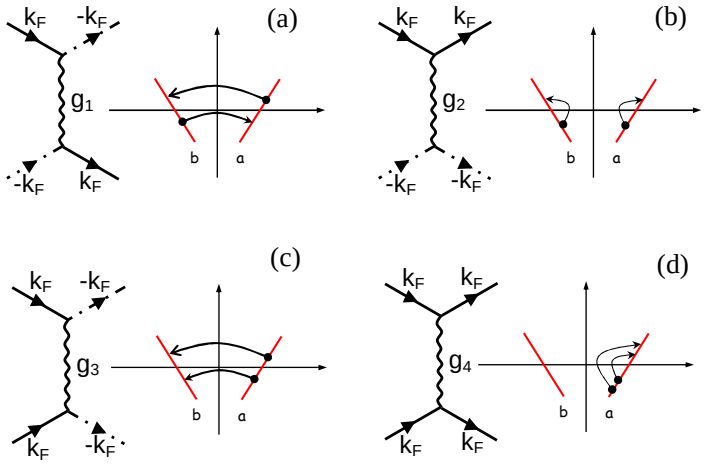

Figure 2.2: Diagrams for possible scattering processes in the 1D interacting Fermi gas. They correspond to transfers between the dispersion branches. (a) Backward scattering, $q = 2k_F$. (b) Forward scattering, $q = 0$. (c) *Umklapp* scattering, $q = 4k_F$. (d) Another possible forward scattering process, $q = 0$.

forward scattering process, Fig. 2.2 (d), the particles are not transfered to the opposite branch and the momentum transfer is $q = 0$.

2.1.3 Instabilities in the 1D system

The aim of studying g-ology model is to determine what kind of instabilities, *i.e.* ground states, are likely to occur in the 1D system. The best way here is to calculate the response functions or generalized susceptibilities within linearized response. The response functions that are expected to be singular for a range of couplings given here are the ones of charge-density wave (CDW), spin-density wave (SDW), and singlet-superconductivity (SS) and triplet-superconductivity (TS). CDW or SDW instability is expected to occur for momentum transfer $q = 2k_F$, reflecting the singularity in the electron-hole (Peierls channel) susceptibility at this wave-vector. SS or TS occurs, if the electron-electron (Cooper pair) susceptibility is singular.

Using the response functions it is possible to rewrite interaction Hamiltonian, Eq. 2.4. The resulting Hamiltonian can be reduced in the mean-field approximation and diagonalized using Bogoliubov transformation. The order parameter appears as a gap Δ opened at the Fermi surface

$$\Delta = 2E_F \exp\left(-\frac{1}{\lambda}\right) \tag{2.5}$$

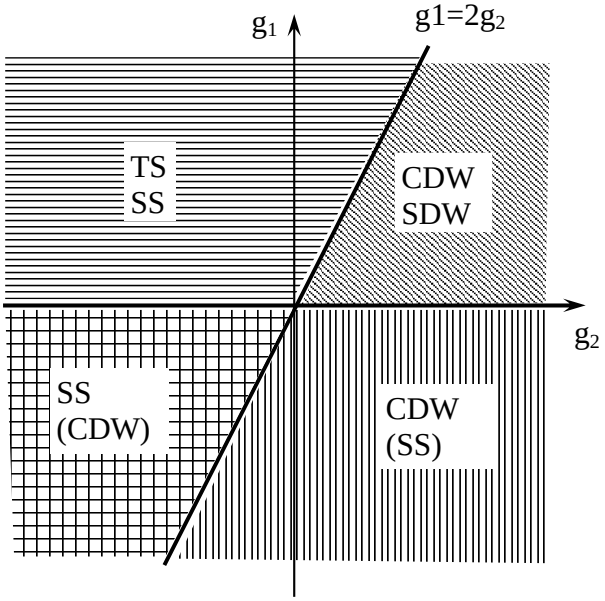

Figure 2.3: Ground states occuring for q1D weakly interacting electron gas, calculated within the mean-field approximation. Only spin-independent couplings g_1, g_2 are considered, and g_3 is taken to be zero (non-half-filled band).

g-ology parameters define λ. A finite gap Δ_{CDW} is obtained for $2g_1 - g_2 < 0$. SDW ordering occurs for $g_2 > 0$, SS for $g_1 + g_2 < 0$ and TS for $g_1 - g_2 > 0$. The full determination of the fluctuations which dominate at $T = 0$ instead of the phase transition requires more advanced techniques than the mean-field approximation. The corresponding g_1, g_2 "phase diagram" for all four types of fluctuation is given in Fig. 2.3. Superconducting and density wave fluctuations are separated by the line $g_1 = 2g_2$, while $g_1 = 0$ separates singlet and triplet fluctuations. The main consequence of the umklapp g_3 (half-filled band) is the formation of the gap in the $q = 0$ charge-charge correlation function, *i.e.* the Mott localization. SDW (AF) is concomittantly favored over the $2k_F$ CDW. Regarding the scope of this Thesis, a principal result, obtained from this diagram, is a suggestion of a boundary between superconducting and density-modulated ground state.

Phenomenology of density waves

Nature of the pairing (Cooper or electron-hole channel) determines the response function, and thus the experimental phenomenology for a given electronic ground state. Density wave instabilities of 1DEG are due to electron-hole pairing, with either parallel or antiparallel spins, for SDW or CDW,

respectively. Density modulations of spin and charge are both defined by $2k_F$ wave vector. When 3D couplings are added density waves are characterized by a metal-to-insulator transition (due to the opening of the energy gap at the Fermi level), accompanied by a drop in magnetic susceptibility. Susceptibility drop for SDW occurs only along the magnetic "easy" axis - *i.e.* the direction of the modulation amplitude. In the presence of the coupling between the electron and phonon systems the $2k_F$ and $4k_F$ electron CDWs are accompanied by the lattice distortion at the same critical vector. The $2k_F$ SDW spin modulation is also accompanied by charge modulation with wave vector $4k_F$, [112]. These couplings allow for the direct observation of the modulations by X-ray diffuse scattering. Even for a negligible coupling between the electron and phonon systems electronic DWs may be observed by refinements of this experimental technique, [33, 34]. A difference between a "standard" $2k_F$ CDW, which is accompanied by a Peierls lattice distortion, and a purely electron CDW depends on the adiabatic ratio E_F/ω_{ph}, where E_F is the Fermi energy, and ω_{ph} the frequency of the corresponding phonon. Peierls lattice distortion appear only in adiabatic limit, where $E_F \gg \omega_{ph}$, whereas in the nonadiabatic limit $\omega_{ph} \gg E_F$ phonon mediates the nearly instantaneous attractive electron-electron interaction.

Finally, we note that coupled 1D electron-phonon systems primarily exhibit Peierls CDW ground state in which electronic density and lattice modulations are established concomitantly and are intimately related, [111]. A starting point for these systems is the 1D electron-phonon Hamiltonian. Such a CDW posseses long wavelength excitations - phasons which can couple to ac electric field and lead to interesting dynamical effects, see Sec. 2.4.

2.1.4 Weak coupling limit of the extended 1D Hubbard model

The *g-ology* Hamiltonian, Eqs. 2.2, 2.3, describes the 1D Fermi gas featuring weak interactions which can be treated perturbatively. It was demonstrated by Emery, [114] that the limit of strong interactions in the extended Hubbard model leads to the similar phase diagram in 1D as the weak-coupling model. Emery's approach starts from the Hubbard model, [113], which, in its simplest form, describes hopping t, between the nearest neighbour sites of the chain, labelled j, and Coulomb repulsion, U between the electrons of the opposite spin on the same site.

$$H = -t \sum_{j,\sigma} c^{\dagger}_{j,\sigma}\, c_{j+1,\sigma} + c^{\dagger}_{j+1,\sigma}\, c_{j,\sigma}$$

$$+ \quad U \sum_{j,\sigma} c^{\dagger}_{j,\sigma} c_{j,\sigma} c^{\dagger}_{j,-\sigma} c_{j,-\sigma} \tag{2.6}$$

$c^{\dagger}_{j,\sigma}$ denotes the creation operator of an electron with spin σ in the Wannier state localized at the jth site. This model is exactly solvable in 1D. In the case of a half-filled band the ground state is antiferromagnetic insulator for any $U > 0$. Writing this Hamiltonian in the momentum representation

$$c_k = \frac{1}{\sqrt{N}} \sum_{i=1}^{N} \exp(-ikR_i) c_i \tag{2.7}$$

and linearizing the dispersion around $\pm k_F$ (Fig. 2.1), a Hamiltonian of the *g-ology* form is obtained. All the couplings g_1, g_2, g_3, g_4 will be equal, since they are all related to the single physical parameter U of the Hubbard Model. Thus, $g_1 < 2g_2$, and, according to *g-ology*, SDW and CDW are formed (Fig. 2.3). This is also consistent with the exact solution of the Hubbard model in 1D, which demonstrated that the ground state should be antiferromagnetic and insulating, [115].

In the next step, the inter-site (nearest-neighbor) interaction term $V \sum_j n_j \, n_{j+1}$ is introduced, in addition to the on-site interaction term. The resulting Hamiltonian is referred to as extended Hubbard model (EHM). The introduction of V distinguishes between the values of *g-ology* couplings. The relation between the g-ology coupling parameters and the EHM parameters is the following:

$$\begin{aligned} U - 2V &\rightarrow g_1 \\ U + 2V &\rightarrow g_2 \\ U - 2V &\rightarrow g_3 \\ U + 6V &\rightarrow 2g_2 - g_1 \end{aligned} \tag{2.8}$$

As already mentioned g_3 is important only when the band is half-filled. However, unlike here for EHM, the *g-ology* deals with $g_3 \ll |g_1|, |g_2|$, as in Bechgaard salts.

2.2 Strongly interacting 1D electron system

In the approach, which is more suitable for strongly non-conducting systems the Hubbard Hamiltonian (Hubbard 1963. [113]) with strong intra-atomic (on-site) interaction is used. The cuprate materials under study in this thesis have almost the same ambient temperature conductivity as $(TMTSF)_2PF_6$. Still, these materials show insulating behavior almost everywhere (750 - 2 K, up to 6 GPa, depending on the material in question) throughout the phase diagram. Other properties, like the appearance of the spin-gap in the ladders subsystem and AF dimers and charge-order in the chains subsystem direct theoretical investigations towards using strong interactions, better suited for well localized systems. Structural elements of these materials, chains and (spin) ladders are very good realisations of different t-J models (drawn in particular from extended Hubbard model - EHM with strong interactions). These models suggest a competition of charge-density wave and superconducting ground states for ladders, the subsystem responsible for charge transport in $Sr_{14-x}Ca_xCu_{24}O_{41}$ materials. The exact nature (*e.g.* pairing symmetry) of these states is not established yet.

2.2.1 Strong coupling limit for cuprates

Electron Hamiltonian of the cuprate systems should incorporate terms related to oxygen orbitals. Therefore, in the standard approach, the following energy parameters are used: ε_p, energy of oxygen O2$p_{x,y}$ orbitals and ε_d, energy of copper Cu3$d_{x^2-y^2}$ orbitals. These orbitals form the CuO_4 square with two inequivalent oxygens - in the rung and in the leg of the ladder, Fig. 2.4. The physical situation depends on the splittings, $\Delta_{pd} = \varepsilon_p - \varepsilon_d$, and hybridization t_0, between these orbitals. In the strong coupling limit on-site (within the copper orbital) repulsive interaction U_d and the splittings Δ_{pd} are considered to be much larger than effective hopping t, which is of the order of hybridization t_0. The ratio U/Δ_{pd} determines the basic physical situation in the cuprates, [74].

When holes are transferred into the cuprate lattice they will be located either at Cu sites if $U_d < \Delta_{pd}$ or in the oxygen orbitals if $U_d > \Delta_{pd}$. In the first case (Hubbard limit), O-sites are eliminated from the picture and the effective Hamiltonian describes hole motion on Cu-sites alone. In the opposite case (charge-transfer limit), which Zhang and Rice assumed for a cuprate layer, it is energetically favorable for doped holes to locate in oxygen orbitals surrounding the Cu-site, and form a singlet state with the hole in copper orbital. Again, they have shown that in this case a single band Hamiltonian describes the motion of this Zhang-Rice singlet through the lattice. Zhang

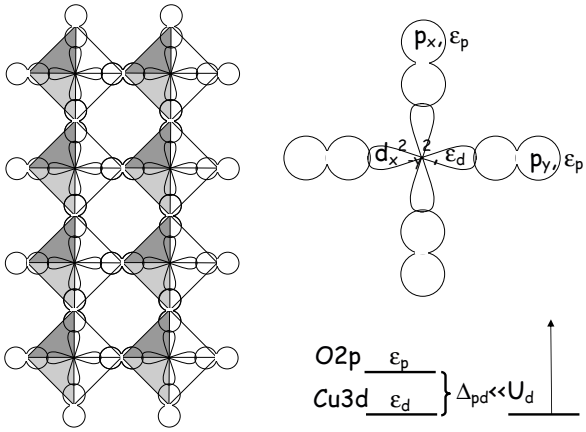

Figure 2.4: Schematic diagram of the hybridization of the O hole ($2p^5$) and Cu hole ($3d^9$) within the CuO_4 square. At oxygen sites only one of the two orbitals is shown. Energy level splitting is also denoted. The squares assembled into a ladder structure are shown.

and Rice started with a Hamiltonian for a 2D cuprate layer, Eq. 2.9, and it can be assumed that this model is also valid for the ladder lattice. That is, the hybridization term in their starting Hamiltonian contains the term t_0 whose sign depends on the phases of the p_x (p_y) and $d_{x^2-y^2}$ wave functions, which depends on the exact lattice geometry. Two oxygen sites within the unit cell are not distinguished for brevity.

$$\begin{aligned} H &= \sum_{j,\sigma} \varepsilon_d d^\dagger_{j,\sigma} d_{j,\sigma} + \sum_{l,\sigma} \varepsilon_p p^\dagger_{l,\sigma} p_{l,\sigma} \\ &+ U \sum_j d^\dagger_{j,\uparrow} d_{j,\uparrow} d^\dagger_{j,\downarrow} d_{j,\downarrow} \\ &+ \sum_{j,\sigma} \sum_{l \in j} t_0 d^\dagger_{j,\sigma} p_{l,\sigma} + \text{H.c.} \end{aligned} \tag{2.9}$$

Here, vacuum is defined as filled Cu3d^{10} and O2p^6 states. Operator $d^\dagger_{j,\sigma}$ creates a hole in the Cu3$d_{x^2-y^2}$ orbital and $p^\dagger_{l,\sigma}$ in O2p_x ($2p_y$) orbitals. At exactly half-filling and for $t_0 = 0$, each Cu-site is singly occupied ($3d^9$), and all the O-sites are empty ($2p^6$) in the hole representation. If t_0 is finite but small (this happens at low doping in cuprates), the virtual hopping process involving the doubly occupied Cu-hole states produces a superexchange (AF) interaction between the neighbouring Cu holes. The Hamiltonian (hybridization term excluded), Eq. 2.9 reduces to spin-$\frac{1}{2}$ Heisenberg model on

the lattice of Cu sites:

$$H_S = J \sum \mathbf{S}_i \mathbf{S}_j \quad , \quad J = \frac{4t_0^4}{\Delta_{pd}^2 U_d} + \frac{4t_0^4}{2\Delta_{pd}^3} \tag{2.10}$$

As the formation of Zhang-Rice singlets is energetically favorable the above presented considerations lead to a possibility to map the Cu-O lattice close to half-filling, onto a lattice formed from only one kind of sites. When these sites are occupied physical situation is that one hole resides in CuO_2 unit cell and caries spin 1/2. In this, mapped lattice, effectively unoccupied sites, are those whose spin state is zero, as they are ZR singlets formed from the always present Cu $3d^9$ hole and doped hole which locates in the oxygen orbitals $2p_x$ ($2p_y$). That is, Zhang and Rice replaced the hybridization term in Eq. 2.9, by an effective hopping Hamiltonian describing the motion of the ZR singlet

$$H_t = \sum_{i \neq j, \sigma} t_{ij} (1 - n_i, -\sigma) d_{i,\sigma}^\dagger d_{j,\sigma} (1 - n_j, -\sigma) \tag{2.11}$$

Noteworthy, the t-J Hamiltonian composed from Eq. 2.10 and 2.11 in the charge-transfer limit taken by ZR, is equivalent to the effective Hamiltonian of the single band Hubbard model in the large U limit.

2.2.2 $t - J$ model for two-leg ladders

The model of two-leg ladders by Dagotto *et al.* [77, 73, 68], cartooned in the Sec. 1.2.6 (compare with Fig. 2.4) consists of two chains each described by a t-J model. The chains are also coupled by t'-J' interactions between them, Fig. 2.5. Note that three oxygens in the ladder are inequivalent and therefore $t \neq t$' and $J \neq J$'. This t-J-t'-J' model considers hopping/coupling along the legs, t/J and along rungs of ladders t'/J':

$$\begin{aligned} H &= J \sum_{i,\lambda=-1,1} \mathbf{S}_{i,\lambda} \cdot \mathbf{S}_{i+1,\lambda} + J' \sum_{i,\lambda=-1,1} \mathbf{S}_{i,\lambda} \cdot \mathbf{S}_{i,-\lambda} \\ &- t \sum_{i,\sigma,\lambda=-1,1} (c_{i,\lambda,\sigma}^\dagger c_{i+1,\lambda,\sigma} + \text{H.}c.) - t' \sum_{i,\sigma,\lambda=-1,1} (c_{i,\lambda,\sigma}^\dagger c_{i,-\lambda,\sigma} + \text{H.}c.) \end{aligned} \tag{2.12}$$

Hole creation operators $c_{i,\sigma}^\dagger$ create ZR singlet at a given site. Physically, this site is mapped from CuO_4 square, as demonstrated for cuprate layer in the previous Section 2.2.1. The index λ denotes sites on the same rung, at one or at the other leg of the ladder. The index i indicates sites along the chains - that is, the legs of ladders.

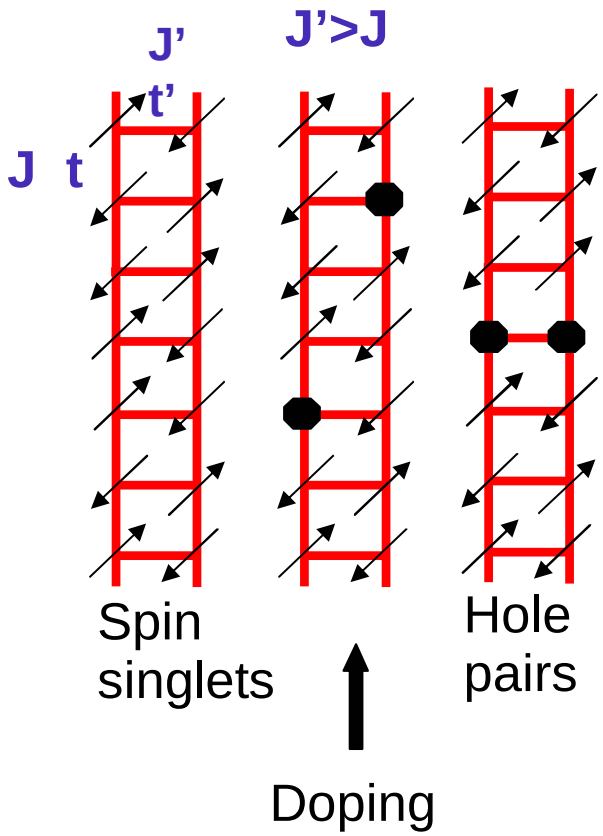

Figure 2.5: Schematic definition of t-J-t'-J' model. Hopping/coupling along the legs, t' and J' and along rungs of ladders t and J are denoted. The arrows denote occupied sites, spin 1/2, while open dots denote holes, which carry no spin due to formation of Zhang-Rice singlets. Suggested mechanism of hole-pairing in the two-leg ladders: When the coupling along the ladder rung J'$> J$ is stronger than along the ladder legs, the ground state is a direct product of spin singlets appearing on the rungs. Doping individual holes to the ladder leads to destroying the singlets, which is energetically unfavorable. Therefore the holes tend to pair-up on the rungs.

In the large J' limit, at half filling, the ground state consists of a set of spin singlets in each rung of the ladder. There is a spin-gap in the spectrum of order J' which corresponds to creating a triplet in one of the rungs. When the system is doped with holes, it is energetically favorable to break as few rung singlets as possible. Therefore, every added pair of holes forms a bound state in a given rung, Fig. 2.5. To this bound state corresponds a pair-field operator

$$\Delta_i = \frac{1}{\sqrt{2}}(c_{i,\lambda,\uparrow}c_{i,-\lambda,\downarrow}) - (c_{i,\lambda,\downarrow}c_{i,-\lambda,\uparrow}) \tag{2.13}$$

The prediction of the gapped spin-liquid ground state was experimentally confirmed, for the q1D cuprate ladders materials, as shown in the Introduction Chapter, Sec. 1.2.6.

Finally, an important step is taken by recognizing that a subspace of rung singlets may be mapped to a linear chain. That is, each rung corresponds to a single site of this chain. The sites in this chain are either doubly occupied (mapped from the bound holes on the rung) or unoccupied (mapped from the two spins forming a rung singlet). In this subspace $|U_{eff}| \propto J$', and the $U_{eff} < 0$, it is attractive. The analogy can be taken with the Hubbard model for a linear chain, see below Sec. 2.2.3 and Fig. 2.6. Therefore, as it was pointed out by Dagotto *et al.* , the ladder model away from half-filling (*i.e.* hole-doped) exhibits SC, or CDW, correlations. We note that the renormalized U_{eff} is probably smaller than t and that a weak coupling g-ology model may also be considered for describing ordering in the ladders. Dagotto *et al.* also checked numerically that binding energy of the pairs is negative for J'/J ratios in the range $0.4 - 4$, and that the pairing correlations do occur immediately when J' is turned on. The balance between the SC and CDW depends on the parameters of the model and more generally on residual interactions between hole pairs, all of which is hard to predict theoretically, [50, 80, 77].

2.2.3 1D EHM in strong coupling limit

In order to clarify Dagotto's conclusion on the competition of SC and CDW in the spin ladders, we will schematically present the possible orderings in 1DEG of a single chain. EHM gives a particularly simple picture of the possible states of the system in the large-U limit, in which t and V related terms are treated as perturbations, [116, 114]. It is not necessarily assumed that large U corresponds to any particular material, and for the present purpose it is merely a limit in which the theoretical properties of one-dimensional systems can easily be related to physically meaningful variables.

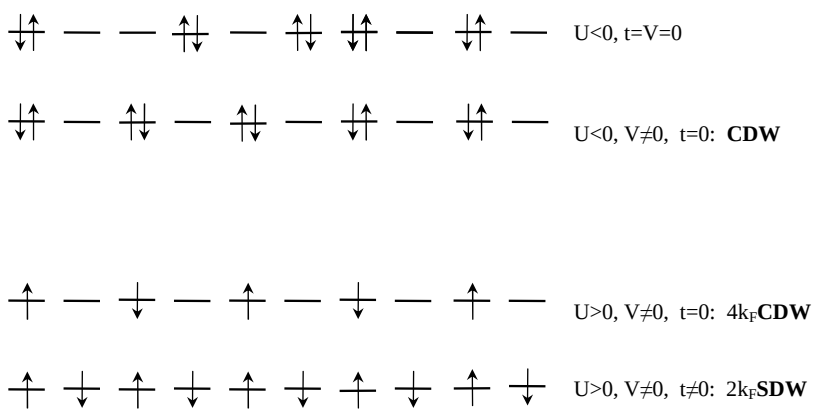

Figure 2.6: Configurations of electrons, spin up, ↑, or spin down, ↓ on a 1D chain when a strong on-site interaction is present, $U \neq 0$. For attractive U, and when inter-site interaction, $V > 0$, is included, a $2k_F$ CDW is formed from electrons paired in singlets. For repulsive U, single electrons form a $4k_F$ CDW at quarter filling. At half-filling, and with hopping allowed a $2k_F$ SDW is formed.

The on-site attraction, $U < 0$

The properties depend upon the sign of U. When this parameter is taken to be positive, it corresponds to the repulsion between the electrons of the opposite spin, occupying the same orbital. However, in strongly polarizable molecules, as well as in the Dagotto model, the direct Coulomb repulsion may be reduced, and the indirect interaction can lead to $U < 0$. The electrons of opposite spin form pairs, to take advantage of the on-site attraction. Molecular sites are either doubly occupied or unoccupied, Fig. 2.6. As mentioned above, this case is physically important here, since Dagotto's conclusion on the spin-ladders leads to the consideration of attractive U.

The ground state is very degenerate because the energy does not depend upon which sites are occupied. CDW states occur in an extreme form when there is an intersite repulsion $V > 0$ but still no hopping t. To minimize the energy, the pairs are equally spaced, as shown in Fig. 2.6 for a half-filled band. The charge density varies periodically from 1 to 0 in the inter-site distance, so the wave vector is just $2k_F$. This is a possible ground state because the system is classical when $t = 0$. More realistically, when $t \neq 0$, the picture is not so static and there is a much smaller modulation of the charge density. Also, density modulation may be incommensurate to the inter-site distance, the electrons cannot be distributed so neatly amongst the sites. However, the wave vector $2k_F$ always characterizes the CDW. This, standard CDW

is usually, due to non-negligible electron-phonon coupling, accompanied by lattice distortion at the same wave-vector $2k_F$. Although, it is in principle possible that a purely electronic CDW is observed, [33, 34].

For the case of inter-site attraction, $V < 0$ singlet superconductivity can arise when hopping, t, is included. The electron pairs are bosons, bound in a singlet state, and it is possible that they become superfluid (and hence superconducting since they are charged) at low enough temperatures. Triplet superconductivity will not occur because the electrons are bound into singlet pairs before long-range triplet correlations can build up.

The on-site repulsion, $U > 0$

Emery, [114] pointed out that in the strongly repulsive case, $U > 0$, for a half-filled band, when all sites are singly occupied, EHM can be mapped onto a spin-1/2 Heisenberg chain, with charges Mott-localized each on its site.

The $2k_F$ SDW instability is clearly visualized for this case where only the spin degrees of freedom have to be considered. Virtual hopping produces an effective antiferromagnetic exchange interaction and the ground state has a modulation of the spin density, which is illustrated in Fig. 2.6. For weaker coupling and a different number of electrons, the state is more dynamic, but the wave vector is still $2k_F$.

CDW states can occur again in an extreme form when there is an intersite repulsion $V > 0$. In contrast to $U < 0$ case, however, single electrons rather than pairs are equally spaced so the period of the CDW is halved and its wave vector is $4k_F$. This is so-called $4k_F$ CDW or Wigner crystal in 1D. It manifests itself as a purely electronic CDW, not accompanied with any lattice distortions. This case is shown in Fig. 2.6 for a quarter-filled band, although the phase separation can occur as well [117]. Once again, hopping makes the CDW weaker and less static. It also mixes in doubly occupied sites and restores the Fermi sea, which may lead to an additional $2k_F$ CDW periodicity. $4k_F$ CDW is generated in *g-ology* picture for a quarter-filled band by strong interactions [110].

Although the above considerations were not assumed to correspond to any particular material, still it was shown that orderings of different nature occur also in the strong coupling limit.

2.3 Reexamined phase diagram of 1D EHM at half-filling

In q1D cuprates an important role is played by localized charges with strong electron-electron interaction. Still, Dagotto's considerations of the ordered phases in the ladders indicate a renormalized, but attractive U is responsible for ordering. Therefore a study of 1D EHM which covers both weak and strong-coupling limit is presumably of importance for the cuprate ladders.

In the strong-coupling limit, Sec. 2.2.3, one can show that the model has two insulating phases, SDW phase and CDW phase, which are separated by a first-order transition line located at $U \simeq 2V$. In the weak-coupling limit g-ology analysis gives a continuous phase transition between the CDW and SDW phases also at $U \simeq 2V$ or $g_1 \simeq 0$, Fig. 2.3. It is then natural to consider that, as the coupling constants are increased, the continuous-transition line changes into the first-order one at a tricritical point in the intermediate coupling regime, [118]. This phase diagram was reexamined both numerically, [119] and analytically. Second-order corrections to coupling constants were calculated to show that the bond-charge-density wave (BCDW, in which the Peierls dimerization occurs spontaneously) phase exists for weak couplings in between the CDW and SDW phases. SDW-BCDW and BCDW-CDW transitions are continuous and the two transition lines merge at a multicritical point into the first-order line $U \simeq 2V$ separating the CDW and SDW phases, Fig. 2.7. Still, definitive results have been obtained only for effective, short-range Coulomb forces. Indications remained that the use of the effective interactions to approximate long-range forces occuring in strongly-correlated systems, does not yield the correct broken symmetry ground-state [121].

A closer inspection of Fig. 2.7 indicates that the BCDW phase occurs for $V \simeq 0.4U$. The possible scenario of the competition between BCDW and SC phase, in this parameter region was, very recently, proposed by Tsuchiizu and Suzumura, [120], in order to analyze the critical behavior for a single cuprate ladder in more detail. Here we just illustrate the further generalization of the EHM Hamiltonian, necessary to these authors to extend the understanding of the doped ladders. The EHM Hamiltonian generalized specifically for the two-leg ladders is split into hopping and on-(inter-)site interaction part, $H = H_0 + H_{\rm int}$. The first part describes the hopping energies along and between the legs:

$$\begin{aligned} H_0 = & -t_{\parallel} \sum_{j,\sigma,l} (c^{\dagger}_{j,l,\sigma}\, c_{j+1,l,\sigma} + \text{H.c.}) \\ & -t_{\perp} \sum_{j,\sigma} (c^{\dagger}_{j,1,\sigma}\, c_{j,2,\sigma} + \text{H.c.}), \end{aligned} \tag{2.14}$$

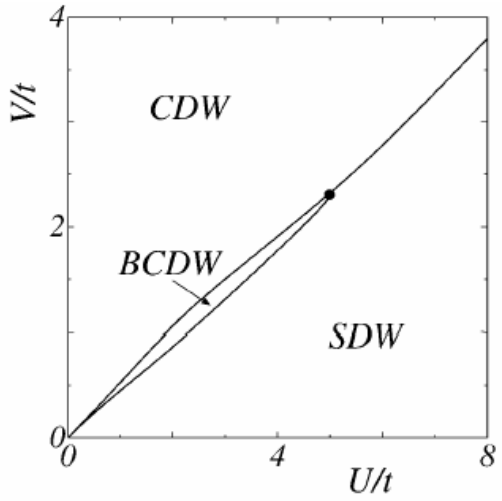

Figure 2.7: Phase diagram of the extended Hubbard model at half-filling. CDW, SDW and BCDW denote, respectively, charge-, spin- and bond-charge-density wave ground states. The bicritical point is at $(U, V) \simeq (5.0t, 2.3t)$. From [118].

where $c_{j,l,\sigma}$ annihilates an electron of spin $\sigma(=\uparrow,\downarrow)$ on the rung j and the leg $l(=1,2)$. The hopping along the rungs is the generalization compared to EHM. The Hamiltonian part $H_{\rm int}$ denotes interactions between electrons:

$$H_{\rm int} = U \sum_{j,l} n_{j,l,\uparrow}\, n_{j,l,\downarrow} + V_{\parallel} \sum_{j,l} n_{j,l}\, n_{j+1,l} + V_{\perp} \sum_{j} n_{j,1}\, n_{j,2}, \qquad (2.15)$$

where U represents on-site repulsion and $V_{\parallel}$ ($V_{\perp}$) represents nearest-neighbor repulsion along legs (rungs) of ladders, with $n_{j,l,\sigma} = c^{\dagger}_{j,l,\sigma}\, c_{j,l,\sigma}$ and $n_{j,l} = n_{j,l,\uparrow} + n_{j,l,\downarrow}$.

For a complete description of the real material the authors also considered finite hole transfer δ_h into the ladders. As can be found in Fig. 2.8 on-site repulsive interaction stabilizes d-wave-like SC state, while BCDW mixed with CDW is obtained due to nearest-neighbor repulsive interactions, with the transition close to $V_{\perp}/U + V_{\parallel}/U \approx 0.4$. The assumed hole transfer was $\delta_h = 1.4$ per ladder, a value which corresponds well to the experiment, Sec. 1.2.4. The authors further emphasize that increasing hole transfer into the ladders reduces the effect of only $V_{\parallel}$ and that the system exhibits a quantum phase transition into the *d*-wave-like (or rung-singlet) superconducting state. In Fig. 2.9 m_t, the magnon excitation gap (spin gap) is shown *vs.* hole transfer. If m_t is regarded as the transition temperature, this depiction may be regarded as a phase diagram for doped cuprate ladders. The

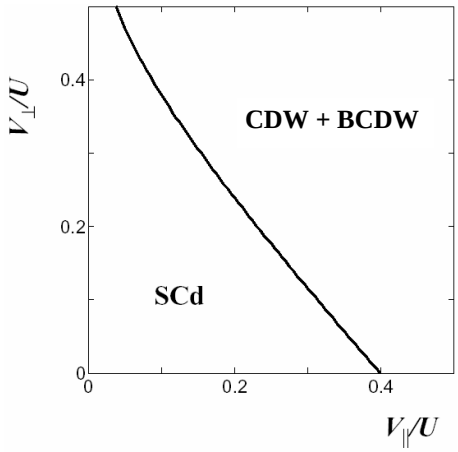

Figure 2.8: The ground-state phase diagram of 1D EHM at half-filling, generalized for ladders, on the plane of $V_\parallel/U$ and $V_\perp/U$, with $U/t_\parallel = 2$, $\delta_h = 1.4$, and $t_\perp = t_\parallel$. From [120].

proposed phase diagram meets difficulties when applied to the real material, since there is no experimental evidence for the quantum critical point (QCP) between the CDW state and the SC state. In order to explain the discrepancy, the dimensionality effect and/or the disorder effect, smearing the QCP, has been suggested by the authors, [120]. We also note that $U/t_\parallel = 2$ does not correspond well to a ratio obtained if standard values of $U = 3.5 - 4$ eV for copper, and $t_\parallel = 0.6$ eV, as calculated in Ref. [83], are taken. We also note that the hole transfer $\delta_h \sim 4$, shown to be necessary for SC, is much above the experimentally observed values, Sec. 1.2.4.

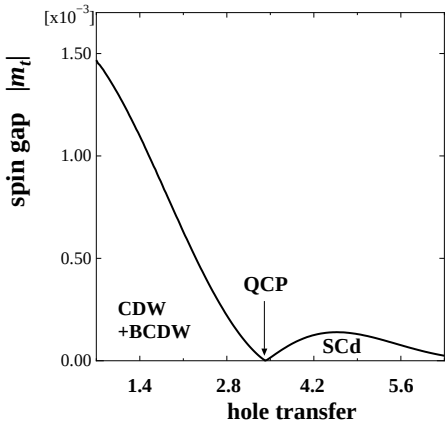

Figure 2.9: The hole transfer dependence of the magnon spin gap m_t with $U/t_{\parallel} = 2$, $V_{\parallel}/U = V_{\perp}/U = 0.25$, and $t_{\perp} = t_{\parallel} = 1$. CDW and BCDW denote, respectively, charge- and bond-charge- density wave ground states. SCd denotes d-wave-like superconducting state. QCP stands for quantum critical point. If m_t is regarded as the transition temperature, this depiction may be regarded as a phase diagram for doped cuprate ladders. From [120].

2.4 CDW phason response to ac field

CDW – dynamics of the phase

The main features of a standard charge density wave (CDW) established in real material in the presence of electron-phonon coupling can be described with Fröhlich 1D electron-phonon Hamiltonian, [122].

$$H = \sum_{k,\sigma} \varepsilon_k \, c^\dagger_{k,\sigma} c_{k,\sigma} + \sum_q \hbar\omega_q (b^\dagger_q b_q + b^\dagger_{-q} b_{-q}) + \sum_{k,q,\sigma} g(k) c^\dagger_{k+q,\sigma} c_{k,\sigma} (b_q + b^\dagger_{-q}) \tag{2.16}$$

where $c^\dagger_{k,\sigma}$ and $b^\dagger_q$ are creation operators for 1D Bloch electron and a longitudinal phonon q with dispersions ε_k and ω_q respectively, and $g(k)$ is the electron-phonon coupling constant. In the mean-field theory in 1D, only the interaction with the phonon at $Q = 2k_F$ is to be considered. Corresponding distortion of the lattice is described by a complex order parameter

$$\Delta e^{i\varphi} = g(2k_F) \langle b_{2k_F} + b^\dagger_{-2k_F} \rangle \tag{2.17}$$

where Δ and φ are real. The displacement field of the lattice is given by

$$\langle b_{2k_F} + b^\dagger_{-2k_F} \rangle e^{2ik_F x} + \text{c.}c. = \frac{2\Delta}{g(2k_F)} \cos(2k_F x + \varphi) \tag{2.18}$$

That is, a charge modulation occurs in the system, accompanied by lattice distortion at similar wave-vector. Standard CDW appears below the so-called Peierls transition, [111]. The carriers condense below a gap 2Δ, in analogy with superconductivity. The condensate here, however, is formed by the electron-hole pairs of opposite spin, coming from the opposite sides of the Fermi surface, involving the wave vector $2k_F$.

The dynamics of this condensate is described in terms of a position- and time- dependent order parameter $\Delta(x,t)$. As $\Delta(x,t)$ is complex, Eq. 2.17, both amplitude and phase fluctuations occur. These can be assumed to be decoupled and

$$\Delta(x,t) = (\Delta_0 + \delta) e^{i\varphi'} \tag{2.19}$$

where Δ_0 is the equilibrium order parameter, and δ and φ' are the fluctuations from the equilibrium value. To lowest order in δ and φ' the amplitude mode corresponds to $2\Delta_0 + 2\delta$, and the phase mode corresponds to $2\Delta_0 i\varphi'$.

The dispersion relations of these modes were evaluated by Lee, Rice and Anderson, [123]. While the amplitude mode has a gap, the phase mode is gapless (which was first pointed out by Fröhlich for an incommensurate DW); the $q = 0$ translational mode corresponds to zero excitation energy, Fig. 2.10.

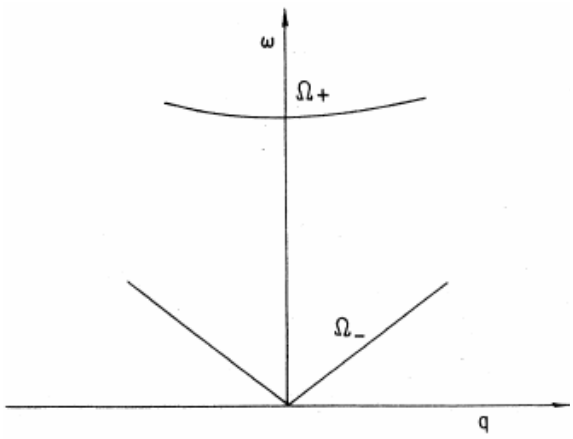

Figure 2.10: Dispersion relation of CDW phase mode, $\Omega-$, and of amplitude mode, $\Omega+$.

The amplitude mode is expected to be Raman active, whereas phase mode carries a dipole moment, as it involves the motion of condensed electrons across the lattice background. Consequently, the $q = 0$ phase mode carries a current. Experimentally, this mode is related to dc and ac conductivity of a CDW condensate. Therefore, most of the descriptions of dynamical collective phenomena of CDW are in terms of the dynamics of the phase only.

The Coulomb interchain interaction affects the phason mode dispersion, [124], [125]. The screened Coulomb singularity occurs in the second term of phason dispersion:

$$\omega_{ph}^2 \sim v_{ph}^2 q_\parallel^2 + \omega_L^2 \frac{q_\parallel^2}{q_\parallel^2 + q_\perp^2} \tag{2.20}$$

There are two limits. If the system as a whole is a dielectric, *i.e.* there are no uncondensed, free carriers, Coulomb interaction is screened when $q_\perp < q_\parallel$ and the phason frequency is raised to a finite value $\omega_{ph} \approx \omega_L$. An instructive analogy may be drawn with electron gas where interactions raise the plasmon frequency to finite value. However, for $q_\perp > q_\parallel$ phasons remain acoustic, *i.e.* we get $\omega_{ph} \sim v_{ph} q_\parallel$. In other words, CDW charge fluctuations can carry the Fröhlich supercurrent. The relative magnitude of $q_\perp$, $q_\parallel$ in the two limits relates to the periodic charge and lattice modulation being in-phase ($q_\perp < q_\parallel$) or out-of-phase ($q_\perp > q_\parallel$) on neighboring chains. If the system contains free carriers these may reduce ω_L by screening the singularity in Eq. 2.20, but only at extremely large wavelengths.

Finally, in the real material, due to free carrier screeening of Coulomb interactions, various interactions between CDW and underlying lattice remove

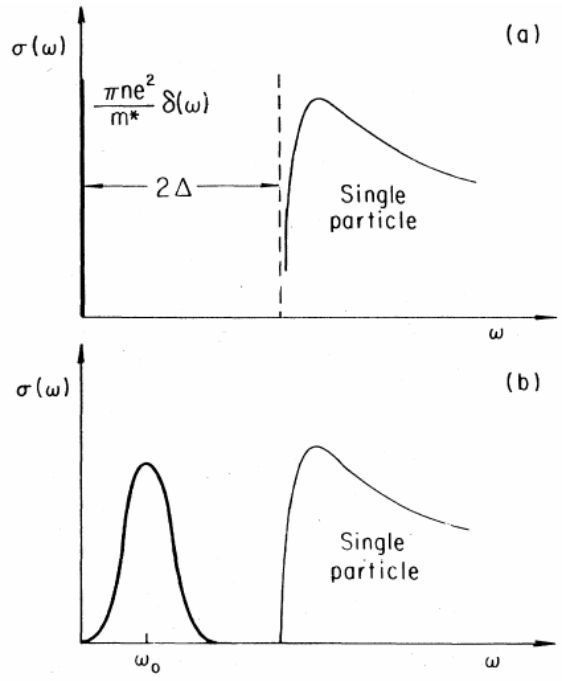

Figure 2.11: Frequency-dependent response of the collective mode (a) without pinning, $\omega = 0$ mode is infinitesimaly narrow (b) with pinning and damping, a finite width pinned mode at finite frequency. The response at $\omega > 2\Delta$ is due to free carrier excitations.

translational invariance and lead to pinning of the phase of the condensate. Such pinning is brought about by the local distortions of the condensate around pinning centers. Free carriers do not screen effectively at $2k_F$, so the pinning effects shift collective mode conductivity to finite – pinning frequency, Ω_0, Fig. 2.11. This is the so-called *pinned* mode, observed in frequency dependent conductivity of standard CDW materials at 10 GHz or higher frequencies.

For modelling pinned mode, as observed within CDW phason response, a simple model satisfies. This is the so-called classical particle model. That is, CDW condensate is described as a classical particle performing damped oscilations in a harmonic, pinning potential. We note that the CDW is described with only one degree of freedom and that free carriers are not taken into account. The corresponding equation of motion is simply the equation for a forced, damped harmonic oscilator. The natural frequency of such a system is the pinning frequency, Ω_0. Within the limit of small displacements, the potential term is simply $\Omega_0^2\varphi$. Damping is taken to be weak γ_0 and E, the applied ac field is harmonic.

$$\frac{d^2\varphi}{dt^2} + \gamma_0 \frac{d\varphi}{dt} + \Omega_0^2 \varphi = \mathrm{e}E/m^* \tag{2.21}$$

m^* is the effective mass of the CDW condensate, *i.e.* the mass of the classical particle representing it, while e stands for the electron charge. The nonuniform nature of pinning has been completely neglected in the above analysis, and this reflects as follows. This model in the above stated underdamped limit describes only the pinned mode and can not simultaneously describe the low-frequency (audio/radio) overdamped modes, as observed in the response of standard CDW materials. These modes can only be described in the strong damping limit of classical particle model.

Littlewood's model of CDW phason response

Littlewood's exposition, [127], starts with Fukuyama, Lee and Rice, [128] model for CDW, which is more realistic than the classical particle one. The model by FLR of an incommensurate charge density wave (CDW) as a deformable medium has been successful in explaining many experimental results both qualitatively and quantitatively, [126]. In this model, the CDW is an elastic medium subject both to impurity pinning forces and an external drive force. Their model leads to an equation of motion

$$m^* \frac{d^2\varphi}{dt^2} + \gamma_0 \frac{d\varphi}{dt} - \kappa \nabla^2 \varphi + \sum_i V(\mathbf{r} - \mathbf{R}_i) \rho_0 \sin[\mathbf{Q} \cdot \mathbf{r} + \varphi(\mathbf{r})] = \rho_c E_z / Q_z \tag{2.22}$$

A sinusoidal CDW, characterized by a nesting vector $\mathbf{Q}$, corresponds to the charge density $\rho(r) = \rho_c + \rho_0 \cos[\mathbf{Q} \cdot \mathbf{r} + \varphi(\mathbf{r})]$. The FLR consider pinning of the phase φ by a random impurity potential $V(\mathbf{r} - \mathbf{R}_i)$. κ is the elastic modulus, which describes the elastic deformation of the phase due to pinning. Here it is assumed that CDW is free to oscillate only in the z direction of applied electric field, E_z.

We note that the term (of Hamiltonian corresponding to this equation of motion), which describes the interaction of charge density with the impurity potential, has the form

$$\begin{aligned} H_{imp} &= \sum_i \int d\mathbf{r} V(\mathbf{r} - \mathbf{R}_i) \rho(\mathbf{r}) \\ &= \sum_i V(\mathbf{Q}) \cos[\mathbf{Q} \cdot \mathbf{R}_i + \varphi(\mathbf{R}_i)] \end{aligned} \tag{2.23}$$

That is, the $Q = 2k_F$ charge density modulation couples only to the respective Fourier component $V(\mathbf{Q})$ of the impurity potential.

The general formulation is based on treating the interaction between CDW and free carriers within a two-fluid model, where the only interaction is that via an electromagnetic field. Total induced current is given by displacement and the conduction current, and CDW polarization current:

$$\mathbf{j}(\mathbf{r},t) = \varepsilon\dot{\mathbf{E}} + \sigma\mathbf{E} + \rho_c\dot{u}\hat{\mathbf{z}} \tag{2.24}$$

Here, $\dot{u} = \frac{\dot{\varphi}}{Q_z}$ is the CDW velocity. ε and σ are the dielectric and conductivity tensors and for the harmonic field $\dot{\mathbf{E}} = -i\omega\mathbf{E}$, the complex conductivity tensor is defined as $\tilde{\sigma} = \sigma(\mathbf{q},\omega) - i\omega\varepsilon(\mathbf{q},\omega)$. Most CDW materials are anisotropic, and the conductivity tensor is accordingly approximated by the diagonal form $\tilde{\sigma} = \tilde{\sigma}_\perp(\hat{\mathbf{x}} + \hat{\mathbf{y}})/\sqrt{2} + \tilde{\sigma}_z\hat{\mathbf{z}}$. Here $\tilde{\sigma}_z$ is conductivity in the best conducting direction, while $\tilde{\sigma}_\perp$ is low conductivity in perpendicular directions.

The formulation is also based on the assumption of the linear response of the CDW. This leads to the linearization of the equation of motion, Eq. 2.22 about some static equilibrium state $u_0(r)$:

$$\sum_{q'}[G_0^{-1}(\mathbf{q},\omega)\delta_{q,q'} + V(\mathbf{q}-\mathbf{q}')]u(\mathbf{q}',\omega) = \rho_c E_z(\mathbf{q},\omega) \tag{2.25}$$

where the bare response function is

$$G_0^{-1}(\mathbf{q},\omega) = -m^*\omega^2 - i\gamma_0\omega + \mathbf{q}\cdot\kappa\cdot\mathbf{q} \tag{2.26}$$

A formal solution to Eq. 2.25 is

$$u(\mathbf{q},\omega) = \rho_c\sum_{q'} G_E(\mathbf{q},\mathbf{q}';\omega)E_z(\mathbf{q},\omega) \tag{2.27}$$

Inserting this formal solution into Eq. 2.24 for the total current, and taking into account the anisotropy of the conductivity we get

$$[\sigma_{tot}(\mathbf{q},\mathbf{q}';\omega)]_z = \tilde{\sigma}_z\delta_{\mathbf{q},\mathbf{q}'} - i\omega\rho_c^2 G_E(\mathbf{q},\mathbf{q}';\omega) \tag{2.28}$$

Last term is the CDW condensate conductivity, which due to the assumed anisotropy affects only the longitudinal component of conductivity, $\tilde{\sigma}_z$. The subscript E denotes that G_E is not any more the bare response function G_0^{-1}, but a response function to an external electric field $G_E^{-1} = G_0^{-1} + V(\mathbf{q}-\mathbf{q}')$.

Uniform pinning

For illustrative purposes, a correspondence between this modelling and the classical particle model may be given if the pinning potential is taken as uniform, $V(\mathbf{q}) = V_0\delta_{q,0}$. Eq. 2.28 reduces to

$$\sigma_{tot}(0,\omega) = \sigma_z - i\omega\varepsilon_z - \frac{i\omega\rho_c^2}{G_0^{-1}(0,\omega) + V_0} \tag{2.29}$$

$\rho_c^2/(G_0^{-1}(0,\omega) + V_0)$ may be regarded as ε_{CDW}, the CDW contribution to the dielectric function. The collective CDW mode may be separated into longitudinal and transverse components.

The transverse mode $q_z = 0, q_\perp \to 0$ may be obtained by finding the poles of total dielectric function. In this case, the single-particle ε_z is negligible since ε_{CDW} diverges, thus:

$$\begin{aligned} G_0^{-1}(0,\omega) + V_0 &= 0 \\ -m^*\omega_T^2 - i\gamma_0\omega_T &= -V_0 \end{aligned}$$

that is, $\omega_T^2 = V_0/m = \Omega_0^2$, the transverse mode frequency is the pinning frequency. Conductivity, Eq. 2.29 shows a weakly damped, γ_0, peak at Ω_0 frequency, as illustrated in Fig. 2.12.

The longitudinal mode $q_\perp = 0, q_z \to 0$ may be obtained by finding zeros of the CDW dielectric function $\varepsilon_z + \rho_c^2/(G_0^{-1}(0,\omega) + V_0)$:

$$\begin{aligned} G_0^{-1}(0,\omega) + V_0 &= \rho_c^2/\tilde{\sigma}_z \\ m^*\omega_L^2 + i\gamma_0\omega_L &= V_0 - i\omega_L\rho_c^2/\tilde{\sigma}_z \end{aligned}$$

At high frequencies, $\omega \gg \sigma_z/\varepsilon_z$ we have $\tilde{\sigma}_z \sim -i\omega\varepsilon_z$, and since the damping term may be neglected, $\omega_L^2 = V_0/m + \rho_c^2/m^*\varepsilon_z$. A very high $\Omega_{pl} = \rho_c^2/m^*\varepsilon$ plasmon-like frequency, much above $\Omega_0 = \sqrt{V_0/m}$ regulates the frequency of the longitudinal mode, $\omega_L \approx \Omega_{pl}$.

At low frequencies, $\omega \ll \sigma_z/\varepsilon_z \to \tilde{\sigma}_z \sim \sigma_z$, the damping term may be regarded as being enhanced $i\gamma_0\omega_L + i\omega_L\rho_c^2/\sigma_z$. That is, damping in this frequency range is regulated by free-carriers conductivity,

$$\gamma = \gamma_0 + \rho_c^2/\sigma_z \tag{2.30}$$

The longitudinal response develops a low-frequency, overdamped $\gamma \gg \gamma_0$, tail. It extends down to a frequency $\tau_0^{-1} = \gamma/V_0 \approx \rho_c^2/(\sigma_z V_0)$, as illustrated in Fig. 2.12. It is important to note that, in principle, such a purely longitudinal, low-frequency mode, can not be experimentally observed by spectroscopy

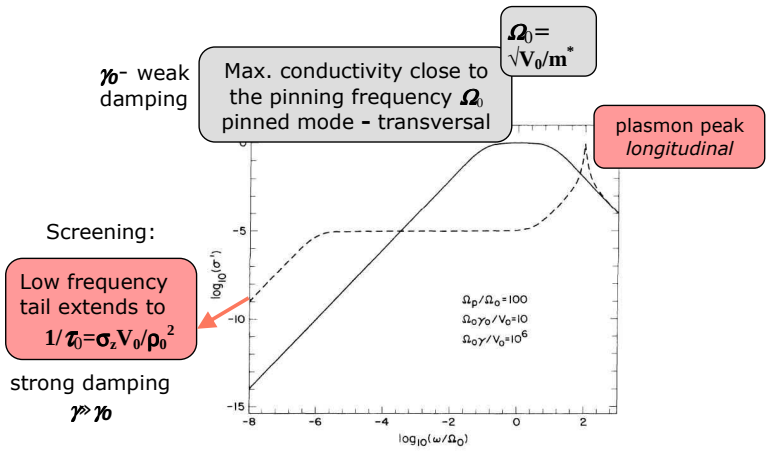

Figure 2.12: The real part of the transverse component of collective conductivity σ' is shown by a solid line. The pinned mode, as a peak at Ω_0 is shown. The dashed line shows the real part of the longitudinal component of the collective conductivity (thus, not expected to be obeservable in the experiment). The high frequency plasmon peak is accompanied by an extra broad dispersion at low frequency, $1/\tau_0$.

techniques, since it exists only for zeros of the dielectric function. On the contrary, the low-frequency mode is experimentally observed, and consequently, this analysis has to be improved to account for this experimental fact.

Nonuniform pinning

Pinned configurations and the local modes of oscillation of the CDW are disordered on a typical length scale ξ - Lee-Rice length. Below this scale the phase is considered constant. Therefore, we have focused at the CDW response to local field, through the response of local modes.

A convenient formulation for highlighting the influence of screeening is obtained by constructing a local CDW response function $G_\rho(\mathbf{q}, \mathbf{q}'; \omega)$ to a fixed external charge. This charge represents one of the free carriers existing in the real material. The local response calculation takes into account a disordered nature of CDW. Previously, the response to external electromagnetic field was given by $G_E(\mathbf{q}, \mathbf{q}'; \omega)$. The response function to a fixed external charge is calculated

$$G_\rho^{-1}(\mathbf{q}, \omega) = G_E^{-1}(\mathbf{q}, \omega) - i\omega\rho_c^2 R(\mathbf{q}, \omega) \tag{2.31}$$

An external current source is introduced $j_{ext}(\mathbf{q}, \omega)$. Electric field is calculated

$$E_z(\mathbf{q}, \omega) = [-i\omega\rho_c u(\mathbf{q}, \omega) + j_{ext}(\mathbf{q}, \omega)]R(\mathbf{q}, \omega) \tag{2.32}$$

where

$$R(\mathbf{q}, \omega) = \frac{q_z^2 - i\omega\mu_0\tilde{\sigma}_\perp}{q_\perp^2\tilde{\sigma}_\perp + q_z^2\tilde{\sigma}_z - i\omega\mu_0\tilde{\sigma}_\perp\tilde{\sigma}_z} \tag{2.33}$$

The skin depths $\omega\mu_0\tilde{\sigma}_i$ are considered to be much larger than localization lengths of CDW $\xi_\perp, \xi_z$. Thus an electrostatic approximation can be made. This leads to the form of $R(\mathbf{q}, \omega) = \tilde{\sigma}_z^{-1}[1 + (\tilde{\sigma}_\perp/\tilde{\sigma}_z)(q_\perp/q_z)^2]^{-1}$. Now, if conductivity anisotropy is considered to be large

$$\xi_z/\xi_\perp < (\tilde{\sigma}_z/\tilde{\sigma}_\perp)^{1/2} \tag{2.34}$$

$R(\mathbf{q}, \omega) = 1/\tilde{\sigma}_z(\omega)$ assumes a simple form, and the local mode will appear essentially longitudinal ($q_\perp = 0, q_z \to 0$) in character (contributing only to the conductivity in the best conductivity direction, $\tilde{\sigma}_z$). In this case

$$G_\rho^{-1}(\omega) = G_E^{-1}(\omega) - i\omega\rho_c^2/\tilde{\sigma}_z(\omega) \tag{2.35}$$

The above expression is inverted and G_E (expressed through G_ρ), that is necessary to calculate the experimentaly measured conductivity, is obtained and inserted in Eq. 2.28. Accordingly, the longitudinal response is also expected to contribute in spectroscopy experiments, which, normally, should observe the conductivity only due to transverse modes. Mixing the character of the modes in CDW materials is essential for understanding spectroscopy results.

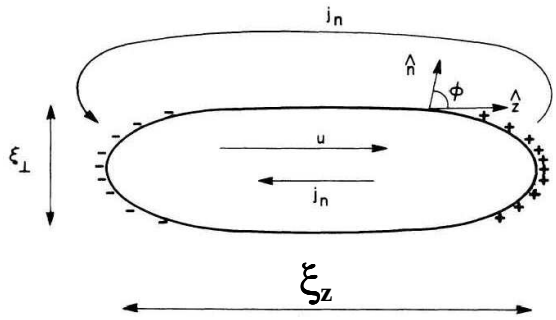

Figure 2.13: The schematic picture of localized mode showing induced polarization charges $(+,-)$ and normal current j_n *backflow*. A long-wavelength $(q \to 0)$ external field induces internal fields at a finite wavelength, comparable to ξ_z domain length scale. The local fields induce *screening* currents of free carriers, which dissipate energy.

Mixing of the mode character and the influence of conductivity anisotropy on the longitudinal character of local mode may be appreciated when the following is considered:

The local mode is considered as a local displacement u, of the CDW, over a region $(\xi_\perp, \xi_z)$, with $u = 0$ outside this region. Within this length scale, the mode has a pinning energy V_0, and it responds to the average internal, local, field $\langle E_z \rangle$. The equation of motion is then

$$(-m^*\omega^2 - i\gamma_0\omega + V_0)u = \langle E_z \rangle \tag{2.36}$$

The determination of local field $\langle E_z \rangle$ depends on the correction of external field for depolarization. Here, the local mode is regarded as polarized inclusion in a medium. In a case of elongated domain, $\xi_\perp \ll \xi_z$, the local field is equal to the external one. Thus the characteristic mode frequency is $\Omega_0^2 = V_0/m^*$, the frequency of the transverse, pinned, mode found for the uniform pinning case. For a different shape of the domain $\xi_\perp > \xi_z$, $\langle E_z \rangle = E_{ext} - P/\varepsilon_z$. Polarization P is given by $\rho_c u$, and the characteristic mode frequency is shifted to $\tilde{\omega}^2 = V_0/m + \rho_c^2/m^*\varepsilon_z$, the frequency of the longitudinal mode, ω_L^2, found previously for the uniform pinning case. Thus a disordered nature of CDW, and respective necessity to regard the local modes of CDW for different domains, has introduced mixing of the character of modes in a natural way.

Results

Measured conductivity, as constructed above, contains single particle conductivity $\tilde{\sigma}_z$ and also the CDW contribution of mixed character

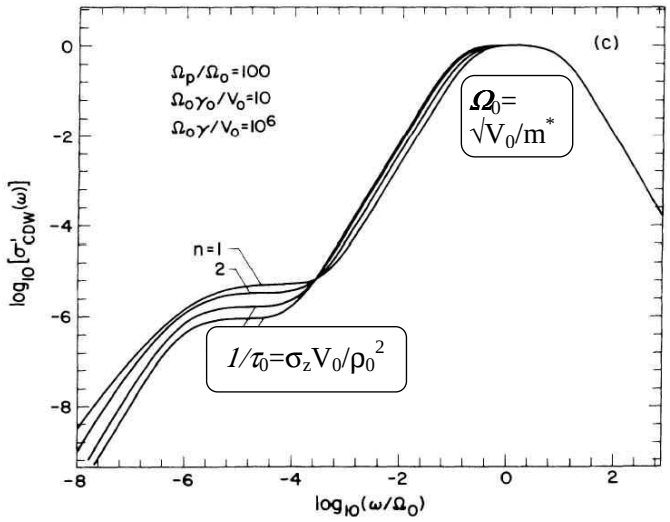

Figure 2.14: The real part of the transverse component of conductivity σ'. The pinned mode, as a peak at Ω_0 is shown. The extra broad dispersion is found at lower frequencies, at $1/\tau_0$, related to the plasmon overdamped tail from Fig. 2.19.

$$[\sigma_{meas}(\omega)]_z = \tilde{\sigma}_z - \frac{i\omega\rho_c^2 G_\rho(\omega)}{1 + i\omega\rho_c^2 G_\rho(\omega)/\tilde{\sigma}_z} \tag{2.37}$$

In order to study the effect of a distribution of modes, the CDW contribution is rewritten in terms of scaled variables.

$$\sigma_{CDW} = \frac{\rho_c^2}{\gamma_0} \frac{-i\omega\tau_0 I(\omega)}{1 + i\omega\gamma_1(\omega) I(\omega)} \tag{2.38}$$

where

$$\gamma_1(\omega) = \tau_0[1 - i\omega\tau_0(\Omega_0/\Omega_{pl})^2]^{-1} \tag{2.39}$$

and

$$I(\omega) = \int_0^\infty dx g(x)[x - (\omega/\Omega_0)^2 - i\omega\tau - i\omega\gamma_1(\omega)]^{-1} \tag{2.40}$$

Two characteristic oscillation frequencies appear, Ω_0 and Ω_{pl}, and two characteristic relaxation times ($\tau_{bare} = \gamma_0/V_0$, $\tau_0 = \rho_c^2/(\sigma_z V_0)$. $g(x)$ is a model distribution of modes. For example, if the distribution of localized modes is taken to be a *delta*–function, $g(x) = \delta(1 - x)$, the Eq. 2.29 is recovered–that is, the uniform pinning case occurs.

In Fig. 2.14, a narrow peak (pinned mode at Ω_0) due to coupling of external ac field to the transverse mode is shown. Bare damping γ_0 (which

applies for transverse modes) probably has its origin in phason-phason or phason-phonon scattering processes.

There also appears an extra broad dispersion at $1/\tau_0$ frequency. It is due to coupling of external ac field to the longitudinal screened mode. This break-down of selection rules corresponds to the longitudinal response mixing in the transverse one due to non-uniform pinning. That is, the tail of the plasmon from Fig. 2.12 mixes into the measured conductivity.

We note that τ_0 is proportional to the single particle conductivity σ_z, and for insulators it is expected to have the Arrhenius activation equal to the conductivity one. This is due to the external field inducing local field on the level of the length scale ξ_z of the local mode. These local fields induce screening currents of free carriers, which dissipate energy resistively, Fig. 2.13. It is precisely the resistive damping which appears in Eq. 2.30, for the uniform pinning case. The proportionality of conductivity and relaxation times τ_0 is well confirmed in various experiments on standard CDW materials, [129, 130, 131, 132].

Additional feature of this analysis is the relation between characteristic relaxation time $\tau_0 = \rho_c^2/(\sigma_z V_0)$ and characteristic pinned mode frequency, $\Omega_0 = \sqrt{V_0/m}$. These two values, as well as σ_z, result from spectroscopy experiments on standard CDW materials, performed in a very broad frequency range. An expression for calculating the CDW condensate effective mass is given by Littlewood:

$$m^* = \rho_c^2/(\sigma_z \cdot \tau_0 \cdot \Omega_0^2) \tag{2.41}$$

Using this relationship, for example, Reagor *et al.* [133] estimated the effective mass for a standard CDW material $(TaSe_4)_2I$ to be 10^4. This value is, indeed, within the experimental limits of 10^2–10^4 for CDW materials, [126]. Eventually, it is appropriate to note that Littlewood's model presents an important tool for connecting the experiment and theory. Our data will also be analyzed in this manner.

3 Experimental techniques

3.1 $(TMTSF)_2PF_6$

3.1.1 $(TMTSF)_2PF_6$ samples and high pressure measurements protocol

We studied a nominally pure $(TMTSF)_2PF_6$ single crystal originating from a batch of high quality crystals. The high quality of the batch was proved in a study of quantum Hall effect (QHE) influence on the linear and non-linear resistivity tensor in magnetic field-induced spin density wave (FISDW) phases of $(TMTSF)_2PF_6$, [11]. The crystal had a standard needle shape and dimensions $3 \times 0.2 \times 0.1\ mm^3$. The four annular contact geometry was used: gold was evaporated on the sample and the leads were attached with silver paste. The contact resistances were 2-3 Ohms. High quality of the crystal was confirmed by the resistivity ratio (ρ_{300K}/ρ_{min} of the order of 1000 (ρ_{min} is the minimum in resistivity just above the SDW transition). All electrical transport measurements were performed along the needle **a**-axis. Resistance measurements in the linear regime were done using the standard AC low frequency technique. In the linear regime, there should be no sample resistance dependence on the applied electric field and this was duly checked by using 1 and 10 μA currents for measurements. High critical currents measurements were performed using a DC pulsed technique with 10 μs short pulses and current amplitudes up to 100 mA. The pulse repetition period was 40 ms, *i.e.* 4000 times longer than the pulse. This is enough to avoid Joule heating of the sample even at the highest amplitudes of 100 mA. Non-heating was also checked by the shape of the pulse displayed on the osciloscope. If heating effects were present when the highest non-pulsed currents were applied (0.3, 1 mA) then the SDW resistance just above T_{sc} should have lowered at increasing current. The inspection of Fig. 4.6, in the next Chapter, demonstrates that there is no difference in resistances measured in the SDW phase using currents from 0.001 to 1 mA.

The pressure cell was plugged on a Helium3 cryostat capable of reaching

0.35 K. Pt-100 and Lakeshore CarbonGlass 500 thermometers were used, as well as RuO_2 thermometer for the temperatures below 2 K.

Pressure was applied in a regular beryllium-copper cell, with silicon oil inside a Teflon cup as the pressure transmitting medium that would not freeze abruptly but solidify continuously. Consequently, reduced were the mechanical stresses and pressure shifts common to the freezing points of other liquids, which allowed numerous thermal cyclings of the same sample without notable cracks.

However, the drawback of such a technique is the requirement to change pressure only when the cell is warmed up to RT. For an accurate pressure determination, we used an InSb pressure gauge[134], located inside the cell close to the sample. The information from the pressure gauge can be also cross-checked by the phase diagram of $(TMTSF)_2PF_6$ [10]. The InSb gauge was calibrated at RT against a manganine gauge establishing a linear pressure dependence of the InSb gauge resistance at a rate of 2.5%/kbar in a 6–12 kbar range. We note that the pressure values, in this and in the following Chapter 4, are in kbar, where 1 kbar equals 0.1 GPa.

Since the pressure could be changed at RT only, the measurements were conducted in 19 consecutive runs, (see Table 3.1, [135]). For all runs, after having applied the pressure at RT, cooling started immediately and continuously down to 0.35 K. The electrical transport measurements done, the sample was warmed back to RT and a subsequent increase or decrease of pressure was immediately applied before next cooling. The temperature sweep rates in cooling and warming did not exceed ± 60 K/h. The change of pressure at RT was checked by the resistance of the InSb gauge: for instance, a 0.8% increase in resistance corresponded to a 300 bar increment in pressure. Respective decrease of the sample resistance at a rate of 10%/kbar at RT was also used as a secondary pressure gauge. Additionally, the pressure coefficient of the InSb resistance measured at RT was equal to that measured at 6 K. Thus, we confirmed that all the pressure steps we made were measured by the InSb gauge with an accuracy of ± 30 bar.

The complete range of pressures applied and the chronological order of the experiment are found in Table 3.1. Starting in run #1, at a pressure $p_1 = 6.8$ kbar, we were able to sweep a 4 kbar wide region with increments ranging from 300 to 100 bar. From run #1 to run #16, pressure was always increased in the same manner, except for a 1400 bar increment in the last run. From run #16 to run #17, we made a large pressure drop of 2350 ± 50 bar. The value was calculated from the InSb resistance, later confirmed by the phase diagram of $(TMTSF)_2PF_6$. Therefore, the R *vs.* T curve for the run #17 was almost identical to the curve of the run #10 (both SDW, T_{SDW} and superconducting, T_{SC} transition temperatures were found identical

within experimental errors). Small pressure increments for run #18 and #19 were again performed in the usual manner. Such a procedure allowed us to investigate the pressure domain 8.65–9.3 kbar with a pressure control that could not have been achieved in early studies.

RUN	pressure (kbar)	T_{SDW} (K)	T_{SC} (K)
1	6.8	7.9	
2	7.1	7.1	
3	7.3	6.6	
4	7.5	6.2	
5	7.7	5.9	
6	7.85	5.6	
7	8.15	5.3	
8	8.35	4.7	
9	8.45	4.4	
10	8.65	3.8	1.18
17	8.65	3.8	1.18
11	8.75	3.5	1.19
18	8.9	2.85	1.21
12	8.95	2.85	1.21
13	9.1	2.45	1.21
19	9.2	1.8	1.21
14	9.3	1.4	1.21
15	9.6		1.195
16	11		1.106

Table 3.1: The complete range of pressures applied on the single crystal of $(TMTSF)_2PF_6$ studied in this work. Number of the run presents the chronological order of the experiment. The observed spin-density wave, T_{SDW} and superconducting, T_{SC}, transition temperatures are also given in the table.

3.2 (La, Sr, Ca)$_{14}$Cu$_{24}$O$_{41}$

3.2.1 Samples and contacts preparation

The q1D cuprate single crystals were synthetized by the group of J. Akimitsu, T. Sasaki and T. Nagata from the Department of Physics, Aoyama-Gakuin University, Kanagawa, Japan. The q1D cuprate materials are prepared in two steps. Initially a stoichiometric mixture of dried powdered $CaCO_3$, $SrCO_3$ (and/or La_2O_3) and CuO is prepared. This mixture may be melted, [71, 70], or calcined (heated and grinded) at high temperature [92], when a solid state reaction happens. This is the way polycrystalline samples are prepared. They are regrinded and sintered into polycrystalline rods, well shaped for floating zone recrystallization, which is a second step. Floating zone method is, basically, a recrystallization by local melting of the polycrystal. A melted zone (obtained by focusing high power light/heat source on the sample) is slowly moved along the crystal, thus allowing it to melt and slowly recrystallize. All these procedures have to be performed in the controlled atmospheres of either oxygen, hydrogen, or inert gasses, in order to control oxydation/reduction levels in the material. Actually, this sample preparation scheme is quite general in a broad field of transition metal oxides, [137]. X-ray diffraction (XRD) is used to check if the preparation procedure has provided single crystals. The obtained single crystals are quite large (*e.g.* 6mm diameter, 10 cm long) and may consist of several domains. Single crystal samples for transport measurements have to be cut away from these large crystals, Fig. 3.1.

The single crystal samples of q1D cuprates were between 3 and 5 mm long, with cross-sections of 0.2-0.4 cm^2. Precision of the cut, *i.e.* the orientation of cut-away single crystal along the axes was also checked by XRD. The macroscopic crystal planes deviated from the crystallographic axes not more than the experimental error of the XRD equipment used, 1^o-3^o, [136].

For the dc resistivity measurements the four annular contact geometry was used. For the complex conductivity only two contacts had to be applied, covering the ends of the sample. This two contact geometry was necessary to avoid the influences from the stray capacitances of test-leads and cables, Fig. 3.1. Electrical contacts to the sample were obtained by a special DuPont 6838 silver paste applied directly on the surface and heated for one hour at 750 K in oxygen flow atmosphere. Thin gold leads (20 μm) were then pasted to the baked contact areas of the sample. Other methods of contact preparation were also tested, *e.g.* gold was evaporated onto the sample surface, or silver paste was applied without heating, or it was baked without oxygen flow atmosphere. Any of those impaired the possibility to measure the intrinsic sample properties. Even with the established contact preparation

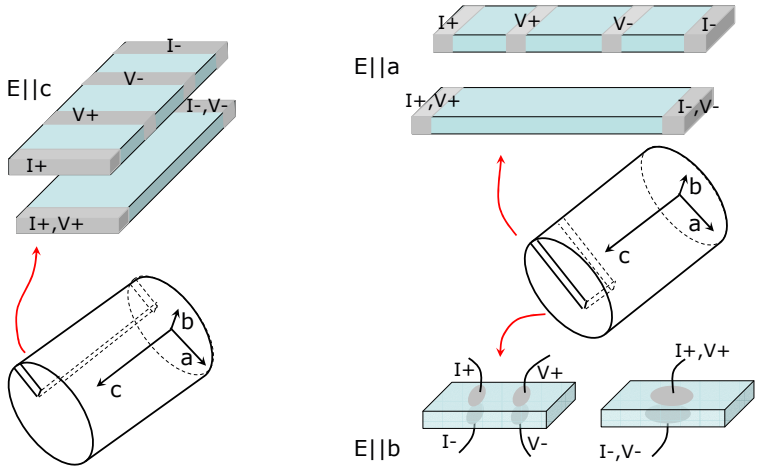

Figure 3.1: Single crystal samples ($5 \times 1 \times 0.2$ mm^3) for transport measurements along c, a or b axis were carefully cut away from a larger single crystal, designated as a cylinder. This larger single crystal was, after synthesis, confirmed by XRD to be single domain. Precision of the cut, *i.e.* the orientation of the cut-away single crystal along the axes was also confirmed by XRD. The macroscopic crystal planes deviated from the crystallographic axes not more than 1^o-3^o. Either four or two contacts were applied for dc resistivity or complex conductivity (LFDS) measurements, respectively .

method, the experimentalist should be ware of the possible artefacts: the room temperature resistivity of the material under study might be too high, the activation energies for resistivity might be strongly enhanced and strong nonlinear conduction effects might appear, as well. Furthermore, the complex conductivity measurements sometimes showed large capacitances where they should be negligible.

3.2.2 dc resistivity measurements

Measurements were performed in the temperature range 300 K - 2 K in a He-cryostat, where He-pumping was used for temperatures below 4.2 K. Pt-100 and Lakeshore CarbonGlass 500 thermometers were used. Temperatures above room temperature up to 750 K were reached in a simple thermostat (an oven) with an on-off temperature regulation. Pt/Pt-Rh10% thermocouple was used as a thermometer. Thermometry was calibrated properly thus the resistance *vs.* temperature curves measured in both of the setups joined smoothly. In a special case of La based compounds, we used a cryostat featuring a sample holder with the heating capability where temperatures up

to 400 K, [138], may be reached. Thus we avoided any possibility of artefacts due to the sample transfer from the thermostat to cryostat, which might have appeared exactly in the very temperature region we wanted to measure as carefully as possible. The results from all three setups coincided perfectly.

In this 2 K -700 K temperature range, measured resistances covered 14-15 orders of magnitude. Therefore, we had to use 4 different setups. For the low frequency lock-in setup, Stanford Research SR830 and Perkin-Elmer 7265 lock-ins were used for lowest resistances of 1 mΩ-1 kΩ. dc current source Keithley 220 and Keithley 182 nanovoltmeter were used in the range of 1 Ω-100 MΩ. These two setups are standard four probe methods. For higher resistances, two probe setups had to be used to avoid a time-constant problem. That is, the measured resistance, R, combined with the input capacitance ($C \approx 5$ nF for the nanovoltmeter), defines a very long time constant RC. And when, as for four probe techniques, the current is applied the sample/voltmeter combination behaves as an RC circuit which takes a long time to charge, *e.g.* $10 \times RC$. So, the dc two probe technique for resistances up to 10-30 GΩ was used. That is, either Keithley 617 electrometer or Keithley 487 picoammeter, were used in V/I mode since here the voltage was applied and the current was measured. Also, these instruments have much higher input impedances than nanovoltmeters. Finally, for resistances up to 1 TΩ the most elaborate two probe ac technique was used. The ac voltage was sourced from the lock-in and applied to the sample. The resulting current was measured by the Stanford Research SR570 current preamplifier, and converted into a voltage read by a lock-in. One has to take care to measure at low enough frequency (down to 0.01 Hz), in order to stay below the low frequency dielectric modes of the sample.

In order to search for possible non-linear effects the resistance was also measured as a function of applied electrical field. These measurements were performed in four probe configuration, using a current source and a nanovoltmeter. Thus, a possible nonlinearity of the contact resistances was excluded.

In two contact measurement, contact resistances influenced the result. Measurements of the intrinsic sample resistivity are, therefore, performed in four contact configuration, to avoid the contact influence. In order to judge on the contact influence in the lowest temperatures region where measurements have to be performed in two probe configuration, we followed the procedure described below.

We have observed two different cases. For (Sr, Ca) materials measured with electric field, E, applied along a and b axis ($E||a$, $E||b$) and for all three directions for La substituted materials, both configurations gave practically identical results - indicating that the contact resistances were negligible in comparison to the sample bulk resistance. In the temperature region of in-

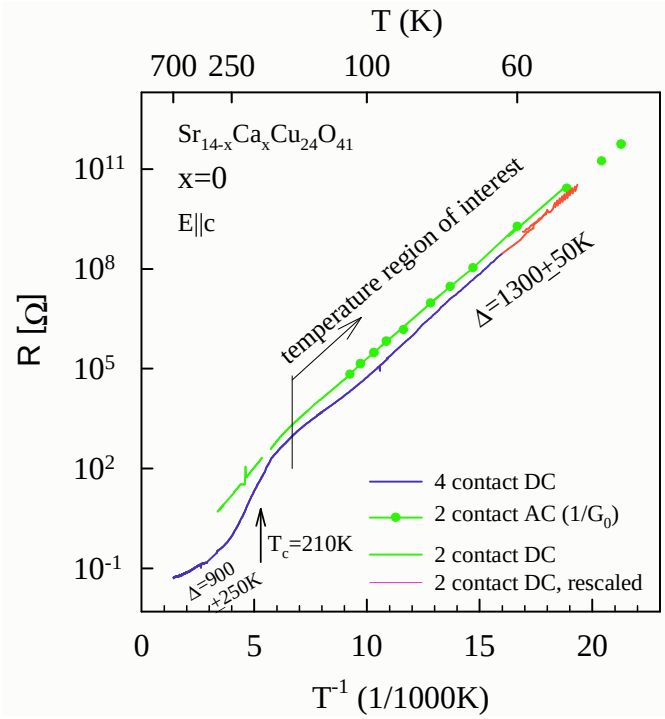

Figure 3.2: Resistances for $Sr_{14-x}Ca_xCu_{24}O_{41}$, $x = 0$ material along the most conducting c axis ($E||c$). ac &dc two and dc four contact configuration results are compared. For all the methods in the temperature region of interest the same activation energies were obtained. Four contact dc reaches 100 MΩ (blue line), two contact dc 30 GΩ (green line) and two contact ac 2 TΩ (green dots). The red line represents two contact dc data rescaled to four contact dc, as an example.

terest, for (Sr, Ca) materials the two contact measurements along the most conducting c axis ($E||c$) gave at least twice larger result when compared to the four contact measurements - implying that the contact resistance is comparable to the sample resistance. Therefore, the procedure is clarified in Fig. 3.2 for the example of $Sr_{14-x}Ca_xCu_{24}O_{41}$, $x = 0$ material. First, we compare the resistance results in two (green line) and in four (blue line) probe configuration in the low temperature region where the resistances do not exceed 100 MΩ. From both two & four contact measurements we find the same activation energies, *i.e.* the ratio between the two and four contact results is constant. We extrapolate on this and conclude that in the temperature region where the resistances exceed 100 MΩ it is possible to rescale (red line) the results obtained in two contact configuration on to the results obtained in four contact configuration. We also note that two probe ac technique results (green circles) coincide perfectly with those from two probe dc technique, and as well, give the same activation energy to the lowest temperatures. Therefore, we conclude that two probe measurements provide results on the intrinsic properties of the material and that influences of contacts, if any, are negligible.

3.2.3 Complex conductivity measurements- low frequency dielectric spectroscopy (LFDS)

Complex conductivity is measured in two contact configuration from the room temperature down to 2 K in a He-cryostat. Thin coaxial cables (Lakeshore, diameter 1 mm, 50 Ω) are used on the sample holder in order to minimize stray capacitances. In order to cover a large frequency and impedance range, two different methods were used to measure the frequency dependence of the complex conductance $Y(\omega) = G(\omega) + iB(\omega)$. At high frequencies (20 Hz–10 MHz) a Hewlett Packard 4284A and Agilent 4294A impedance analyzers were used. The high frequency limit F (in MHz) is determined by the cabling length L (1.5 meters for our cryostat). The rule of the thumb is $FL < 15$ - basically, the wavelength should be much longer than the cabling length. At low frequencies (0.01 Hz–10 kHz) a set-up for measuring high-impedance samples was used. The ac voltage is applied to the sample. The current response of the sample is transformed to the voltage by a Stanford Research SR570 current preamplifier, and subsequently detected by a dual-channel digital lock-in, Stanford Research SR830. It is important to stress that we obtained the same results by using both methods in the frequency range 20 Hz–10 kHz where these methods overlap.

Concerning ac signal levels, higher voltages were carefully avoided in order to stay in the linear regime. We used either 20 or 50 mV, which resulted with electric fields on the sample of up to 200 mV/cm. For the cuprate materials under study the non-linear effects are almost negligible, 2-3 %, at the electric fields up to 10 V/cm, see Sec. 5.1. Thus, we consider this low enough levels, still giving strong enough signals.

Further, by taking into account the results of open-circuit measurements, we have assured that the stray capacitances do not influence the imaginary part of conductivity in the frequency window 0.01 Hz–10 MHz and in the temperature range of our study. Effectively, we subtracted the results of open-circuit measurement $Y(\omega)_{open} = G(\omega)_{open} + iB(\omega)_{open}$ from the $Y(\omega)$ results for the sample, [139]. This procedure removes background influences and improves the sensitivity of measurement. The background level of sample holder installed with coaxial cables is as small as $C_b = B(\omega)_{open}/\omega = 0.45$ pF. Coaxial cores are signal pathways, while shields have to be interconnected as close as possible to the sample. This nullifies the cable capacitance. The observed background capacitance C_b is due to the unshielded pins to which the sample is attached.

From the real and imaginary parts of the conductance, Fig. 3.3, left panel, obtained after subtracting the background, the components of the dielectric

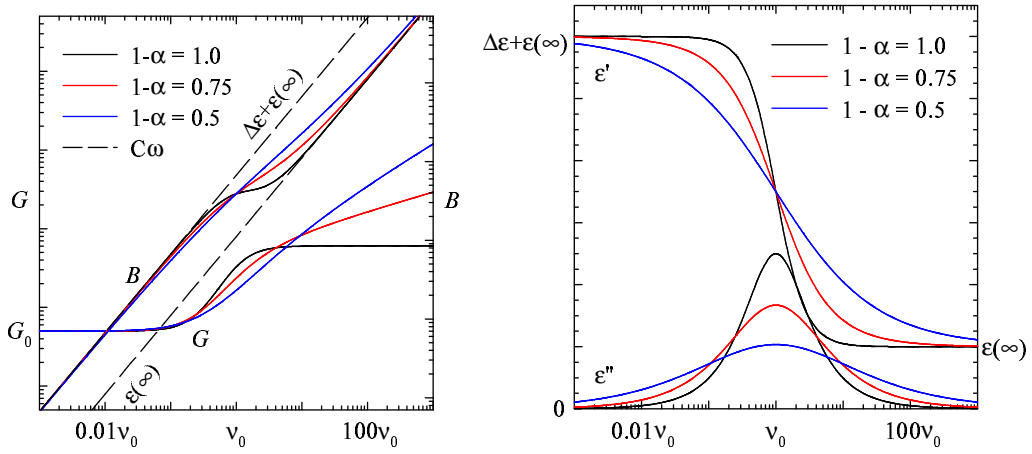

Figure 3.3: Left panel: The typical forms of real, G, and imaginary, B, parts of the conductance which are eventually transformed into the real, ε', and imaginary, ε'', parts of the dielectric function, according to Eqs. 3.2. Right panel: The typical forms of real and imaginary parts of the dielectric function, that can be described by Havriliak-Negami function, Eq. 3.3, for different $1-\alpha$ parameter values.

function were extracted using the relations

$$\varepsilon_0\varepsilon'(\omega) = \frac{l}{S}\frac{B(\omega)}{\omega} \tag{3.1}$$

$$\varepsilon_0\varepsilon''(\omega) = \frac{l}{S}\frac{G(\omega)-G_0}{\omega} \tag{3.2}$$

where ε_0 is the permittivity of vacuum, 8.858 pF/m. G_0 is the dc conductivity obtained at low frequencies where $G(\omega)$ is independent of ω. $\frac{l}{S}$ is the ratio between the sample length l (*i.e.* length between the contacts) and the cross section S. This ratio is called the aspect ratio.

The observed dielectric response can be well fitted by the phenomenological Havriliak-Negami (HN) function [140], Fig. 3.3. This is a generalized form of Debye function, widely used to describe the relaxation processes in disordered systems.

$$\varepsilon(\omega) - \varepsilon_{\mathrm{HF}} = \frac{\Delta\varepsilon}{1+(i\omega\tau_0)^{1-\alpha}} \tag{3.3}$$

$\Delta\varepsilon = \varepsilon_0 - \varepsilon_{\mathrm{HF}}$ is the relaxation strength, and ε_0 and $\varepsilon_{\mathrm{HF}}$ are the static and high frequency dielectric constant, respectively. τ_0 and $1-\alpha$ are the central relaxation time and the shape parameter which describes the symmetric

broadening of the relaxation time distribution function, respectively. The observed dielectric response in the frequency window of 0.01 Hz–10 MHz, for the various materials under study, was successfully fitted to a single HN mode. Measured data were fitted by using the least squares method in the complex plane [142, 143, 139]. Such an approach takes into consideration both real and imaginary part of the dielectric function while at the same time strongly improves the resolution if compared with the method in which the real and imaginary parts are treated separately, [141]. The complex plane method proved itself to be a powerful tool to resolve reliably a mode if it contributes to the measured capacitance with at least 0.5 pF. The capacitance measurement resolution is of the order ± 0.01 to 0.03 pF. For the aspect ratios (Eq.3.2) of the samples we worked with, 70-300/cm, 0.5 pF would amount to the minimum observable dielectric modes of 400-1500 with the resolution as good as ± 10.

Since the complex conductivity has to be measured in 2 contacts, we need to judge on the contact influence. Firstly, we note that G_0 low-frequency conductivities obtained here correspond perfectly to two contact dc resistivities - the activation energies are also the same, see Fig. 3.2. Secondly, the central relaxation time τ_0 obtained here behaves in an activated manner characterized by this same activation energy, see Chapter 5, Fig. 5.1. Therefore, we conclude that the contacts do not influence the intrinsic sample properties, despite being comparable to the bulk for the case of $Sr_{14-x}Ca_xCu_{24}O_{41}$ materials measured along c axis. In the case of (Sr, Ca) materials measured along a or b axis ($E||a$, $E||b$) and for all three directions for La substituted materials the contact resistances were anyhow negligible in comparison to the sample bulk resistance. As described before, if contact preparation failed, large capacitances may be observed in the temperature region where they should be negligible. In some cases, where the two contact measured resistivity was at least 3 times larger than the four contact one, an additional dielectric mode was observed. The latter effect is a known artefact due to poor contacts, [129].

We combine our dc/LFDS results with the quasi-optical microwave and far infrared (FIR) optical conductivity results obtained by the group of prof. M. Dressel and his coworkers B. Gorshunov, P. Haas and T. Rõõm at University of Stuttgart, Germany. The Stuttgart group utilized a coherent source quasi-optical spectrometer, for frequencies 5 to 25 cm^{-1} (150-750 GHz), for direct measurements of $\varepsilon'(\omega)$ and $\varepsilon''(\omega)$, [144]. From the far infrared (FIR) up to 10 000 cm^{-1} the polarized reflection was determined by a Fourier transform spectrometer. Combined data sets were analyzed by the Kramers-Kronig relations in order to obtain the spectra of $\varepsilon'(\omega)$, $\varepsilon''(\omega)$, and conductivity $\sigma(\omega)$.

4 Investigation of phase diagram of $(TMTSF)_2PF_6$

In this work, an optimised pressure control (see Section 3.1) was used to investigate the critical region of the phase diagram (see Fig. 1.1) of $(TMTSF)_2PF_6$, which features the phase boundary between the spin density wave, SDW, and superconducting state, SC. We have studied the pressure and temperature dependence of resistance and superconducting critical current, [135].

4.1 Experimental observations

4.1.1 Metallic state : $T > T_{SDW}$, $T > T_{SC}$

In Fig. 4.1a, we show the resistance *vs.* temperature below 20 K for a set of characteristic pressures from 6.8 to 9.2 kbar together with the data at 11 kbar where a direct metal-to-SC transition is observed. The temperature dependence of resistance in the metallic state (we concentrate on temperatures below 20 K) is quadratic, as expected when the electron scattering is dominated by electron-electron interactions, see Sec. 1.1.2, [27, 145].

We have noticed a shift of R *vs.* T curves by temperature independent resistance value after each pressure run (Table 4.1, see also Sec. 3.1), without any change of the actual temperature dependence. The resistance curves are usually shifted 0.1–0.2 mΩ upwards after each run (see caption of Fig. 4.1a). This effect is most clearly seen in the metallic state below 20 K since the absolute values of resistance (1–2 mΩ) become then comparable to the offset. An example of this offset is shown in the inset of Fig. 4.1a. The two resistance curves result from run #10 and #17, *i.e.* they were measured at equal pressures, but with 7 runs performed in-between. The behaviour of run#17 can be made equal to the run #10 provided an offset of 2.5 mΩ is subtracted from resistance values of the earlier run #10. We tend to relate this effect to an increase of residual resistance due to a cumulative creation of defects after each temperature cycle. We will show later that such defects are not cracks,

RUN	pressure (kbar)	T_{SDW} (K)	T_{SC} (K)	Δ_{SDW} (K)	R_∞ (mΩ)	c vol%	I_c (mA)
1	6.8	7.9		9.38	12.1	0.03	
2	7.1	7.1					
3	7.3	6.6					
4	7.5	6.2					
5	7.7	5.9					
6	7.85	5.6					
7	8.15	5.3		6.35	12.0	0.09	
8	8.35	4.7					
9	8.45	4.4		5.74	11.30	0.2	
10	8.65	3.8	1.18	5.56	10.60	0.3	
17	8.65	3.8	1.18				.001
11	8.75	3.5	1.19	5.58	8.772	0.36	
18	8.9	2.85	1.21	6.90	2.473	1.25	0.15
12	8.95	2.85	1.21	6.70	2.146	1.4	0.3
13	9.1	2.45	1.21	6.90	0.320	5	7
19	9.2	1.8	1.21	6.30	0.0452	17	35
14	9.3	1.4	1.21	6.80	0.0022	89	
15	9.6		1.195				
16	11		1.106			100	35

Table 4.1: The complete range of pressures applied on the single crystal of $(TMTSF)_2PF_6$ studied in this work. The run number gives the chronological order of experiment. The observed spin-density wave, T_{SDW} and superconducting, T_{SC}, transition temperatures are given. The SDW activation energy, Δ_{SDW}, asymptotic resistances, R_∞ and the volume proportion c (vol%) of the metallic phase when the sample is in coexistence region are obtained from the fits of R *vs.* T data to the corrected Arrhenius law, Eq. 4.3. I_c are critical currents for the suppresion of SC phase.

as they would add junctions in the sample, that would be easy to detect in superconducting state. The added defects could be of point disorder nature of unknown origin. It should be noted that such phenomenon was previously unreported. Still, it can not be excluded from all the previous studies, since such extensive thermal cyclings were not performed before.

However, the metallic state resistance was the only feature influenced by extensive thermal cycling of the sample. The resistance values in the SDW state, which are orders of magnitude higher, were not influenced by the thermal cycling and we could not notice any influence on determination

of transition temperatures. Since the plot of resistance *vs.* T^2 (see Fig. 4.1b) reveals the existence of quadratic temperature dependence below about 12 K with residual resistance increasing slightly after each pressure run, we have decided to use the residual resistance value obtained in the run #1 as the reference value, assuming that the sample was the least damaged in the first run, as compared to all subsequent runs. In so doing, we have noticed that the resistance is weakly pressure dependent at 20 K and becomes insensitive to pressure below 10 K in the investigated pressure domain.

4.1.2 SDW region: $p < 8.6$ kbar, $T \lesssim T_{\mathrm{SDW}}$

As the SDW region, we denote low pressure, low temperature region where the transition to SDW state is observed as a sharp increase of resistance (Fig. 4.2a) without any hysteretic behaviour when sweeping temperature up and down. The exact point of transition is defined as the temperature of the maximum of logarithmic derivative of resistance with respect to the inverse temperature, $\partial(\ln R)/\partial(1/T)$ *vs.* T. In Fig. 4.2b, we show these maxima corresponding to the R *vs.* T curves above. Activation energy values, Δ_{SDW}, are well defined inside broad temperature spans, especially for the pressures in this region, 6.8–8.45 kbar (Fig. 4.3). We note here that the asymptotic resistance at infinite temperature, R_∞, remains constant in this pressure range, as expected in the standard semiconducting model.

4.1.3 SC region: $p > 9.43$ kbar, $T \lesssim T_{\mathrm{SC}}$

This pressure domain has been briefly investigated at two subsequently applied pressures (9.6 and 11 kbar). A direct transition from metallic to superconducting state has been observed, Fig. 4.4. T_{SC} was defined as the onset of resistance drop. These two pressures differ only in T_{SC}, which are 1.195 ± 0.005 K and 1.106 ± 0.005 K, respectively. The transitions are very narrow and no hysteresis has been observed at T_{SC}. The remaining shift of less than 3 mK observed between cooling and warming curves can be attributed to the finite speed of temperature sweep, ±1 mK/s and the thermal inertia of the pressure cell. The mean pressure dependence $\partial T_{\mathrm{SC}}/\partial p \approx -0.07$ K/kbar is in agreement with the value already reported by Schulz *et al.* [51].

4.1.4 Coexistence region: $8.6 < p < 9.43$ kbar

The coexistence region has been denoted as the regions of the phase diagram where both SDW and metallic (eventually SC) states clearly manifest. These

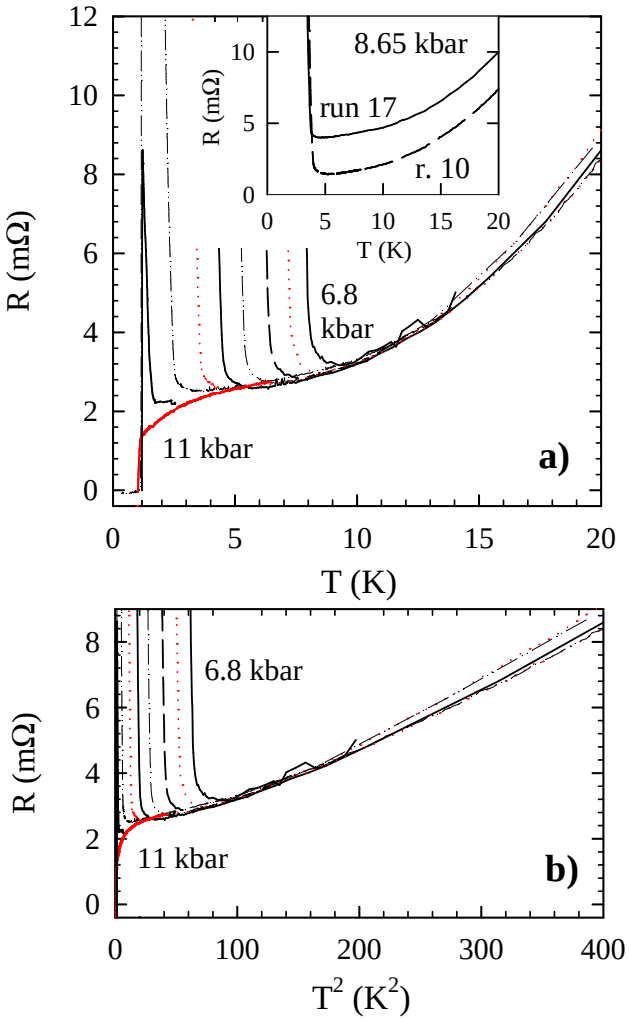

Figure 4.1: (a) Resistance *vs.* temperature curves for the usual set of pressures (see legend in Fig. 4.2), the sharpness of transitions may be fully appreciated. In the inset: A detail of the minimum in the R *vs.* T curves. For runs 10 and 17, both measured at 8.65 kbar, residual resistance shift amounted to 2.5 mΩ. (b) Resistance *vs.* temperature squared curves for the given list of pressures. Low temperature behaviour approaches the T^2 law of 3D metals.

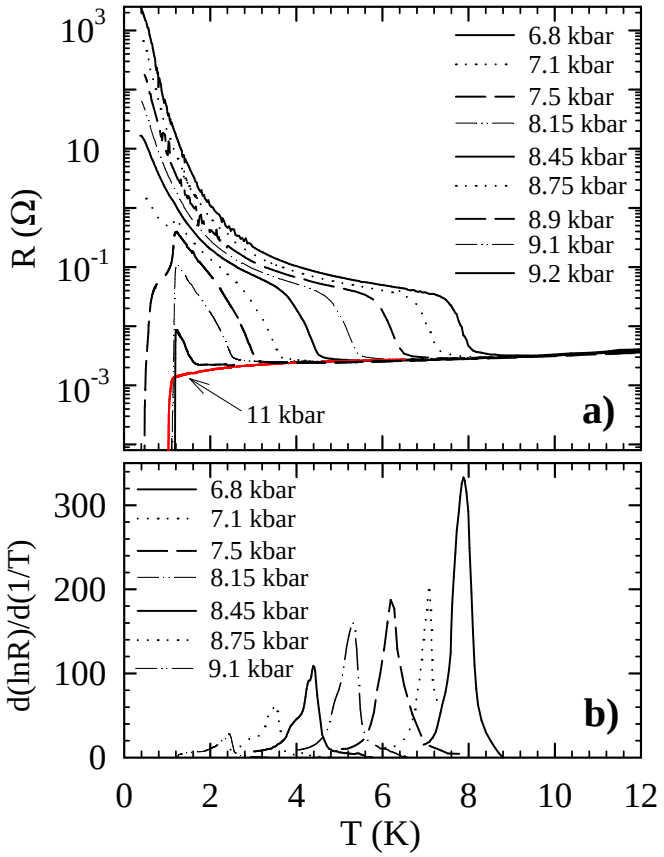

Figure 4.2: (a) The logarithm of resistance *vs.* temperature in cooling, at different pressures. Above the SDW transition (step-like features), resistance decreases as expected for a metal. (b) T_{SDW} is defined as a peak in the derivative of logarithm of resistance over inverse temperature, $\partial(\ln R)/\partial(1/T)$ *vs.* temperature, T.

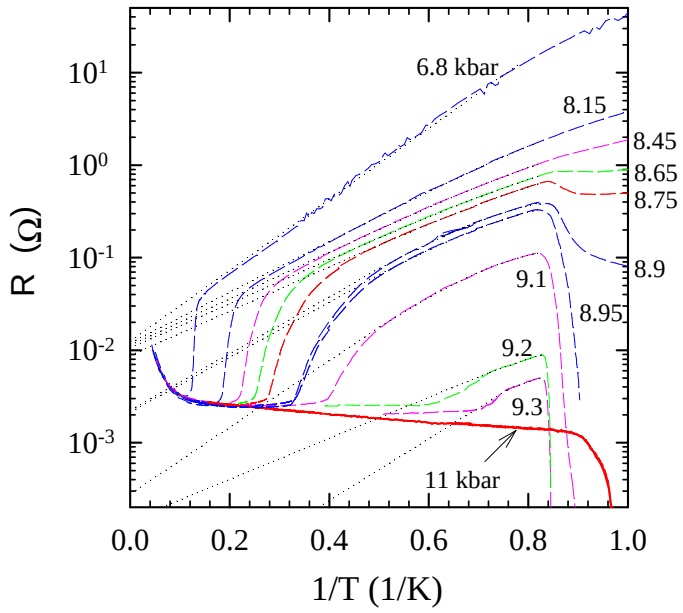

Figure 4.3: The logarithm of resistance *vs.* inverse temperature for a given range of pressures, depicts behaviour in the SDW phase. Fits to the corrected Arrhenius law (dotted straight lines, Eq. 4.3) give the same asymptotic resistances R_∞, for the curves inside pure SDW region. Inside the SDW/M region asymptotic resistances decrease by several orders of magnitude.

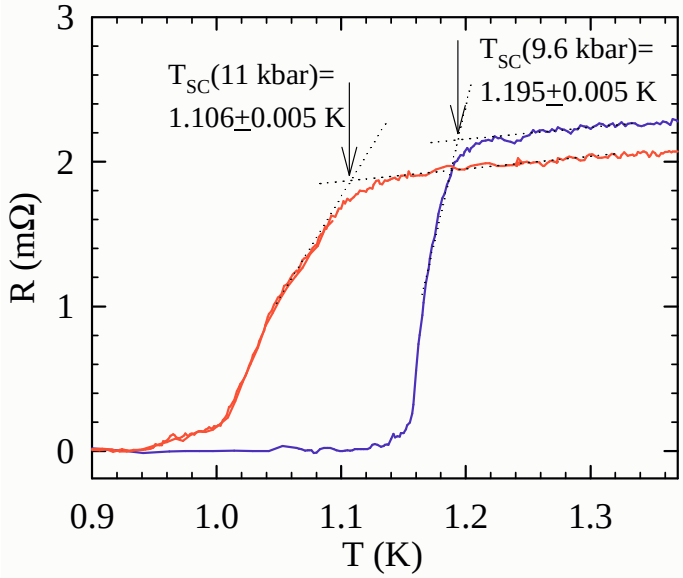

Figure 4.4: Resistance *vs.* temperature for two pressures, where a direct transition from metallic to superconducting state has been observed. T_{SC} was defined as the onset of the resistance drop, the exact temperature being located where the dotted extrapolation lines cross (arrows). No hysteresis has been observed.

regions are denoted SDW/Metal and SDW/SC, respectively. Taking the advantage of good pressure control, we managed to investigate eight pressure points with the same sample in this narrow pressure range. They were measured in two groups of five and three consecutive runs (see Table 4.1). The second group was measured after a large pressure decrease. This decrease was precisely targeted to reproduce a point (8.65 kbar) in the lower end of the pressure range of interest. This provided a check for our capability of accurately controlling the pressure, but also an opportunity to investigate in more detail this pressure range in the usual manner by small pressure increments. As already noted, 8.65 kbar runs #10 and #17 gave almost identical R *vs.* T curves except for the residual resistance offset.

$8.6 < p < 9.43$ kbar, $T_{SC} \lesssim T \lesssim T_{SDW}$: SDW/Metal

As shown in Fig. 4.5, a strong hysteretic behaviour is observed, in this pressure and temperature range, between cooling and warming resistance curves, suggesting an inhomogeneous electronic structure. This could be due to phase segregation, with the existence of metallic domains (Metal), in SDW background of strongly temperature dependent characteristics (size and relative disposition). This phase segregation region is denoted SDW/Metal, or SDW/M.

The extremal hysteretic resistance loop is recorded when the temperature sweep starts above T_{SDW}, reverses below T_{SC} and ends above T_{SDW} again. Different hysteretic loops appear when the temperature sweep is reversed between T_{SC} and T_{SDW} (see Fig.4.5a for a representative situation at 9.1 kbar). T_{SC} values determined from either cooling or warming curves are equal (Fig. 4.5b), within a few mK, as for the direct metal-to-SC transitions described above. It is quite interesting to note that a highly similar hysteretic behaviour of the thermopower was observed in the CDW state of $(NbSe_4)_{10}I_3$ [146].

$8.6 < p < 9.43$ kbar, $T \lesssim T_{SC}$: SDW/SC

In the pressure range, where SDW transitions are still well defined, R *vs.* T curves are characterised by a sharp resistance drop at $T = 1.2 \pm 0.01$ K. We start with a reasonable assumption that this feature is a manifestation of condensation of free-electron (M) domains into superconducting (SC) domains (while SDW domains remain unaltered). The SC domains could either percolate, and form large domains or, they could link, thanks to sufficiently narrow weak-links allowing for Josephson effect between them. Both mechanisms lead to zero resistance state. The following considerations will confirm

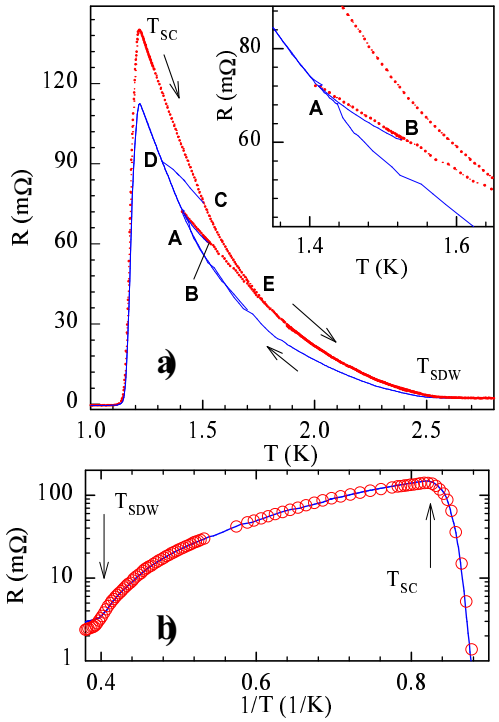

Figure 4.5: a)Resistance *vs.* temperature at 9.1 kbar, inside the coexistence range. Solid and dotted lines denote cooling and warming, respectively. The extremal hysteretic loop is recorded when the temperature sweep starts from above T_{SDW}, then cooling continues through points A, D, through T_{SC}, and into superconducting state. Below, at least 1 K, the sweep may be reversed and warming proceeds through T_{SC}, C, E and back above T_{SDW} into the SDW phase. Different hysteretic loops appear when the temperature sweep is reversed between T_{SC} and T_{SDW}. Loop 1: cooled from above T_{SDW} to **A**, reversed, warmed to **E** and further to above T_{SDW}. Loop 2: warmed from below T_{SC} to **C**, reversed, cooled to **D** and further to below T_{SC}. Loop 3: cooled from above T_{SDW} to **A**, reversed, warmed to **B**, reversed, warmed to **A** and further to below T_{SC}. Inset: The position of point **B** is shown. b) Extremal curves $\log R$ *vs.* $1/T$ plot in cooling (solid line) and in warming (open points). The warming curve is rescaled by a factor defined by the ratio of peak resistance values from the upper panel. This rescaled warming curve coincides perfectly with the cooling one.

our starting assumption.

Initially, at $p = 8.65$ kbar, the resistance drops to about 30% of the resistance which would be observed if an Arrhenius behaviour of the SDW state was extended below 1.2 K, Fig. 4.3. This drop occurs only if small (1 to 10 μA) measuring currents are used. For higher currents (100 μA), the resistance drop disappears and the usual Arrhenius behaviour is recovered. Then at 8.9 kbar, for the lowest currents, the resistance drops to zero (below our measurable limit of 0.001 mΩ). At 8.9 kbar the resistance drop is suppressed concomitantly with the increase of current as shown in Fig. 4.6. Still, for the current of 1 mA, the resistance drop is far from being completely suppressed (it was not possible to use higher current in order to avoid the Joule heating of the sample, see Section 3.1). Generally, the detection of zero resistance at the lowest pressures inside the SDW/SC region requires the lowest measuring current and/or lowest possible temperatures.

As pressure is further increased to 9.1–9.3 kbar, a sharp drop of resistance to zero within 30–40 mK below the onset temperature is obtained regardless the weak amplitude of the current. In this pressure range, we used the pulse technique to determine the critical current, I_c without heating effects: at 9.1 kbar, $I_c = 7$ mA, while at 9.3 kbar, I_c increased up to 30–40 mA as shown in Fig. 4.7. At 11 kbar, the critical current is of the same order of magnitude.

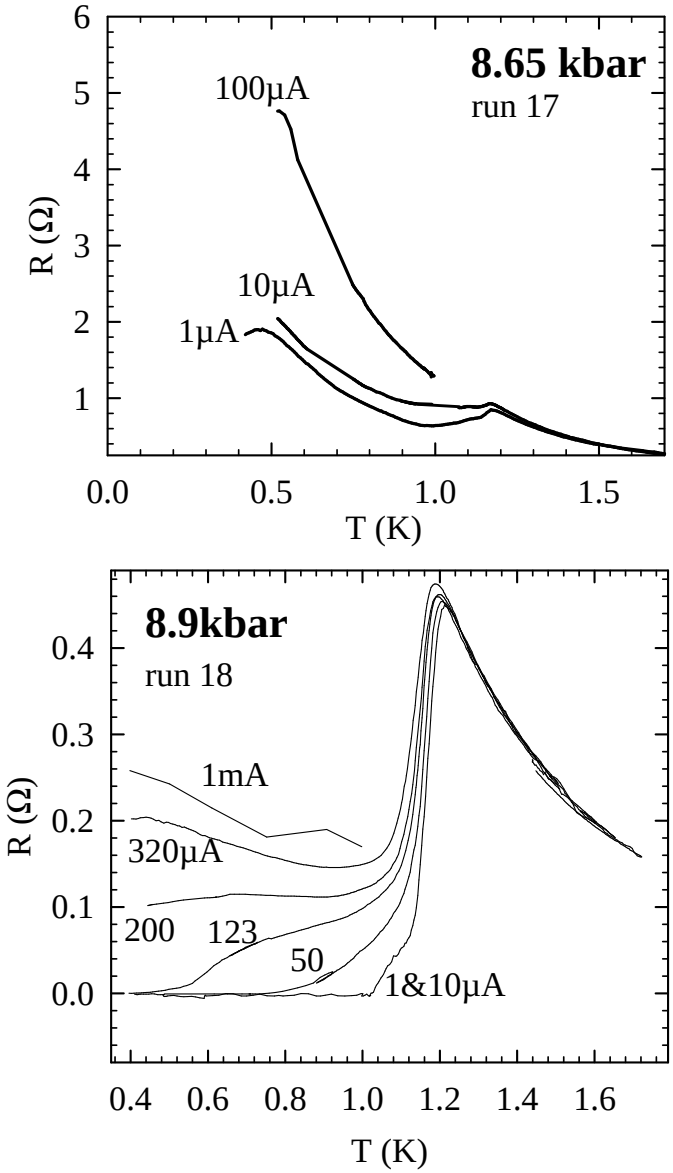

Figure 4.6: Resistance dependence on the measurement current at 8.65 and 8.9 kbar. At 8.65 kbar, zero resistance is not observed even for the lowest currents. For high currents, the insulating behavior is fully recovered. At 8.9 kbar, zero resistance is reached for currents as high as 123 μA and it was not possible to suppress the resistance drop completely even with a 1 mA measurement current.

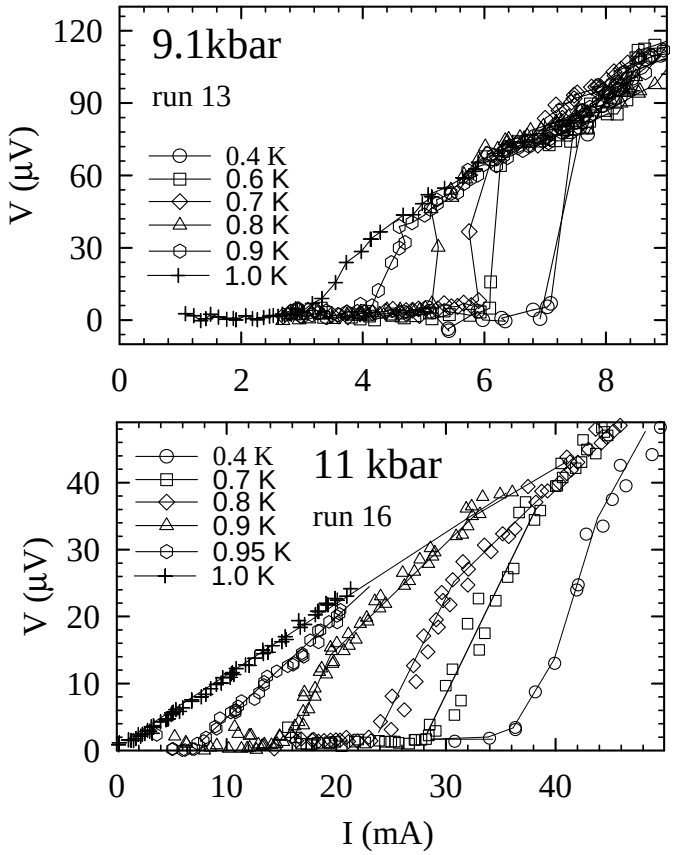

Figure 4.7: Voltage–current, V-I characteristics of the sample at various pressures. (a) At 9.1 kbar, at the lowest temperature of 0.4 K, the critical current ($I_c = 7$ mA) is order(s) of magnitude higher than at only 0.2 kbar lower pressure. (b) At 11 kbar, the SC state is considered to be homogeneous and I_c reaches the maximum value of 35 mA.

4.1.5 Detailed p, T phase diagram of $(TMTSF)_2PF_6$

An accurate determination of both transition temperature and pressure enables us to provide a precise T_{SDW} *vs.* pressure line, up to the critical point (p_c=9.43 kbar, 1.2 K) where the suppression of SDW instability occurs and SC phase is fully established. That is, for all runs below p_c, we have observed well defined and narrow metal-to-SDW transitions. For pressures close to the critical point, the transitions are becoming broader as reported in [12] and [47]. The authors claimed that the transition broadening is prohibitive for an accurate study of the T_{SDW} *vs.* pressure phase boundary at pressures close to p_c. However, thanks to the good quality of our sample (RRR=1000, while RRR=10 in [12]), broadening was much lower, and this effect did not prevent the determination of transition temperatures even at pressures close to the critical point. This is a salient result of this work.

Our data combined with the study of Biškup *et al.* which have determined normal state-to-SDW transition temperatures in the range 1 bar to 7.5 kbar, allow to present a p, T phase diagram of $(TMTSF)_2PF_6$ displayed in Fig. 4.8. The empirical formula, which takes into account the fact that p_c is found at $T_{SC} = 1.2$ K, and not at $T = 0$ K reads

$$T_{SDW}(p) = T_1 - [(T_1 - T_{SC}) * (p/p_c)^3] \tag{4.1}$$

Here, T_{SC} is the experimental value whereas $T_1 = T_{SDW}(1bar)$ and p_c are free parameters. Fits to Eq. 4.1 give best parameter values $T_1 = 12.0 \pm 0.15$ K and $p_c = 9.43 \pm 0.04$ kbar. T_1 and p_c values correspond excellently to the experimental ones despite the fact that they were obtained as the only free parameters in the fit. It is also interesting to note that T_{SDW} pressure dependence seems to be a pure cubic one.

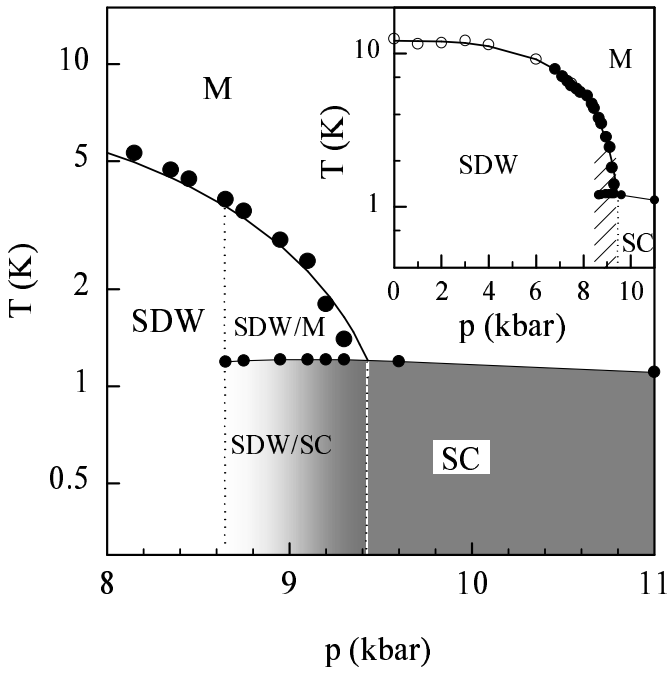

Figure 4.8: High pressure–low temperature phase diagram of $(TMTSF)_2PF_6$ material. SDW/M denotes the region where metallic, M, and SDW phases coexist inhomogeneously, below T_{SDW} line (large full points). Below $T_{SC} = 1.20 \pm 0.01$ K line (small full points), this coexistence switches into the coexistence of SC and SDW phases. A gradient in shading (SDW/SC region) below T_{SC} denotes the increase in volume proportion of SC phase in the bulk sample. Inset: Our diagram is completed with data taken from Biškup *et al.* (open points). Solid curve is the fit to our empirical formula for T_{SDW} *vs.* p dependence (Eq. 4.1).

4.2 Quantification of domain fraction in coexistence region

There are several features in our experimental data substantiating the coexistence of phases, SDW/M above 1.2 K and SDW/SC below 1.2 K. Hysteresis presented in Fig. 4.5 is the primary, still only qualitative one. The other two features, besides evidencing for the coexistence, lead us to the possibility of quantification of the phases volume fraction in the bulk. Indeed, we consider the orders of magnitude change in the critical current, as presented in Figs. 4.6 and 4.7 directly proportional to the change in the effective cross-section taken up by superconducting domains for SDW/SC coexistence region. For the SDW/M region we intend to show that the change in the effective cross-section taken up by metallic domains may be incurred from the orders of magnitude change in resistance of the sample for pressures inside the 8.65 – 9.43 kbar region.

In the following, we assume that the sample in the inhomogeneous region behaves as a composite of two materials. We consider these two materials to have the properties of the sample at 11 kbar (pure SC ground state) and 6.8 kbar (pure SDW ground state) respectively.

$T < T_{SC}$: Quantification of SDW/SC domain fraction

At 11 kbar, the pressure is sufficiently far above the critical pressure to have a fully homogeneous state, metallic or SC, depending on temperature. it is emphasized by the measurements of the critical current from 0.4 to 1.0 K (Fig. 4.7b). That is, one may divide U/I for the highest currents, which completely suppress SC state, as to recover a resistance comparable to those measured above T_{SC} at the same pressure (values of order of mΩ). Obviously, high currents take the sample from purely superconducting state to a purely metallic state. We hereby conclude that superconductivity is here homogeneous through the whole cross-section of the sample with the critical current density of $J_c = 200$ A/cm^2. Since T_{SC} is nearly constant in the whole pressure range of the inhomogeneous region, so should be the critical current density.

In the inhomogeneous region, we can model the sample as alternating SDW channels and superconducting channels. For simplification purposses only, the channels are assumed to extend longitudinally from one end of the sample to the other. A change of pressure is equivalent to a change of cross-section, c, of the SC channels and of the SDW channels, $1 - c$. We use crude approximation that c is temperature independent. In the inhomogeneous region, in the absence of weak links along the superconducting channels, the

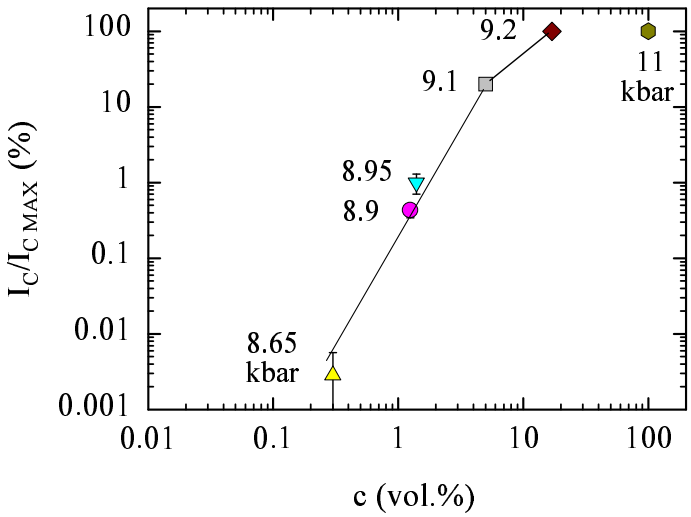

Figure 4.9: Correlation between the critical current I_c at 0.4 K, in SDW/SC region and volume fraction c (vol.%) of metallic phase in the bulk sample, in the range $T_{\rm SC} < T < T_{\rm SDW}$ in the SDW/M region. Values of I_c and c are given in Table 4.1.

SC fraction c of the sample cross-section is given by the respective I_c value divided by $I_{cMAX} = 35$ mA measured at 11 kbar, in the pure SC state. Accordingly, at pressures in the inhomogeneous region, the critical current is lowered, *e.g.* at 9.1 kbar, $I_c = 7$ mA (Fig. 4.7a). The respective values for different pressures are given in the Table 4.1.

The resistance recovered for currents above the critical value at 9.1 kbar is only 12 mΩ, *i.e.* about 8 times smaller than the resistance of sample just above $T_{\rm SC}$ at this same pressure (see Fig. 4.3). As this recovered resistance is still higher than metallic resistance (found at these temperatures and higher pressures) this feature can be ascribed to an electric field overcoming the field required for the depinning of SDW, which coexists with the restored metallic phase. Actually, we calculate the electric field to be of the order of 20 mV/cm at the measuring current of 7 mA (T =1 K) using the data for the 9.1 kbar pressure run. This electric field is about four times the value of the depinning field measured in $(TMTSF)_2PF_6$ [27] or $(TMTSF)_2AsF_6$, [26] at ambient pressure. The conductivity at high currents is therefore the sum of sliding SDW conductivity (which still depends weakly on current) and the conductivity of *decondensated* free electrons in metallic domains.

$T_{SC} < T < T_{SDW}$: Quantification of SDW/M domain fraction

The principle of additive conductivities leads us to another procedure, for quantification of the SDW/M domain fraction. We come back to the resistance curves and extract the metallic fraction, c, and SDW fraction, $1 - c$, from the resistance data in the $T_{SC} < T < T_{SDW}$ temperature range. As for SDW/SC region, we model the sample as alternating insulating (SDW) channels and free electrons channels. The channels are, again, assumed to extend longitudinally from one end of the sample to the other. Thus, the fraction parameter c is related to effective cross-sections. Using this "rigid model", the Arrhenius law conductivity can be corrected as:

$$\sigma(T) = c\sigma_m + (1 - c)\sigma_{SDW} \tag{4.2}$$

In terms of the resistance we get:

$$1/R(T) = c/R_m + (1 - c)/R_{SDW} \tag{4.3}$$

where R_m is the resistance of a 100% metallic sample and $R_{SDW} = R_\infty exp(\Delta_{SDW}/T)$. Fitting the experimental resistance data to Eq. 4.3 gave quite good fits as presented in Fig. 4.3 with the series of dotted lines. The fit parameters c, Δ_{SDW} and R_∞ are given in the Table 4.1. The observed decrease of R_∞ with pressure is a clear demonstration of increase of the metallic fraction of the sample. The observed evolution of Δ_{SDW} with pressure is less clear. In pure SDW region it decreases with pressure, scaled with the transition temperature. Indeed $2\Delta_{SDW} = 2.4T_{SDW}$, although the BCS factor would be 3.52. Further, in the inhomogeneous SDW region, while T_{SDW} falls of, Δ_{SDW} assumes more or less constant value. We attribute such a result to a rather large error in the fitting procedure since available data were from a very narrow temperature range, $T_{SC} < T < T_{SDW}$.

Correlation of two quantification procedures

Our study shows that the coexistence region extends over the 8.65 kbar–9.43 kbar range (Δp = 0.78 kbar). Fig. 4.9 shows the correlation between two independent quantifications of non-SDW fraction c. These were obtained either by critical current measurements at 0.4 K, in SDW/SC region (y-axis, I_{cMAX} =35 mA), or by resistance measurements (x-axis, c from the corrected Arrhenius law) in $T_{SC} < T < T_{SDW}$ range, in SDW/M region. The sample was modelled as alternating SDW channels and M or SC channels extending longitudinally from one end of the sample to the other. If this model was valid, a proportionality between the two independent quantifications of the non-SDW fraction would have been observed in the complete 8.65 kbar–9.43

kbar coexistence range. Since it was not the case, we suggested a plausible existence of two regions. In the higher inhomogeneous region (9.1–9.43 kbar), proportionality between two quantifications occurs. Here indeed, as modelled, SC domains extend from one end of the sample to the other and the critical current is proportional to volume fraction. In the lower inhomogeneous region (8.65–9.1 kbar), the Josephson junctions (or phase slip centers [147]) are present along the conducting channels in SDW/SC region. Therefore, the critical current is lowered disproportionaly to volume fraction of the domains.

4.3 Phase segregation scenario

It is the experimental data which have imposed the search of an approach based on variational theory leading to an inhomogeneous phase with energy lower than that of homogenous states. In the following, we present the model developed by M. Héritier from Laboratoire de Physique des Solides, Orsay, France, [135]. He proposed a discussion of experimental data in the framework of the Fermi liquid picture, which is expected to be valid in this low temperature part of the phase diagram. The relative stabilities of different phases have to be studied: the metal, spin density wave and superconducting phase, but also all the possible regions where coexist either a SDW phase and a metallic phase, or, at lower temperature, a SDW phase and a superconducting one.

Our experimental data reveal (Section 4.1) the coexistence of two different phases, either SDW/Metal or SDW/SC, depending on the temperature. Presumably, this coexistence corresponds to a segregation in direct space and not in the reciprocal space. It is quite plausible that such a segregation is not produced on a microscopic scale ($l \ll \xi$, where ξ is the correlation length) or a mesoscopic scale ($l \sim \xi$), but rather on a macroscopic scale ($l \gg \xi$). The latter is much more favorable regarding the carrier localisation energy necessary to spatially confine the electrons, but also to interface energy necessary to create domain walls between different orders.

M. Héritier gives very simple and general arguments proving that, near enough to the critical line for the formation of an homogeneous SDW phase, a *spatially heterogeneous* phase has a lower free energy than the *homogeneous* SDW phase. The origin of such a phenomenon is due to the following essential physical features :

- The relevant quantity on which depends SDW order stability is $t_b^{'}$. Applying a pressure increases $t_b^{'}$ and, therefore, SDW free energy $F_m\left(t_b^{'}\right)$, up to a critical value $t_b^{'**}$ at which homogeneous SDW phase disappears.

- The SDW stability decreases very strongly near $t_b^{'**}$. The slope of critical line is very large.

- The relevant quantity to stabilize the SDW phase near $t_b^{'*}$ is b, the unit cell parameter along the $y-$direction. Indeed, increasing b strongly decreases $t_b^{'}$, and, therefore, strongly lowers $F_m\left(t_b^{'}\right)$.

- It is always favorable to create a heterogeneous phase : one part, the volume of which is $(1-c)\,\Omega$, has a cell parameter $b+\delta b_1$ and is magnetic, with a lower magnetic free energy because of the higher b parameter ; the other part, the volume of which is $c\Omega$, is metallic and has a cell parameter $b-\delta b_2$, (Ω is the total volume), which imposes $\delta b_2/\delta b_1 = (1-c)/c$. The latter relation implies the constant volume assumption which is considered in the present model. The elastic energy cost for such a deformation is, indeed, proportional to $(\delta b)^2$ and, therefore of second order, while the deformation allows to gain a magnetic free energy proportional to the first order quantity $\left(\frac{\partial F_m}{\partial t_b^{'}}\right)\left(\frac{\partial t_b^{'}}{\partial b}\right)\delta b$. The larger the slope $\left(\frac{\partial F_m}{\partial t_b^{'}}\right)$, the larger is free energy lowering.

The physical picture is as follows: at the homogeneous critical line the metallic and SDW phases are in equilibrium, c=1 − c=1/2, Figs. 4.10, 4.11. For a pressure lower than the critical one, *i.e.* $t_b^{'} < t_b^{'**}$, total free energy is lowered by the formation of macroscopic domains of metallic and of SDW character, respectively. For simplicity these domains are assumed to extend longitudinally from one end of the sample to the other. The metallic ones have a lower b parameter, and the SDW ones have a larger b. Elastic energy cost is

$$\begin{aligned}\Delta E_{elastic} &= (1-c)\,K\,(\delta b_1)^2 + cK\,(\delta b_2)^2 \\ &= \frac{1-c}{c}K\,(\delta b_1)^2 \end{aligned} \tag{4.4}$$

where K is an elastic constant. The magnetic free energy lowering, compared to the homogeneous phase free energy, is given by

$$\Delta F_m = (1-c)\left(\frac{\partial F_m}{\partial t_b^{'}}\right)\left(\frac{\partial t_b^{'}}{\partial b}\right)\delta b_1 - cF_m\left(t_b^{'}\right) \tag{4.5}$$

This linear approximation is quite satisfactory because the derivative is quite large. By minimizing the total free energy $\Delta F_{total} = \Delta E_{elastic} + \Delta F_m$ with respect to δb_1 and c , we find that the stable phase is *heterogeneous*, with a

fraction c of metallic phase forming macroscopic metallic domains parallel to the a-axis:

$$c = \frac{1}{2} - \frac{2K\ sgn\left(t_b^{'} - t_b^{'*}\right)\left|F_m\left(t_b^{'}\right)\right|}{\left(\frac{\partial F_m}{\partial t_b^{'}}\right)^2\left(\frac{\partial t_b^{'}}{\partial b}\right)^2} \tag{4.6}$$

The free energy of the heterogeneous phase is given by

$$\Delta F_{total} = -\frac{1}{4}\frac{\left[\frac{1}{4K}\left(\frac{\partial F_m}{\partial t_b^{'}}\right)^2\left(\frac{\partial t_b^{'}}{\partial b}\right)^2 - F_m\left(t_b^{'}\right)\right]^2}{\frac{1}{4K}\left(\frac{\partial F_m}{\partial t_b^{'}}\right)^2\left(\frac{\partial t_b^{'}}{\partial b}\right)^2} < 0 \tag{4.7}$$

The fraction of metallic phase decreases as $t_b^{'}$, *i.e.* as the applied pressure decreases and vanishes when:

$$\left|F_m\left(t_b^{'} = t_{b1}^{'}\right)\right| = \frac{1}{4K}\left(\frac{\partial F_m}{\partial t_b^{'}}\right)^2\left(\frac{\partial t_b^{'}}{\partial b}\right)^2 \tag{4.8}$$

Here $t_{b1}^{'}$ is defined, Fig. 4.10, *i.e.* as the lower critical pressure for the formation of heterogeneous phase. For $t_b^{'} < t_{b1}^{'}$, the stable phase is a homogeneous SDW phase, Fig. 4.11.

In a symmetrical way, for a pressure higher than the critical pressure, *i.e.* $t_b^{'} > t_b^{'**}$, total free energy is also lowered by the formation of described metallic and SDW domains. An expression quite similar to the case $t_b^{'} < t_b^{'**}$ can be obtained. Again, it is found that $c = 1/2$ on the "homogeneous critical line" and increases with $t_b^{'}$, *i.e.* with the applied pressure and goes to 1 when :

$$F_m\left(t_b^{'} = t_{b2}^{'}\right) = \frac{1}{4K}\left(\frac{\partial F_m}{\partial t_b^{'}}\right)^2\left(\frac{\partial t_b^{'}}{\partial b}\right)^2 \tag{4.9}$$

which defines $t_{b2}^{'}$, the upper critical pressure for the formation of an heterogeneous phase. For $t_b^{'} > t_{b2}^{'}$, the stable phase is an homogeneous metal.

In Fig. 4.10, it is schematically displayed the pressure dependence of magnetic condensation energy and the extent of the stability for the spatially inhomogenous phase. The energy of inhomogenous phase (continuous line) is lower than that of unstable homogenous phase (dashed line).

It should be stressed that the energy necessary to form domain walls between the metallic and magnetic domains was not taken into account. The energy necessary to localize the carriers within a domain was also not taken into account. Since the domains are believed to be macroscopic, the corresponding corrections should be quite small.

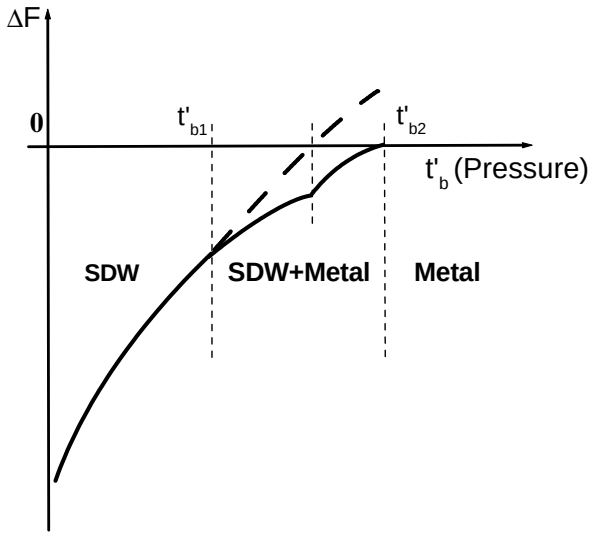

Figure 4.10: Schematic behaviour of the free energy *vs.* nesting deviation parameter $t_b^{'}$ (x-axis). This parameter (being a measure of deviation from ideal nesting) corresponds well to the applied pressure.

Clearly, at lower temperatures, the macroscopic metallic domains should undergo a transition to a superconducting order, since the phase diagram exhibits a competition between magnetic and superconducting orders. Therefore, the formation of heterogeneous phase, with coexisting SDW and superconducting domains has to be investigated. Similar calculations can be done by including the superconducting phase free energy, F_s, assumed to be independent of $t_b^{'}$. Such an approximation is certainly valid in the narrow pressure range considered here. No assumption will be made, neither on the physical mechanism inducing superconductivity, nor on symmetry of order parameter. It shall only be supposed that F_s is given by the usual mean field expression. As above, the total free energy is found to be lowered by the formation of heterogeneous phase, on both sides of the "homogeneous critical line", with a volume c of superconducting domains and a volume $(1-c)$ of SDW domains. c vanishes for $t_b^{'} \leq t_{b3,}^{'}$ where the lower critical value $t_{b3}^{'}$ is given by :

$$-F_m\left(t_{b3}^{'}\right) = \frac{1}{4K}\left(\frac{\partial F_m}{\partial t_b^{'}}\right)^2\left(\frac{\partial t_b^{'}}{\partial b}\right)^2 - F_s \tag{4.10}$$

Since $F_s < 0$, the coexistence region gets broader when the superconducting order grows as $T \to 0$. In the same way, in the superconducting region of the homogeneous phase diagram, the total free energy is lowered by the formation

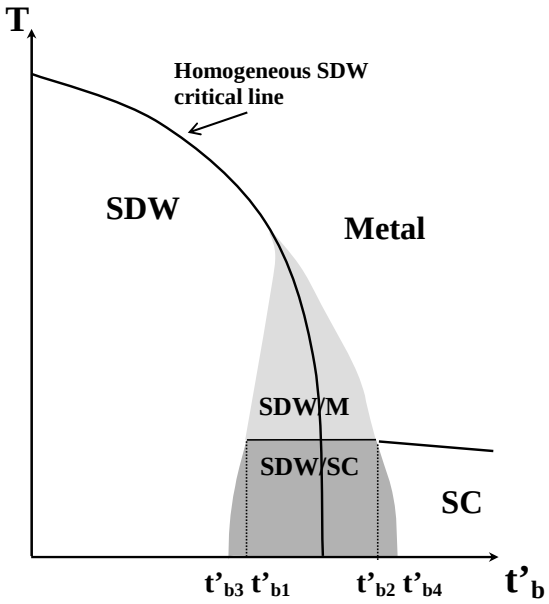

Figure 4.11: Schematic phase diagram showing the inhomogeneous SDW/M and SDW/SC phases in the vicinity of critical border. The nesting deviation parameter $t_b^{'}$ corresponds well to applied pressure (x-axis). T stands for temperature.

of a fraction$(1-c)$ of SDW domains. On the "homogeneous critical line", $c = 1/2$ and increases when $t_b^{'}$ increases, up to an upper critical value $t_{b4}^{'}$, given by ;

$$F_m\left(t_{b4}^{'}\right) = \frac{1}{4K}\left(\frac{\partial F_m}{\partial t_b^{'}}\right)^2\left(\frac{\partial t_b^{'}}{\partial b}\right)^2 + F_s \tag{4.11}$$

In order to explicitly calculate the critical lines, it is necessary to evaluate magnetic free energy $F_m\left(t_b^{'}\right)$, together with the standard mean field expression for F_s. In principle [148], this allows a complete determination of critical lines $c = 0$ and $c = 1$, which limit the stability of heterogeneous phase in the $(T, t_b^{'})$ plane, or the (T, p) plane, correspondingly. A schematic illustration of the theoretical phase diagram is displayed in Fig. 4.11.

It should be emphasized that, within this model, pressure variation of the superconducting critical temperature T_c in the heterogeneous phase is not expected, exactly as we experimentally observed, Fig. 4.8. Nevertheless, it is expected that superconducting ordering increases the width, $t_{b4}^{'} > t_{b2}^{'}$ and $t_{b3}^{'} < t_{b1}^{'}$, of the pressure range in which the heterogeneous phase is stable, because it lowers the total free energy, Fig. 4.11.

The maximum width of the stability region of heterogeneous phase is

obtained at zero temperature. We consider the following numerical values of the parameters entering the model : $t_b^{'} = 10K$, see Sec. 1.1.4, [149][150]; $\frac{\partial t_b^{'}}{\partial p} =$ 1K/kbar, [22][151], compare with Sec. 3.1; $\frac{1}{b}\frac{\partial b}{\partial p} = 3\ 10^{-3}$ kbar^{-1}[152]. These values can be taken as typical. M. Héritier's model predicts a pressure range of stability of the heterogeneous phase of the order of 1 kbar. The agreement with our experiment (inhomogeneous region width, 0.8 kbar, Sec. 4.1.4) can be regarded as extremely good, if we consider the crudeness of the analysis.

4.4 Discussion: DW and SC coexist in Bechgaard-Fabre salts $(TM)_2X$

This new visit to the p, T phase diagram of $(TMTSF)_2PF_6$ provides a better understanding of the boundary region between SDW and SC ground states. The experimental results suggest that a picture of coexisting SDW and SC macroscopic domains prevails in a narrow pressure domain of ≈ 0.8 kbar below critical pressure marking the establishment of an homogeneous SC ground state. In spite of a volume fraction of a SC phase strongly depressed at decreasing pressure in the coexistence regime we could not detect any significant change in T_{SC}.The early claim for the absence of SDW/SC coexistence in the vicinity of the critical pressure [46] based on the observation of an EPR response typical for the superconducting instability, can now be understood by the impossibility of the EPR technique to observe the very broad signal coming from the SDW domains.

M. Héritier developed a very simple model which, on the basis of quite general arguments, predicts the formation of a heterogeneous phase, in which coexist metallic and magnetic domains and, at lower temperatures, magnetic and superconducting domains. This result provides quite a plausible interpretation of data reported here. Obviously, the same kind of arguments might apply to other competing instabilities. What M. Héritier proposed is a variational theory saying that it is possible to find an inhomogenous phase with free energy lower than the energy of homogenous phases (SDW or metal). As a variational constraint, constant total volume of the sample is taken. However, free energy lowering is not due to constraint. If the constraint is relaxed, the free energy of inhomogenous state could still decrease and become even more stable than that of the homogenous state. However, in such a case, the model should rely very much on the detailed pressure dependence of the SDW condensation energy versus pressure.

It is important to point out that the coexistence region in the vicinity of SDW/SC boundary, reported here, is a feature of the respective region of

the generalized phase diagram of Bechgaard-Fabre salts, TM_2X, and not just a particularity of $(TMTSF)_2PF_6$ material. Recently, this phenomenon has been reported to arise in other members of this materials family. Only the applied pressures were larger, as to position the material in the proper region of generalized phase diagram. In the recently discovered superconductor of the TM_2X family, $(TMTTF)_2PF_6$, the reentrance to SC was observed, under very high pressures 4.73 -5.26 GPa, below a metal-to-SDW transition, [7]. However, the extreme pressure conditions made a detailed study impossible. When a compound, $(TMTTF)_2BF_4$, with a smaller anion was chosen, the SDW-SC phase segregation was observed in the pressure range 33.5-37.5 kbar, Fig. 4.12, [153]. As in our study, the inhomogeneous coexistence has been established from critical current measurements. $(TMTTF)_2BF_4$ results are in perfect correspondence with ours on $(TMTSF)_2PF_6$ (see Fig. 4.3). Additionaly , in the $(TMTTF)_2BF_4$, the upper critical field is shown to be large and pressure independent, $H_{c2} = 2$ T, which certainly indicates the penetration of the field in the insulating regions in a similar way to Josephson vortices in layered superconductors. The observation of a large increase of the upper critical field H_{c2} is an immediate consequence of the existence of magnetic macroscopic domains in the superconducting phase. This had been reported long time ago by Greene and Engler for $(TMTSF)_2PF_6$[61] and Brusetti *et al.* for $(TMTSF)_2AsF_6$[47].

A similar situation may be encountered with the coexistence of two possible anion orderings, namely (1/2,1/2,1/2) and (0,1/2,1/2), in $(TMTSF)_2ReO_4$ under pressure, detected by x-ray diffuse scattering [154]. We may anticipate that the coexistence domain will also be characterised by a segregation between metallic regions (associated to the (0,1/2,1/2) order) and (1/2,1/2,1/2) anion-ordered insulating regions [155]. A coexistence between SDW and SC orders has also been mentioned in this latter compound in the narrow pressure domain 8 ± 0.25 kbar [155].

Finally, Duprat and Bourbonnais [157] have recently performed a calculation of the interference between SDW and SC channels using the formalism of renormalisation group at temperatures below the 1D-to-3D cross-over [158], in the presence of strong deviations to the perfect nesting. This calculation shows the possibility of reentrant superconductivity in the neighbourhood of the critical pressure and can explain the deviations of the Δ/T_{SDW} ratio from the BCS ratio in the vicinity of critical pressure due to the non-uniform character of the SDW gap over the Fermi surface. Similar deviations are also obtained, for the same physical reason, in a simple mean field treatment by Gorkov, [156]. It is likely that merging the results of reference, [157] with the present coexistence model could improve the overall theoretical description.

As this Thesis was being completed, a study directly motivated by our

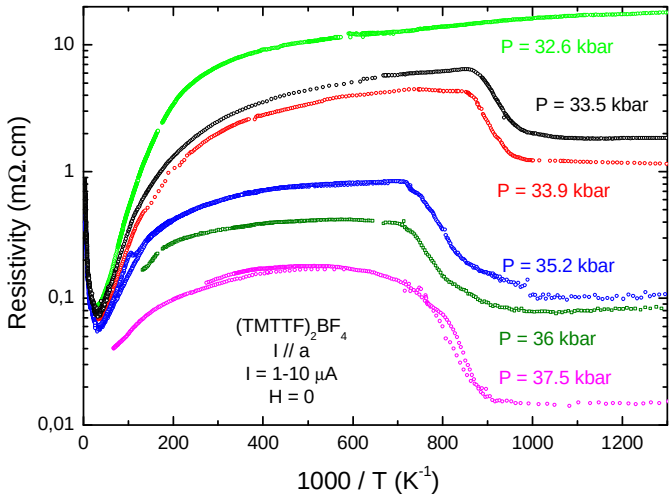

Figure 4.12: Logarithm of the resistance *vs.* inverse temperature for $(TMTTF)_2BF_4$ is shown, for the given range of pressures inside coexistence region. The metal-to-SDW transition, behavior to the corrected Arrhenius law inside the SDW/metal region and a transition to the SC state are depicted. In SC state, zero resistivity is obtained only for the highest pressures, indicating also SDW/SC coexistence. From Ref. [153].

experimental results was published by Podolsky *et al.* , [159]. The authors investigated competition between antiferromagnetism (SDW) and triplet superconductivity in q1D electron systems. They unified the two orders in an SO(4) symmetric framework and demonstrated the existence of such symmetry in one dimensional Luttinger liquids. SO(4) symmetry requires a first order transition between antiferromagnetic and unitary triplet superconducting phases, and a weakly first order transition between antiferromagnetic and normal (metallic) phases near the SO(4) symmetric point. The authors claim that this explains coexistence regions between superconducting and SDW phases, and between SDW and metallic phases, which were observed for $(TMTSF)_2PF_6$ and other TM_2X materials.

5 Investigation of phase diagram of $(La, Sr, Ca)_{14}Cu_{24}O_{41}$

5.1 Evidence for CDW along legs of ladders in $Sr_{14}Cu_{24}O_{41}$

For $Sr_{14-x}Ca_xCu_{24}O_{41}$ materials the total hole count is $\delta_h = 6$. Approximately five of these holes are found in the chains subsystem, while approximately one is found to be transferred to the ladders subsystem, at least at higher temperatures. The holes in the ladders appears to be mobile and responsible for the electrical transport in $Sr_{14-x}Ca_xCu_{24}O_{41}$ materials. This initial presentation will address the parent compound of the $Sr_{14-x}Ca_x$-$Cu_{24}O_{41}$ family of materials - $Sr_{14}Cu_{24}O_{41}$. This is the only material in which there are no Sr/Ca substitutions, so the related disorder is minimal.

5.1.1 Correspondence of dc transport and LFDS

In Fig. 5.1 (bottom panel) we present the results of dc resistivity ρ_{dc} *vs.* inverse temperature, $1/T$, for $Sr_{14}Cu_{24}O_{41}$. The measurements were performed along the c-axis, that is, along the legs of ladders. The temperature range of measurement was from 750 K down to 50 K. We observed single particle electrical transport characterized by quite high RT conductivity of 500 $\Omega^{-1}cm^{-1}$, confirming the existence of mobile holes transferred in the ladders. Also, we observed insulator-to-insulator phase transition, determined from a peak in the logarithmic derivative of resistivity. The peak in the derivative is centered at 210 K, characterized by full width at half maximum (FWHM) of 40 K. So, the insulator-to-insulator transition critical temperature is taken to be $T_c = 210 \pm 20$ K. This transition is quite broad, FWHM/$T_c = 20\%$. It may be compared with $(TMTSF)_2PF_6$, where $T_{SDW} = 12 \pm 0.1$ K, and

FWHM/T_c = 2%, see Chapter 4 or Ref. [27]. The width of the transition that we observed in $Sr_{14}Cu_{24}O_{41}$ indicates a certain level of intrinsical disorder in the nominally pure single crystal samples studied here. Both insulator phases, above and below the phase transition, are primarily characterized by well defined, but different, activation energies ($\rho_{dc} \propto e^{\Delta/k_BT}$). In the high temperature (H.T.) phase activation energy $\Delta_{\mathrm{H.T.}}$ = 900 K is lower than $\Delta_{\mathrm{L.T.}}$ = 1300 K in the low temperature (L.T.) phase.

The frequency dependence of conductivity, σ'(ω), and the real, ε'(ω), and imaginary parts, ε"(ω), of the dielectric function, for a few selected temperatures, are displayed in Fig. 5.2. The radio-frequency relaxation is clearly observed as a peak in the ε" spectrum accompanied by a step-like decrease of ε'. These spectra can be described in terms of a generalized Debye expression (Sec. 3.2.3). Solid lines in Fig. 5.2 are fits to this formula:

$$\varepsilon'(\omega) + i\varepsilon''(\omega) = \Delta\varepsilon/[1 + (i\omega\tau_0)^{1-\alpha}]. \tag{5.1}$$

As already presented in more detail in Sec. 3.2.3, $\Delta\varepsilon$ is the strength of the relaxation, τ_0 is a central relaxation time and $1-\alpha$ describes the symmetrical broadening of the relaxation times distribution. Temperature dependences of the relaxation parameters, for $Sr_{14}Cu_{24}O_{41}$, obtained from the fits are shown in Fig. 5.1.

As can be seen from Fig. 5.1, a dielectric mode of order of $\Delta\varepsilon = 10^4$-10^5 appears in the L.T. phase, below 110 K. It was not possible to use complex conductivity technique above 110 K for $Sr_{14-x}Ca_xCu_{24}O_{41}$, x=0, since the dielectric mode left the upper boundary of our experimental frequency window, see Section 3.2.3. An assumed behavior of $\Delta\varepsilon$ for x=0 is represented by a dashed line, based on that observed for x=3 and 9, see Sec.5.3 and Refs. [160, 161]. That is, on decreasing temperature, a sharp growth of $\Delta\varepsilon$ starts in the close vicinity of T_c and reaches the huge value of the order of $10^4 - 10^5$ at T_c = 140 K and T_c = 10 K for x = 3 and 9, respectively. These T_c values correspond perfectly to the temperature of the phase transition as determined in the dc resistivity measurements. Therefore, we can conclude that this perfect correspondence, between ac and dc results, is valid for x=0 also, with T_c = 210 K.

The dielectric mode is further characterized by $1 - \alpha = 0.8$ parameter. That is, the distribution of the relaxation times is broader than Debye (Debye $1 - \alpha = 1$). This distribution narrows towards a Debye one along with the decrease in the mode strength in the temperature range below 70 K. In the bottom panel of Fig. 5.1 both the central relaxation time τ_0 and the dc resistivity are shown. Again, a strong correspondence between dc and ac results has to be noted in that $\rho_{dc} \propto \tau_0 \propto e^{\Delta_{\mathrm{L.T.}}/k_BT}$ below T_c. The energy

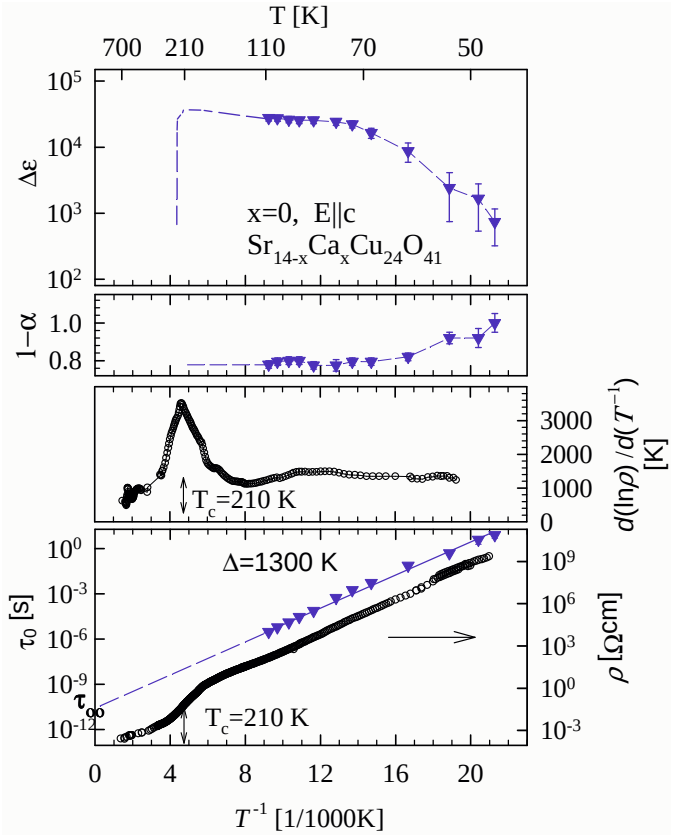

Figure 5.1: dc and LFDS measurements for $Sr_{14}Cu_{24}O_{41}$ are performed along the c axis. Inverse temperature $1/T$ dependences of the dc resistivity and of the low-frequency dielectric relaxation parameters are shown, Eq. 5.1. Top panel: the strength $\Delta\varepsilon$ of the dielectric relaxation. Assumed behavior of $\Delta\varepsilon$ is represented by a dashed line. Second panel from the top: the parameter 1-α which describes the symmetrical broadening of the relaxation times distribution. At temperatures below 70 K, simultaneously with a decrease in $\Delta\varepsilon$, 1-α increases towards 1 – the distribution becomes more Debye-like. Bottom panel: Both the central relaxation time τ_0 and the dc resistivity are thermally activated $\rho_{dc} \propto \tau_0 \propto e^{\Delta_{\mathrm{L.T.}}/k_B T}$ below T_c with an activation energy $\Delta_{\mathrm{L.T.}} \approx 1300$ K. $T_c = 210 \pm 20$ K is determined from a peak in the logarithmic derivative of the resistivity, as presented in the second panel from the bottom. The dashed line in the bottom panel denotes the extrapolation of τ_0 to a high temperature value, the attempt time, τ_∞.

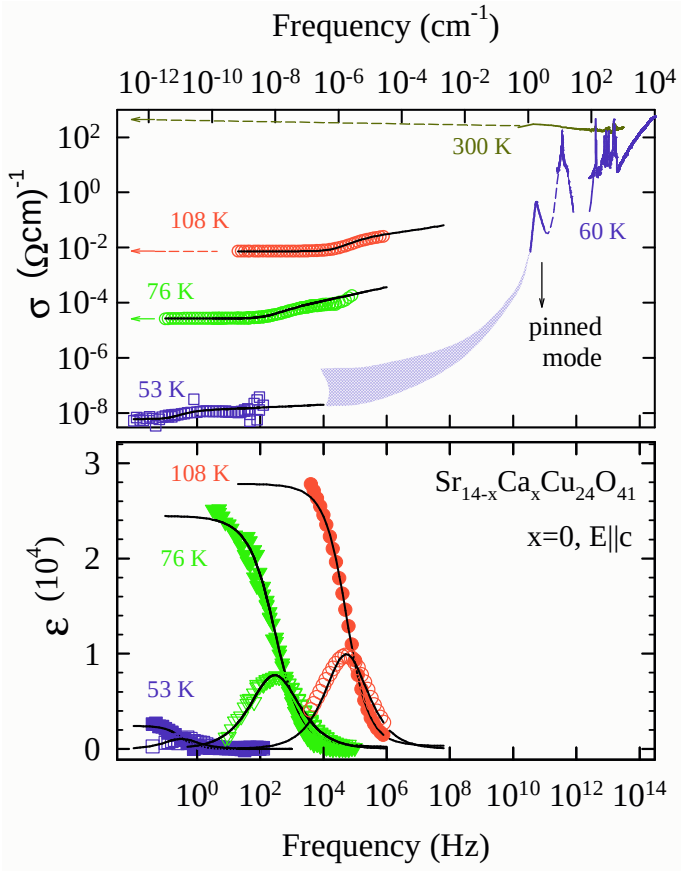

Figure 5.2: Broad-band spectra for $Sr_{14}Cu_{24}O_{41}$, measured along the legs of ladders, *i.e.* c axis, at a few selected temperatures are shown. Conductivity, the real part - σ', is shown in the upper panel and complex dielectric function is shown in the lower panel (imaginary ε" and real ε' parts, open and closed symbols, respectively). The full lines are from fits to the generalized Debye expression, Eq. 5.1. A mode in microwave range at 1.8 cm^{-1}, is detected by Kitano *et al.* [162]. The horizontal arrows on the left denote the dc conductivity. Decrease of the infrared conductivity (data by the Stuttgart group, [78]) at low temperatures corresponds to the opening of energy gap. Some phonon features become visible at the lowest temperatures. Shaded area, as a guide for the eye, connects the two frequency ranges.

gap $\Delta_{\mathrm{L}.T.} \approx 1300$ K has already been stated above. The dashed line in the bottom panel of Fig. 5.1 denotes the extrapolation of τ_0 to a high temperature value, the attempt time, τ_∞. The attempt time is of the order 10^{-10}-10^{-11} s, much larger than usual quasi-particle relaxation times of 10^{-15} s.

Very large attempt time, along with the enormous strength of the dielectric mode (enormous dielectric constant) corresponds to a collective relaxation mechanism – the charge density wave (CDW) phason response to ac electric fields. The broad mode ($1 - \alpha = 0.8$) indicates that the CDW is pinned in the random background potential. Standard feature of the CDW phason response is also the correspondence of the activation energy for the central relaxation time τ_0 with the dc resistivity one. Therefore, the low temperature energy gap $\Delta_{\mathrm{L}.T.} \approx 1300$ K is identified as the CDW gap, Δ_{CDW} and the transition temperature $T_c = 210 \pm 20$ K is identified as insulator-to-CDW phase transition temperature T_{CDW}.

An other feature of the CDW phason response to ac electric fields is the *pinned* mode, see Sec. 2.4. This mode is, in general, expected to appear in microwave/far-infrared range, [126]. We follow the assignment of the conductivity peak observed in the microwave range, at 1.8 cm^{-1} (see Fig. 5.2) to the CDW *pinned* mode, proposed by Kitano *et al.* [162, 163]. Also shown in Fig. 5.2 are quasi-optical microwave/FIR range (5-10000 cm^{-1}) conductivity data for x=0 material, taken from Ref. [78]. FIR range conductivity starts to decrease at temperatures lower than 240 K. This temperature agrees nicely with the CDW phase transition temperature $T_{\mathrm{CDW}} = 210$ K as determined from dc/LFDS. The FIR conductivity starts to decrease, below approximately 2500 cm^{-1}. The CDW gap value extracted from dc/LFDS measurements, corresponds well to the edge seen in the FIR conductivity spectra, ≈ 900 cm^{-1}.

While the above confirms standard CDW phason response is observed, the decrease in the dielectric mode strength below 70 K, deserves further elaboration. We suggest that this observation indicates a decrease in the effective number of holes condensing in the CDW in the ladders. Presumably, the holes from ladders back-transfer to the chains. This process was already proposed in Sec. 1.2.5, based on the inelastic neutron scattering and X-ray diffraction results for chains. In this manner, a contradiction is removed with the standard CDW phason model where temperature independent dielectric strength is expected.

5.1.2 Nonlinear conductivity

CDW sliding conductivity

A standard feature of the CDW response to dc electric fields is the nonlinear, sliding conductivity, [126]. A very simple, "classical-particle" model, [164], accounts for a variety of experimental findings in standard CDW response both to dc and ac fields. This model assumes that the dynamics of the phase of the order parameter is important. The phase is regarded as a classical variable, and it is regarded to be uniform throughout the system. The phase couples directly to the pinning potential provided by inhomogeneities in the system. The electric-field-dependent conduction is a direct consequence of the depinning and consequential translational motion of the CDW condensate. Within the above classical-particle model, sliding CDW conductivity can not exceed the conductivity of an uncondensed system with an equal number of carriers. Here we note that, in 1954., in his model for superconductivity, Fröhlich envisioned that a condensate, being incommensurate to the lattice should be able to conduct freely if dc electric field is applied.

In a realistic system, the phase of the condensate is not uniform. Pinning potential may be due to commensurability between the CDW modulation and the lattice. Pinning may also be due to randomly distributed impurities or lattice defects. Here we distinguish two cases, weak and strong pinning. In the case of weak pinning, the density wave phase adjusts to impurity fluctuations, but is a constant over the length of Lee-Rice domains, [128] which contain many impurity sites. In the case of strong pinning, local distortions of the condensate are favored, where the phase is fully adjusted to obtain a maximum energy gain. Depinned CDW condensate motion is damped due to the back-flow of the free carriers, see Sec. 2.4. Thus, contribution of condensate sliding to conductivity is limited and related to the applied dc electric field. In the commensurate case, it appears that only $N = 3$ commensurability is expected to be detected experimentally. For $N = 2$, the CDW order parameter becomes real, *i.e.* it has only amplitude, but no phase. Phason response is thus not expected. For $N \geq 4$, commensurability pinning is considered to be weaker than the impurity pinning.

dc electric field sufficient for depinning of the CDW is denoted *threshold field*, E_T. E_T is related to the energy barrier which has to be overcome for depinning of the condensate $\mathbb{E}_{barrier} = \mathrm{e}\rho_0(2\pi/\mathbf{Q})E_T$, where ρ_0 is carrier concentration and $\mathbf{Q}$ is the CDW wave vector. $\mathbb{E}_{barrier}$ is associated with the pinning potential V_0.

The threshold field for standard DW materials was observed to decrease with temperature decreasing away from the DW transition, [126]. This tem-

perature dependence for the case of impurity pinning was calculated by Maki, although for SDW, [27], but the arguments are general enough to be valid for CDW also. It was successfully applied to different samples of $(TMTSF)_2PF_6$ material, where SDW is observed. At lower temperatures the threshold field assumes constant values for SDW materials, while for CDW it attains a minimum and starts to strongly increase with further decrease in temperature.

In general, for density waves, the experimentally observed thresholds correlate with the temperature scale. Therefore in $(TMTSF)_2PF_6$, mV/cm thresholds are observed at temperatures of the order of 1-10 K. As standard CDW transition temperatures are an order of magnitude higher, the thresholds observed in standard CDW materials ($NbSe_3$, *o*-TaS_3, $K_{0.3}MoO3$) are of the order of 0.1-1 V/cm when measured at temperatures around 100 K. Depending on the $(TMTSF)_2PF_6$ sample impurity contents, thresholds of the order of 5-30 mV/cm for weak and strong pinning, respectively, were found [27]. For a standard CDW material *o*-TaS_3 also, higher impurity content leads to the increase of threshold, up to 30 V/cm (see Fig. 5.5). In some cases, very high threshold fields may be related to commensurability pinning $N = 3$. As an example, we mention q1D organic material $Cu(DMe\text{-}DCNQI)_2$, [165, 143] where commensurate CDW $N = 3$ is established below ~ 50 K. An important increase of the threshold field value, up to 130 V/cm was observed at 34 K. There, the CDW LRO is achieved in the whole bulk of the sample. A similar effect was observed in q1D organic material TTF-TCNQ when $N = 3$ CDW is induced under pressure, [166].

Contact quality influence on nonlinear conductivity in $Sr_{14}Cu_{24}O_{41}$

In order to check for the sliding conductivity in $Sr_{14}Cu_{24}O_{41}$, dc resistance, R, dependence on the applied electric field E was measured along the *c*-axis, $E||c$. As shown in Fig. 5.3, in the first and second stack of panels, we found that R does not deviate more than 2%, at the highest fields applied, 10 V/cm, from the low field value, (upper panel). A characteristic threshold electric field, above which the sliding conductivity starts, is not observed, as shown in the panels on the left, where R is shown *vs.* E on linear scale. The dashed boxes within the panels of Fig. 5.3 are blown-up and presented as the next lower panel. In this manner, we may follow R *vs.* E down to the smallest electric fields. Indeed, the negligibly small nonlinearity emerges from the noise background. In the panels on the right the resistance is shown *vs.* logarithm of the electric field. Presenting data in this manner illustrates how an apparent threshold field may be derived. In conclusion, no signs of the sliding mechanism were found.

In Fig. 5.3, in the third and fourth stack of panels, it is shown that a large nonlinearity occured for the high quality sample where we used improper contact preparation method. However, the threshold was not observed, *i.e.* nonlinearity emerged immediately from the noise background. Since this is the four probe measurement, the observed nonlinearity is not due to the contacts *per se*. That is, contact nonlinearity does not enter the result. Still, since the contact resistances were at least order of magnitude higher than the sample bulk resistance, the improper current injection occured, and also large unnested voltages were measured. This scenario was confirmed, when the proper contact application was performed and nonlinearity dissappeared for this sample. As already explained above, in the panels on the right the resistance is shown *vs.* logarithm of the electric field.

Our results are apparently contradictory to those of Maeda *et al.* [168]. They claimed that sliding conduction by the q1D charge-ordered state ($4k_F$ CDW) along the legs of ladders occurs in $Sr_{14}Cu_{24}O_{41}$. They derived threshold fields of the order of 0.5 V/cm in the temperature range 100 – 160 K, Fig. 5.4, left panel. Our inspection of the data presented by these authors indicated the following. If their data are presented *vs.* electric field shown on the linear, instead on the logarithmic scale, the behavior as we observed for a good contacts case (Fig. 5.3) is recovered. No threshold field may be derived. The nonlinearity emerges from the noise background. Conductivity deviates not more than 3-4%, at the highest fields applied, 4-5 V/cm, from the low field value. In our opinion this removes the contradiction. We regard that their data are consistent with ours.

Further, Blumberg *et al.* ,[167] reported also a sliding non-linear conductivity. That is, they claimed to observe a strong non-linear effect and to be able to derive a threshold field $E_T = 0.2$ V/cm. By inspection of their data, shown in Fig. 5.4, right panel, we estimate that the nonlinear effect at twice the threshold field is of the order of 50%. For comparison we also note in their data that, already at 1 V/cm, conductivity increases for 100%, above the low field value. The nonlinearity of exactly this magnitude we obtained only for the sample where improper contact preparation method was applied. The resistance data of Blumberg *et al.* are also presented *vs.* electric field shown on the logarithmic scale. Here, we were not able to transform to the linear scale, and no precise comparison with our data was possible.

Fröhlich conductivity and screening by free carriers

As shown in Fig. 5.4, right panel, Blumberg *et al.* also derived a second threshold, $E_T^{(2)}$. They relate this threshold to the crossover to a regime of free sliding, rigid condensate as envisioned by Fröhlich in 1954. in his model

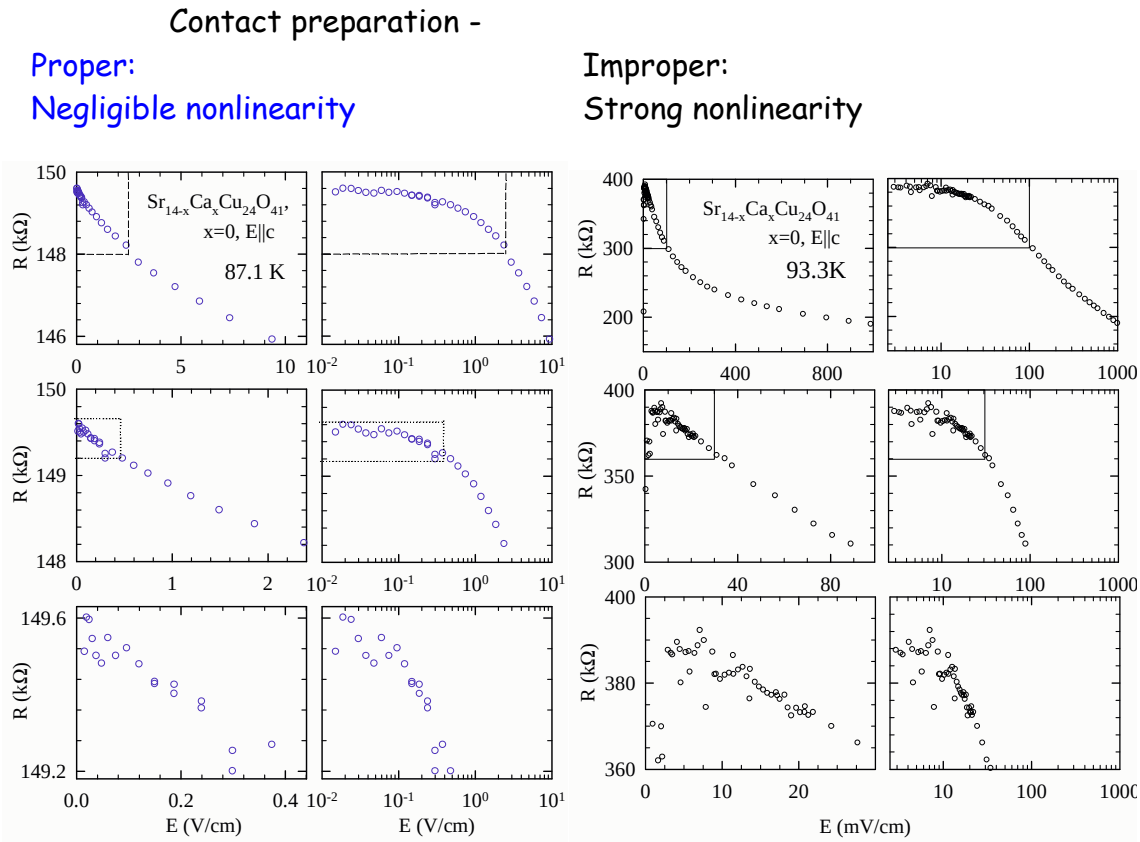

Figure 5.3: Resistance *vs.* electric field applied along the *c*-axis, for Sr_{14}-$Cu_{24}O_{41}$. The results for different contact preparation cases (see Sec. 3.2) are shown either in the first and second stack or in the third and fourth stack of panels. In the first (third) stack, the electric field is shown on linear, and in the second (fourth) stack on logarithmic scale. From top to bottom the dataset is the same, for the respective cases, but the scale is being enlarged. This is denoted by the dashed boxes. For properly prepared contacts, a negligible nonlinearity, 2% at the maximum field of 10 V/cm, is observed. On the contrary, for improperly prepared contacts, a strong nonlinearity is observed - the conductivity doubled at the highest fields applied. Different apparent thresholds, depending on the scale, are derived in the second (fourth) stack of panels. In the first (third) stack of panels thresholds can not be derived. The apparent nonlinearity starts from the lowest fields - emerging from the noise background (bottom panel).

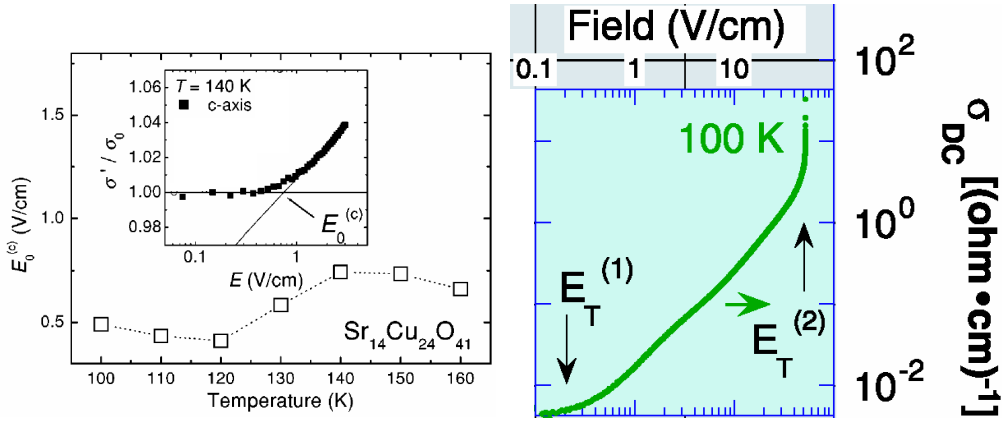

Figure 5.4: Left panel: The threshold field E_0 as a function of temperature. The authors, Maeda *et al.* [168], identified E_0 as the onset of sliding conduction. The inset shows how E_0 was derived from the nonlinear conductivity σ' normalized to low field conductivity value σ. Right panel: The strong nonlinear conductivity observed by Blumberg *et al.* ,[167] at 100 K. The authors identified thresholds $E_T^{(1)}$ and $E_T^{(2)}$ as the onset of sliding and Fröhlich conductivity, respectively.

of superconductivity. In Fröhlich model the screening effects of the free carriers are not taken into account. Therefore, in order to observe Fröhlich conductivity in a given material the screening has to be ineffective, [169]. Contrary to this, we observe that the screening is still well effective in $Sr_{14}Cu_{24}O_{41}$ at 100 K. We infer this from the fact that both the central relaxation time, τ_0, and dc resistivity, ρ_{dc}, show the same activated behavior from T_{CDW} down to the lowest temperatures, 45-50 K. In Littlewood's model (Sec. 2.4) it was shown that this $\tau_0 \propto \rho_{dc}$ behavior is due to the CDW relaxation damped by the free-carriers, which flow around the pinned CDW and produce screening currents. Therefore we conclude that for $Sr_{14}Cu_{24}O_{41}$ the screening is still effective at 100 K and thus no Fröhlich conduction may be observed.

Relation of $\Delta\varepsilon$ and E_T

In the classical particle model for CDW, the dielectric strength $\Delta\varepsilon$ is related to the threshold electric field E_T for the nonlinear conduction.

$$\varepsilon_0 \Delta\varepsilon E_T = \frac{Me}{\pi ab} \tag{5.2}$$

The term on the right side represents the number of chains (or other 1D structures, ladders or stacks) per cross-section area. a and b are the lattice

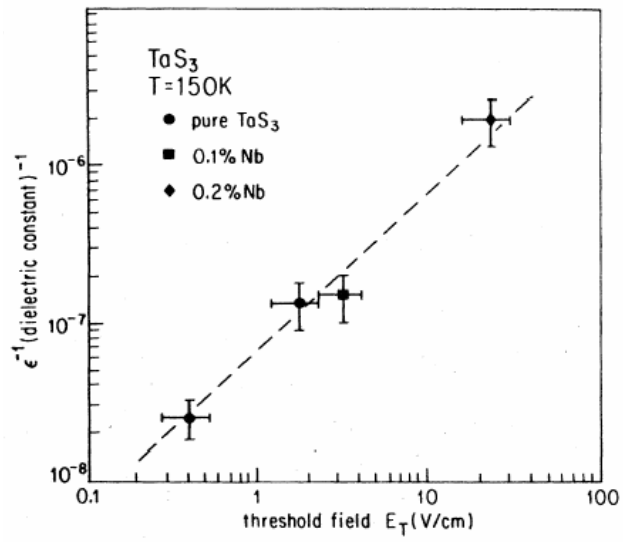

Figure 5.5: Inverse low-frequency dielectric constant ε' (4 MHz) *vs.* threshold field E_T in *o*-TaS_3 alloys at 150 K. From Ref. [170]

parameters, and M is the number of carriers per unit cell. e is the electron charge of 1.6×10^{-19} C.

The relation given by Eq. 5.2 was experimentally confirmed to be valid for a standard CDW material, *o*-TaS_3, Wu *et al.* , [170]. For *o*-TaS_3 samples, disordered due to alloying with NbS_3, Wu *et al.* observed a much smaller $\Delta\varepsilon \approx 10^5$ than in the pure material and correspondingly enhanced sliding threshold of 30 V/cm, Fig. 5.5. This material presents a CDW transition at about 200 K and the studies of nonlinearity were done at 150 K. Therefore, it is well suited for comparison with CDW in $Sr_{14}Cu_{24}O_{41}$. For $Sr_{14}Cu_{24}O_{41}$, an intrinsically disordered material, characterized by even lower $\Delta\varepsilon \approx 3 \times 10^4$, an even higher threshold might be extrapolated, at least 100 V/cm.

An estimate for E_T in $Sr_{14}Cu_{24}O_{41}$ based on the observed dielectric strength $\Delta\varepsilon$, may also be given directly, using Eq. 5.2. Here it is necessary to remind that only holes transferred into ladders are mobile, condense into CDW and enter this calculation, see Sec. 1.2.6. One hole transferred per ladder equals 4 mobile holes per one approximate superstructure cell, since this cell contains 4 formula units, Fig. 1.12 and 1.13. Therefore, we set M= 4. The cross-section of the superstructure cell, perpendicular to ladders is $a \cdot b \approx 150\mathring{A}^2$. This direct calculation leads to an even higher estimate for E_T of the order 10^3 V/cm, obviously much above the maximum applied field of 10 V/cm. For *o*-TaS_3, this direct calculation also gave an order of magnitude higher estimates compared to the values obtained in the experiment,

[126]. A good quantitative agreement was obtained for the SDW material $(TMTSF)_2PF_6$ at 2–3 K, with $M = 1/2$, $a \cdot b \approx 100\mathring{A}^2$, $\Delta\varepsilon \approx 3 \times 10^9$ and $E_T \approx 5 - 10$ mV/cm, [27, 44].

We also refer here to the threshold field $E_T = 0.2$ V/cm derived by Blumberg *et al.* for $Sr_{14}Cu_{24}O_{41}$. They also observed radio-frequency dielectric mode of dielectric strength $\Delta\varepsilon \approx 4 \times 10^6$. That is, two orders of magnitude stronger than the mode we observed. Using this comparison and relying on Eq. 5.2, *i.e.* on the proportionality $E_T \propto \Delta\varepsilon^{-1}$ we estimate that in our case the threshold field should be two orders of magnitude higher, around 20 V/cm. This value is two times above our experimental limit. In this manner we may conclude that an apparent contradiction between Blumberg *et al.* and ours data, is removed. We also note that the τ_0 they observed were for a magnitude larger, as expected for higher quality samples. Here, we might conclude that the samples studied by Blumberg *et al.* were of significantly higher quality. However, the response they observed is much broader $(1 - \alpha = 0.6)$, which indicates a higher level of randomness in the impurity distribution.

5.1.3 Standard features of CDW ground state in $Sr_{14}Cu_{24}O_{41}$

Response to dc fields

A standard feature of the CDW phason response to dc fields is sliding conductivity. However, we have not observed sliding conductivity and the related threshold electric field. We suggest that sliding conductivity is not observed due to the too small electric fields (up to 10 V/cm) applied in this study. Presumably due to the sample quality dependence, the threshold field was above the experimental limit in our study. We can anticipate two possible origins for a very large E_T. Either, it is due to the strong pinning to randomly distributed centers resulting from intrinsically disordered structure of $Sr_{14}Cu_{24}O_{41}$. Or, it is possible that CDW in $Sr_{14}Cu_{24}O_{41}$ is commensurate with $N = 3$ and thus strongly pinned to the ladders lattice background.

Such, presumably very large, threshold field also correlates with relatively small observed dielectric strength of the radio-frequency dielectric mode, see Fig. 5.5. The relation between E_T and $\Delta\varepsilon$, Eq. 5.2, is modelled within a simple clasical particle model of CDW, [126].

Response to ac fields - m^* calculation

The two signatures of the CDW phason response to ac fields are observed in $Sr_{14}Cu_{24}O_{41}$. The radio-frequency mode is activated down to the lowest temperatures measured, 45-50 K. The *pinned* mode was identified at 1.8 cm^{-1} by Kitano *et al.* [162, 163]. The ac response that is observed in $Sr_{14}Cu_{24}O_{41}$ is extremely reminiscent, phenomenollogicaly, of the CDW phason response in most well-known 1D compounds like $K_{0.3}MoO_3$, $NbSe_3$, TaS_3, and $(TaSe_4)_2I$ [126].

As we discuss next, this holds qualitatively as well as quantitatively. We will describe the dynamical response of $Sr_{14}Cu_{24}O_{41}$ utilizing a standard theory for CDW systems as presented in Sec. 2.4. The pinning frequency Ω_0 is related to the radio-frequency mode central relaxation time τ_0 and to dc conductivity σ_z measured along the c-axis. This relationship, as shown below, allows us to estimate the effective mass m^*:

$$m^* = \frac{e^2 \rho_0}{\sigma_z \tau_0 m_0 \Omega_0^2} \tag{5.3}$$

Below we describe the variables used in this calculation.

$\Omega_0 = 0.34 \times 10^{12}$ [rad/s] (1.8 cm^{-1}) - CDW pinning frequency, [162].

σ_z [$\Omega^{-1}m^{-1}$] - conductivity along the c-axis at selected temperatures, taken from our experiment, Fig. 5.2. Longitudinal conductivity was calculated by multiplying the inverse of the resistance $1/R_4[\Omega^{-1}]$ with the sample aspect ratio, $\frac{l}{S} = 3000 m^{-1}$.

τ_0 [s] - central relaxation time, at selected temperatures, taken from our experiment, Fig. 5.1.

$\rho_0 = 1 \times 10^{27}$ [m^{-3}] - carrier concentration, inferred from crystal and electronic structure of $Sr_{14-x}Ca_xCu_{24}O_{41}$. In this calculation we assumed one hole per ladder. That is, 4 mobile holes reside in the ladders per approximative superstructure unit cell, Sec. 1.2.6).

m^* - the effective mass m^* is just the multiplication factor which multiplies electron mass $m_0 = 9.1 \times 10^{-31}$[kg].

The calculated effective mass values, for a few selected temperatures, are shown in the Table 5.1. The pinning frequency and carrier concentration are temperature independent. Only the product $\sigma_z \tau_0$ introduces temperature variation in the calculated values of m^*. We take m^* $\approx$100 value as a temperature average, since effective mass is considered to be temperature

x=0

T	$\sigma_z\tau_0$	m^*
108 K	12.5×10^{-7}	80
68 K	10×10^{-7}	100
53 K	5×10^{-7}	200

Table 5.1: T is temperature in Kelvin. The selected temperatures cover the range where the dielectric response measurements were done. $\sigma_z\tau_0[\Omega^{-1}\mathrm{m}^{-1}\mathrm{s}]$ is a product of dc conductivity σ_z and τ_0 central relaxation time, resulting from measurements along the c-axis. The values of these parameters may also be read from Figs. 5.1 and 5.2.

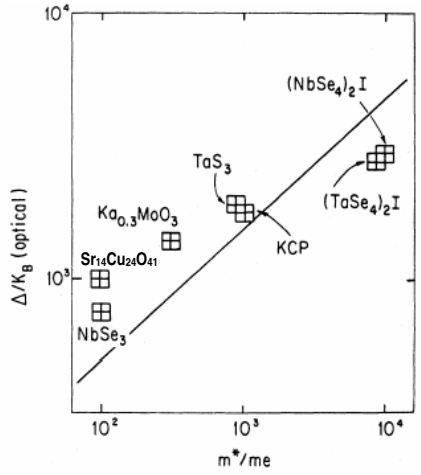

Figure 5.6: Effective mass m^* *vs.* the activation energies and Δ_{CDW} for various standard CDW compounds. Our result for $Sr_{14}Cu_{24}O_{41}$ is also shown. The solid line represents the relation $m^* \propto \Delta^2_{\mathrm{CDW}}$. From Ref. [126]

independent [126]. The value for the effective mass for $Sr_{14}Cu_{24}O_{41}$ material calculated here should be compared to the standard $m^* = 1$ for SDW [37] or to the standard $m^* = 10^2 - 10^4$ for CDW [126]. As can be found from Fig. 5.6 the range of the CDW effective mass values is related to the values of the CDW energy gap. Values of $m^* \approx$100 and $\Delta_{\mathrm{CDW}} = 1300$ K situate Sr_{14}-$Cu_{24}O_{41}$ material close to the standard CDW materials presented in Fig. 5.6. Any discrepancies are easily attributed to the fact that relation $m^* \propto \Delta^2_{\mathrm{CDW}}$ is controlled by the value of the electron-phonon coupling constant, which is weak, compared to electron-electron interaction, in $Sr_{14}Cu_{24}O_{41}$.

5.1.4 Conclusions

In dc electrical transport we observed a transition to a low-temperature insulating state below $T_c = 210\ K$ characterized by the activation energy $\Delta = 1300$ K. We presented evidence that this transition corresponds to a charge-density wave formation along the ladders, the subsystem responsible for charge transport, in q1D cuprate $Sr_{14}Cu_{24}O_{41}$. While the *pinned* mode was previously reported in the microwave frequency range, in the radio frequency range we observed thermally activated mode, characterized by similar activation energy as dc transport. Quasi-coherent microwave and FIR measurements also corresponded to these results, [78, 160]. We estimated the effective mass of CDW condensate to be $m^* \approx 100$, within the range of values for standard CDW materials. Although sliding conductivity was not observed in this study, we note independent reports of nonlinear conductivity. The apparent contradiction is presumably due to different quality of samples. This is a known influence in studies of q1D materials. Our results confirm the theoretical prediction, that a competing CDW ground state exists in q1D cuprates in addition to superconductivity.

However, we note that some issues remain: the observed CDW occurs below an insulator-to-insulator transition, indicating strong electron-electron interaction in the ladders subsystem. These strong interactions are probably necessary to render the non-metallic phase at high temperatures. It is interesting to note that below the transition the activation energy increases, from $\Delta_{H.T.} = 900$ K to $\Delta_{CDW} = 1300$ K. This difference may be regarded as being due to the additional, "CDW proper" gap opening. This only remotely reminds of the standard metal-to-insulator transition occuring in the standard CDW materials. We also note that the spin-gap is 2–3 times smaller than the CDW gap. For a standard CDW material this is not observed. Instead, the gaps in spin and charge sector open concomitantly and they are of the same size.

5.2 Localization of holes in chains of $La_ySr_{14-y-x}Ca_xCu_{24}O_{41}$

An understanding is necessary on the nature of the spin/charge state and in particular on the charge dynamics in the chain subsystem of nonisovalently substituted compounds $La_ySr_{14-y-x}Ca_xCu_{24}O_{41}$, which posses a reduced hole count, $\delta_h = 6 - y$. We remind that for $\delta_h \leq 5$ compounds all holes reside in the chains. No ordering of any kind has been reported for these compounds. In order to clarify the mechanism of the charge transport, we have studied $La_3Sr_3Ca_8Cu_{24}O_{41}$ and $La_{5.2}Ca_{8.8}Cu_{24}O_{41}$. These particular compounds are characterized by low hole counts $\delta_h = 6 - 3 = 3$ and $\delta_h = 6 - 5.2 = 0.8$, respectively. Our dc resistivity and low frequency dielectric spectroscopy results cover a broad frequency range from dc to 1 MHz. The compounds have been studied in a wide temperature range from 750 K to 35 K, [171].

5.2.1 dc conductivity indicates hopping charge transport mechanism

In Fig. 5.7 we present for $La_3Sr_3Ca_8Cu_{24}O_{41}$ and $La_{5.2}Ca_{8.8}Cu_{24}O_{41}$ compounds the dc conductivity measured along the c-axis, *i.e.* , along the chains, as a function of temperature. The compounds will also be denoted as La_3 and $La_{5.2}$, respectively.

That is, for $La_{5.2}$ and La_3, above respective $T_c = 330$ K and 300 K, the dc conductivity follows a simple activation behavior $\sigma_{dc}(T) \approx \exp(-2\Delta/T)$. The activation energies $2\Delta = 4200$ K and 3200 K were observed for $La_{5.2}$ and La_3, respectively. The fits to the simple activation behavior are depicted by solid lines in the insets. As directly seen from the $\log \sigma_{dc}(T)$ *vs.* $T^{-1/2}$ plot, presented in the main panels of Fig. 5.7, below T_c down to 50-35 K the conductivity perfectly follows Mott's variable-range hopping (VRH) behavior

$$\sigma_{dc}(T) = \sigma_0 \exp\left[-(T_0/T)^{\frac{1}{1+d}}\right] \tag{5.4}$$

with the dimensionality of the system $d = 1$. That is, the fits to this law appear as straight lines in the main panels, where the horizontal scale is the inverse square-root of temperature. T_c is determined by the crossing of extrapolated fitting curves, with the error bar of ± 15 K.

These results clearly demonstrate the hopping mechanism of charge transport in one dimension; at T_c it crosses over from nearest-neighbor hopping to variable-range hopping. The cross-over temperature T_c is given by $T_c = \Delta/(2\alpha c)$ [172, 173]. Here the energy of sites near the Fermi energy

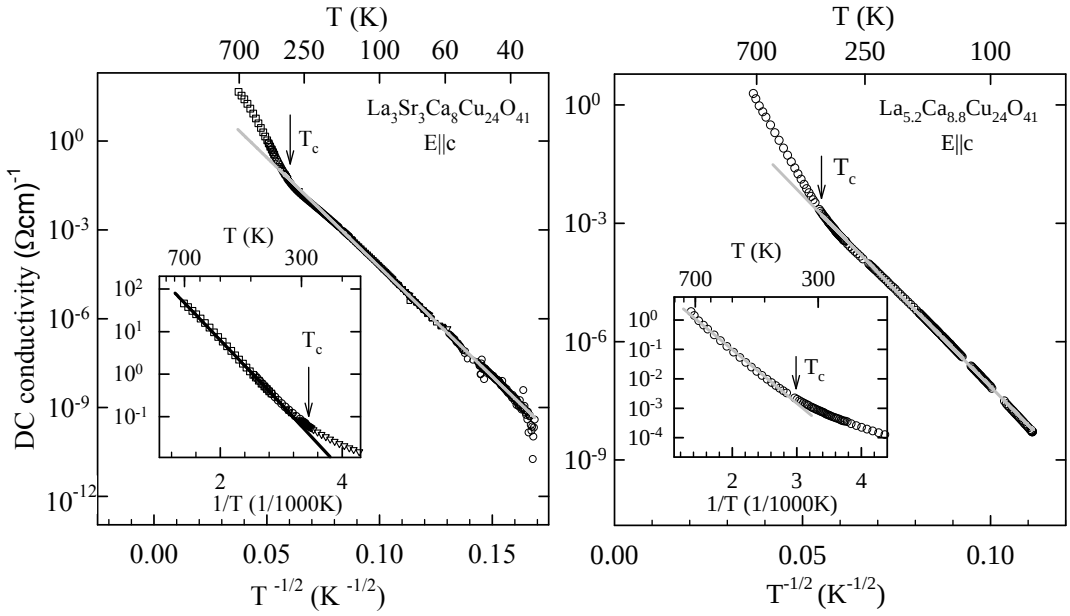

Figure 5.7: dc conductivity σ_{dc} of $La_3Sr_3Ca_8Cu_{24}O_{41}$ and $La_{5.2}Ca_{8.8}$-$Cu_{24}O_{41}$ along the c-axis *vs.* $T^{-1/2}$. Above respective T_c = 300 K and 330 K, σ_{dc} follows a simple activation behavior, which indicates the nearest-neighbor hopping charge transport mechanism (full lines in the insets). Below T_c the behavior $\sigma_{dc} \propto \exp(T^{-1/2})$ is observed (full lines in the main panels) corresponding to the regime of variable-range hopping in one dimension.

available for hops, has an uniform distribution in the range $-\Delta$ to $+\Delta$, the c is the distance between the nearest Cu chain sites and α^{-1} is the localization length. By using respective $\Delta = 1600 - 2100$ K and $c = 2.77\mathring{A}$, we find $\alpha^{-1} \approx 1\mathring{A}$. The values of the VRH activation energies for $La_{5.2}$ and La_3, $T_0^{exp} = 5 \cdot 10^4$ K and $T_0^{exp} = 2.9 \cdot 10^4$ K, respectively, are obtained from the fit of our data to Eq. 5.4. These values are very close to those expected theoretically for $La_{5.2}$ and La_3: $T_0^{th} = 8\Delta c\alpha \approx 4.6 \cdot 10^4$ K and $T_0^{th} = 8\Delta c\alpha \approx 3.5 \cdot 10^4$ K, respectively.

5.2.2 Frequency dependent measurements also indicate hopping transport mechanism

For brevity, we present the results only for $La_3Sr_3Ca_8Cu_{24}O_{41}$ compound. The features of the frequency dependent conductivity observed for $La_{5.2}Ca_{8.8}$-$Cu_{24}O_{41}$ correspond well, and lead to the same conclusions as the results for $La_3Sr_3Ca_8Cu_{24}O_{41}$.

Fig. 5.8 demonstrates the conductivity $\sigma(\nu, T)$ spectra of $La_3Sr_3Ca_8Cu_{24}O_{41}$ over a broad frequency range for different temperatures. Our LFDS results are more instructive when combined and analyzed with the quasi-optical microwave and far infrared optical conductivity results in the 6-350 cm^{-1} range, taken from Ref. [171].

As confirmed by our fit (see below), the kinks in $\sigma(\nu, T)$ on the left side of the lowest-frequency phonon are of electronic (non-phonon) origin and we assign this contribution to the hopping of holes in the chains. Excluding the phonon component, the electronic conductivity can be expressed as the sum of two terms

$$\sigma(\nu, T) = \sigma_{dc}(T) + A(T) \cdot \nu^s \qquad s \approx 1 \tag{5.5}$$

where $\sigma_{dc}(T)$ is given by Eq. 5.4. We note that the frequency independent behavior is found in the radio-frequency range for all temperatures (open symbols in Fig. 5.8). Similar dependences have been observed in a variety of disordered systems [174]. The frequency-dependent component $\sigma_{ac}(\nu, T) = A(T) \cdot \nu^s$ is found to contain a temperature dependent prefactor $A(T)$. The cross-over frequency ν_{co} from the frequency independent to the frequency dependent conductivity can be estimated from the condition that the ac hopping length has to be smaller than the dc hopping length in order that $\sigma_{ac}(\nu, T)$ overcomes $\sigma_{dc}(T)$ [172]. For one-dimensional VRH, the dc hopping length is given by $R_0 = (\Delta c/2\alpha T)^{1/2}$, and the ac hopping length is $R_\nu = \frac{1}{2}\alpha \ln(\nu_{ph}/\nu_{co})$, where the attempt frequency ν_{ph} depends on the electron-phonon interaction. Assuming $\nu_{ph} \approx 10^{12}$ s^{-1}, we find for the cross-over frequency ν_{co} the values 0.15 cm^{-1}, 0.015 cm^{-1} and 0.0006 cm^{-1} for $T = 300$

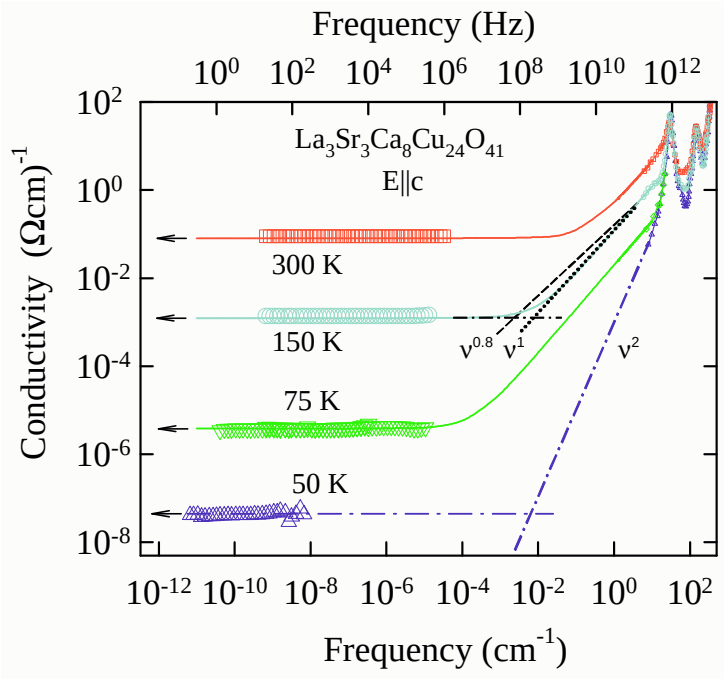

Figure 5.8: Broad conductivity spectra combined from our dc/LFDS results and microwave/FIR results taken from Ref. [171]. Spectra are obtained for $La_3Sr_3Ca_8Cu_{24}O_{41}$ along the c-axis at selected temperatures. Hopping conduction of the form ν^s, $s \approx 1$, is found between 6 and 20 cm^{-1} for $T \geq 75$ K, while a featureless, frequency independent behavior is found in the radio-frequency range for all temperatures. The arrows denote the dc values. The full lines are fits to Eq. 5.5. A pure power law contributions with $s = 0.8$ and 1 are shown for $T = 150$ K by a dashed and dotted line, respectively. At 50 K only a ν^2 contribution (dashed-dotted line) due to the low-energy phonon tail is observed.

K, 150 K and 75 K, respectively. These values coincide nicely with those obtained when the ν^s fits in 6 – 20 cm^{-1} range are extrapolated to lower frequencies (Fig. 5.8). In particular, the choice of the exponent $s = 1$ appears to be the most appropriate. For example, at $T = 150$ K we find $\nu_{co} \approx 0.0027$ cm^{-1} and 0.013 cm^{-1}, for $s = 0.8$ and 1, respectively. Experimentally we are not able to distinguish between the $\nu^{0.8}$ and ν^1 dependences due to relatively narrow frequency range in which $\sigma \sim \nu^s$ behavior is detected. At $T \leq 50$ K the hopping vanishes because the charge carriers are frozen out, and we observe only the ν^2 contribution to the conductivity associated with the low-energy phonon (Lorentzian) tail.

5.2.3 Hopping transport is due to localized holes in chains

We now comment on the hopping transport found in the chains of $La_3Sr_3Ca_8Cu_{24}O_{41}$, as well as $La_{5.2}Ca_{8.8}Cu_{24}O_{41}$, in comparison with disordered non-crystalline insulators. Firstly, for the latter compounds the value of the exponent in Eq. 5.4 is commonly found to be 1/4, corresponding to hopping in 3 dimensions; it becomes 1/2 if electron-electron interaction plays a role [175]. However, electron-electron interactions are expected to have a significant impact on the correlated many-electron hopping, only when the temperature T is larger than T_0, which is far from experimental range since $T_0 = 2.9 - 5 \cdot 10^4$ K, [172, 176]. The situation is different for systems consisting of parallel chains of finite length where small disorder leads to weakly localized states [177]. This model gives the temperature exponent 1/2 as found in our experiment. We conclude that the exponent 1/2 confirms the one-dimensional nature of the electronic structure of chains in $La_ySr_{14-y-x}Ca_xCu_{24}O_{41}$, which is in accord with the crystallographic structure [70, 71]. Secondly, the obtained values for T_0 indicate the standard regime of the VRH where the hopping distance $R_0 = (\Delta c/2\alpha T)^{1/2}$ is larger than the localization length α^{-1}; the extremely small $\alpha^{-1} \approx 1\mathring{A}$ shows that the system is far from the metal-insulator transition. Following the usual interpretation of the VRH law, from $T_0 = 16\alpha^3/n(E_F)$ we find the electronic density of states at the Fermi level $n(E_F) \approx 5.5 \cdot 10^{24}$ $eV^{-1}cm^{-3}$. Finally, a straightforward consequence of the observed VRH conduction is that its extrapolation indicates a zero conductivity at $T = 0$, in accord with the theory developed for disordered non-crystalline insulators.

Generally, a frequency-dependent conductivity varying as $A(T) \cdot \nu^s$, where $s \approx 1$, does not necessarily imply hopping conduction [172]. However, we suggest that dc VRH conduction as well as the power-law ac conduction are

attributed to the same set of localized states near the Fermi level. The value of the exponent close to one indicates that the observed ac conductivity is due to phonon-assisted hops between spatially distinct sites similarly to the dc contribution, and not to the photon absorption for which $s \approx 2$ is usually found [172]. Note that we did not find the latter in the whole measured frequency range, despite the theoretical prediction that with increasing frequency there is a cross-over from the regime dominated by phonon-assisted $\sigma_{hopping} \approx \nu^s$, $s \leq 1$ to that dominated by photon-assisted conduction which varies as ν^s, $s \approx 2$. The conductivity observed at 50 K, which follows a ν^2 behavior, is in our case simply a phonon tail, and is not due to hopping.

5.2.4 A comparison between $Sr_{14-x}Ca_x$... and $La_ySr_{14-y-x}Ca_x$... materials

At this point, we compare the electrical transport properties observed for $La_ySr_{14-y-x}Ca_xCu_{24}O_{41}$ and for $Sr_{14}Cu_{24}O_{41}$ material. Also a reference on the results for other $Sr_{14-x}Ca_xCu_{24}O_{41}$ materials will be necessary, [171, 160].

Firstly, we note that, in contrast to $Sr_{14}Cu_{24}O_{41}$, in $La_ySr_{14-y-x}Ca_xCu_{24}O_{41}$ materials no signature of the CDW phason response to dc and ac electric fields is found. In addition to a featureless radio-frequency response, we also did not observe electric-field dependence of dc conductivity up to 25 V/cm, in the temperature range 326 K- 50 K. Finally, no signature of the pinned mode in the microwave frequency range was found for $La_ySr_{14-y-x}Ca_xCu_{24}O_{41}$ materials.

Secondly, we analyze and compare in more detail the dc conductivity results, as presented in Fig. 5.9 for La_3 and $La_{5.2}$ along the ones for $Sr_{14}Cu_{24}O_{41}$. Very different RT resistivities have to be noted: 1400, 13 and 0.002 $(\Omega\text{cm})^{-1}$, respectively. Inspection of the logarithmic derivatives, presented in the lower panel, allows quantification of differences in the observed conductivity temperature dependences. For $Sr_{14}Cu_{24}O_{41}$ high temperature insulating phase and low temperature CDW phase are characterised by well defined activation energies, and a phase transition in between, observed as a peak in the logarithmic derivative. For $La_ySr_{14-y-x}Ca_xCu_{24}O_{41}$ materials, no transition is observed, only a crossover from nearest-neighbor hopping behavior at high temperatures, where an activation energy can be defined, to a VRH behavior below respective crossover temperatures $T_c \approx 300 - 330$ K.

In Fig. 5.10 we compare the dc transport parameters, *i.e.* RT resistivity, activation energy and crossover/transition temperature for $La_ySr_{14-y-x}Ca_xCu_{24}O_{41}$ and $Sr_{14-x}Ca_xCu_{24}O_{41}$ materials. The data for another nonisovalently substituted material $Y_1Sr_5Ca_8Cu_{24}O_{41}$, hole count $\delta_h = 5$, by Mo-

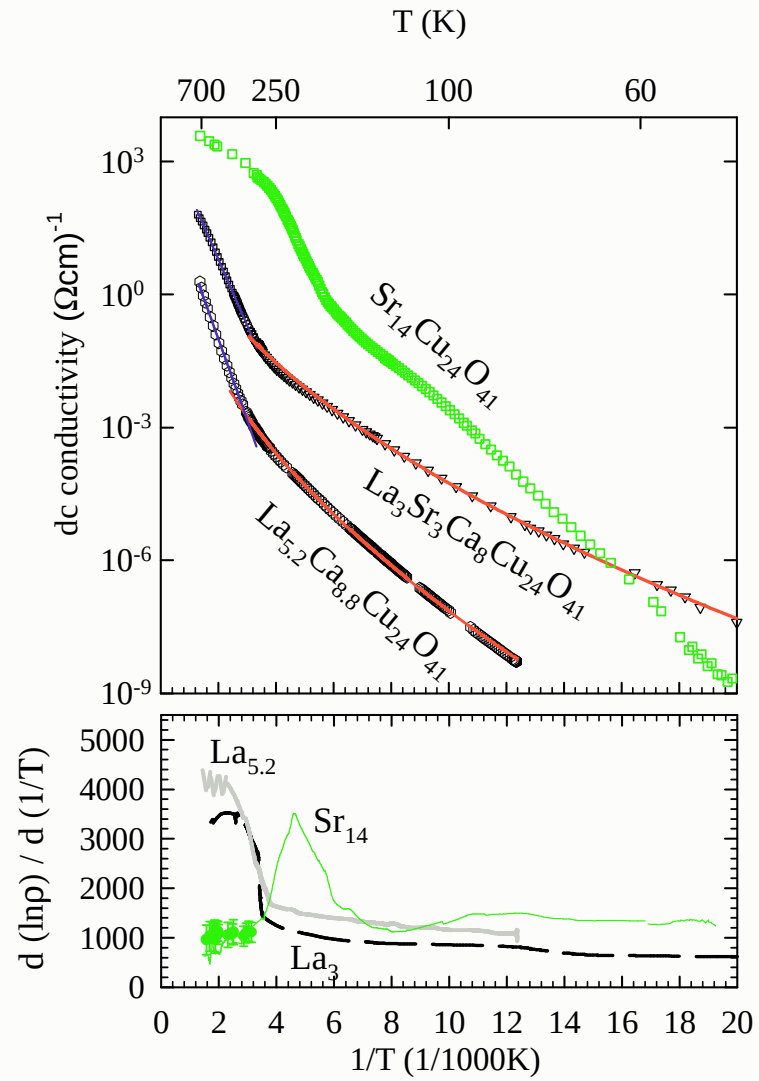

Figure 5.9: Upper panel: dc conductivity σ_{dc} of $La_3Sr_3Ca_8Cu_{24}O_{41}$ and $La_{5.2}Ca_{8.8}Cu_{24}O_{41}$ compared to the one for $Sr_{14}Cu_{24}O_{41}$, along the c-axis, *vs.* inverse temperature. Solid, weakly curved lines are fits to Mott's VRH law, Eq. 5.4. Lower panel: corresponding logarithmic derivatives clarify the differences between the behavior of nonisovalently substituted compounds, denoted La_3 and $La_{5.2}$ and the parent compound, denoted Sr_{14}. For Sr_{14} well defined activation energies, in the high, 900 K, and especially in the low temperature insulating phase, 1300 K, may be found, with the phase transition observed as a peak in the logarithmic derivative at 210 K. On the contrary, for La-substituted materials only a change in the slope is observed for $La_{5.2}$ and La_3 at respective crossover temperatures, 330 K and 300 K. At high temperatures, well defined activation energies of 4200 K and 3200 K, respectively are found. Activation behavior changes over to a VRH law behavior for $La_{5.2}$ and La_3, with characteristic energies $5 \cdot 10^4$ K and $2.9 \cdot 10^4$ K, respectively.

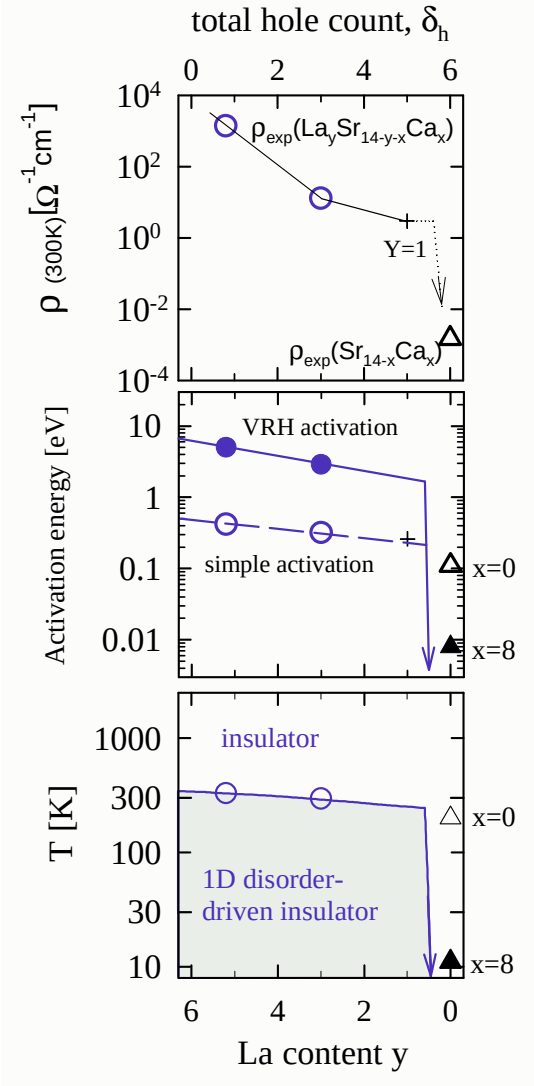

Figure 5.10: dc electrical transport data for $Y_1Sr_5Ca_8Cu_{24}O_{41}$ by Motoyama *et al.* , [84], crosses, complements our data for $La_3Sr_3Ca_8Cu_{24}O_{41}$, $La_{5.2}Ca_{8.8}Cu_{24}O_{41}$, circles. These are compared to $Sr_{14}Cu_{24}O_{41}$ and $Sr_6Ca_8Cu_{24}O_{41}$, denoted with triangles and also as x=0, x=8, respectively. The La(Y) content corresponds to hole count, $\delta_h = 6 - y$. Upper panel: RT resistivity for $\delta_h \leq 5$ is at least three orders of magnitude higher than for $Sr_{14-x}Ca_xCu_{24}O_{41}$ materials. Middle panel: $\delta_h \leq 5$ materials may be characterized by simple activation, or by VRH activation energy, above and below the crossover temperature, respectively. These energies are higher than the activation energy of x=0, either in the high temperature insulating phase or in CDW. The energy difference is pronounced for x=8. Lower panel: The denoted temperatures for La_3 and $La_{5.2}$ are only crossover temperatures where a change occurs in the hopping transport mechanism. They do not correspond (vertical arrow) to CDW transition temperatures for x=0, x=8.

toyama *et al.* , [84] complete the picture. The symbols on the right side, x=0 and x= 8 denote the parent compound $Sr_{14}Cu_{24}O_{41}$ and isovalently substituted $Sr_6Ca_8Cu_{24}O_{41}$, respectively. Comparison with the latter member of $Sr_{14-x}Ca_xCu_{24}O_{41}$ family is important, since Ca-content in this material is similar to Ca-content of presented La(Y) substituted materials. That is, if we set y to 0 in $La_ySr_{14-8-y}Ca_8Cu_{24}O_{41}$ we get x=8 material.

In the upper panel, it is important to note that for materials where $\delta_h \leq 5$ it is not possible to account for the resistivity decrease by a mere increase in the hole number. Also, the localization length $\alpha^{-1} \approx 1\mathring{A}$ is quite similar for both $La_{5.2}$ and La_3, while their RT resistivity differs for two orders of magnitude. Regardless of this observation, the most important result shown in this figure is that RT resisitivities of materials where $\delta_h \leq 5$ are at least three orders of magnitude higher than for materials $\delta_h = 6$. This difference is denoted by a vertical arrow.

In the middle panel and lower panel we note that the energy and temperature scales are different for the two families of materials. For x=0 the difference is not pronounced as for x=8 material, which has an order of magnitude lower energy/temperature scale. We note that La-content, which changes the number of holes dramatically, has only a minor influence on energy/temperature parameters in $\delta_h \leq 5$ materials. On the contrary, Ca-content in $\delta_h = 6$ materials has a major influence on energy/temperature scale. This occurs despite the fact that the redistribution of holes between the ladders (one hole in x=0) and chains (five holes in x=0) is minimal upon Ca-substitution. The difference in the influence of La-content and Ca-content and the respective hole count on the energy/temperature scales between $\delta_h \leq 5$ and $\delta_h = 6$ materials is denoted by vertical arrows, separating these families of materials.

5.2.5 Conclusions

The investigations of the frequency and temperature dependent conductivity yield clear evidence that nonisovalently substituted $La_3Sr_3Ca_8Cu_{24}O_{41}$ and $La_{5.2}Ca_{8.8}Cu_{24}O_{41}$ are insulators with hopping transport along the chains. At microscopic scale, we propose that strong local distortions of the chains due to irregular coordination of La^{3+}, Sr^{2+} and Ca^{2+} ions [70, 71] induce a non-periodic potential in which holes reside. The VRH conductivity can be then viewed as a result of distorted distribution of microscopic conductivities, as predicted in Anderson localization theories. Therefore, copper-oxygen chains in nonisovalently substituted $La_ySr_{14-y-x}Ca_xCu_{24}O_{41}$ can be considered as a one-dimensional system in which disorder, associated with random distribution of holes, causes the Anderson localization. We assume that the chain subsystem behaves as a one-dimensional disorder-driven insulator for the whole range of La-substituted materials, *i.e.* for the whole range of hole counts $0 \leq \delta_h < 6$.

Featuring at least three orders of magnitude higher resistivity at RT, the charge transport in $La_ySr_{14-y-x}Ca_xCu_{24}O_{41}$ was ascribed to a hopping mechanism in the chain subsystem - a different one than the transport in a gapped insulator $Sr_{14}Cu_{24}O_{41}$(hole count $\delta_h = 6$). This confirms our assumption from Sec. 5.1- that the charge transport in $Sr_{14-x}Ca_xCu_{24}O_{41}$ is due to the mobile holes residing in the ladders. This also yields a definite evidence that CDW in $Sr_{14}Cu_{24}O_{41}$ is established in the ladders, as we suggested [160, 167].

While no ordering is observed for the chains in $La_ySr_{14-y-x}Ca_xCu_{24}O_{41}$, for the chains in $Sr_{14}Cu_{24}O_{41}$ it was previously shown that a charge gap opens due to the charge order (CO) related to spin-ordering according to the antiferromagnetic dimers pattern. Note that the CO is established in the chains concomitantly with the CDW phase in the ladders. Thus, a possibility is revealed for the existence of a phase transition in the phase diagram of $(La,Sr,Ca)_{14}Cu_{24}O_{41}$ compounds. We propose that the disordered chains subsystem $0 \leq \delta_h < 6$ crosses over into a charge-ordered gapped insulator at $\delta_h = 6$. However, the way how the transport switches from the chains to the ladders in $5 < \delta_h < 6$ range is still an open issue. Is there a phase transition from La-substituted to La-free materials and how the phase diagram of the former merges with the one of the latter should be resolved by further experiments on materials with very low La content, which corresponds to $\delta_h \lesssim 6$.

5.3 Suppression of CDW, in ladders of $Sr_{14-x}Ca_xCu_{24}O_{41}$, by Ca-substitution, x=0, 3, 6, 8, 9, 11.5

Superconductivity is established at pressures above 3 GPa in the isovalently substituted compounds $Sr_{14-x}Ca_xCu_{24}O_{41}$. It is only observed for high Ca-content materials, $10 \leq x \leq 13.6$, [106]. We have shown for the parent compound $Sr_{14}Cu_{24}O_{41}$, x=0, that CDW is established in the ladders, where mobile holes are found. These findings confirm theoretical suggestions that, due to the quasi one-dimensional nature of ladders, a CDW may compete with the occurrence of superconductivity in the hole-doped ladder system. Obviously, upon Ca-substitution, CDW has to give way to SC ground state.

Here we present the results of our further investigation, which addressed the Ca substituted materials, $Sr_{14-x}Ca_xCu_{24}O_{41}$, x=0, 3, 6, 8, 9, 11.5. We intended to clarify the question of the competition (or balance?) between the two ground states for all $Sr_{14-x}Ca_xCu_{24}O_{41}$ materials. We performed two different sets of experiments. Firstly, we extended the picture obtained for $Sr_{14}Cu_{24}O_{41}$ by measuring $Sr_{14-x}Ca_xCu_{24}O_{41}$ compounds of different Ca-contents $x \neq 0$. Secondly, we also studied the transport anisotropy for different x materials.

5.3.1 dc transport $E||c$, $0 \leq x \leq 11.5$

In Fig. 5.11 we present the results of dc resistivity ρ_{dc} *vs.* inverse temperature $1/T$, in comparison for all the compounds under study, x=0, 3, 6, 8, 9, 11.5. The symbol $E||c$ denotes measurements along the c-axis, that is, along the legs of ladders. The temperature range of measurement was from 750 K down to 2 K. All the materials show comparable and high RT conductivities in the range 300–1200 $\Omega^{-1}cm^{-1}$, Table 5.2, confirming the existence of mobile holes transferred in the ladders.

The energy gaps become, Table 5.2, larger when going from high temperatures into the CDW phase, indicating that an additional gap opens for $0 \leq x \lesssim 6$, Fig. 5.11. While in the standard CDW, a transition from the metallic state to the insulating state is observed due to the opening of an energy gap [126], in the present case the transport in the high temperature (H.T.) phase is already non-metallic. We explain this by electron-electron interactions within the ladders, leading towards a Mott-insulator. As far as CDW ground state observed in $Sr_{14-x}Ca_xCu_{24}O_{41}$ is concerned, we suggest that it might fall between the two well defined limits of charge order: the CDW order of itinerant charges and the charge order (CO) of localized

charges.

The transition broadens substantially with increasing x, as reflected by an increase of the transition width and a decrease of the peak height of $d(\ln\rho)/d(T^{-1})$ plotted in the lower left panel of Fig. 5.11. The broadening might be attributed to disorder introduced by Ca-substitution; a well known effect in quasi-1D compounds [27]. For x=8, 9, Fig. 5.11, Δ_{CDW} is strongly suppressed, when compared with $\Delta_{\mathrm{H}.T.}$, which is here 2-3 times higher. Therefore, in the logarithmic derivative only a step-like feature appears. The width of the step we consider analogous to the width of the peak at half maximum (FWHM) for x=0, 3, 6, see Sec. 5.1.1. That is, the transition broadening is further documented, since the relative width of the step (normalized to the respective temperature scale) for x=8, 9 is larger than FWHM divided by respective T_c for x=0, 3, 6.

Correspondingly to CDW gap, transition temperature decreases from 210 K for $x = 0$ to 7 K for $x = 9$, as denoted by arrows in Fig. 5.11. For x=11.5 at a crossover temperature $T_{co} = 6.5$ K ρ_{dc} activation energy changes, from $\Delta_{\mathrm{H}.T.} = 22$ K to $\Delta_{\mathrm{L}.T.} = 5$ K. The ratio $2\Delta_{\mathrm{L}.T.}/3.52T_{co} = 0.4$ is much lower than one. And we note that for x=0, 3, 6, 8, 9, where we identify CDW transition the ratio is $2\Delta_{CDW}/3.52T_c \approx 3$. In a mean-field theory like BCS this ratio should be one, and in the real q1D systems it is usually enhanced above one. Therefore, we can not consider that T_{co} for x=11.5 corresponds to a phase transition. We note that dc resistivity of x=11.5 is metallic like from RT down to about 100 K where it changes over into insulating behavior, and that $\Delta_{\mathrm{H}.T.}$ is defined only below 50 K.

c-axis	σ(300K) (Ωcm^{-1})	T_c (K)	$\delta T_c/T_c$	Δ_{CDW} (K)	$\Delta_{\mathrm{H.T.}}$ (K)
x=0	500	210	0.1	1300 ± 50	900 ± 250
x=3	400	140	0.3	1100 ± 50	800 ± 100
x=6	300	55	0.4	300 ± 40	280 ± 60
x=8	600	11	0.35	80 ± 10	160 ± 20
x=9	1200	7	0.4	30 ± 5	100 ± 20
x=11.5	1000	$T_{co} = 6.5$			

Table 5.2: dc transport parameters for $Sr_{14-x}Ca_xCu_{24}O_{41}$ materials: RT conductivity, CDW transition temperature, relative transition width, CDW activation energy, and high temperature insulating phase activation energy.

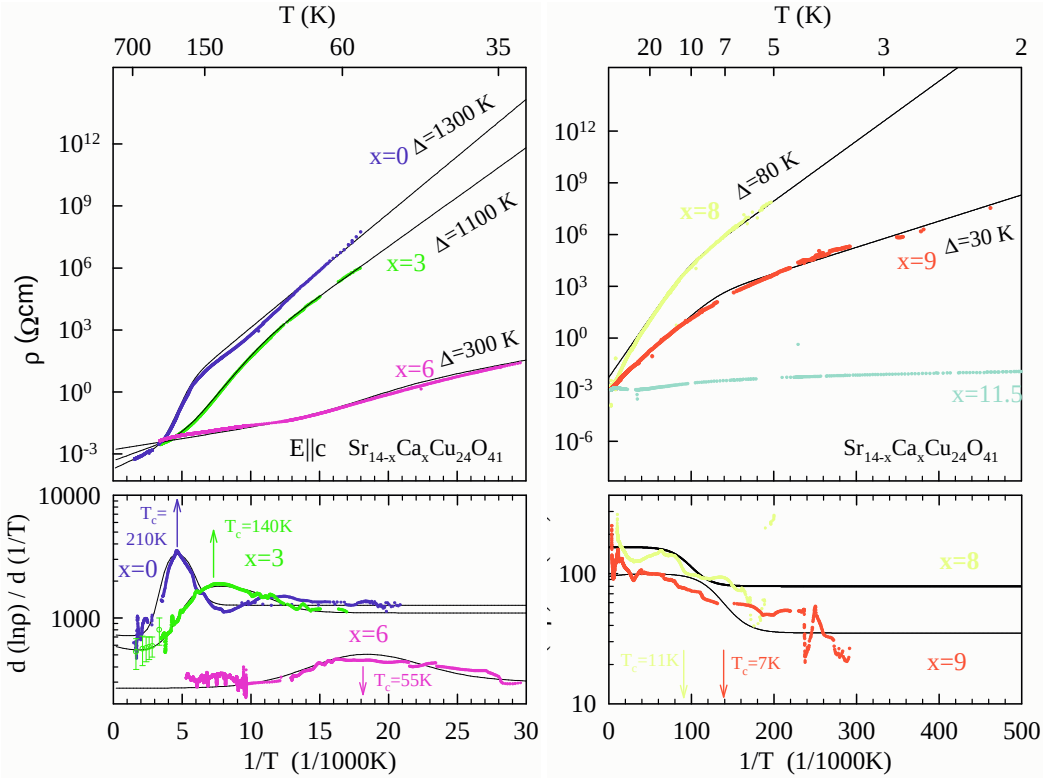

Figure 5.11: The dc resistivity is activated $\rho_{dc} \propto e^{\Delta_{CDW}/k_BT}$ below T_c with activation energies Δ_{CDW} denoted. The high temperature phase is also characterized by a well defined activation energy $\Delta_{\mathrm{H.T.}}$. For x=0, 3, 6 $\Delta_{\mathrm{H.T.}}$ is lower than Δ_{CDW} and transition temperature T_c can be determined from a peak in the logarithmic derivative of the resistivity. For x=8,9 $\Delta_{\mathrm{H.T.}}$ becomes 2-3 times higher than Δ_{CDW} and in the logarithmic derivative only a step-like feature appears. For x=11.5 there is no transition to CDW phase. At a crossover temperature T_{co} = 6.5 K only ρ_{dc} activation energy changes, from 22 K to 5 K. In all panels the full lines guide the eye.

5.3.2 ac response $E||c$, $0 \leq x \leq 9$

In the frequency range 0.01 Hz - 1 MHz the spectra of the dielectric function were obtained from the complex conductance measured at 2 K$< T <$200 K. All measurements were done along the crystallographic c-axis of high-quality single crystals.

A specific analysis of the radio-frequency complex conductance allowed to follow-up the CDW dielectric response through the respective phase transition temperature ranges for x=3, 6, 8, 9 materials. It was not possible for x=0 since the feature which allowed this analysis was out of the frequency window. This analysis will be demonstrated for x=3. In the left panels of Fig. 5.12 normalized, $\frac{G-G_0}{G_0}$, real part of the conductivity, G *vs.* frequency is shown. G_0 stands for low-frequency, equal to dc, conductivity, see Sec. 3.2. The imaginary part of the conductivity, B is also shown at several temperatures. What is particular is, that at temperatures 150 K and 159 K, the CDW dielectric mode has left the frequency window. G remains constant within the frequency window, while the contribution to the static dielectric constant is still observed as *tails* in B. As B is proportional to the frequency, the static dielectric constant may be extracted from this proportionality, $\varepsilon_0 = B/\omega$. Corresponding ε' tails are shown in the right panel where real, ε', and imaginary, ε", parts of the dielectric function are shown. Naturally, central relaxation time τ_0 and the shape parameter $1-\alpha$ can not be extracted in this manner (see Fig. 5.17). At lower tempratures, where the mode is inside the frequency window these two parameters are extracted along $\Delta\varepsilon$ by a standard procedure described in Sec. 3.2, as for $x = 0$.

A pronounced dielectric relaxation is observed for all compositions x=3, 6, 8 and 9, as well as for x=0 (see also Fig. 5.2) providing evidence for the CDW formation [78, 160]. In Fig. 5.12, right panel, we show for x=3, the screened loss peak (ε") centered at τ_0^{-1}, which moves toward lower frequencies and smaller amplitudes with decreasing temperature. The main features of this relaxation do not qualitatively change on Ca-substitution, for $0 \leq x \leq 9$: the dielectric strength $\Delta\varepsilon = \varepsilon_0 - \varepsilon_{HF} \approx 5 \times 10^4$, the symmetric broadening of the relaxation-time distribution given by $1-\alpha \approx 0.8$, and the central relaxation time τ_0, which closely follows a thermally activated behavior in a manner similar to the dc resistivity; $\tau_0(T) \propto \rho(T)$ (see also Fig. 5.1).

Our results clearly demonstrate that a phase transition to the CDW ground state is strongly suppressed by Ca-substitution. This demonstration is based on the strong correspondence between dc resistivity and LFDS results. In Fig. 5.13 this is depicted for three representative Ca-contents x. On decreasing temperature, a sharp growth of $\Delta\varepsilon$ starts in the close vicinity of T_c and reaches the huge value of the order of $10^4 - 10^5$ at $T_c = 140$ K and

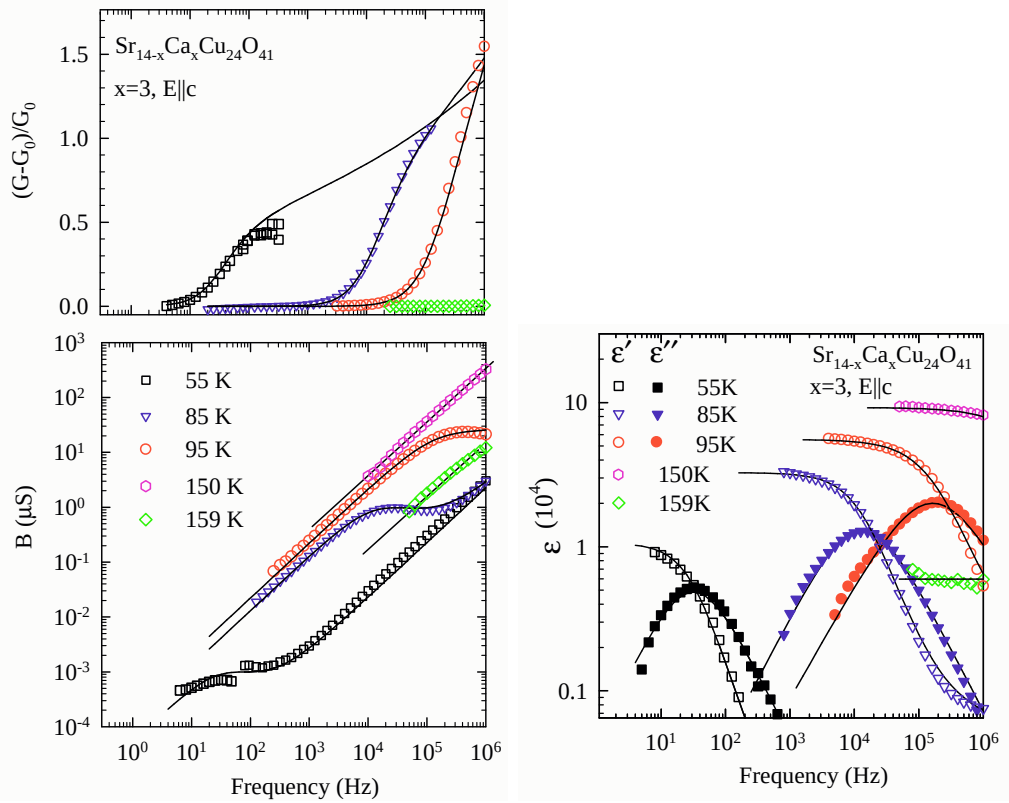

Figure 5.12: Left panels: LFDS data analysis for the example of x=3. Normalized, $\frac{G-G_0}{G_0}$, frequency-dependent real part of the conductivity, is shown in the upper left panel. In the lower left panel the imaginary part of the conductivity, B is also shown at several temperatures. The *tails* at 150 K and 159 K are due to the dielectric strength of the dielectric modes appearing at frequencies above the experimental frequency window. Right panel: Corresponding real and imaginary parts of the dielectric function as a function of frequency. The full lines are from fits by the generalized Debye expression: $\varepsilon(\omega) - \varepsilon_{HF} = \Delta\varepsilon/[1 + (\imath\omega\tau_0)^{1-\alpha}]$. The full lines in the *tails* at 150 K and 159 K simply denote the dielectric strength of the modes existing above the experimental frequency window.

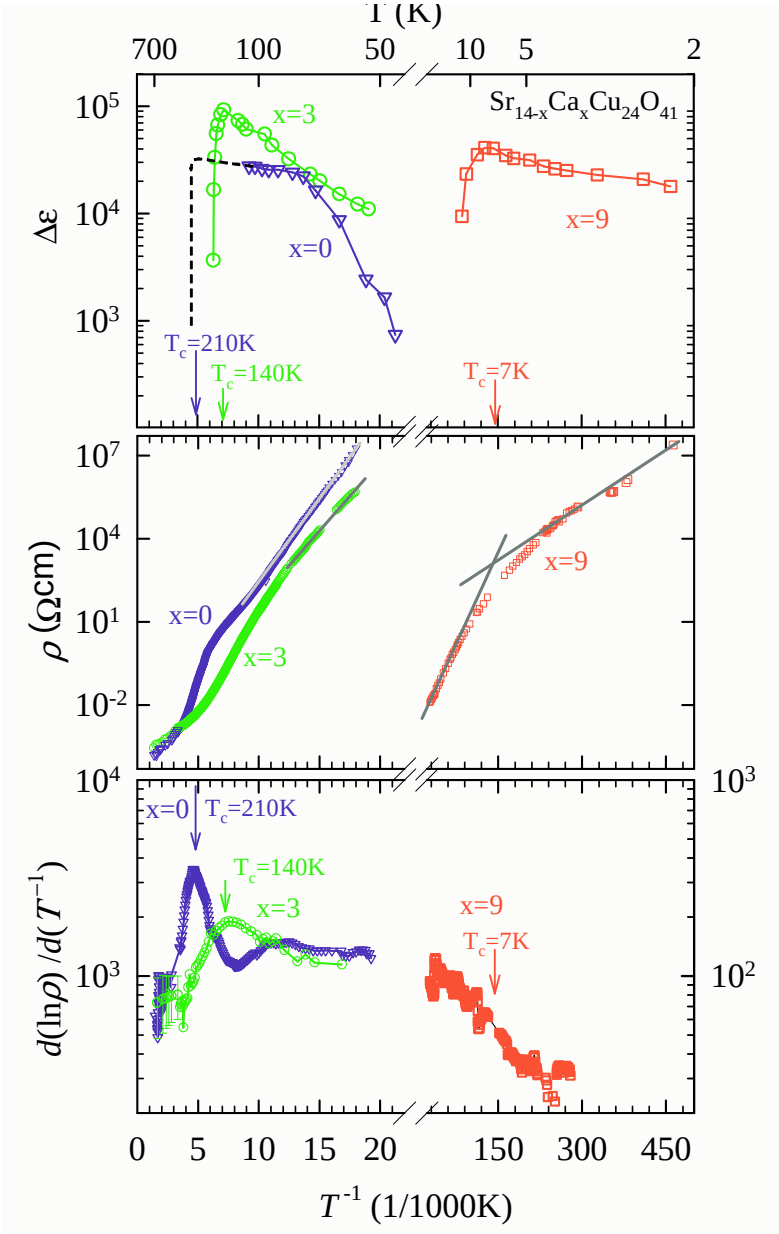

Figure 5.13: Temperature dependence of the dielectric strength $\Delta\varepsilon$ of the CDW radio-frequency related mode (upper panel) and dc resistivity ρ (middle panel) in $Sr_{14-x}Ca_xCu_{24}O_{41}$ for three representative Ca-contents x. dc and LFDS measurements are performed along the c axis. The arrows indicate the CDW phase transition temperature T_c, as determined from the logarithmic derivative of the resistivity, presented in the lowest panel. The temperatures where $\Delta\varepsilon$ attains maximum, correspond perfectly to these T_c, for the respective material. In the upper panel the full lines guide the eye, while in the middle panel the lines represent fits by Arrhenius functions. An assumed behavior of $\Delta\varepsilon$ for $x = 0$, based on that observed for $x = 3$ and 9, is represented by a dashed line.

$T_c = 7$ K for $x = 3$ and 9, respectively. These T_c values perfectly correspond to the temperature of the phase transition as determined in the dc resistivity measurements, indicated by pronounced peaks at T_c in the derivative of the resistivity. The overall decrease of $\Delta\varepsilon$ below T_c for x=0 is substantial. This issue was already addressed in Sec. 1.2.5 and 5.1.1. We suggested that a back-transfer of holes from ladders to chains starts below 70 K. Based on the decrease of $\Delta\varepsilon$, this assumption may be extended for x=3. It has to be noted that the decrease becomes much less pronounced for x=9, indicating a minor, if any back-transfer for this material.

Finally, we comment on the Stuttgart group microwave/FIR results [78, 160]. The conductivity decreases below approximately 2500 cm^{-1} for $x = 0$ and 3, and around 25 cm^{-1} for $x = 9$, which we associate with the opening of the CDW gap. This decrease is only observed for x= 0, x= 3 and x= 9 at temperatures lower than 240 K, 150 K and 20 K, respectively. These temperatures nicely agree with the CDW phase transition temperature T_c as determined from dc and LFDS (Fig. 5.13). Moreover, the CDW gap values Δ_{CDW} extracted from these measurements (1300 K $\approx$ 900 cm^{-1}, 1100 K $\approx$ 750 cm^{-1} and 30 K $\approx$ 20 cm^{-1}, for x=0, 3 and 9, respectively) correspond well to the edges seen in the optical conductivity spectra.

5.3.3 Features of CDW phason response in $\mathbf{Sr_{14-x}Ca_xCu_{24}O_{41}}$, $0 \leq x \leq 9$, $E||c$

As shown above, the CDW phason response to ac electric fields is qualitatively similar for all $0 \leq x \leq 9$. Below, we summarize additional similarities.

Firstly, we note that the dc field dependence was consistent for all $0 \leq x \leq 9$. That is, it featured only a negligible nonlinearity for the representative Ca-contents x=3,9, similarly to the one described before for x=0 - no sliding conductivity was observed. For x=3,9 as well as for x=0, the applied electric fields reached 10 V/cm, see Sec. 5.1.2.

Secondly, we note that besides for x=0, the pinned mode was detected for x=3, but not for x=9, [163]. The latter may be due to the screening by the larger number of free carriers in this compound. Since we observe the screened temperature-dependent response in the radio-frequency range centered at τ_0^{-1} (see Fig. 5.12), which represents a fingerprint of the CDW phason response, see Sec. 2.4, for x=0 all the way up to x=9, we can safely assume that the pinned mode always exists around $\Omega_0 \approx 1.8$ cm^{-1}. Using the same analysis as in Sec. 5.1.3, and assuming that the number of holes remains close to 1 in the ladders of $0 \leq x \leq 9$, we estimate the effective mass $m^* \approx 100$. There is basically no dependence on temperature or Ca content

for x between 0 and 9.

Thirdly, we identified an additional feature of the CDW phason response in complex conductivity results for the whole range of materials $0 \leq x \leq 9$. It is based on the observation of non-negligible high frequency dielectric constant, ε_{HF}. This is observed in LFDS measurements as the contribution to the real part of the dielectric function above the CDW radio-frequency mode, *e.g.* at 1 MHz. That is, ε_{HF} contains the dielectric strength of pinned mode, as well as single-particle contributions with modes in the optical frequency range. All these contributions are not expected to be above $\varepsilon_{HF} \approx 10$. For the aspect ratios of the samples under study, ε_{HF} of this magnitude would be below measurable limit. Contrary to this, we observed measurable ε_{HF}^{exp} as given in Table 5.3. We compare the experimental values with the theoretical ones ε_{HF}^{th}, calculated according to an expression relating the plasma frequency, Ω_{plasma}, and the energy gap characterizing the 1D system, Δ, [37]:

$$\varepsilon_{HF}^{th} = 1 + \frac{1}{6}\frac{\Omega_{plasma}^2}{\Delta^2} \tag{5.6}$$

We note from Table 5.3 that the best correspondence is obtained when calculating with $\Delta_{\mathrm{H.T.}}$, and not Δ_{CDW}. Although, if ε_{HF}^{exp} is assumed to be the dielectric strength of the (CDW) pinned mode, then Δ_{CDW} should be a better choice. In any case, we suggest that the observed ε_{HF}^{exp} confirms the existence of pinned mode for higher Ca-contents, which existence was only assumed for x=9, see just above.

c-axis	Ω_{plasma} (eV)		Δ_{CDW} (K)	ε_{HF}^{th}		$\Delta_{\mathrm{H.T.}}$ (K)	ε_{HF}^{th}		ε_{HF}^{exp}
x=0	0.5		1300	4		900	8		< 10
x=3	0.7		1100	9		800	16		< 10
x=6	0.8		300	150		300	150		100 ± 100
x=8	0.87		80	2500		160	600		500 ± 100
x=9	0.9		30	15000		100	1500		800 ± 100

Table 5.3: Δ_{CDW}, $\Delta_{\mathrm{H.T.}}$: CDW(H.T.) gap from dc resistivity and/or LFDS. Ω_{plasma}: plasma frequency from optical measurements by Osafune *et al.* , [75]. $\varepsilon_{HF}^{exp/th}$: the observed and theoretically calculated values of high frequency dielectric constant.

5.4 Evidence for anisotropic CDW in ladder planes

Following the study of $Sr_{14-x}Ca_xCu_{24}O_{41}$ compounds of different Ca-contents $x \neq 0$, we also studied the transport anisotropy for different x materials. In particular, when discussing the suppression of the CDW ground state in $Sr_{14-x}Ca_xCu_{24}O_{41}$, the dimensionality and its relation to the Ca-substitution (or pressure) is important. Our intention was to resolve whether the nesting arguments have to be taken into acount. Resolving the issue for CDW ground state would certainly clarify the picture for the competing SC state.

All experiments were conducted on high-quality single crystals along the three crystallographic axis: c- (along the ladder legs), a- (along the ladder rungs) and b- (perpendicular to the ladder planes). The dc resistivity and ac complex conductivity of $Sr_{14-x}Ca_xCu_{24}O_{41}$ (x=0, 3, 6, 8, 9 and 11.5) were investigated in the temperature range 2 K$< T <$700 K.

5.4.1 dc transport $E||c$, $E||a$, $E||b$, $0 \leq x \leq 11.5$

We compare the dc transport properties of $Sr_{14-x}Ca_xCu_{24}O_{41}$ along all three directions. Fig. 5.14 reveals for three representative Ca-contents x=0,3, 9 that the phase transition temperatures T_c, when measured along the c- and a-axis, are equal in value and have the same dependence on Ca substitution, Table 5.4. The same holds for the energy gaps in the high temperature phase above T_c and in the CDW ground state, which both are isotropic. The energy gaps become larger when going from high temperatures into the CDW phase, indicating that an additional gap opens for $x \lesssim 6$, as discussed in Sec. 5.3.1. The substantial transition broadening with increasing x, observed for measurements along the ladder legs is also observed along the ladder rungs, with similar transition widths, Fig. 5.14. The above results and correspondences are also found for x=6, 8 compounds, not shown in Fig. 5.14. For x=11.5 (where no CDW transition occurs) the a-direction dc transport properties of the insulating phase were similar to the previosly shown for the c-direction, Table 5.4.

While dc transport within the ladder (c,a) plane shows a set of properties similar for both directions, the dc resistivity along the third, b-direction, perpendicular to the ladder planes shows a distinct behavior, Table 5.4, Fig. 5.14. Different activation energies are observed, and no phase transition is registered. For x=3, 9, indeed, we observe a single activation in the whole temperature range. For x=0 the activation energy is larger at high temperatures than any of the observed for the c,a plane and changes over

below 170 K to a twice lower value. The simple activation process observed for the b-direction indicates that the charge transport perpendicular to the ladder planes probably happens via nearest-neighbor hopping, as expected between disordered chains. Particularly, the large Δ for x=0, changing over to a smaller one, Table 5.4, reminds of the hopping transport mechanism we observed along disordered chains of $La_ySr_{14-y-x}Ca_xCu_{24}O_{41}$ compounds, Fig. 5.9, Sec. 5.2.1. We finish the exposition for the b-direction by concluding that the CDW certainly does not develop a long range order in 3D for any x.

Finally, a word is in order to comment the issue of the CDW phase transition temperature and the in-plane extent of the CDW order. The peak in $d(\ln\rho)/d(T^{-1})$ is a clear sign of the phase transition and we can safely assume that the long-range-order is established below T_c in the ladder plane (c,a) for $x\lesssim 6$. In contrast to that, for x=8, 9, only a change in the slope is observed in the resistivity, for both in-plane directions, indicating that the CDW order, with only a finite in-plane correlation length, is established.

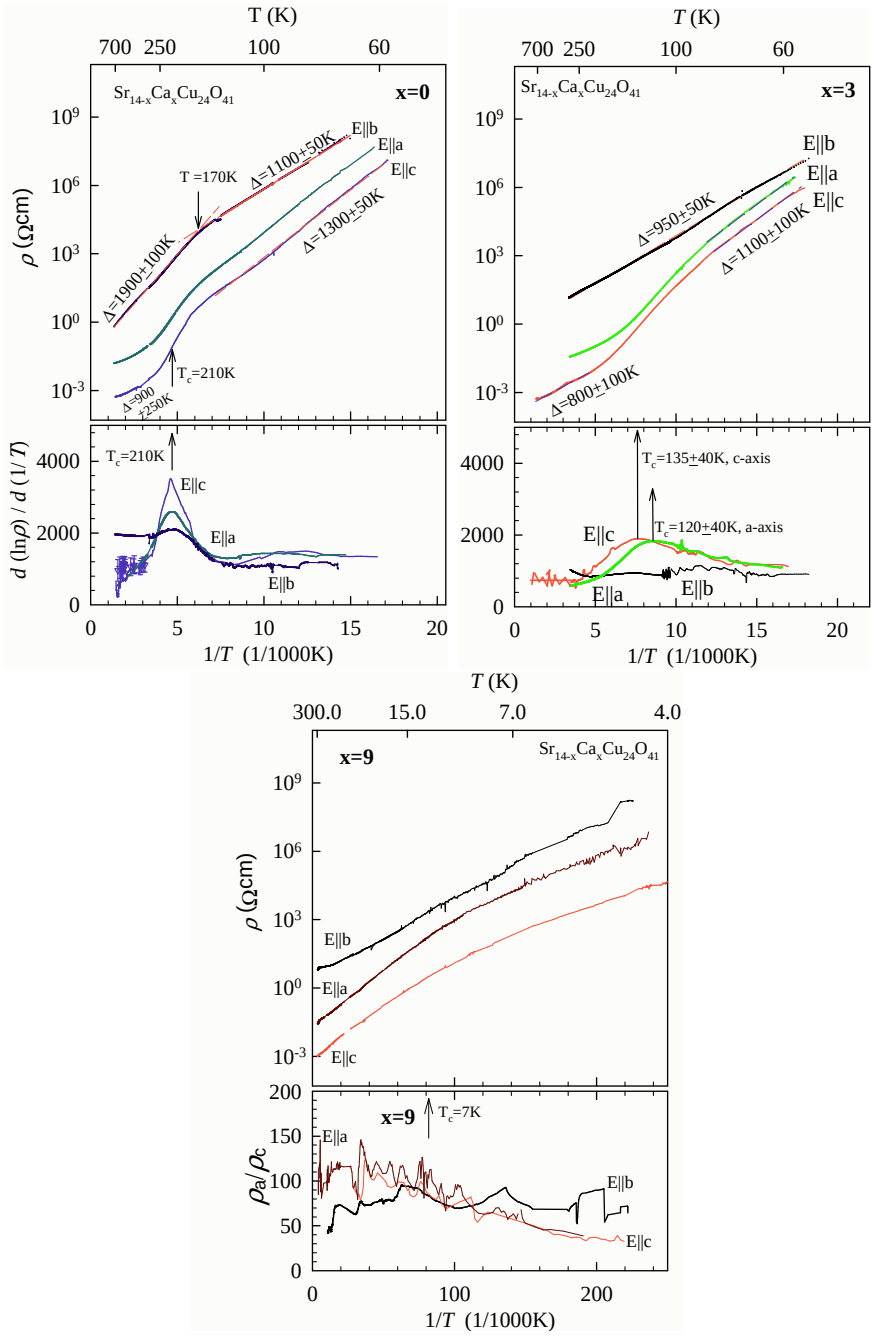

Figure 5.14: dc resistivity data for three representative compositions x=0, 3, 9, measured along three directions, is shown in the upper panels. Corresponding logarithmic derivatives of the resistivity for all directions are shown in the lower panels,. In the a-, and c-direction (see Sec. 5.3.1), a peak for x=0, 3 (or a step for x=9) in $d(\ln\rho)/d(T^{-1})$) indicates that CDW order is established (only a short-range one for x=9, see text). For the b-direction no such features - *i.e.* no ordering is observed. ρ_{dc} is thermally activated and the activation energies (denoted in the upper panels) are isotropic in the (c, a) ladder plane, both in CDW and HT insulating phases. Different activation energy is observed perpendicular to the ladder plane, in b-direction. For x=3, 9 this activation energy is constant in the temperature range of study, while for x=0 a crossover is observed at 170 K.

	σ_{RT} (S/cm)	T_c (K)	Δ_{CDW} (K)	$\Delta_{\mathrm{H.T.}}$ (K)	ρ_i/ρ_j 300K	ρ_i/ρ_j CDW	$\Delta\varepsilon_{max}$ at T_c	$\Delta\varepsilon_c/$ $/\Delta\varepsilon_a$
x=0								
c-axis	500	210	1300 ± 50	900 ± 250			3×10^4	7.5
					ρ_a/ρ_c	ρ_a/ρ_c		
a-axis	17	210	1300 ± 50	800 ± 300	30	15	4×10^3	
		T_{co}	$\Delta_{\mathrm{L.T.}}$		ρ_b/ρ_c	ρ_b/ρ_c	no	
b-axis	0.03	170	1100 ± 50	1900 ± 100	10000	300	mode	
x=3								
c-axis	400	140	1100 ± 50	800 ± 100			1×10^5	2.5
					ρ_a/ρ_c	ρ_a/ρ_c		
a-axis	28	120	1100 ± 50	800 ± 300	13	3	4×10^4	
					ρ_b/ρ_c	ρ_b/ρ_c	no	
b-axis	0.07	—	950 ± 50	950 ± 50	6000	15	mode	
x=6								
c-axis	300	55	300 ± 40	280 ± 60			9×10^4	—
					ρ_a/ρ_c	ρ_a/ρ_c		
a-axis	70	55	300 ± 40	360 ± 60	4	5	—	
x=8								
c-axis	600	11	80 ± 10	160 ± 20			5×10^4	∞
					ρ_a/ρ_c	ρ_a/ρ_c	no	
a-axis	54	11	80 ± 10	160 ± 20	10	12	mode	
x=9								
c-axis	1200	7	30 ± 5	100 ± 20			4×10^4	∞
					ρ_a/ρ_c	ρ_a/ρ_c	no	
a-axis	40	7	30 ± 5	100 ± 20	30	150	mode	
					ρ_b/ρ_c	ρ_b/ρ_c	no	
b-axis	0.15	—	70 ± 10	70 ± 10	10000	30000	mode	
x=11.5		T_{co}	$\Delta_{\mathrm{L.T.}}$	$\Delta_{\mathrm{H.T.}}$		ρ_i/ρ_j	no	
c-axis	1000	6.5	5	22 -below 50K		L.T.	mode	
					ρ_a/ρ_c	ρ_a/ρ_c	no	
a-axis	100	6.5	5	22 -below 50K	10	50	mode	

Table 5.4: dc transport parameters for $Sr_{14-x}Ca_xCu_{24}O_{41}$ materials, measured in all three directions: room temperature conductivity, CDW transition temperature, CDW activation energy, high temperature insulating phase activation energy, anisotropy at 300K, anisotropy in CDW phase. For comparison LFDS data, *i.e.* the maximum values of dielectric strength, for the c- and a-directions, where the dielectric dispersion was observed, are shown. The ratio of maxima, $\Delta\varepsilon_c/\Delta\varepsilon_a$, can be correlated with the dc anisotropy ρ_a/ρ_c.

5.4.2 ac response $E||c$, $E||a$, $0 \leq x \leq 9$

Fig. 5.15 shows the conductivity spectra in a broad frequency range measured along the ladder rungs, $E||a$, for three representative Ca-contents x=0,3 9. For x=0, 3, as well as for x=6, not shown, a strong temperature dependent relaxation of the dielectric function $\varepsilon(\omega) = \varepsilon$'$+i\varepsilon$" is found, as seen in the insets. Our dc/LFDS data are combined with microwave/FIR data obtained by Stuttgart group, taken from Ref. [161].

Fits by the generalized Debye expression Eq. 5.1 yield the main parameters of this relaxation: the dielectric strength $\Delta\varepsilon = \varepsilon_0 - \varepsilon_{HF} \approx 10^3$, the symmetric broadening of the relaxation-time distribution given by $1-\alpha$, and the central relaxation time τ_0. These fits are shown as solid lines in the Insets of Fig. 5.15. Also, we show the corresponding Cole-Cole plots which relate ε' and ε" components, confirming that the quality of fits, and the reliability of the data, is equal for the results obtained along the ladder rungs and the ladder legs direction, Fig. 5.16.

In Fig. 5.17, for the representative compound x=3, we compare the main parameters from measurements along the ladder legs and along the ladder rungs. Qualitatively similar results were obtained for x=0 and 6. While the dielectric strength along the rungs is an order of magnitude smaller than the one observed along the legs (for x=0, see Fig. 5.16), the thermally activated behaviors are almost identical for both directions, lower panel, Fig. 5.17. The activation energy is similar to that of the dc conductivity in the CDW phase, Table 5.4. The dielectric response sets in below the phase transition temperatures T_c=210 K (x=0), 140 K (x=3), and 55 K (x=6) in the same manner as found along the ladder legs. That is, the dielectric strength $\Delta\varepsilon$ reaches maximum at the same temperatures for both the a- and the c-axis. The width of the relaxation in both directions is similar, $1 - \alpha \approx 0.8$.

These result suggests that the same mechanism, *i.e.* the screening of a CDW phason due to Coulomb interaction [125], is responsible for the ac properties in both directions of $Sr_{14-x}Ca_xCu_{24}O_{41}$, along the ladder legs and along the ladder rungs. For higher Ca content x=8 (not shown here) and x=9 the analogy breaks down since no such dispersion is detected for $E||a$ down to 4.2 K, Fig. 5.15, 5.16.

In the third direction ($E||b$), we find no signature of a CDW-related dielectric response at any Ca-substitution. Two compositions x=0 and 3 have been studied in detail. A completely featureless radio-frequency conductivity is observed, as for $La_ySr_{14-y-x}Ca_xCu_{24}O_{41}$ compounds. Indeed, as in dc, ac measurements show similarity between the transport along the disordered chains of $La_ySr_{14-y-x}Ca_xCu_{24}O_{41}$ materials and the transport perpendicular to the ladder planes in $Sr_{14-x}Ca_xCu_{24}O_{41}$.

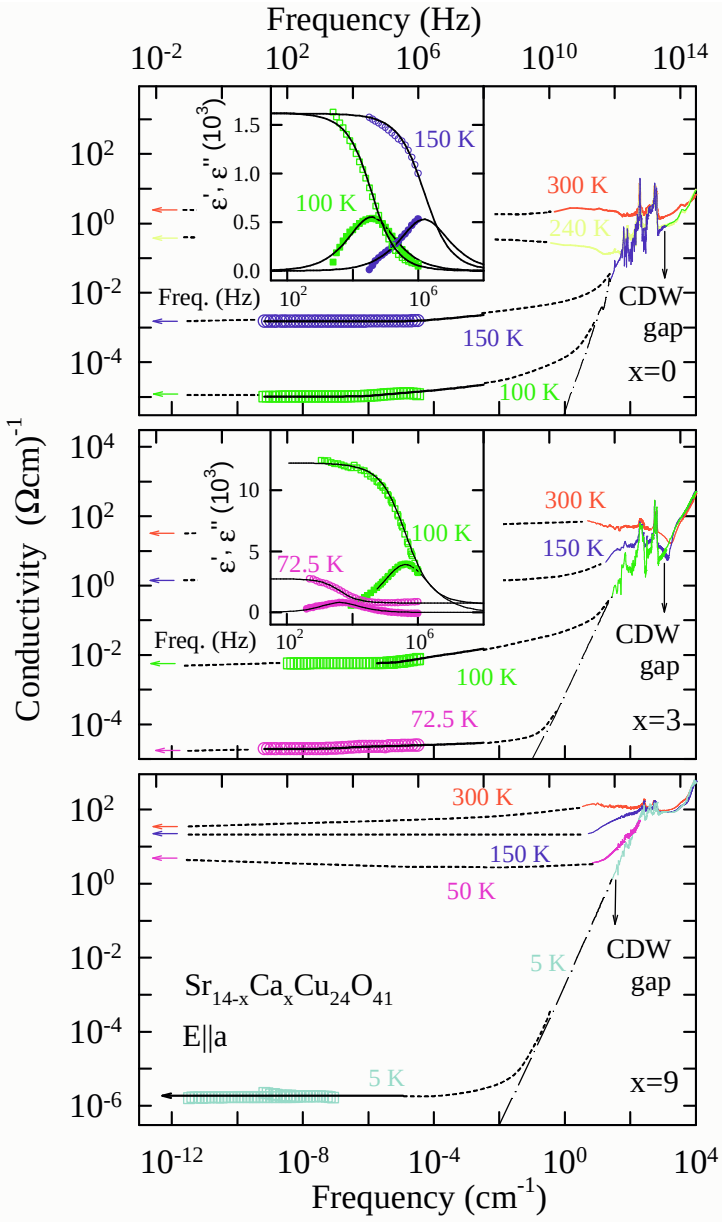

Figure 5.15: Broad-band spectra of conductivity and complex dielectric function (real ε' and imaginary ε" parts) of $Sr_{14-x}Ca_xCu_{24}O_{41}$ along the a crystallographic axis for Ca contents x=0, 3 and 9 at a few selected temperatures. Strong temperature dependent dispersion of ε' and ε" (insets, the full lines are from fits to the generalized Debye expression, Eq. 5.1), seen also as smooth increase in the conductivity spectra, is a fingerprint of the screened CDW collective response. This response is observed at all $T < T_c$ for x=0 and 3, but not for x=9. Decrease of the infrared conductivity at low T corresponds to the opening of an energy gap. At the lowest T only the lowest-frequency phonon tail is seen and represented with the dash-dot ν^2 line. Infrared conductivity data are taken from Ref. [161]. The arrows denote the dc conductivity. Dotted lines are guides to the eye.

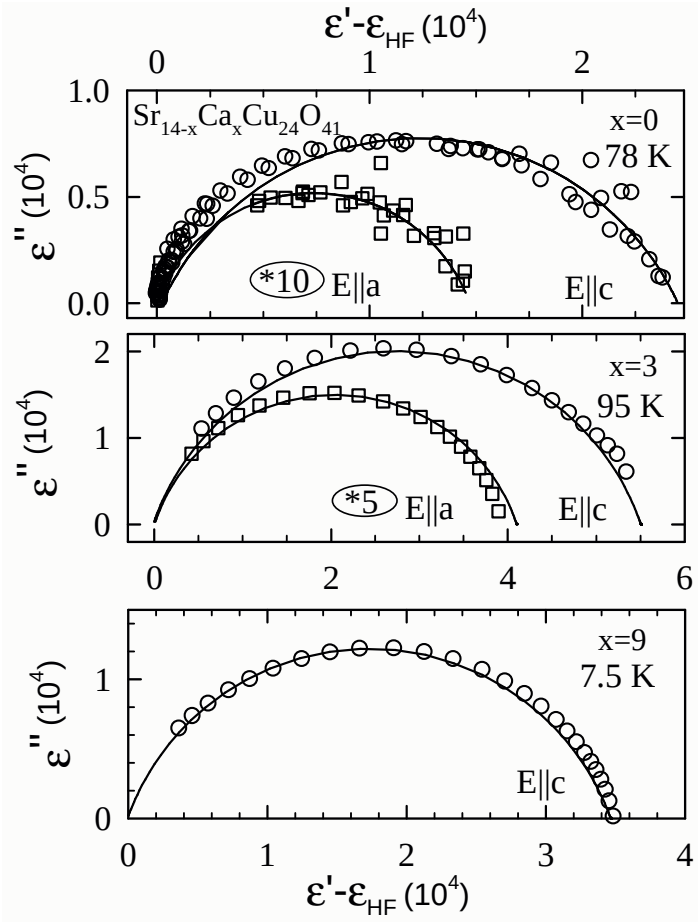

Figure 5.16: Representative Cole-Cole plots of the dielectric dispersion which occurs due to the anisotropic collective CDW response of $Sr_{14-x}Ca_x$-$Cu_{24}O_{41}$ for x=0 (upper panel) and x=3 (middle panel) measured along the ladder legs, $E||c$ and rungs, $E||a$. Note that plots for the response along the a-axis are blown-up 10 (x=0) and 5 (x=3) times. The plot for x=9 is also shown (lower panel). Significantly, no dispersion in the a-direction was observed. Full lines are from fits to the generalized Debye expression, Eq. 5.1. The intersections of the arcs with ε'$-\varepsilon_{HF}$ axes indicate the values of $\Delta\varepsilon$.

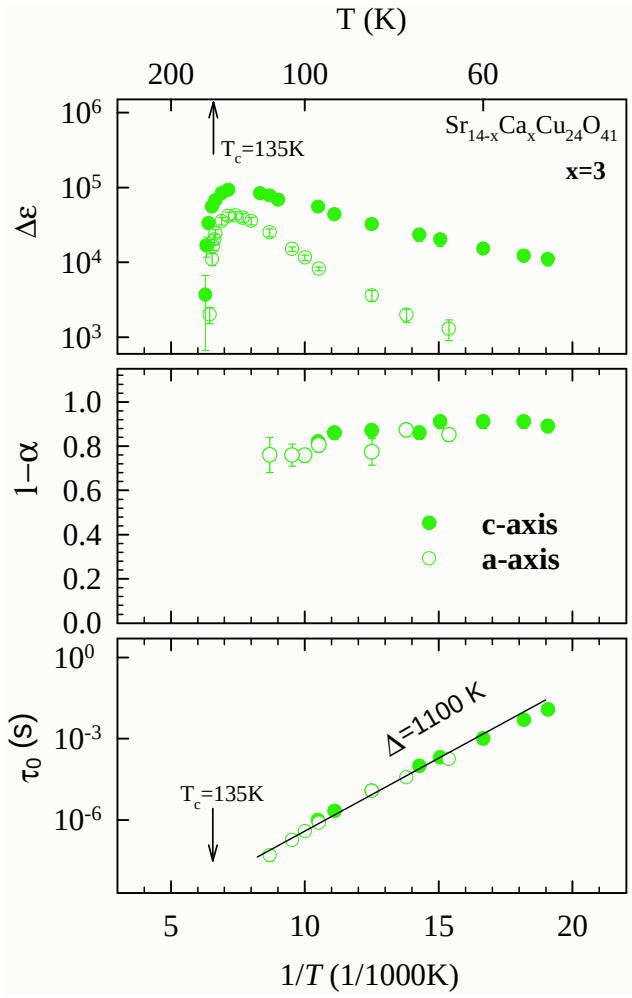

Figure 5.17: Radio-frequency dielectric relaxation parameters for representative compound x=3, obtained for ac field applied along the c- and a-axis. Upper panel: the strength $\Delta\varepsilon$ of the dielectric relaxation. The maximum value of $\Delta\varepsilon$ is found at the same temperature, for both directions. This temperature coincides to T_c determined from a peak in the logarithmic derivative of the dc resistivity, Fig. 5.14. Middle panel: the parameter 1-α which describes the symmetrical broadening of the relaxation times distribution is the same for both directions. Lower panel: the central relaxation time τ_0 is the same for both directions. τ_0 is thermally activated $\tau_0 \propto e^{\Delta_{CDW}/k_BT}$ below T_c, with an activation energy $\Delta_{CDW} \approx 1100$ K equal to dc resistivity activation energy.

In Fig. 5.15, we combine our results with microwave/FIR spectra (in the range 5-10 000 cm^{-1}) taken from Ref. [161]. The energy gap associated with the CDW formation is also seen in the infrared spectra for $E||a$ (arrows in Fig. 5.15), where the conductivity at the lowest frequencies decreases upon cooling. The estimated gap values for different x correspond well to those determined from the activated dc resistivity both for $E||a$ and $E||c$, Table 5.4. The phonon bands become less pronounced for higher Ca contents x due to screening by free carriers. At low T only a ν^2 contribution (Fig. 5.15, dash-dot line) of the low-energy phonon wing is observed.

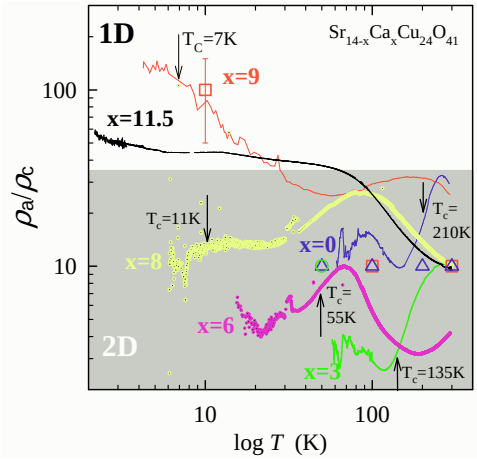

Figure 5.18: Temperature dependence of the conductivity anisotropy σ_c/σ_a of $Sr_{14-x}Ca_xCu_{24}O_{41}$ for different Ca contents x. Lines and symbols stand for dc and ac (FIR range, 50 cm^{-1}) anisotropy, respectively: x=0 (blue line, triangles), x=3 (green line, circles), x=6 (magenta line), x=8 (yellow line), x=9 (red line, squares). The higher and lower anisotropy regimes, denoted as 1D and 2D, are shown in the respective white and grey backgrounds. Anisotropy data may also be found in the Table 5.4

5.4.3 Dimensionality *vs.* x - correspondence of dc and ac results

The conductivity ratio $\sigma_c/\sigma_a = \rho_a/\rho_c$ shown in Fig. 5.18 characterizes the anisotropy of the system within the ladder plane. At all temperatures the anisotropy is of the order of 10 for Ca contents $x \leq 8$, indicating a dimensionality of the ladder subsystem close to 2D, Table 5.4. For x=9 the strong rise of the anisotropy below 40 K, most pronounced in the CDW phase, reveals a cross-over into the 1D regime, which develops for high Ca contents at low temperatures. 1D regime seems to be a low temperature feature, since also for x=11.5, where no CDW is established, the anisotropy is enhanced in the insulating phase at low temperatures. It is also worth noting that the anisotropy in the CDW dielectric strength reflects the dc anisotropy. As shown in Table 5.4, ρ_a/ρ_c values in CDW phase correlate with $\Delta\varepsilon_c/\Delta\varepsilon_a$ for x=0, 3. Also, for x=9 where no mode is observed in the ladder rungs direction ($\frac{\Delta\varepsilon_c}{\Delta\varepsilon_a} = \infty$), ρ_a/ρ_c is very large, as commented above.

5.4.4 Within (c,a) ladder plane CDW develops 2D LRO

In a 1D metal one expects the development of a CDW only along the chain axis. Hence the existence of the loss peak as the signature of the screened phason relaxation in the perpendicular direction (along the ladder rungs) is completely unexpected, [127]. On the other hand, due to interchain coupling the DW nesting vector is $Q(2k_F, \pi/b)$, see Sec. 1.1.3 for the case of $(TMTSF)_2PF_6$. Thus Q^{-1} is not parallel to the chain axis. When the interchain coupling is due to finite overlaps $t_\perp$ (and not to interchain Coulomb interactions - page 74) the charges condensed in the DW have a degree of freedom in the overlap direction. According to this line of reasoning, the DW phason response might occur for an ac electric field applied perpendicular to the chains.

However, until now, the phason screened dielectric relaxation was only observed for ac electric field applied along the best conductivity axis of the quasi-1D compounds. In our best knowledge, so far, there was no attempt to measure it along the less conductivity axes. In $Sr_{14-x}Ca_xCu_{24}O_{41}$ we find that the radio-frequency loss peak centered at τ_0^{-1} decays Arrhenius-like for both directions $E||c$ and $E||a$; these are well established features to characterize the CDW phason screened response, Sec. 2.4. On the other hand, CDW phason pinned mode was not observed for direction $E||a$. We suggest that the pinned mode frequency is raised along a-direction, due to dc-anisotropy. Mode at such raised frequency could not have been observed in the microwave measurements along a-axis, reported by Kitano *et al.* , [162], in which the upper bound of the frequncy window was 100 GHz. Our reasoning is based on Littlewood's model, Sec. 2.4, where τ_0^{-1}, σ_{dc} and pinning frequency Ω_0 are related. Since τ_0^{-1} are the same for both c- and a-directions, we get: $\Omega_0^2(a) = \Omega_0^2(c) \times [\sigma_{dc}(c)/\sigma_{dc}(a)]$. Taking $\Omega_0(c) = 1.8$ cm^{-1} [162] and $\sigma_{dc}(c)/\sigma_{dc}(a) \approx 10$, we calculate the pinning frequency of the CDW along the ladder rungs (a-axis) $\Omega_0(a) \approx 5$ cm^{-1} (=150 GHz).

The dielectric strength of the loss-peak found along the a-axis is about 10 times smaller than the one observed along the c-axis, which corresponds to the single-particle conductivity anisotropy, Table 5.4. Most interestingly, for the x=9 compound the large dc anisotropy, $\sigma_{dc}(c)/\sigma_{dc}(a) \geq 100$, indicates a highly 1D nature at low T when the CDW state is established; in this case the screened phason relaxation is only observed along the c-axis.

In brief, our findings indicate that a CDW in the (c,a)-ladders plane develops 2D long-range order. In addition, based on the observed anisotropic phason-like dispersion we may extrapolate from the standard phason response model in 1D, to a 2D model of phason dispersion.

5.5 Discussion: Competing and coexisting ground states in ladders and chains

5.5.1 Phase diagram for ladders

Fig. 5.19 summarizes our results on the charge transport along the ladders in $Sr_{14-x}Ca_xCu_{24}O_{41}$. We identified a insulator-to-insulator phase transition. The low-temperature phase for all $0 \leq x \leq 9$ was identified to be the charge density wave ground state. A strong decrease of the CDW phase transition temperature T_c and the CDW single-particle gap Δ_{CDW} induced by Ca-substitution is striking. Concomitant broadening of the transition was also observed. The high-temperature (HT) phase features insulating behavior, in opposition with a metallic behavior normally observed above standard DW transitions. The HT phase activation energy, $\Delta_{\mathrm{H.T.}}$, is smaller or comparable to Δ_{CDW} for $x \lesssim 6$. For higher Ca-contents the HT phase shows 2-3 times larger activation energy than CDW. Also, HT insulating phase persists at Ca-substitution levels, x=11.5, but only below 80 K, while CDW is suppressed already for x>9. The insulating behavior for $10 \leq x \leq 13.6$ can be suppressed under pressure. The applied pressure of 3-6 GPa, recovers metallic behavior, and superconductivity sets in at low temperature. Superconducting transition temperature T_{SC} reaches a maximum value of 12 K under pressure of 4 GPa, [69, 106, 107]. It is useful to note that for $x = 0$ pressure of 6.5 GPa removes the CDW phase and suppresses insulating HT phase. However, no superconductivity is observed down to lowest temperatures, [106].

Fig. 5.19 also corelates our results with the results for gapped spin-liquid ground state in the ladders. While CDW-gap is strongly suppressed with Ca-substitution, spin-gap persists almost unchanged (30 meV) up to Ca-content x=12. The CDW phase transition temperature T_c, coincides only for x=0,3 with the crossover temperature T^*, which separates the high temperature paramagnetic regime from the spin-liquid ground state. The NMR results by Piskunov *et al.* , [104], indicate that the spin-gap is opened for x=12 below 100 K. This result implies that T^* line deviates from T_c behavior for $x > 2$ and remains at about 100 K for all x up to ~ 12.

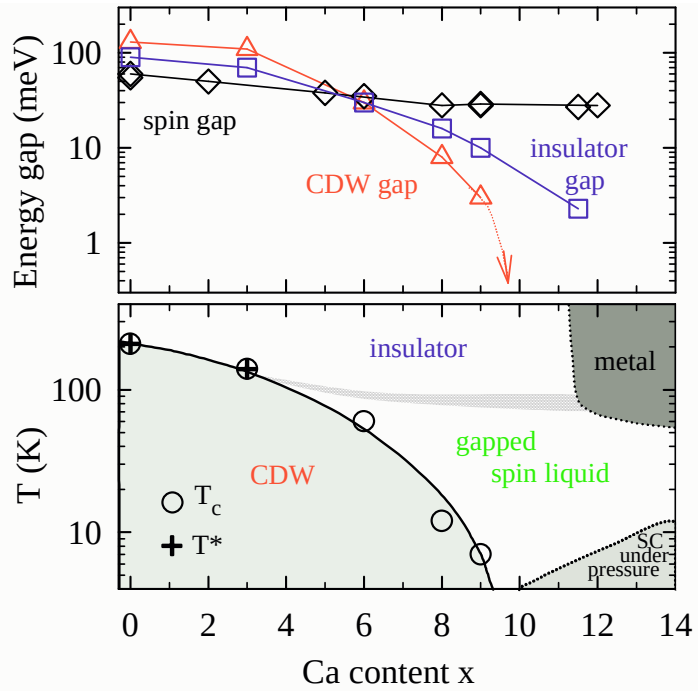

Figure 5.19: Upper panel: Dependences of the energy scales in the ladders of $Sr_{14-x}Ca_xCu_{24}O_{41}$ on the calcium content. CDW gap Δ_{CDW} (triangles) is the largest scale at low contents, $x < 6$. The spin gap (diamonds) in the ladders, $\Delta_{spin}^{ladders}$, is also shown (data from Fig. 1.29). It can be considered Ca-content independent (Sec. 1.2.6). The high temperature phase features insulating behavior with well defined activation energy $\Delta_{H.T.}$, squares. Lower panel: Qualitative phase diagram for $Sr_{14-x}Ca_xCu_{24}O_{41}$ as a function of Ca-content. The CDW phase is determined by the CDW critical temperature T_c (open circles), which coincides with the paramagnetic – spin-gapped phase crossover-temperature T^* (crosses) [96, 178] for x=0, 3. As the spin-gap persists unchanged up to x=12, T^* is also not significantly suppressed, as denoted by a broad diffuse line [104]. Above 50 K and for $x > 11$ HT phase features metallic behavior [84]. Superconducting phase appears for $10 \leq x \leq 13.6$, below 12 K, under pressures above 3 GPa [106].

5.5.2 Origin of HT insulating phase and CDW ground state and mechanism that governs their suppression

In the following, we first address the issue of origin of HT insulating phase. We assume the existence of a conducting band for the holes residing in ladders, so Fermi wave vector $2k_F$ can be defined. Within the description of Zhang-Rice singlet we find that hybridization between O2p and Cu3d levels allows for derivation of a single-band effective Hamiltonian, [74]. Within this model a given site, *i.e.* a CuO_4 square, may either contain an unpaired electron with spin 1/2 (which resides on the Cu^{2+} ion) or the site may be empty when the Zhang-Rice singlet forms (a hole within the O2p orbitals of the square is strongly bound to Cu^{2+} ion, due to hybridization). No double occupancy is allowed. In the present case for ladders, we note that hole number is very low, 1 hole per 7 rungs. Thus, the ladder band is very close to half-filling, $f = 1/2$, with one unpaired spin 1/2 electron at almost every site. In the case of $Sr_{14-x}Ca_xCu_{24}O_{41}$, $2k_F = 2\pi f/c_L$, where $c_L = 3.9\mathring{A}$ is the ladder lattice parameter. We get $1/k_F \approx 2.5\mathring{A}$.

In the Drude model the mean free path Λ for the ladders is calculated from the RT conductivity:

$$\sigma = \frac{4e^2}{h}\frac{z}{ab}\Lambda$$

where a and b are the other two lattice parameters and $z = 4$ is the number of ladders per unit cell cross-section, ab. We get $\Lambda \approx 1\mathring{A}$.

Ioffe and Regel, [182], argued that as the extent of disorder increases in a metallic system, there was a limit to metallic behavior; when the quasiparticle mean free path Λ becomes less than its de Broglie wavelength $2\pi/k_F$, coherent metallic transport would not be possible. Thus, the Ioffe- Regel criterion for occurence of insulating behavior is

$$k_F\Lambda < 2\pi$$

Based on the Ioffe-Regel criterion, Mott proposed that a metal-insulator (M-I) transition must occur when the disorder is sufficiently large that Ioffe-Regel criterion is satisfied. In recognition of Anderson's early work on disorder induced localization, Mott called this M-I transition the "Anderson transition". In other words, a system of noninteracting electrons turns into an Anderson localized insulator, as increasing disorder causes the localization of the Bloch wave functions, [181].

In cuprate ladders, at RT, $\Lambda \approx 1\mathring{A}$ is quite smaller than $2\pi/k_F \approx 15\mathring{A}$. This certainly indicates that insulating behavior of cuprate ladders might be,

at least partially, attributed to Anderson localization. However, an Anderson insulator is not expected to cross-over to metallic state under pressure - contrary to what is observed in ladders. We note that organic 1D materials like $(TMTSF)_2PF_6$ also feature $k_F\Lambda < 2\pi$. However, unlike insulating cuprate ladders discussed here, these organics show metallic conductivity even at highest temperatures. They belong to so-called bad metals, which besides having a "too short" mean free path also fail to exhibit resistivity saturation, [183].

On the other hand, in a clean 1D metallic system, at half-filling $f = \frac{1}{2}$, as the electron interaction U is switched on, a gap arises in the energy spectrum and the system turns into a Mott or charge-ordered insulator, [180]. Since the band-filling in the cuprate ladders is close $f = \frac{1}{2}$ and the on-site Coulomb repulsion is $U = 3{-}4eV$ ($U/4t > 1$), Mott localization seems to be a plausible origin of the insulating phase at high T, as well as of CDW ground state.

A word is in order on the equivalency of Ca-substitution and pressure effects on the lattice parameters of $Sr_{14-x}Ca_xCu_{24}O_{41}$, [70, 71, 179]. The inter-layer lattice parameter b is the most susceptible, at room temperature it decreases for 6-8 %, either by Ca-substitution from x=0 to x=13, or under 8 GPa for x=0. Corresponding changes of the intra-layer ladder parameters a and c are small, $\approx 1\%$. Importantly, this also shows that the dimensionality of the ladder subsystem does not change, in accord with our electrical transport anisotropy data at high temperature.

We can now address the issue of mechanism which might govern the suppression of the HT insulating phase and CDW ground state. Firstly, the hole transfer increases upon Ca-substitution, [76, 75]. Presumably it increases also under pressure, as the pressure and Ca-substitution influence the crystallographic parameters in the same manner. Higher hole count in the ladders increases the deviation from half-filling and moves the system towards metallic state. Secondly, the Ca-substitution or pressure decrease the ladder parameters a and c, and correspondingly increase wave-function overlaps in the ladder plane. Consequently, localization might be also removed by decreasing $U/4t$.

As for the CDW suppression, we first point out that the worsened nesting induced by Ca-substitution can not cause the CDW suppression since the anisotropy in the ladder plane does not change. Therefore, we can apply similar arguments to discuss the suppression of CDW. CDW phase is clearly less robust than HT phase since Ca-substitution $x > 9$ is enough to suppress it fully. In analogy with HT phase, we consider for CDW phase suppression the effects of band-filling deviation and of increase of overlaps in the ladder plane (*i.e.* decrease of $U/4t$). In addition, a decrease of the b-parameter might be expected to influence the inter-site Coulomb repulsion V. These

effects must come into play together with the influence of disorder.

A rapid CDW suppression might be attributed to a disorder introduced by Ca-substitution at Sr sites, which is indicated by broadening of the CDW phase transition with Ca-substitution. We remind that, at microscopic scale, strong local distortions of the ladders due to irregular coordination of Sr^{2+} and Ca^{2+} ions [70, 71] occur by Ca-substitution. Also, reducing the b parameter increases disorder in the ladder layer through increased coupling with the chain layer.

We also note the work of Tsuchiizu and Suzumura, [120] where the suppression of CDW (and the appearance of SC phase) was parametrized by the decrease in the ratio of intersite (nearest-neighbor) V and on-site U interactions within the extended Hubbard model for the doped ladder. Their results for the ladders also correspond to the results for a 1D chain where also a decrease in V/U ratio induces transition from CDW to SC phase, [80]. Also, they relate V with band-filling deviation (hole transfer).

5.5.3 Correspondence of phase diagrams of ladders and chains

To emphasize the influence of coupling between the subsystems we construct the phase diagram for ladders and the phase diagram for chains in $Sr_{14-x}Ca_x$-$Cu_{24}O_{41}$, Fig. 5.20. These phase diagrams feature a high degree of correlation between the two subsystems. Both 2D CDW long-range order in the ladders and 2D charge-order (CO) in the chains crosses over to a short range order for $x \gtrsim 6$. The latter persists shortly and fully vanishes for $x \gtrsim 11$. Complexity is added through the features of the spin-sector. AF dimer pattern (AFD) in the chains is intimately related to the CO and shows the same x dependence. For high Ca-contents, *i.e.* $x \gtrsim 11$, it is replaced by antiferromagnetic (AF) order at low temperatures. In contrast, the gapped spin-liquid ground state in the ladders is more robust and persists up to $x = 13.6$. Moreover, it remains finite even when SC state is established under pressure. It is not known if AF order in the chains persists under pressure when SC is established in the ladders. This possibility poses the question of concepts, which may result from the coexistence of superconductivity and magnetism, but in different subsystems of a composite material.

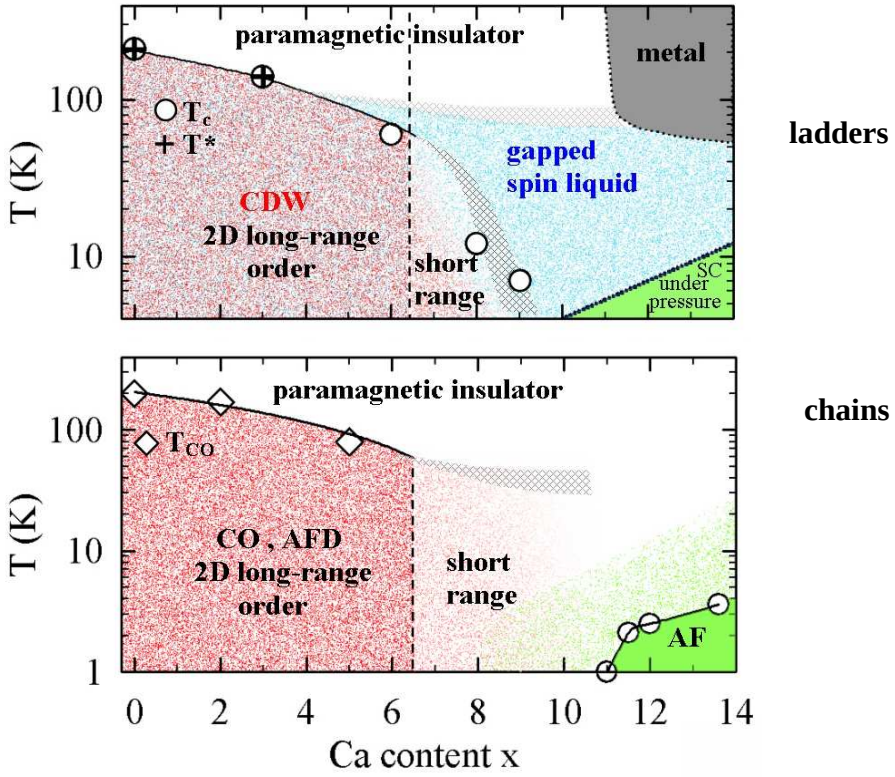

Figure 5.20: The correspondence between the phase diagrams for ladders and chains is emphasized. The diagrams present the data for both charge and spin sector. Upper panel (ladders): charge-density wave 2D LRO is established below T_c, circles. The crossover from the LRO to short range order is denoted by phasing out of the red background. The gapped spin liquid (blue background) exists below T^* denoted by crosses and also by a broad diffuse line. It persist even for x, where superconductivity is established under pressure (green). Lower panel (chains): The crossover to a 2D ordering at the same T_{co} for the charge and spin-sectors is due to complementarity between the arrangement of the spins and holes in the chains. Destruction of LRO is again denoted by dephasing the red background. AF dimer pattern is replaced by an AF long-range order for $x > 11$ (green).

5.5.4 Nature of CDW ground state in ladders

Our result that a phason-like dispersion (seen as broad screened relaxation modes) exists along both the rungs and legs of ladders indicates that the ground state in the ladders of $Sr_{14-x}Ca_xCu_{24}O_{41}$ is not of the standard CDW type. The collective excitations of this charge order are similar to a long wave excitation of CDW phason. However, further experiments have to clarify whether such a (anisotropic) dispersion is a unique feature of the charge order in ladders or whether it is common to quasi-2D systems with charge order. While in principle we do not see a reason why a CDW formed in a system of coupled chains would not respond in perpendicular direction, this question deserves a more elaborate theoretical consideration.

Further, $Sr_{14-x}Ca_xCu_{24}O_{41}$ ladders are, as expected for cuprate materials, a strongly coupled system. Indeed, experimental observations suggest that strong electron-electron interaction gives rise to a Mott-localized high temperature phase. In the same manner, the ground state might be the charge ordered state of partially localized charges. That is, CDW in the ladders might fall between the two well defined limits of charge order: the CDW order of itinerant charges and the charge order of localized charges. However, as stated above the collective excitations are similar to CDW and even the condensate effective mass $m^* \approx 100$ is within the range of values (although in the lower limit) for a standard CDW with non-negligible electron-phonon coupling.

Discussing the nature of the broken symmetry ground states in a 1D half-filled band with arbitrarily long-range Coulomb interaction Mazumdar and Campbell [121] started by pointing out that nesting arguments should not be applied since there is no single-particle (band) picture for nonzero correlations. Still, they obtained inequalities based on the arbitrarily strong Coulomb parameters, which defined the parameter space for the existence of broken symmetry states. One of these inequalities leads to, and is consistent with, the CDW/SDW boundary obtained in the continuum limit (valid for weak coupling) of the extended Hubbard model. Exactly at this boundary, using weak coupling approach (g-ology) Tsuchiizu *et al.* , [120] have shown that a bond-CDW (BCDW) phase exists in between CDW and SDW. Using the same approach they also investigated the doped two-leg Hubbard ladder and provided a qualitative phase diagram where a BCDW (p-wave: angular momentum $l = 1$) coexists with CDW (s-wave: angular momentum $l = 0$) for strong nearest-neighbor repulsion and gives way to d-wave-like SC. This phase diagram is highly similar with the experimental phase diagram of cuprate ladders. Study by Schollwöck *et al.* , [184] of a doped two-leg ladder used the approach applicable for arbitrary interaction strength. They

obtained a ground state for the ladder where CDW coexists with a d-wave-like density wave (angular momentum $l = 2$). The ground state in the ladders might be the one of these exotic charge-ordered phases. However, there is no theoretical prediction about collective excitations in such a phase and how they should respond to applied dc and ac fields.

It is useful to compare experimental results for a material where the CO, occuring due to localization and strong coupling is well documented, with those for $Sr_{14-x}Ca_xCu_{24}O_{41}$ ladders. One example is the charge order associated with a $4k_F$ CDW - Wigner crystal ground state due to electron-electron interactions, established in the q1D material, Fabre salt $TMTTF_2AsF_6$ [185]. A fingerprint of CO: a charge disproportionation was detected in NMR measurements by Chow *et al.* , [186]. In contrast to that, no signature of charge disproportionation has been detected in NMR measurements in the ladders of $Sr_{14-x}Ca_xCu_{24}O_{41}$, Fig. 1.27, [98].

The CO transition in $TMTTF_2AsF_6$ was also detected from a divergence in the dielectric strength at T_{co}. The results for $TMTTF_2AsF_6$, Fig. 5.21, show no temperature dependence in the position of the peak of the $\varepsilon'(\omega)$. This indicates a temperature-independent central relaxation time. Thus, such a relaxation can not be due to CDW phason response, but it could be related to short-wavelength excitations of CDW, like solitons, or charged-domain walls, [143]. On the contrary, ac field response of the ladders shows the central relaxation time thermally activated in the same manner as the dc conductivity.

We also compare, $1/\varepsilon'$, the inverse of the real part of the dielectric function for $TMTTF_2AsF_6$ and for ladders of $Sr_{14-x}Ca_xCu_{24}O_{41}$, x=3, measured in the c- and a-directions. It was observed for $TMTTF_2AsF_6$ that $1/\varepsilon'$ in the vicinity of T_c follows the Curie law $1/\varepsilon' \propto 1/|T_{co} - T|$. On the contrary, $1/\varepsilon'$ in the ladders does not show the same behavior, Fig. 5.22.

Therefore, we conclude that ground state established in the ladders of $Sr_{14-x}Ca_xCu_{24}O_{41}$ is not similar to the well documented charge-order observed in $TMTTF_2AsF_6$.

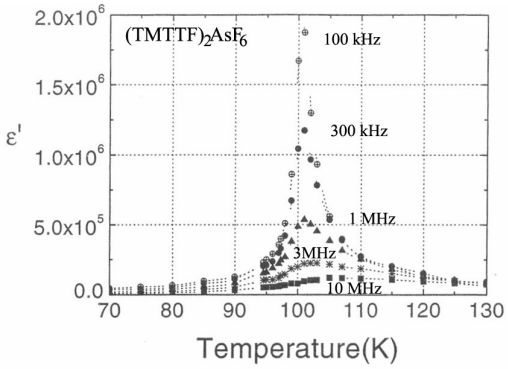

Figure 5.21: Temperature dependence of the real part of the dielectric function for $TMTTF_2AsF_6$ at various frequencies. From Ref. [185].

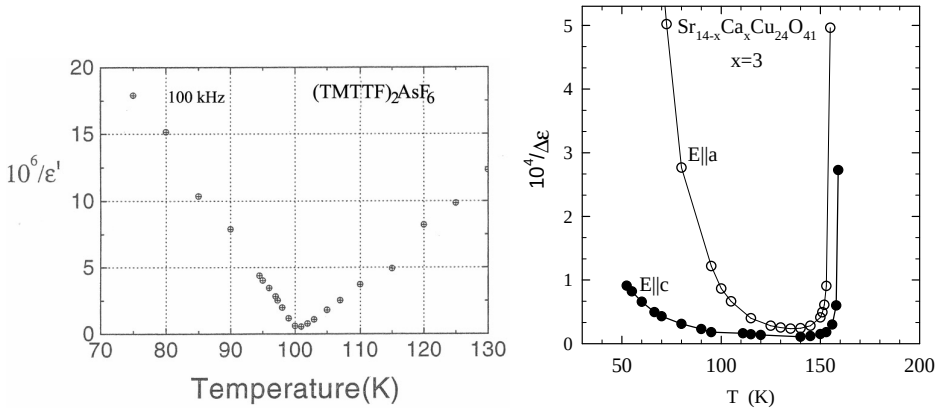

Figure 5.22: Temperature dependence of the inverse of the real part of the dielectric function for $TMTTF_2AsF_6$ (left panel, from Ref. [185]) and $Sr_{14-x}Ca_xCu_{24}O_{41}$, x=3, c- and a-directions, measured at 100 kHz (right panel).

5.5.5 Superconductivity in ladders

Finally, we address briefly the SC ground-state established for $10 \leq x \leq 13.6$ and under high pressure, 3-6 GPa, below 12 K. We discuss this SC ground state in relation to Dagotto's model for superconductivity in ladders. In this model, singlet pairing interaction in the ladder rung acquired the role of renormalized, attractive U_{eff} for the ladder projected onto a 1D chain. In other words - the spin-gap has still to be observed in the metallic state just above SC transition - as, indeed, is the case, [104, 108]. In this line of reasoning the absence of SC, while the spin-gap is observed when x=0 is rendered metallic under pressure, is intriguing. The observation of low-lying spin-excitations within the spin-gap for x=12, under pressure where SC sets in, and the absence of these for x=0 resolves the issue. However, this indicates that SC arises only when a large enough density of carriers appears at the Fermi level, which contradicts Dagotto's model. Observation of Hebel-Slichter peak, [108], in NMR spin-lattice relaxation rate at T_{SC} also indicates that a finite gap exists in the quasiparticle excitation for all wave vectors (directions). This s-wave-like character also contradicts d-wave-like SC suggested by Dagotto. Fujiwara *et al.* suggest that SC state is not established by hole-pairing on the same rung, but on the neighboring ones.

In the end of the exposition of our results and the respective discussions, we note that the nature of charge-density wave is intricately related with the nature of superconductivity in $Sr_{14-x}Ca_xCu_{24}O_{41}$ compounds. Whether these ground states are unconventional and of non-s-wave symmetry, as theoretically expected, is not clear yet. Further research is needed to clarify these issues.

6 Summary and Concluding Remarks

This study of quasi-one-dimensional materials has concentrated on understanding and improving the experimental phase diagrams. Especially, the competition and/or coexistence of superconductivity and density-wave phases was addressed by studying the charge transport properties. q1D materials from two different families were studied: single chain $(TMTSF)_2PF_6$, from the family of organic Bechgaard-Fabre charge-transfer salts and (La, Sr, Ca)$_{14}Cu_{24}O_{41}$, composite chain/ladder cuprates. While research interest in the q1D cuprates is relatively new, the research on Bechgaard-Fabre salts continues for the last 25 years. In the generic phase diagram of Bechgaard-Fabre salts there are still univestigated regions and thus they may still be regarded as new materials. Also, any work on other q1D materials is much more instructive if it is compared to the results obtained on the representative compound of the family, $(TMTSF)_2PF_6$.

A detailed study of dc resistivity and superconducting critical currents in the high pressure region (6.8-11 kbar) of $(TMTSF)_2PF_6$ phase diagram was performed, with a control of the pressure which could not be achieved in the early studies. A narrow pressure region, 8.65 - 9.43 kbar, was determined where SDW/metal and SDW/SC coexisted. That is, below metal-to-SDW transition parts of the sample remained metallic. Eventually, when the temperature is lowered below 1.2 K the metallic parts undergo metal-to-SC transition. The volume proportion, c (vol%) of the metallic (and/or SC phase) was increasing with pressure in the coexistence region. At a given pressure, two estimates for c (vol%) were obtained. The nonlinear correlation of the estimates indicated two different regimes. In the higher inhomogeneous region (9.1–9.43 kbar), domains (or percolated paths) span the length of sample. In the lower inhomogeneous region (8.65–9.1 kbar) Josephson junctions (or phase slip centers) are present along the conducting channels in the SDW/SC region. Similar coexistence phenomena were recently observed in other members of $(TM)_2X$ family, as well as in the layered organic κ-$(BEDT\text{-}TTF)_2X$

compounds.

A very simple coexistence model was proposed, based on a variational theory calculation. It indicated that it is possible to find an inhomogenous phase with a free energy which is lower than the energy of the homogenous phases (SDW or metal). It explains fairly well our experimental findings. On the other hand, some other, microscopic models, explain our results only qualitatively.

For q1D cuprates the strong coupling limit applies, on the contrary to $(TMTSF)_2PF_6$, where the weak-coupling is appropriate. When discussing the competition/coexistence of DW and SC in the q1D cuprates of the formula $A_{14}Cu_{24}O_{41}$ (A=Sr, Ca, La, Y...) phase diagram, the theoretical approach is more difficult and not well developed. Two families were investigated, $Sr_{14-x}Ca_xCu_{24}O_{41}$ materials where exist 6 holes per formula unit, one out of which resides in the ladders for $x = 0$ material, while Ca-substitution increases this hole count slightly. We also studied $La_ySr_{14-y-x}Ca_xCu_{24}O_{41}$ materials, where exist $6 - y$ holes, all residing in the chains.

We have shown the dc and ac charge transport in the chains of $La_ySr_{14-y-x}Ca_xCu_{24}O_{41}$ is due to hopping of holes. While the chain subsystem in $La_ySr_{14-y-x}Ca_xCu_{24}O_{41}$ materials behaves as a one-dimensional disorder-driven insulator, a 2D charge-order occurs in the chain subsystem of $Sr_{14-x}Ca_xCu_{24}O_{41}$ ($T^* = 200$ K for x=0). This charge-order is intimately related to the spin-ordering according to AF dimers (AFD) pattern, showing the same T^* *vs.* x dependence. 2D CO and AFD pattern in the chains cross over to a short range order for $x \gtrsim 6$. For $x \gtrsim 11$, AFD pattern is replaced by AF order at low temperatures.

On the other hand, in $Sr_{14-x}Ca_xCu_{24}O_{41}$, holes transferred to the ladders are mobile and responsible for the electrical transport. This is strongly supported by the observation that RT resistivity of $La_ySr_{14-y-x}Ca_xCu_{24}O_{41}$ materials, where transport occurs in the chains, is at least three orders of magnitude larger than for $Sr_{14-x}Ca_xCu_{24}O_{41}$.

The way how the transport switches from the chains in La-substituted to the ladders in La-free materials, is still an open issue. Is there a phase transition and how the phase diagram of the former merges with the one of the latter should be resolved by further experiments on materials with very low La content, in the hole count $\lesssim 6$ range.

The studies of charge transport in $Sr_{14-x}Ca_xCu_{24}O_{41}$ were performed for x=0, 3, 6, 8, 9, 11.5. For the parent compound, $Sr_{14}Cu_{24}O_{41}$, in dc resistivity an insulator-to-insulator transition at $T_c = 210$ K was observed. The low temperature insulating phase was identified as charge density wave (CDW) with CDW single-particle gap $\Delta_{CDW} = 1300$ K. That is, the fingerprints of CDW phason response to ac electric fields, which is a collective relaxation

mechanism, were observed. As the first, a narrow phason mode, *pinned* mode, was previously found in the microwave frequency range. As the second, by low-frequency dielectric spectroscopy (LFDS) we observed a broad thermally activated mode in radio-frequency range. From these results we estimated CDW condensate mass to be $m^* \approx 100$, a value which is within the range reported for standard CDW materials. Quasi-coherent microwave and FIR measurements also corresponded with the identification of CDW phase.

However, dc electric field dependent, sliding conductivity was not observed in our study of CDW phase in $Sr_{14}Cu_{24}O_{41}$. On the contrary, independent groups reported different observations of nonlinear conductivity. We suggest that this apparent contradiction might be due to different quality of studied single crystals. In our study, it might be that, due to too low electric fields applied, CDW sliding was not detected. This uncertainty could be resolved by further experiments on samples from different batches.

Further, the dc and ac transport anisotropy study within the ladder (c,a) plane of $Sr_{14}Cu_{24}O_{41}$ showed a set of properties similar for both directions. The phase transition temperatures T_c, when measured along the c-axis and a-axis, are equal in value and the same holds for the Δ_{CDW}. The ac properties in both ladder plane directions correspond to the CDW phason response. Along the perpendicular, b-direction, a distinct behavior with different activation energies, and no phase transition, is registered. In addition, no signature was found of a CDW-related dielectric response. This indicates that the charge transport perpendicular to the ladder planes probably happens via nearest-neighbor hopping, as expected between disordered chains.

For $Sr_{14-x}Ca_xCu_{24}O_{41}$, $0 < x \leq 9$, a strong decrease with Ca-substitution, of the CDW phase transition temperature, with concomitant transtion broadening, and the CDW single-particle gap, was observed (for x=9, T_c=7 K, $\Delta_{\mathrm{CDW}} = 30$ K). For x=11.5 no ordering was found. As well as for the parent compound x=0, the anisotropy study of dc and ac transport for $0 < x \leq 9$ showed a set of properties similar for both ladder plane directions. Only for x=8,9 the CDW phason relaxation was not detected for $E||a$ down to 4.2 K. Again, as for x=0, the transport in the perpendicular direction ($E||b$), was of a distinctive, presumably hopping character. The (c,a) plane anisotropy in the CDW dielectric strength reflected the dc anisotropy, as ρ_a/ρ_c values in CDW phase correlate with $\Delta\varepsilon_c/\Delta\varepsilon_a$ for x=0, 3. For x=9 where no mode is observed in the ladder rungs direction ($\frac{\Delta\varepsilon_c}{\Delta\varepsilon_a} = \infty$), $\rho_a/\rho_c = 150$ is very large only in the low temperature region, indicating a highly 1D nature.

The dc and ac transport anisotropy results imply that CDW develops in the (c,a)-ladders plane with a 2D long-range order (LRO), which crosses over to a short range order for $x \geq 6$. We note, that at the same Ca-substitution levels, the CO in the chains changes over from 2D LRO to a short range

one. For $x \leq 11.5$, both CDW and CO disappear from the respective phase diagram. Such a correlated behavior stresses an interplay between the ladders and the chains.

The high temperature (HT) phase, existing above the CDW phase, is characteristic for the insulating behavior occuring in spite of high RT conductivity ($\approx$500 S/cm, very similar to those of metallic $(TMTSF)_2PF_6$). The insulating HT phase persists up to x=11.5-12, while the CDW is suppressed already for $x > 9$. The HT phase activation energy, $\Delta_{H.T.}$, is smaller or comparable to Δ_{CDW} for $x \lesssim 6$. For higher Ca-contents the HT phase shows 2-3 times larger activation energy than CDW.

Complexity is added in the description of the ladders through the features of the spin-sector. The ground state of the ladders is a gapped spin-liquid. The spin-gap ($\Delta_{spin}^{ladders} = 350$ K) is almost independent of Ca-substitution and persists for x=12, unlike the CDW gap. The magnitudes of the two gaps are very different: for x=0, $\Delta_{spin}^{ladders}$ is 2-3 times smaller than the CDW gap, while for x=9, the spin-gap is an order of magnitude larger.

Above 3 GPa in $Sr_{14-x}Ca_xCu_{24}O_{41}$, $10 \leq x \leq 13.6$, the pressure suppresses the insulating HT phase, recovering metallic behavior before superconductivity is established. The spin-gap is not removed by the application of pressure, at least up to 3.5 GPa. Surprisingly, the low-lying spin excitations are observed within the spin-gap. These observations raise the question on the nature of SC phase. Apparently, the SC posseses an s-wave character, in the meaning that a finite gap exists in the quasiparticle excitations. On the other hand, theoretical considerations suggested d-wave symmetry, although the lack of rotational symmetry of the ladders prevents an exact symmetry classification.

It is not known whether AF order in the chains for $x > 11$ persists under pressure when SC is established in the ladders. This possibility raises the question about concepts, which may stem from the coexistence of superconductivity and magnetism, but in the different subsystems of a composite material.

Finally, the origin of the HT insulating phase and CDW ground state in the ladders and the mechanism for their suppression is given. As the HT insulating phase is suppressed under pressure, and metallic behavior recovered, Anderson localization is excluded as the main origin of the insulating behavior. Since the band-filling in the cuprate ladders is close to $f = \frac{1}{2}$ and the on-site Coulomb repulsion is $U = 3 - 4eV$ ($U/4t > 1$), Mott localization seems to be a plausible origin of the HT insulating phase. This phase is removed under Ca-substitution/pressure either by the deviation from half-filling (which might be induced by even slight hole transfer into the ladders) or by an increase in intraladder overlap integrals, when $U/4t$ decreases. We

note here the equivalency of Ca-substitution and pressure effects. As the anisotropy in the ladder plane is not affected by Ca-substitution/pressure, the worsened nesting can not cause the CDW ground state suppression. Still, CDW phase is clearly less robust and, while similar arguments as for HT phase, can be applied for CDW suppression, the influence of disorder must also come into play. Disorder in the ladders is introduced by Ca-substitution at Sr-sites, but also by an increase in coupling with the chain layer. The latter changes the intersite Coulomb repulsion V, which might also influence the stability of the CDW phase.

Our observation of anisotropic CDW phason-like response in the ladder, and the fact that the cuprates are a strongly coupled system indicated that the CDW ground state in the ladders is not of the standard type. In particular, more work is needed to clarify, whether the anisotropic phason-like dispersion is a unique feature of the charge order in the ladders, or whether it is common to quasi-2D systems with charge order. CDW in the ladders might fall between the two well defined limits of charge order: the CDW order of itinerant charges and the charge order of localized charges. The ground state in the ladders might be the one of the exotic charge-ordered phases, characterized by non-s-wave like pairing. However, there is no theoretical prediction about collective excitations in such phases and how they should respond to applied dc and ac fields.

In the end, the nature and the suppression of charge-density wave in the ladder planes is intertwined with the scenario for superconductivity in the ladders of $Sr_{14-x}Ca_xCu_{24}O_{41}$ compounds. The question remains whether these states are unconventional and further research is needed to clarify these issues.

7 Kolektivna elektronska stanja novih kvazijednodimenzionalnih materijala

S.1 Kvazi1D Bechgaardova sol $(TMTSF)_2PF_6$ - još uvijek novi materijal

Zajednička karakteristika mnogih jako koreliranih elektronskih sustava jest blizina supravodljive faze, SV, nekoj vrsti magnetski uređenog izolatorskog stanja. Ta stanja su ili antiferomagnetsko, AF, ili stanje vala gustoće spina, VGS. Primjeri uključuju niskodimenzionalne organske materijale [1, 2], teške fermione [3], i slojne kupratne visokotemperaturne supravodiče (HTSC), [4]. Posebno je kod organskih materijala ubrzo uočeno da teškoće u opisivanju tih susjednih faza moguće proizlaze iz njihove međusobne interakcije, [5]. Može se postaviti pitanje je li se bliske faze podupiru ili natječu, Sl. S.1.

Kvazijednodimenzionalni organski supravodiči, Bechgaard-Fabre soli, su ponajbolje karakterizirani sistem koji pokazuje koegzistenciju SV i VGS faza. Ta porodica spojeva karakterizirana je generaliziranim faznim dijagramom, Sl. S.1. Primjena tlaka stabilizira neko od stanja koja se na dijagramu nalaze desno od položaja pojedinog materijala. Prototipni i najviše studirani materijal $(TMTSF)_2PF_6$ ima idealan položaj u faznom dijagramu za proučavanje prijelaza iz VGS u SV stanje, [10, 17, 19, 20]. Općenito, $(TMTSF)_2PF_6$ posjeduje bogat fazni dijagram te je stoga i dalje predmet istraživanja, [11, 12, 16, 17, 18]. U svakom radu na kvazi 1D materijalima, pa i za ovu Tezu, vrlo je instruktivno uspoređivanje s rezultatima za prototipnu Bechgaardovu sol, $(TMTSF)_2PF_6$.

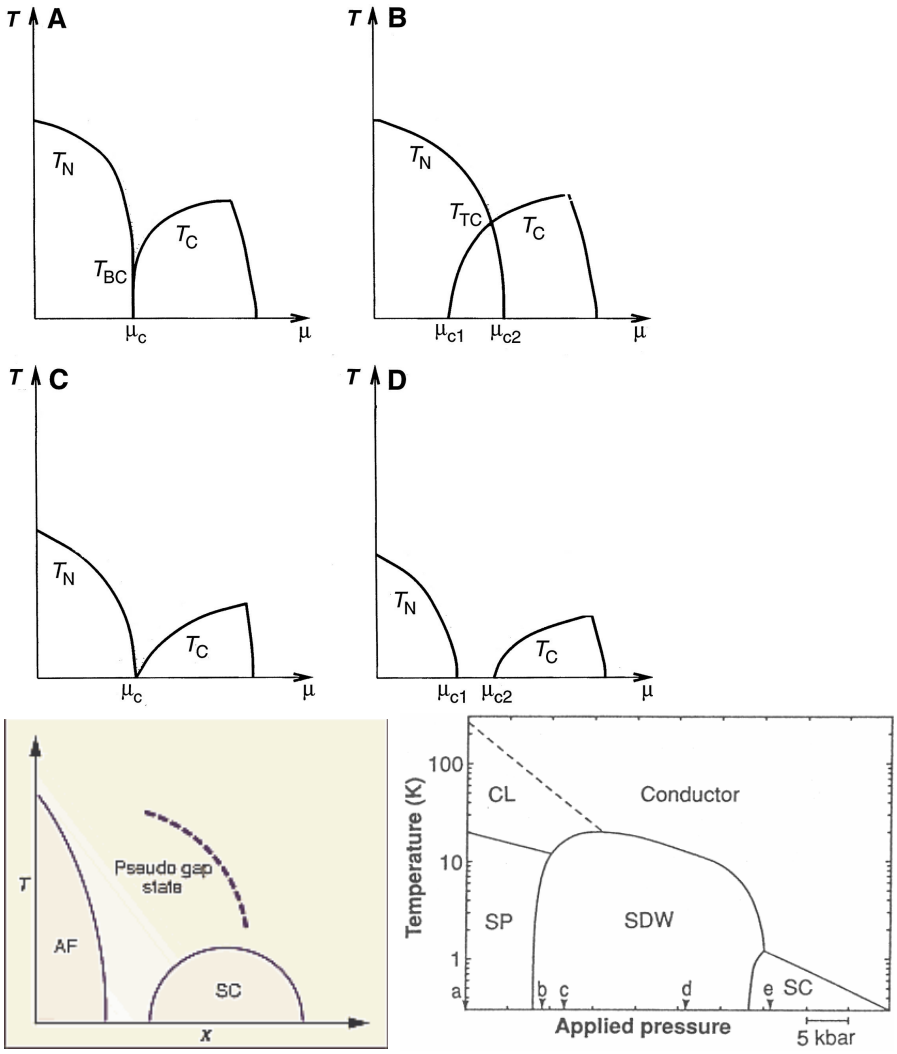

Slika S.1: Gore: Teorijski fazni dijagrami za slučajeve blizine AF/VGS i SV osnovnih stanja. T_N i T_c su temperature prijelaza u navedena stanja, [8]. (A) prijelaz prvog reda koji završava u bikritičnoj točki T_{bc}. (B) dva prijelaza drugog reda koji se sastaju u četverokritičnoj točki T_{tc}. (C) prijelaz drugog reda u kvantnoj kritičnoj točki. (D) dva prijelaza drugog reda s kvantno neuređenom međufazom. Uspoređeno s eksperimentom: Dolje lijevo, HTSC slojni kuprati. Pri niskom dopiranju x, uspostavlja se AF uređenje. Pri višim dopiranjima javlja se SV faza s pseudoprocijepom, [9]. Dolje desno, Bechgaard-Fabre soli. SV i VGS faze imaju zajedničku granicu. Naznačeni su položaji u generaliziranom faznom dijagramu za: $(TMTTF)_2PF_6$(a), $(TMDTDSF)_2PF_6$(b), $(TMTTF)_2Br$(c), $(TMTSF)_2PF_6$(d), $(TMTSF)_2ClO_4$(e) , [10].

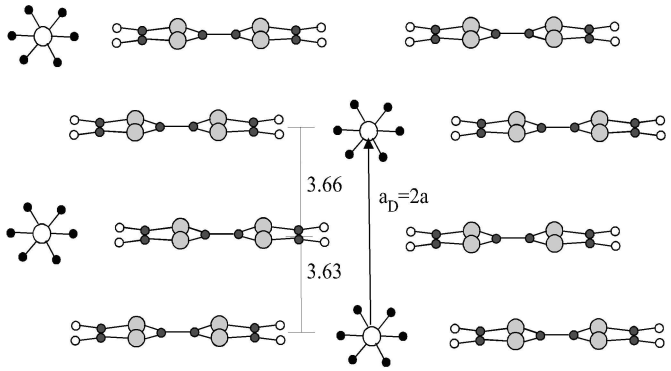

Slika S.2: Prikaz slaganja molekula TMTSF i aniona u kristalu. Pogled je u smjeru b-osi, prikazana je ac-ravnina.

S.1.1 Kristalografska i elektronska struktura, te osnovna stanja $(TMTSF)_2PF_6$

Bechgaardove $(TMTSF)_2X$ i Fabreove soli $(TMTTF)_2X$, općenito TM_2X, su izostrukturalni spojevi. TMTSF/TMTTF, tetrametiltetra(selena/tia)-fulvalen je planarna organska molekula. U njoj 4 ugljikova atoma, mogu biti zamijenjena sa 4 selenova ili sumporova atoma. Te molekule s anorganskim ionima, X = PF_6, AsF_6, SbF_6, BF_4, ClO_4, Re_4, NO_3..., formiraju soli, tzv. spojeve s prijenosom naboja. Anioni mogu biti centrosimetrični, kao u $(TMTSF)_2PF_6$, ili necentrosimetrični, kada anionsko uređenje igra ulogu. Selen bazirane soli sintetizirao je prvi K. Bechgaard, [14]. Parametri triklinske jedinične ćelije su a=3.65 Å, b=7.711 Å, c=13.522 Å, α=83.39^o, β=86.27^o i γ=71.01^o. Molekule TMTSF/TMTTF se slažu (kao novčići) u stupce duž a-smjera i time stvaraju naglašeno anizotropnu elektronsku strukturu, Sl. S.2.

Preklapanje p-orbitala Se-atoma u a-smjeru stvara vrpcu, koja je četvrt-popunjena zbog prijenosa naboja s aniona (1 elektron/2 molekule). Anizotropija električne vodljivosti $\sigma_a : \sigma_b : \sigma_c \sim 300 : 1 : 0.03$ na sobnoj temperaturi potvrđuje proračune transfer integrala $t_a \approx 0.2\mathrm{e}V : t_b \approx 0.02\mathrm{e}V : t_c < 0.001\mathrm{e}V$, [22]. Stoga se $(TMTSF)_2PF_6$, kao i ostali spojevi iz porodice, smatraju kvazi-1D vodičima. Vodljivost na sobnoj temperaturi je velika, $\sigma_a(300\mathrm{K}) \approx 600\Omega^{-1}cm^{-1}$, i metalna se svojstva uočavaju do najnižih temperatura, sve do metal-izolator prijelaza [25]. Omjer, označavan sa RR, vodljivosti na sobi i vodljivosti upravo iznad prijelaza karakterizira kvalitetu uzoraka i može dostići i 1000 za najkvalitetnije uzorke, [27]. Ispod metal-izolator prijelaza na $T_{\mathrm{VGS}} = 12$ K javlja se stanje vala gustoće spina. Magnetska susceptibilnost $(TMTSF)_2PF_6$ vrlo nalikuje onoj regularnog

antiferomagneta. Magnetska laka os je orijentirana duž b-smjera, [28]. Istraživanjima protonske magnetske rezonancije ukazano je na modulaciju gustoće spina s valnim vektorom $\mathbf{Q}_{\mathrm{VGS}}$ =(0.5, 0.20-0.24,-0.06±0.20) i amplitudom 0.08 μ_B, [24, 29]. Istraživanjima difuznog raspršenja X-zraka uočena je modulacija gustoće naboja elektronskog sistema (ne modulacija rešetke) sa sličnim valnim vektorom $\mathbf{Q}_1$ =(0.5±0.05, 0.25±0.05,0.25±0.20) i amplitudom od 0.1 elektrona po TMTSF molekuli, [33, 34].

Prijelaz u VGS fazu uzrokovan je specifičnim svojstvom *ugnježđenja* Fermi površine $(TMTSF)_2PF_6$. Fermi površina (FP) je, zbog konačnog t_b, formirana od dviju valovitih ploha, moduliranih duž b-osi, dok je modulacija duž c-osi zanemariva. Translacijom za vektor $\mathbf{Q} \approx (2k_F, \frac{\pi}{b})$ te se plohe savršeno ugnježđuju. Time je zapravo shematski prikazano povezivanje velikkog broja orbitala sa suprotnih ploha, a među kojim je mala razlika u energiji $E(\mathbf{k}) = E(\mathbf{k} + \mathbf{Q})$. To vodi na divergenciju odzivne funkcije (magnetske susceptibilnosti) $\chi_0(\mathbf{q} \approx \mathbf{Q})$ kada $T \to 0$ i naposlijetku do prijelaza u stanje vala gustoće spina. Modulacija spina je dana sa $S(x) = S_0 \cos(\mathbf{Q}\mathbf{x} + \varphi(x)) = S_0 \cos(2k_F x + \varphi(x))$ i uočena je eksperimenalno, kao što je gore spomenuto, [24, 29].

Prijelazom u VGS stanje otvara se procjep 2Δ na FP, [37]. Otpornost pokazuje izolatorsko ponašanje $R = R_0 e^{\Delta/T}$. Za visoko kvalitetne uzorke $\Delta \approx$ 21 K. Dakle, eksperimentalno određene vrijednosti procjepa i temperature prijelaza zadovoljavaju BCS relacija $2\Delta = 3.52 T_{\mathrm{VGS}}$, [27]. Time je potvrđen i teorijski pristup opisu VGS u $(TMTSF)_2PF_6$. Naime, u aproksimaciji srednjeg polja Hubbardov Hamiltonijan za 1D elektronski plin vodi na eksponencijalnu ovisnost $2\Delta_{\mathrm{VGS}}$ o interakciji U. I proračun T_{VGS} na osnovi magnetske susceptibilnosti 1D elektronskog plina vodi na takvu ovisnost, što zajedno vodi na BCS relaciju.

Istaknuta svojstva VGS faze su odgovori na istosmjerno i izmjenično električno polje. Odgovor na istosmjerno električno polje je nelinearan zbog proklizavanja VGSa iznad određenog električnog polja praga [38]. Proklizavanje VGSa je praćeno fenomenom uskopojasnog šuma, [39]. Odgovor na izmjenično polje je karakteriziran enormnom dielektričnom konstantom reda 10^8-10^9 [45].

Temperatura prijelaza T_{VGS} relativno se lako potiskuje primjenom hidrostatskog tlaka. To je i naznačeno položajem $(TMTSF)_2PF_6$ u generaliziranom faznom dijagramu TM_2X porodice, Sl. S.1. Kako bi se pojasnio utjecaj tlaka potrebno je detaljnije modelirati FP, kao i disperzijske relacije. Prije spomenuti valni vektor $\mathbf{Q} \approx (2k_F, \frac{\pi}{b})$ vrijedi za slučaj savršenog ugnježđenja, dok je realni materijal karakteriziran određenim stupnjem nesavršenosti ugnježđenja. Ponovo se razmatra susceptibilnost 1D elektronskog plina, i računa se s disperzijskom relacijom koja uzima u obzir

nesavršeno ugnježđenje

$$E(\mathbf{k}) = E_0 + v_F\left(|k_x| - k_F\right) - 2t_\perp \cos(k_y b) - 2t'_\perp \cos(k_y b) \qquad \text{(S.1)}$$

Zadnji član opisuje nesavršenost ugnježđenja, $t'_\perp = t_\perp^2/t_\parallel = t_b^2/t_a$. Za $(TMTSF)_2PF_6$ na ambijentalnom tlaku taj član nije zanemariv. Koristeći vrijednosti transfer integrala izračunate od Granta, [22], $t'_\perp \approx 1-2$ meV. Na energijskoj skali to je usporedivo sa Δ_{VGS}, što objašnjava zašto već desetak kbar dostaje za potiskivanje VGSa, [12].

U ovom modelu tlak povećava član $t'_\perp$. Naposlijetku se gubi divergencija u susceptibilnosti i iznad kritične vrijednosti

$$t'_\perp = t_\perp^{**} \qquad \text{(S.2)}$$

VGS biva potisnut i stabilizira se nedistorzirani kvazi 1D metal.

Istraživanja električnog transporta pri tlakovima iznad 9-10 kbar pokazala su da takav kvazi 1D metal prelazi u supravodljivo stanje ispod $T_{\mathrm{SV}} \approx 1.2$ K [21]. Primijetimo, ova se SV faza uspostavlja u blizini VGS stanja, Sl. S.1, a u teorijskom prikazu za 1D elektronski plin VGS faza nastaje u blizini tripletne SV faze [50]. Eksperimentalno je pokazano da uistinu priroda sparivanja u SV fazi $(TMTSF)_2PF_6$ nije simetrije s-tipa. Najčvrstija potvrda tripletne, p-tip supravodljivosti dolazi iz istraživanja ^{77}Se nuklearne magnetske rezonancije na $(TMTSF)_2PF_6$ pod tlakom, [60]. Ova studija je preko Knightova pomaka direktno proučavala spinsku susceptibilnost, za koju je ustanovljeno da se ne mijenja pri metal-SV prijelazu.

Dakle, kao što je i naznačeno u generaliziranom faznom dijagramu, javlja se područje tlaka (9-10 kbar) gdje se SV i VGS faze $(TMTSF)_2PF_6$ materijala nalaze u blizini. VGS-SV prijelaz nije moguće istražiti u izotermičkom eksperimentu, zbog ekperimentalne nemogućnosti mijenjanja tlaka pri tako niskim temperaturama. No, vrlo je rano uočeno, pri izobaričkim mjerenjima električnog transporta u tom području tlakova, da se na temperaturama ispod metal-VGS prijelaza javlja i VGS-SV prijelaz, [61, 47]. Isto je uočeno i tehnikom elektronske paramagnetske rezonancije (EPR), [46].

S teorijskog gledišta, spajanje VGSa i SV oko kritičnog tlaka, bilo je intenzivno studirano. Prvotna istraživanja su predložila ili postojanje kvantne kritične točke ili faznog prijelaza prvog reda između tih faza, Sl. S.1. Yamaji, je pak, predložio da se nešto ispod kritičnog tlaka stvara *semimetalna* VGS faza gdje opstaju džepovi nekondenziranih nosilaca naboja. Naime, tu se VGS ne otvara preko cijele FP, zbog vrlo nesavršenog ugnježđenja, [63]. Na neki način VGS i SV faze koegzistiraju u realnom prostoru, dolazeći s različitih područja recipročnog prostora. Yamaji je zaključio da ipak to nije vjerojatno jer bi toliko umanjena FP smanjila efektivno SV

vezanje, $gN(0)$, što bi dalje vodilo na eksponencijalno smanjenu temperaturu prijelaza, [64, 65, 66]. Preostaje u svakom slučaju pitanje kako bi se takva koegzistencija realizirala u kristalu, bi li to bilo na mikroskopskoj skali ($l \ll \xi$, gdje je ξ korelacijska duljina), na srednjim skalama ($l \sim \xi$), ili pak na makroskopskoj skali ($l \gg \xi$), tj. koje bi uređenje bilo energijski povoljnije?

Svakako, studije su granice između VGS i SV faza u $(TMTSF)_2PF_6$ bile ograničene ili eksperimentalnim ograničenjima, ili kvalitetom uzoraka. Dotle je teorijskim nedostajao pokušaj kvantificiranja relacije između dviju faza. Naša su istraživanja pokrenuta kako bi se razlučile kvalitativne i kvantitativne karakteristike te regije faznog prostora $(TMTSF)_2PF_6$. Time smo željeli pokušati pružiti osnove za uspješno modeliranje uočene koegzistencije, s mogućom širom primjenom na druge sisteme karakterizirane blizinom SV i magnetskih faza.

S.2 Kvazi 1D kuprati (La, Sr, Ca)$_{14}$Cu$_{24}$O$_{41}$ - kompleksni sistem

Kvazi 1D kuprati $A_{14}Cu_{24}O_{41}$ (A=Sr, Ca, La, Y...) su kompozitni materijali. Spinovi i naboji se uređuju unutar strukturalnih elemenata lanaca i ljestvica. Monokristali su prvi put sintetizirani 1988., [70, 71], a 1992. Dagotto je sugerirao mogućnost SV ili VGN korelacija u modelu spinskih ljestvica, te je naposlijetku SV stanje otkriveno u $Sr_{0.4}Ca_{13.6}Cu_{24}O_{41}$, pod tlakom [69]. Ključno je u Dagottovu konceptu bilo dopiranje ljestvica šupljinama. U ovim materijalima podsistem ljestvica je intrinsični izvor šupljina, tako da se pokazalo kako su (La, Sr, Ca)$_{14}$Cu$_{24}$O$_{41}$ uspješna eksperimentalna realizacija teorijskog koncepta. Stoga je u nastavku potrebno pojasniti koncepte spinskih ljestvica i lanaca te dopiranja šupljinama.

S.2.1 Kristalografska i elektronska struktura, raspored spina i naboja kod kvazi 1D kuprata

Ion bakra u kupratnim strukturama karakteriziran je ili spinom $S = \frac{1}{2}$ (Cu^{2+}) ion ili šupljinom (Cu^{3+} ion), spina $S = 0$. Šupljina se zapravo smješta u orbitale koordiniranih kisika i stvara sa spinom bakra Cu^{2+} tzv. *Zhang-Rice* singlet. Time se razvezuju stupnjevi slobode spina i naboja te se uspostavlja komplementarnost rasporeda spina i naboja.

U kupratima $S = \frac{1}{2}$ spinovi se mogu raspoređivati u različite strukture, lance, ljestvice ili ravnine. Spinovi raspoređeni u ravnine ili lance stvaraju antiferomagnetsko uređenje, dugodosežno u ravnini, kvazi-dugodosežno u lancu. Ljestvice, pak nisu negdje između tih 1D i 2D granica već posjeduju sasvim posebna svojstva. Teorijska razmatranja pokazala su postojanje spinskog procjepa, tj. konačna energija potrebna je za stvaranje spinskog pobuđenja sa $S = 1$. Pojava spinskog procjepa relativno je zorna u granici jakog vezanja, tj. tu se uzima kako je veza duž prečke ljestvica jača od veze duž samih ljestvica, $J' > J$. Stoga se osnovno stanje može smatrati produktom spinskih singleta, jednog po prečki, Sl. S.3. Tada je ukupni spin ljestvica jednak nuli, a za razbijanje para s prečke je potrebna konačna energija. Kad se takva pobuđenja i stvaraju, njihove korelacije su čisto kratkodosežne, te se stoga to stanje naziva *spinskom tekućinom*. Krajnji je korak u modeliranju ljestvica dopiranje šupljinama, Sl. S.3. Pri nižim dopiranjima i jakom vezanju sistem preferira vezanje dviju šupljina na istoj prečki. Inače bi te šupljine razbijale spinske singlete, što je energijski vrlo nepovoljno. Takva tendencija sparivanju vodi na prihvaćanje mogućnosti pojave supravodljivosti. No u takvom 1D sistemu, SV je u kompeticiji sa

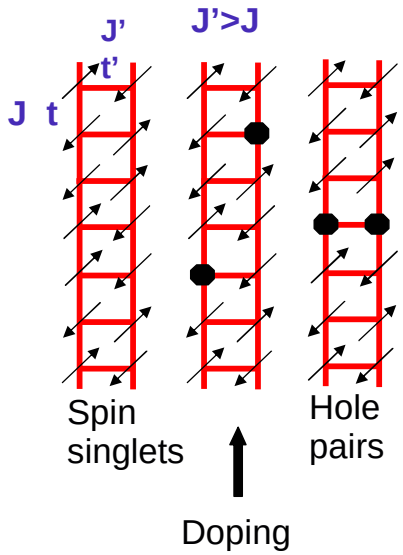

Slika S.3: Predloženi mehanizam sparivanja u ljestvicama. Kada je vezanje na prečki jače J'$> J$ nego duž ljestvica, osnovno stanje je direktan produkt spinskih singleta. Ubacivanje pojedinih šupljina razbija singlete, no radi energijske povoljnosti šupljine teže sparivanju na pojedinoj prečki, [68, 81].

osnovnim stanjem vala gustoće naboja. Koje će stanje prevladati ovisi o detaljima modela, ili još bolje, o detaljima interakcije u materijalu, što je teško predvidjeti teorijski, [50, 80, 77].

Bakar i kisik grade funkcionalnu strukturu kvazi 1D kuprata. Dvije osnovne podstrukture grade te kompozitne materijale, to su CuO_2 lanci i Cu_2O_3 ljestvice. Četverokut CuO_4 je osnovni gradbeni elemenat. U lancima se CuO_4 slažu linearno duž c-smjera tako da dijele stranice, a zatim međusobno paralelno duž a-smjera u slojeve koji onda čine podsistem lanaca. Dotle, u podsistemu ljestvica se stvaraju cik-cak lanci, koji se paralelno slažu duž a-smjera i naposlijetku stvaraju slojnu strukturu u kojoj se prepoznaju ljestvice kao funkcionalni elementi, Sl. S.4,S.5. Sloju koji sadrži ljestvice koordinirani su (Sr, Ca, La) atomi, tako da skupa čine podsistem. Naizmjeničnim slaganjem dvaju podsistema duž b-smjera gradi se ortorompski kristal kvazi 1D kuprata. Kad bi CuO_4 četverokuti bili idealni kvadrati dva podsistema bila bi nesumjerljiva u omjeru $1 : \sqrt{2}$. Nesumjerljivost, ipak postoji i u realnom materijalu. Stoga se za jediničnu ćeliju duž c-smjera uzima samo aproksimativno, iz praktičnih razloga duljina približne sumjerljivosti $10 \times c_C = 7 \times c_L = c' \approx 27.5$ Å. Četiri formulske jedinke $(La, Sr, Ca)_{14}Cu_{24}O_{41}$ ulaze u jednu takvu ćeliju. Tu je parametar lanaca $c_C \approx 2.75$ Å, a ljestvica $c_L \approx 3.9$ Å, Sl. S.5. U poprečnim smjerovima

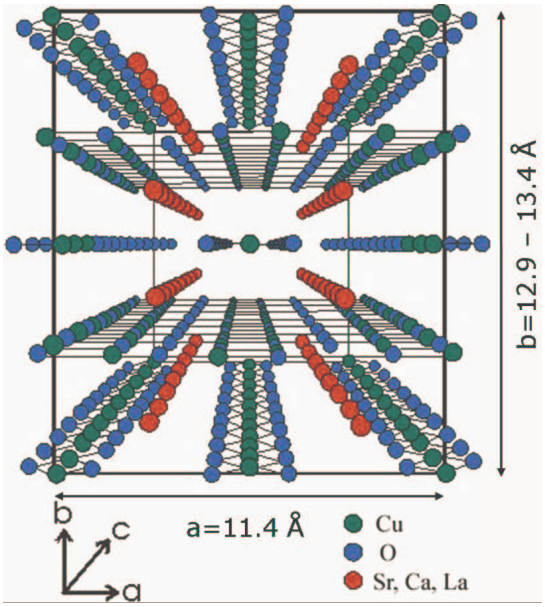

Slika S.4: Prostorni prikaz (La, Sr, Ca)$_{14}$Cu$_{24}$O$_{41}$ strukture, kristal je ortorompski. Naizmjenično slaganje slojeva CuO_2 lanaca Cu_2O_3 ljestvica s koordiniranim Sr, Ca, La atomima (crveno) zorno je prikazano. I lanci i ljestvice imaju parametre $a \approx$11.5 Å i $b \approx$12.9 - 13.4 Å. Jedino je b-parametar ovisan o sadržaju Sr, Ca, La. Ref. [70, 71].

podsistemi su istih parametara, $a \approx$11.5 Å i $b \approx$12.9 - 13.4 Å. b parametar je jedini značajno ovisan o vrsti atoma (Sr,Ca,La...).

Podsistem lanaca je struktura naglašene jednodimenzionalnosti. Duž lanaca ioni bakra su povezani 90^o Cu-O-Cu vezama putem feromagnetske izmjene. Međusobno su lanci razvezani, Sl. S.5. Nadalje, jake antiferomagnetske 180^o Cu-O-Cu veze putem izmjene stvaraju funkcionalnu strukturu ljestvica, no veza među susjednim ljestvicama unutar ravnine je slaba zbog slabe feromagnetske 90^o Cu-O-Cu veze i triangularnog rasporeda Cu-iona, koji rezultira frustracijama i daljnjim razvezivanjem sloja u niz zasebnih ljestvica.

Elektronska struktura osnovnog materijala $Sr_{14}Cu_{24}O_{41}$ bila je računata *ab initio* na maloj aproksimativnoj superstrukturnoj ćeliji koja sadrži jednu formulsku jedinku, f.j. No ova je kalkulacija izvedena uz pretpostavku o metalnim svojstvima sistema, što vodi do konačne gustoće stanja na Fermi nivou, u suprotnosti sa eksperimentalno ustanovljenim izolatorskim svojstvima.

Dopiranje šupljinama u materijalima (La, Sr, Ca)$_{14}$Cu$_{24}$O$_{41}$ u potpunosti je intrinsično, što potvrđuju već i jednostavna stehiometrijska razmatranja.

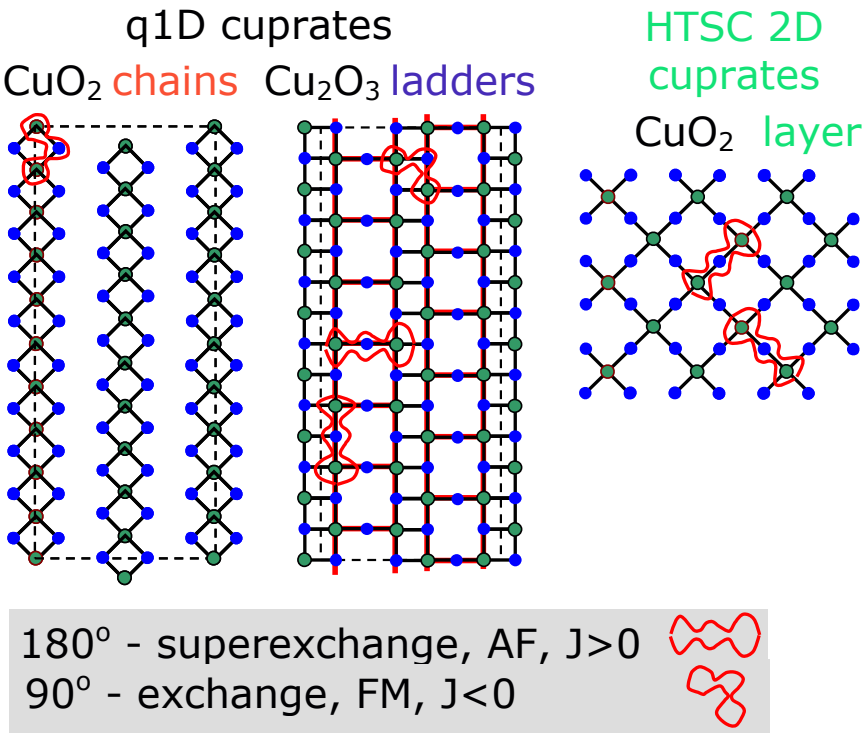

Slika S.5: Podsistemi lanaca i ljestvica čine strukturu kvazi1D kuprata. Podsistemi su nesumjerljivi u c-smjeru, pa je prikazana aproksimativna superstrukturna ćelija približne sumjerljivosti 7:10. 180^o Cu-O-Cu veze stvaraju funkcionalnu strukturu ljestvica, no veza među susjednim ljestvicama unutar ravnine je slaba zbog slabe feromagnetske 90^o Cu-O-Cu veze i triangularnog rasporeda Cu-iona. Unutar podsistema/sloja lanaca, lanci su međusobno razvezani što podsistemu daje naglašeno 1D strukturu. Podsistemi su nesumjerljivi duž c-smjera: parametar ljestvica c_L ≈3.9 Å, parametar lanaca c_C ≈2.75 Å.

U $Sr_{14-x}Ca_xCu_{24}O_{41}$ materijalima postoji 6 šupljina po f.j. $\delta_h = 6$, te je gustoća $6 \times 10^{21}\text{cm}^{-3}$. Neizovalentna supstitucija Sr^{2+} ili Ca^{2+} sa La^{3+} (ili Y^{3+}) smanjuje δ_h. Raspodjela šupljina komplementarna je raspodjeli spinova, Sl. S.3. Kao i stehiometrija, tako i račun Madelung energije za osnovni materijal $Sr_{14}Cu_{24}O_{41}$ vodi na to da se sve šupljine nalaze na lancima. No, ovaj račun ukazuje na to da postoji tendencija redistribucije šupljina na ljestvice uz supstituciju Sr sa Ca [85]. Ta je tendencija potvrđena i računom sume valencije veza, *bond-valence-sum* [86] baziranom na kristalografskim podacima o duljini Cu-O veza, [70, 71].

Svakako su ekperimentalna svojstva (La, Sr, Ca)$_{14}Cu_{24}O_{41}$ uvjetovana redistribucijom šupljina između podsistema. No već i za 'jednostavni' osnovni materijal $Sr_{14}Cu_{24}O_{41}$ nije jasno koji je mehanizam istosmjerne vodljivosti, iako se pretpostavlja da visoka vodljivost na sobi potječe iz podsistema ljestvica. Tako da je osnovno pitanje gdje su šupljine u $Sr_{14}Cu_{24}O_{41}$ na sobnoj temperaturi i kakva je njihova redistribucija s promjenom temperature i Ca-supstitucijom.

Eksperimentalno su prvo Osafune *et al.* , [75] mjerenjima optičke vodljivosti $\sigma(\omega)$ na sobi, pristupili rješavanju pitanja redistribucije u izovalentno dopiranim $Sr_{14-x}Ca_xCu_{24}O_{41}$. Interpretacijom uočenog transfera spektralne težine pokazali su kako mora postojati transfer šupljina s lanaca na ljestvice pri Ca supstituciji. No apsolutne vrijednosti su bazirali na pretpostavci da za $Sr_{14}Cu_{24}O_{41}$ na sobi već postoji jedna šupljina na ljestvicama, dok se preostalih pet nalaze na lancima. Vidjet ćemo da je ta pretpostavka bila ispravna.

Eksperiment koji je najdirektnije pristupio problemu redistribucije, između ostalog i za širu porodicu (La, Sr, Ca)$_{14}Cu_{24}O_{41}$ izveli su Nücker *et al.* , [76]. Mjerili su polarizacijski ovisnu finu strukturu apsorpcije X-zraka blizu ruba apsorpcije, NEXAFS (*near-edge x-ray absorption fine structure*). Ta je metoda sposobna razlučiti orijentaciju orbitale kisika u koju je smještena šupljina. Kako su te orbitale različito orijentirane za lance i ljestvice, to je moguće u apsolutnom iznosu odrediti broj šupljina u pojedinom podsistemu. Istraživanjima neizovalentno supstituiranih materijala, $\delta_h \leq 5$, $La_3Sr_3Ca_8Cu_{24}O_{41}$, $Y_3Sr_{11}Cu_{24}O_{41}$ i $La_2Ca_{12}Cu_{24}O_{41}$, ustanovili su da se sve šupljine kod njih nalaze na lancima. No, kod izovalentno supstituiranih, $\delta_h = 6$, $Sr_{14-x}Ca_xCu_{24}O_{41}$, ustanovili su da se broj šupljina blago povećava s Ca-supstitucijom od 0.8 do 1.1. Na lancima dakle preostaje uvijek oko 5 šupljina, H1 oznaka na Sl. S.6. Sada preostaje pitanje redistribucije šupljina snižavanjem temperature, jer su izloženi eksperimenti izvedeni na sobi. U nastavku će biti prikazana i istraživanja rasporeda šupljina (ili komplementarnog rasporeda spinova) unutar podsistema, na sobi, kao i na nižim temperaturama.

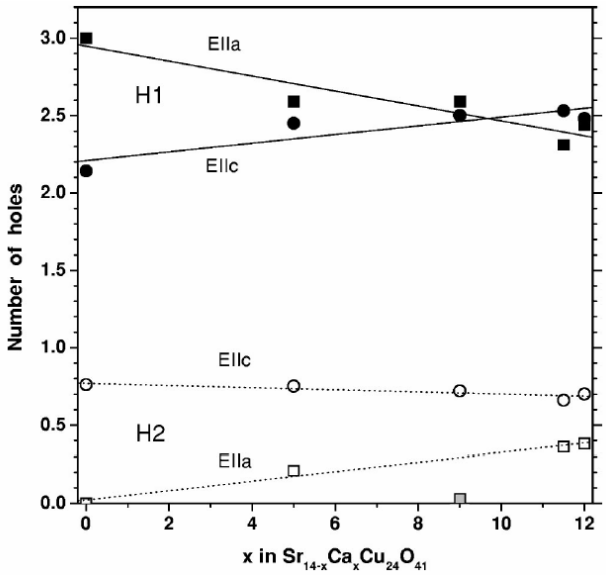

Slika S.6: Broj šupljina po formulskoj jedinki izveden iz renormaliziranih spektralnih težina NEXAFS mjerenja na $Sr_{14-x}Ca_xCu_{24}O_{41}$. Zasebno su prikazani doprinosi od šupljina smještenih u kisikove orbitale orijentirane duž smjera ljestvica ili duž smjera prečkica. H1 su brojevi za lance, H2 za ljestvice. Iz Ref. [76].

S.2.2 Posebne karakteristike podsistema lanaca i ljestvica

Podsjetimo, raspored šupljina je komplementaran rasporedu spinova. Magnetska susceptibilnost kao tehnika istražuje svojstva podsistema spina cjelokupnog uzorka (*bulk*). Ipak su i ti rezultati doveli do saznanja o redistribuciji šupljina kod (La, Sr, Ca)$_{14}$Cu$_{24}$O$_{41}$ materijala, [88, 89, 84]. Početna je pretpostavka da ljestvice zbog spinskog procjepa vrlo malo doprinose, te da ova tehnika zapravo mjeri spinove na lancima. Carter *et al.* [89] su to ustvrdili na osnovu mjerenja za materijal Cu_2O_3 gdje su ljestvice jedini element. Motoyama *et al.* [84] su ustanovili kod neizovalentno supstituiranih materijala, gdje se sve šupljine nalaze na lancima, da susceptibilnost pokazuje Curie ponašanje paramagneta. Dakle su spinovi na lancima slobodni i ne javlja se nikakvo uređenje. Susceptibilnost je bila proporcionalna broju spinova na lancima umanjenom za broj šupljina preostalih nakon supstitucije.

Kod izovalentno supstituiranih $Sr_{14-x}Ca_xCu_{24}O_{41}$, rezultati NEXAFS ukazali su na to da se jedna šupljina nalazi na ljestvicama, dok ih je pet na lancima. No ponašanje susceptibilnosti je odstupalo od Curie oblika, tj. opadanje (naglašeno za $Sr_{14}Cu_{24}O_{41}$) ispod 70 K je ukazivalo na otvaranje spinskog procjepa i na lancima. Matsuda *et al.* [88] i Carter *et al.* [89] ukazali su da se takva susceptibilnost lanaca može opisati modelom antiferomagnetskih, AF dimera. AF dimer model je baziran na organiziranju spinova duž lanca u AF vezane parove. Eksperimentalne rezultate interpretirali su s AF vezanjem od $J = 130$ K i brojem od $N_D = 2.0$ dimera na svakih 10 mjesta lanca. No ovi su rezultati ipak posredni i nekonkluzivni.

Izravno istraživanje spinskog uređenja na lancima izvedivo je neelastičnim raspršenjem neutrona, Sl. S.7. Dvije nezavisne grupe, Eccleston *et al.* , [91] i Regnault *et al.* , [90] istraživale su osnovni materijal $Sr_{14}Cu_{24}O_{41}$ na najnižim temperaturama, 5-20 K. Ustanovili su da je razmak spinova u dimeru jednak dva parametra lanca, $2c_C$, a da je razmak među dimerima $3c_C$. Dakle, dva dimera i 6 šupljina nalaze se na svakih 10 mjesta lanca. Superstruktura koju bi se očekivalo u ovom modelu je $5c_C$. No zbog niske interne simetrije superstrukturnog motiva ($5c_C$=$2c_C$ intradimer+ 3 c_C interdimer) dobitak u energiji od stvaranja superstrukture bi vjerojatno bio niži od frustracije zbog interakcije lanaca sa nesumjerljivim ljestvicama. Tako bi svaka pojava takve superstrukture u rezultatima difrakcije X-zraka trebala biti pripisana toj interakciji, [82, 93]. Ipak direktna opservacija X-zrakama [94], ali na 50 K ukazala je na pojavu superstrukture zbog uređenja naboja, no periodičnosti 4 c_C, sa 5 šupljina i 2.5 dimera na 10 mjesta lanca,

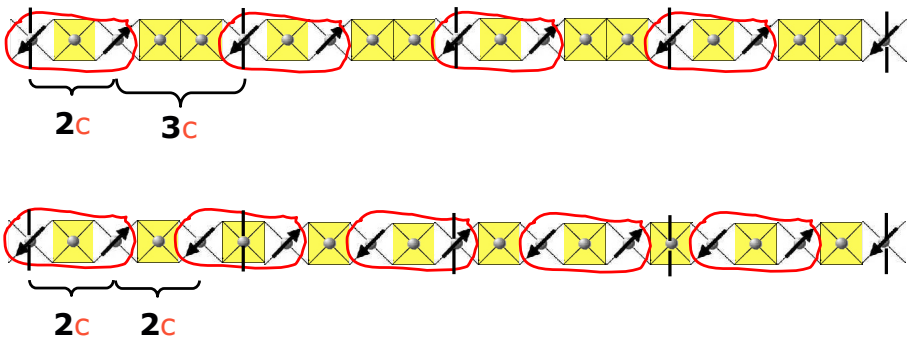

Slika S.7: Spinsko (crvene strelice) uređivanje u AF dimere (zaokruženo) uz komplementarno uređenje naboja (šupljina) (žuti kvadrati) za Sr_{14}-$Cu_{24}O_{41}$ lance. Gornji model, periodičnost 5 c_C, 6 šupljina, prema neutronskim mjerenjima na 5-20 K. Donji model, periodičnost 4 c_C, 5 šupljina, prema difrakciji X-zraka na 50 K.

Sl. S.7. Kontradikcija između ovih rezultata zapravo ukazuje na promjenu broja šupljina sa sniženjem temperature. Naime, vjerojatno je na najnižim temperaturama gdje su vršena neutronska mjerenja došlo do retransfera šupljina sa ljestvica nazad na lance, tj povećanja broja sa 5 na 6.

Model AF dimera interpretirao je pojavu spinskog procjepa na lancima i usporedio ga sa jačinom izmjene unutar dimera $J = 130$ K. NMR nudi mogućnost direktne opservacije procjepa mjerenjem temperaturne ovisnosti relaksacije spin-rešetka. No najbitnije jest to da NMR razlikuje lance od ljestvica, ^{63}Cu NMR mjerenja na polikristalima $Sr_{14-x}Ca_xCu_{24}O_{41}$, $x = 0, 3, 6, 9$ pokazala su da procjep, 140 K, ne ovisi o supstituciji [95]. Za x=0 ustanovljeno je i neutronskim mjerenjima [88, 92, 91] i NMR mjerenjima monokristala [98, 96] da procjep iznosi oko 140 K. No aktivacijsko ponašanje $1/T_1$ iz kojeg je određen procjep u NMRu javlja se tek ispod 50 K, znači procjep i spinsko uređenje se uspostavljaju tek ispod te temperature. Struktura NMR spektara omogućuje uvid u temperaturnu ovisnost spinskog uređenja. Takigawa *et al.* [98] mjerili su ^{63,65}Cu NMR ali i nuklearnu kvadrupolnu rezonanciju, NQR, pogodnu za razmatranje uređenja naboja. Ukazali su na cijepanje centralne NMR linije ispod $T^* = 200$ K što je posljedica neravnopravnosti mjesta u lancu zbog pojave AF dimera. NQR je pak pokazao da se upravo ispod 50 K na lancima počinje javljati preraspodjela naboja objašnjiva istim modelom, Sl. S.7, kojim su objašnjeni rezultati niskotemperaturnog neutronskog raspršenja. Naravno, NQR registrira nabojni sektor, komplementaran spinskom.

Može se zaključiti, barem za x=0 materijal, da pojava AF dimera počinje

ispod $T^* = 200$ K, dok se dugodosežno uređenje uspostavlja tek ispod 50 K praćeno otvaranjem spinskog procjepa. Shodno tome, ispod 50 K javlja se i komplementarno uređenje naboja, koje uzrokuje snažnu lokalizaciju šupljina na lancima.

Dok je spinski procjep na lancima pomalo neočekivan, dotle je spinska tekućina kao osnovno stanje podsistema ljestvica bila očekivana, još po Dagottovu modelu za jedne spinske ljestvice. Mjerenja ^{17}O NMR na materijalima $x = 0$ i 3 pokazala su prijelaz iz paramagnetskog u stanje spinske tekućine ispod $T^*(x = 0) \approx 200$ K i $T^*(x = 3) \approx 140$ K [96]. Mjerenja ^{63,65}Cu NMR na $x = 0$ su na osnovu spektara pokazala prijelaz na ljestvicama ispod iste $T^*(x = 0) \approx 200$ K [98]. Dok centralna linija ne pokazuje promjene, i ne cijepa se kao za lance, satelitske linije su šire i pokazuju temperaturno ovisnu strukturu ispod 200 K. Određivanje spinskog procjepa iz aktivacijskog ponašanja temperaturne ovisnosti $1/T_1$ spin rešetka relaksacije ukazalo je da procjep $\approx$ 300 K, ne ovisi o supstituciji za $x > 3$ [95, 103, 98, 104]. Za $x = 0$ i 2 pokazalo se da je procjep određen iz tih NMR mjerenja čak i dvostruko veći nego onaj određen iz mjerenja neutronskog raspršenja, što je, pretpostavljamo, posljedica toga što je NMR procjep određen u području 100 do 300 K, a neutronska mjerenja su vršena na niskim temperaturama, ispod 100 K. Najvažnije je primjetiti da spinski procjep na ljestvicama ne nestaje sve do najviših supstitucija, x=12, pri kojima se javlja i supravodljivost pod tlakom. To je važno jer je spinski procjep ljestvica važan u mehanizmu sparivanja šupljina transferiranih sa lanaca.

Kako izgleda da su šupljine na ljestvicama dobro lokalizirane zbog AF dimera i komplementarnog uređenja naboja, vjerojatno je da se električni transport u $Sr_{14-x}Ca_xCu_{24}O_{41}$ materijalima odvija na ljestvicama. Materijali $0 \leq x \leq 11$ pokazuju izolatorsko ponašanje u cijelom području temperatura ispod 300 K. Vodljivost duž smjera ljestvica je 1-2 reda veličine bolja nego poprečno, u smjeru prečkica [84]. Anizotropija ne ovisi značajno o x. Primjetljivo je da $Sr_{14}Cu_{24}O_{41}$ nije tako jaki izolator kao neizovalentno supstituirani materijali, gdje su sve šupljine na lancime i vjerojatno su dobro lokalizirane. Vodljivost na sobi $Sr_{14-x}Ca_xCu_{24}O_{41}$ materijala je ≈ 500 $\Omega^{-1}cm^{-1}$. Najprimjetljivije je u rezultatima mjerenja otpornosti opadanje aktivacijske energije s x. Za $x \geq 11$ javlja se i metalna vodljivost iznad 70-100 K. Primjena tlaka iznad $p_c \approx 3$GPa na materijalima $10 \leq x \leq 13.6$ vodi na pojavu supravodljivosti, kao što je teorijski predviđeno, ispod $T_{SV} \approx 10$ K [84, 69, 107, 106]. Također je ustanovljeno za x=0 kako niti tlak od 8 GPa ne uspostavlja SV stanje, iako potiskuje izolatorsko ponašanje.

Za supstitucije gdje javlja SV stanje pod utjecajem tlaka ustanovljeno je i da opstaje spinski procjep. No mjerenjima NMR $1/T_1$ *vs.* T pod tlakom na x=12 ustanovljeno je da se unutar spinskog procjepa javljaju

niskoenergijske magnonske ekscitacije, kakvih nema za x=0, [104, 108]. To vodi na zaključak da se SV stanje javlja samo pod uvjetom da su te ekscitacije moguće. Fujiwara *et al.* interpretirali su pojavu tih ekscitacija kao posljedicu slobodnog gibanja holon-spinon vezanog stanja jedne prečkice. Vezanje dvaju takvih stanja s dvaju susjednih prečkica vodi na supravodljivost.

Priroda izolatorske faze, povezana s prirodom električnog transporta na ljestvicama, kao i potiskivanje te faze su jedno od neodgovorenih pitanja na kraju ovog pregleda. Karakterizacija te faze i odnos izolatorske i SV faze, te spinskog procjepa, tj. kreiranje faznog dijagrama fokus je istraživanja koja će biti prikazana.

S.3 1D sistemi - teorijski pregled

S.3.1 Fazni dijagram 1D Fermi plina - model *g-ologije*

$(TMTSF)_2PF_6$ je, kao kvazi1D materijal, visoke vodljivosti na sobi i anizotropnih metalnih svojstava do najnižih temperatura, skoro idealan materijal za primjenu modela 1D Fermi plina. Preduvjet nastanka takvog molekularnog vodiča je delokalizacija naboja, koja u $(TMTSF)_2PF_6$ nastaje između TMTSF molekula u stupcu. Granica slabog vezanja je opravdana kada su elektronske interakcije manje od širine vrpce $4t$, što je i realizirano u TMTSF materijalima. Osnovna stanja $(TMTSF)_2PF_6$ (ovisno o tlaku) su $2k_F$ SDW i tripletna supravodljivost.

Model *g-ologije* uspješno opisuje fazni dijagram i nestabilnosti u 1D Fermi plinu sa slabim međudjelovanjem. Model sadrži osnovne posljedice postojanja slabih međudjelovanja: natjecanje među nestabilnostima, kao i 1D fluktuacije, [50]. U ovisnosti o konstantama vezanja, tj. valnom vektoru međudjelovanja, javljaju se različita osnovna stanja: singletna ili tripletna supravodljivost kao i valovi gustoće naboja ili spina (VGN ili VGS).

Karakteristično je za 1D sisteme da jake fluktuacije, termičke ili kvantne, onemogućavaju dugodosežno uređenje na bilo kojoj temperaturi $T \geq 0$, [80, 1]. U aproksimaciji srednjeg polja te se fluktuacije ne uzimaju u obzir, i time se omogućava uređenje na $T > 0$. U realnom materijalu, nezanemarivo međudjelovanje između 1D struktura umanjiti će utjecaj fluktuacija i dozvoliti uređenje na $T > 0$. Stoga je aproksimacija srednjeg polja korisna kako bi se pokazalo da je natjecanje supravodljivog i stanja valova gustoće osnovni problem u kvazi1D materijalima.

Hamiltonijan neinteragirajućeg fermionskog plina u 1D sadrži samo član koji predstavlja kinetičku energiju. Blochova stanja su osnovna stanja i prikladna je reprezentacija u prostoru impulsa. Posebnost je 1D sistema što se Fermi površina (FP) svodi na dvije točke, koje se nalaze na $-k_F$ i k_F. Interakcije se uvode perturbativno, a posebnost FP (ograničenja na prijenos impulsa) dozvoljava samo četiri različita procesa međudjelovanja, određena parametrima g_1, g_2, g_3 i g_4. Elektron-elektron interakcije su po svojoj prirodi ili Coulombske ili prenošene fononom. Mogući procesi, interakcije, u 1D fermionskom plinu su dijagramatski prikazani na slici S.8. Prvi proces, raspršenje prema nazad, sadrži doprinose kratkodosežnih, lokalnih interakcija. To su doprinosi koji se javljaju zbog Paulijeva principa, ili zbog Coulombskog odbijanja dvaju elektrona koji se nalaze u istoj orbitali. Raspršenje prema naprijed povezano je s dugodosežnim interakcijama. Prijenos impulsa $4k_F$ povezan je s pojavom *Umklappa*. *Umklapp* je moguć ako je vrpca polupopunjena jer je tada vektor recipročne

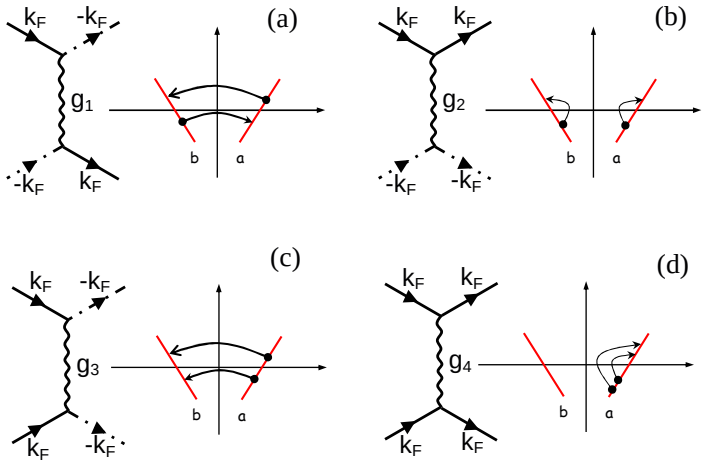

Slika S.8: Dijagrami mogućih procesa raspršenja u 1D Fermi plinu. Dijagrami korespondiraju prijenosu čestica između grana disperzije. (a) Raspršenje prema nazad, $q = 2k_F$. (b) Raspršenje prema naprijed, $q = 0$. (c) *Umklapp* raspršenje, $q = 4k_F$. (d) Dodatni mogući proces raspršenja prema naprijed, $q = 0$.

rešetke jednak $4k_F$ i može poništiti prijenos impulsa pri raspršenju. Ta je situacija realizirana u Fabre solima $(TMTTF)_2X$ gdje je umklapp generiran nevelikim Coulombskim potencijalom X aniona, tj. $g_3 \ll g_1, g_2$, [109]. U Bechgaardovim solima ova je pojava od manjeg utjecaja. Četvrti je mogući proces također raspršenje prema naprijed, no čestice se ovdje ne prenose na suprotnu stranu FP.

Najbolji način za određivanje koje nestabilnosti, tj. osnovna stanja se mogu očekivati u 1D sistemu je račun odzivnih funkcija ili poopćenih susceptibilnosti u granicama linearnog odziva. Odzivne funkcije za koje se očekuje singularnost za dani opseg parametara vezanja g_i su one za val gustoće naboja (VGN) ili spina (VGS) te za singletnu (SS) ili tripletnu (TS) supravodljivost. VGS ili VGN javljaju se za prijenos impulsa $q = 2k_F$, odražavajući singularnost u elektron-šupljina (Peierls kanal) susceptibilnosti za taj valni vektor. SS ili TS javljaju se kad je odzivna funkcija singletnog ili tripletnog elektron-elektron, Cooperovog para singularna. Odgovarajući fazni dijagram za sve četiri vrste nestabilnosti zadan je linijom $g_1 = 2g_2$ koja odvaja supravodljiva od stanja vala gustoće dok $g_1 = 0$ odvaja singletna od tripletnih stanja. Glavna je posljedica umklappa, g_3 stvaranje procjepa na $q = 0$ u naboj-naboj korelacionoj funkciji, tj. nastanka Mott lokalizacije. U kontekstu ovog pregleda, najvažniji je rezultat naznaka postojanja granice između SV i stanja vala gustoće.

Fenomenološki, stanja vala gustoće značajno se razlikuju od SV. No svakako je teže međusobno razlikovati stanja valova gustoće. Valni vektor $2k_F$ definira modulaciju gustoće i u VGNu i VGSu. Oba su stanja u realnom 3D materijalu karakterizirana metal-izolator prijelazom i padom susceptibilnosti, no kod VGSa ova opada samo u smjeru amplitude modulacije spina. Vezanje između elektronskih i fononskih sistema, vodi na pojavu distorzije rešetke koja prati pojavu valova gustoće. Utjecaj na rešetku se može pratiti metodom raspršenja X-zraka, [33, 34]. Valovi gustoće se odlikuju i dugovalnim pobuđenjima, fazonima koji se vežu na vanjsko elektromagnetsko polje i vode na zanimljive dinamičke efekte, vidi str. 206.

Prošireni 1D Hubbardov model u granici slabog vezanja

Dok prošireni 1D Hubbardov model u granici slabog vezanja svakako korespondira modelu g-ologije, dotle je Emery, [114] pokazao da i u granici jakog vezanja dobivamo isti fazni dijagram. Parametri koji definiraju Hubbardov hamiltonijan korespondiraju parametrima g-ologije. Tj., svi g_i će biti isti, i jednaki parametru U koji opisuje unutaratomsko, Coulombsko, odbijanje dvaju elektrona smještenih na istom mjestu. No, kad se uvede i međuatomska interakcija V, parametri g_i se mogu razlikovati. Korespondencija je slijedeća:

$$\begin{aligned} U-2V &\rightarrow g_1 \\ U+2V &\rightarrow g_2 \\ U-2V &\rightarrow g_3 \\ U+6V &\rightarrow 2g_2-g_1 \end{aligned} \tag{S.3}$$

S.3.2 1D elektronski sistem s jakim međudjelovanjem-kupratni materijali

Elektronski Hamiltonijan kupratnog sistema treba uzeti u obzir i članove povezane s kisikovim orbitalama. Stoga se barata sa slijedećim parametrima: ε_p, energija O2$p_{x,y}$ orbitala i ε_d, energija Cu3$d_{x^2-y^2}$ orbitala. Fizikalna situacija ovisi o cijepanju $\Delta_{pd}=\varepsilon_p-\varepsilon_d$, i hibridizaciji t_0, između tih orbitala. U granici jakog vezanja odbojni U_d (u orbitali bakra) i cijepanje Δ_{pd} uzima se puno većim od efektivnog preskakanja t, koje je reda hibridizacije t_0 između bakrovih i kisikovih orbitala. Omjer U/Δ_{pd} određuje osnove fizikalne situacije u kupratima, [74].

Ako je $U_d < \Delta_{pd}$ šupljine će se smještati u orbitale bakra, a ako je $U_d > \Delta_{pd}$ tada će dopirana šupljina biti smještena u orbitale kisika koje okružuju bakar i formirati će tzv. Zhang-Rice singlet sa onom šupljinom koja se već nalazi u orbitali bakra. Zhang i Rice su prikazali jednovrpčani t-J Hamiltonijan koji opisuje gibanje ZR singleta kroz 2D rešetku bakra i kisika, no za pretpostaviti je da je koncept primjenjiv i na ljestvice. Tako se i rešetka bakrova i kisika može preslikati na rešetku sa jednom vrstom mjesta, bliskom polupopunjenju. U toj rešetki na svakom mjestu se nalazi po jedna šupljina koja nosi spin 1/2, dok je ponegdje dopirana dodatna šupljina koja stvara ZR singlet - pa je to mjesto efektivno nezauzeto, a sistem je zbog toga blago odmaknut od polupopunjenja. Dok je efektivni t-J model Zhanga i Ricea razvijen za 2D kupratnu ravninu, dotle su Dagotto *et al.* [77, 73, 68] predstavli model spinskih ljestvica kao dva međusobno povezana 1D lanca, gdje postoje i t', J' između susjednog para lanaca, dakle, duž prečkica ljestvica, Sl. S.3. Ako je J'$> J$, osnovno je stanje ljestvica skup singleta formiranih na prečkicama. Tako nastaje i procjep u spektru spinskih pobuđenja jer je potrebno uložiti J' da bi se stvorio triplet. Stoga se dopirane šupljine teže naći na istoj prečkici kako bi se razbilo što manje singleta

Važan je korak u Dagottovu razmatranju uočiti da se potprostor prečkica može preslikati na jednostavni lanac. Mjesta na tom lancu su ili dvostruko okupirana (dvije dopirane šupljine s jedne prečkice) ili prazna (singletirani spinovi prečkice). Iz tog preslikavanja proizlazi da je na tom lancu $|U_{eff}| \propto J$', i $U_{eff} < 0$ - privlačan. Ta situacija korespondira Hubbard modelu za lanac koji u blizini polupopunjenja pokazuje SV ili VGN korelacije.

Naime prošireni Hubbardov model za lanac u granici jakog U, gdje se t i V tretiraju kao perturbacije daje relativno jednostavnu sliku mogućih stanja sistema.

Na primjer, za privlačni U i međuatomsku interakciju, $V \neq 0$, supravodljivost se može javiti ako se omogući preskakanje t, dok se VGN može javiti ako je $t = 0$, Sl. S.9. Stoga su Dagotto *et al.* i pretpostavili mogućnost pojave SV ili VGN stanja u kupratnim ljestvicama. Također je važno primijetiti da se ta stanja u 1D sistemu očekuju i u slučaju jakog vezanja.

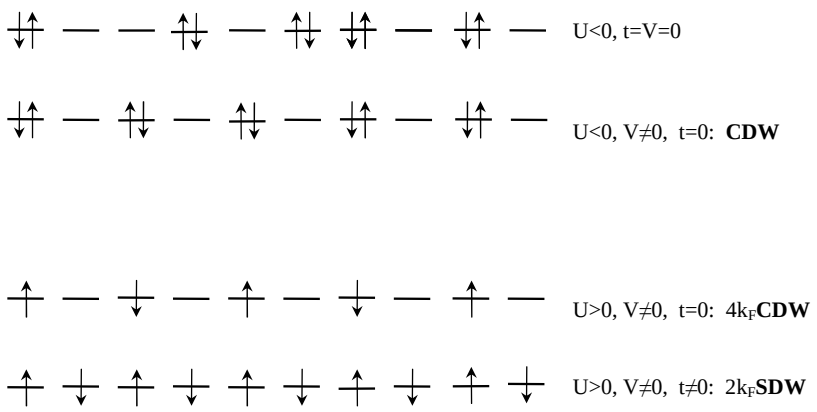

Slika S.9: Raspoređivanje elektrona, spin gore, $\uparrow$, ili spin dolje, $\downarrow$ na 1D lancu u prisustvu jakog unutaratomskog međudjelovanja $U \neq 0$. Za privlačni U, i kad je međatomsko međudjelovanje uključeno, $V > 0$, formira se $2k_F$ VGN(CDW) od electrona sparenih u singlete. Za odbojni U, samostalni electroni formiraju $4k_F$ VGN pri četvrt-popunjenju. Pri polu-popunjenju, i dozvoljenim preskakanjem t, $2k_F$ formira se VGS(SDW).

S.3.3 VGN fazonski odgovor na vanjsko izmjenično električno polje

Standardni val gustoće naboja koji se javlja u realnim materijalima, gdje postoji vezanje elektronskog i fononskog podsistema može se opisati Fröhlichovim Hamiltonijanom, [122].

$$H = \sum_{k,\sigma} \varepsilon_k \, c^\dagger_{k,\sigma} c_{k,\sigma} + \sum_q \hbar\omega_q (b^\dagger_q b_q + b^\dagger_{-q} b_{-q}) + \sum_{k,q,\sigma} g(k) c^\dagger_{k+q,\sigma} c_{k,\sigma} (b_q + b^\dagger_{-q}) \quad \text{(S.4)}$$

gdje su $c^\dagger_{k,\sigma}$ i $b^\dagger_q$ operatori stvaranja za 1D Blochov elektron te za longitudinalni fonon q s disperzijama ε_k i ω_q i gdje je $g(k)$ elektron-fonon konstanta vezanja. U aproksimaciji srednjeg polja uzima se samo interakcija s $Q = 2k_F$ fononom. Ispod Peierlsova prijelaza u sistemu se javlja modulacija naboja praćena distorzijom rešetke opisanom kompleksnim parametrom uređenja $\Delta e^{i\varphi}$. Nosioci naboja se kondenziraju ispod procjepa 2Δ, no kondenzat se formira od parova elektron-šupljina suprotnog spina, koji dolaze sa suprotnih strana FP.

Dinamika kondenzata može biti opisana prostorno vremenski ovisnim parametrom uređenja $\Delta(x,t)$. Moguće su fluktuacije i amplitude i faze, a disperzijske relacije su odredili Lee, Rice i Anderson, [123]. Amplitudni mod ima procjep, ali je fazonski mod akustičan. $q = 0$ fazonski mod odgovoran je za električni transport i istosmjernu i izmjeničnu vodljivost VGN kondenzata. Stoga se dinamika VGNa i opisuje kao dinamika faze.

U realnom materijalu, zasjenjenje Coulombske interakcije slobodnim, nekondenziranim, nosiocima uklanja translacijsku invarijantnost i vodi na zapinjanje faze kondenzata. Efekti zapinjanja pomiču vodljivost kolektivnog moda na konačnu, frekvenciju zapinjanja. To je tzv. zapeti (*pinned*) mod koji se detektira na 10 GHz ili višim frekvencijama.

Za modeliranje zapetog moda, kakav se detektira u fazonskom odgovoru VGNa, dostatan je jednostavan, tzv. model klasične čestice. U tom modelu VGN kondenzat ima samo jedan stupanj slobode, a slobodni nosioci nisu uzeti u obzir. Prigušene oscilacije materijalne čestice koja predstavlja kondenzat, u periodičnom potencijalu zapinjanja opisane su jednostavnim jednadžbama za harmonički oscilator. Frekvencija zapinjanja Ω_0 je vlastita frekvencija takvog model-sistema. Masa čestice je zapravo efektivna masa VGN kondenzata. Neuniformna priroda zapinjanja nije uzeta u obzir i zbog toga ovaj model ne može istovremeno opisati zapeti mod i pregušene niskofrekventne dielektrične modove uočene u audio/radio frekventnom području. Ti se modovi mogu opisati samo zasebno, u granici jakog prigušenja.

Littlewoodov model fazonskog odgovora VGNa

VGN kao deformabilni, elastični medij je bolje opisan jednadžbom gibanja danom od Fukuyama, Lee i Rice, [128].

$$m^*\frac{d^2\varphi}{dt^2}+\gamma_0\frac{d\varphi}{dt}-\kappa\nabla^2\varphi+\sum_i V(\mathbf{r}-\mathbf{R}_i)\rho_0\sin[\mathbf{Q}\cdot\mathbf{r}+\varphi(\mathbf{r})]=\rho_c E_z/Q_z \quad \text{(S.5)}$$

Sinusoidalni VGN, karakterističnog vektora ugnježđenja $\mathbf{Q}$, opisan je s gustoćom naboja $\rho(r) = \rho_c + \rho_0\cos[\mathbf{Q}\cdot\mathbf{r}+\varphi(\mathbf{r})]$. FLR uzimaju u obzir zapinjanje faze φ na nasumični potencijal $V(\mathbf{r}-\mathbf{R}_i)$. κ je elastični modul, koji opisuje elastičnu deformaciju faze nastalu zbog zapinjanja. Ovdje se pretpostavlja da VGN može oscilirati samo uzduž lanaca i vezati se samo na E_z komponentu električnog polja.

Littlewoodova [127], općenita formulacija bazira se na tretiranju interakcije između VGNa i slobodnih nosilaca u modelu dviju tekućina, gdje je jedina interakcija preko elektromagnetskog polja. Totalna inducirana struja je dana sa strujom pomaka, normalnom strujom vođenja i polarizacijskom strujom VGNa:

$$\mathbf{j}(\mathbf{r},t)=\varepsilon\dot{\mathbf{E}}+\sigma\mathbf{E}+\rho_c\dot{u}\hat{\mathbf{z}} \quad \text{(S.6)}$$

Ovdje je $\dot{u}=\frac{\dot{\varphi}}{Q_z}$ brzina VGNa. ε i σ su dielektrični i tenzor vodljivosti, a za harmoničku pobudu $\dot{\mathbf{E}} = -i\omega\mathbf{E}$, tenzor kompleksne vodljivosti je definiran kao $\tilde{\sigma} = \sigma(\mathbf{q},\omega) - i\omega\varepsilon(\mathbf{q},\omega)$. Kako su VGN materijali većinom anizotropni, tenzor vodljivosti može biti aproksimiran dijagonalnim oblikom $\tilde{\sigma}=\tilde{\sigma}_\perp(\hat{\mathbf{x}}+\hat{\mathbf{y}})/\sqrt{2}+\tilde{\sigma}_z\hat{\mathbf{z}}$. Ovdje je $\tilde{\sigma}_z$ vodljivost u najvodljivijem smjeru, dok je $\tilde{\sigma}_\perp$ niska vodljivost u poprečnim smjerovima. Littlewoodova formulacija se zasniva i na linearnom odzivu, što vodi na linearizaciju jednadžbi gibanja, Jed. S.5 oko nekog ravnotežnog stanja $u_0(r)$:

$$\sum_{q'}[G_0^{-1}(\mathbf{q},\omega)\delta_{q,q'}+V(\mathbf{q}-\mathbf{q}')]u(\mathbf{q}',\omega)=\rho_c E_z(\mathbf{q},\omega) \quad \text{(S.7)}$$

gdje je gola odzivna funkcija

$$G_0^{-1}(\mathbf{q},\omega)=-m^*\omega^2-i\gamma_0\omega+\mathbf{q}\cdot\kappa\cdot\mathbf{q} \quad \text{(S.8)}$$

U slučaju uniformnog zapinjanja, gdje je potencijal zapinjanja dan sa $V(\mathbf{q}) = V_0\delta_{q,0}$ kolektivni VGN mod može biti razdvojen u longitudinalnu i transverzalnu komponentu. Transverzalni mod $q_z = 0, q_\perp \to 0$ nalazimo tražeći polove dielektrične funkcije. To je zapravo zapeti mod, $\omega_T^2 = \Omega_0^2$.

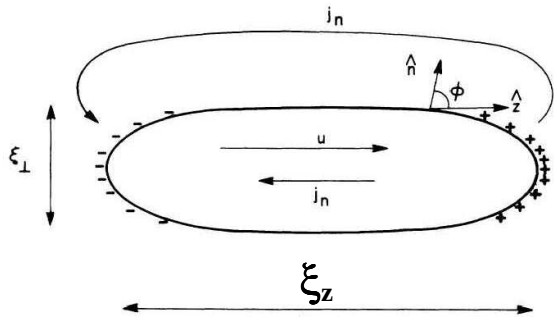

Slika S.10: Shematski prikaz lokalnog moda. Prikazani su inducirani naboji $(+,-)$ i normalna protustruja j_n (*backflow*). Dugovalno ($q \to 0$) vanjsko polje inducira unutarnja polja konačne valne duljine, usporedive s ξ_z, dimenzijom domene. Lokalna polja induciraju zasjenjenjujuće protustruje slobodnih nosilaca, koje disipiraju energiju.

Longitudinalni $q_\perp = 0, q_z \to 0$ nalazimo tražeći nule te iste funkcije. Na niskim frekvencijama longitudinalni mod je snažno pregušen pod utjecajem slobodnih nosilaca, $\gamma = \gamma_0 + \rho_c^2/\sigma_z$. Iako u principu longitudinalne modove nije moguće detektirati spektroskopskim tehnikama, niskofrekventna dielektrična spektroskopija detektira upravo ove pregušene modove.

Kako bi riješio kontradikciju, Littlewood ovu analizu unaprijeđuje razmatranjem neuniformnog zapinjanja. Zapete konfiguracije i lokalni modovi oscilacije VGNa neuređeni su na tipičnoj skali ξ - Lee-Rice duljini. Ispod te skale - tj. unutar LR domene faza se može smatrati konstantnom te je potrebno razmatrati odziv VGNa na lokalno polje, kroz lokalne modove. Uzima se u obzir i zasjenjenje slobodnim nosiocima i računa se lokalni odgovor na vanjski naboj (zapravo jedan od tih slobodnih nosilaca). Dobiva se da su lokalni modovi u biti longitudinalnog karaktera (zbog anizotropije vodljivosti) i zbog toga se može očekivati i detektiranje longitudinalnog odziva u spektroskopskim eksperimentima. Miješanje karaktera modova može se razumjeti i na slijedeći način: Lokalni mod je lokalni pomak u, Sl. S.10, energija zapinjanja je V_0, a mod odgovara na efektivno lokalno polje $\langle E_z \rangle$

$$(-m^*\omega^2 - i\gamma_0\omega + V_0)u = \langle E_z \rangle \tag{S.9}$$

Ovisno o obliku domene (danom sa $\xi_\perp$, ξ_z, a ti su nasumični - neuniformni) frekvencija lokalnog moda može biti ili ona transverzalnog moda ili ona longitudinalnog, tako da se u odgovoru cijelog materijala javlja miješani karakter modova, Sl. S.11.

Važno je uočiti da je τ_0 proporcionalan jednočestičnoj vodljivosti σ_z. Ta je proporcionalnost izvrsno dokumentirana različitim eksperimentima na

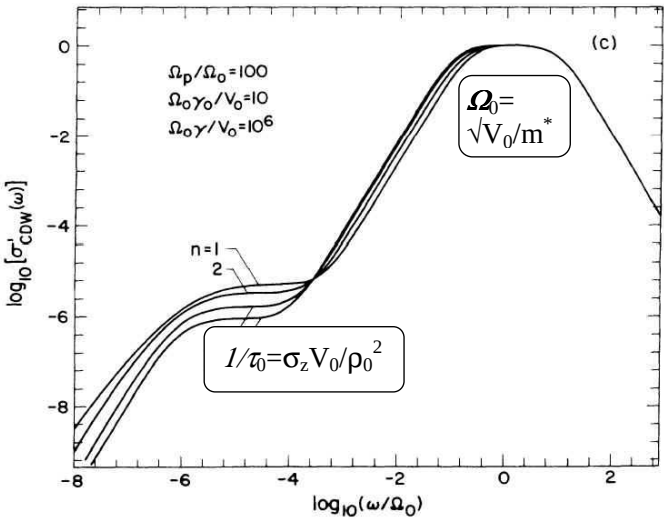

Slika S.11: Realni dio transverzalne komponente vodljivosti σ'. Zapeti mod, prikazan je kao vrh na Ω_0. Vrlo široka disperzija na niskim frekvencijama, na $1/\tau_0$, potječe od pregušenog kraka longitudinalnog moda.

standardnim VGN materijalima, [129, 130, 131, 132]. Dodatna je važnost ove analize povezanost između relaksacijskog vremena $\tau_0 = \rho_c^2/(\sigma_z V_0)$ i frekvencije zapetog moda $\Omega_0 = \sqrt{V_0/m}$. Kako su te dvije veličine izravno mjerive u eksperimentu (kao i jednočestična vodljivost σ_z) to je omogućilo Littlewoodu da izvede izraz za određivanje efektivne mase VGN kondenzata:

$$m^* = \rho_c^2/(\sigma_z \cdot \tau_0 \cdot \Omega_0^2) \tag{S.10}$$

Na kraju, prikazani model svakako predstavlja važno sredstvo u povezivanju eksperimenta i teorije, i naši će eksperimentalni rezultati biti analizirani na taj način.

S.4 Istraživanje faznog dijagrama $(TMTSF)_2PF_6$

S.4.1 Eksperiment i Rezultati

Istraživan je jedan monokristal $(TMTSF)_2PF_6$, visoke kvalitete (RR=1000, [135]), koja je potvrđena i prethodnim radom u kojem su korišteni uzorci iz iste sinteze, [11]. Uzorak je bio standardnog oblika i dimenzija $3 \times 0.2 \times 0.1\ mm^3$. Kontakti su izvedeni naparavanjem zlata i lijepljenjem Au-žica Ag-pastom. Mjerenja električnog transporta standardnom tehnikom s *lock-in* pojačalom su vršena duž a-smjera. Pri mjerenjima je provjereno mjeri li se u Ohmskom režimu otpora. Kritične struje mjerene su istosmjernom pulsnom tehnikom, strujama do 100 mA, opisanom u Ref. [11, 135]. Korišten je He-3 kriostat do temperatura od 0.3 K. Za primjenu tlaka korištena je Be-Cu tlačna ćelija (bomba). Tlačni medij bilo je silikonsko ulje što je omogućilo mnogostruko termičko cikliranje bez oštećivanja uzorka. Za mjerenje tlaka korišten je kristal InSb [134] koji pokazuje linearnu ovisnost otpornosti o tlaku, 2.5%/kbar. Promjena tlaka je kontrolirana i promjenom otpornosti $(TMTSF)_2PF_6$ prema stopi 10%/kbar. Kronološki redoslijed primijenjenih tlakova, u koracima od 100-300 bar, s preciznošću ±30 bar, nalazi se u Tablici S.1. Mjerenje je izvedeno u 19 ciklusa, gdje se odmah nakon promjene tlaka na sobi, hladilo do najniže temperature i nazad.

U metalnom stanju, $T > T_{\mathrm{VGS}}$, $T > T_{\mathrm{SV}}$, ispod 20 K, u području tlakova 6.8 to 9.2 kbar uočena je očekivana kvadratna ovisnost otpora o temperaturi, koja se javlja kad je elektronsko raspršenje dominirano elektron-elektron interakcijama [27, 145].

U području VGS faze $p < 8.6$ kbar, $T \lesssim T_{\mathrm{VGS}}$, uočeno je područje tlakova gdje je metal-VGS prijelaz vidljiv iz naglog, aktivacijskog porasta otpora, $R_{\mathrm{SDW}} = R_\infty exp(\Delta_{\mathrm{SDW}}/T)$. Temperatura prijelaza je određena iz maksimuma logaritamske derivacije otpora $\partial(\ln R)/\partial(1/T)$ *vs.* T. Aktivacijske energije, su dobro definirane Δ_{VGS}, posebno za tlakove, 6.8–8.45 kbar. Asimptotski otpori R_∞ za beskonačnu temperaturu su jednaki, što se i očekuje u standardnom poluvodičkom modelu.

U području SV faze $p > 9.43$ kbar, $T \lesssim T_{\mathrm{SV}}$ istraživali smo pri dva tlaka, 9.6 i 11 kbar. Uočene su temperature prijelaza T_{SV}, slijedom 1.195 ± 0.005 K i 1.106 ± 0.005 K . Prijelaz iz metalnog u SV stanje definiran je kao početak opadanja otpora. Prijelazi su oštri i histereza nije uočena. Ovisnost temperature prijelaza o tlaku reproducira poznate vrijednosti iz Ref. [51], tj. $\partial T_{\mathrm{SC}}/\partial p \approx -0.07$ K/kbar.

Područje faznog dijagrama, $8.6 < p < 9.43$ kbar, u kojem smo uočili

ciklus	tlak (kbar)	T_{VGS} (K)	T_{SV} (K)	Δ_{VGS} (K)	R_∞ (mΩ)	c vol%	I_c (mA)
1	6.8	7.9		9.38	12.1	0.03	
2	7.1	7.1					
3	7.3	6.6					
4	7.5	6.2					
5	7.7	5.9					
6	7.85	5.6					
7	8.15	5.3		6.35	12.0	0.09	
8	8.35	4.7					
9	8.45	4.4		5.74	11.30	0.2	
10	8.65	3.8	1.18	5.56	10.60	0.3	
17	8.65	3.8	1.18				.001
11	8.75	3.5	1.19	5.58	8.772	0.36	
18	8.9	2.85	1.21	6.90	2.473	1.25	0.15
12	8.95	2.85	1.21	6.70	2.146	1.4	0.3
13	9.1	2.45	1.21	6.90	0.320	5	7
19	9.2	1.8	1.21	6.30	0.0452	17	35
14	9.3	1.4	1.21	6.80	0.0022	89	
15	9.6		1.195				
16	11		1.106			100	35

Tablica S.1: Popis ciklusa i primijenjenih tlakova. Redni broj ciklusa označava kronološki redoslijed eksperimenata. Dane su temperature prijelaza u VGS, T_{VGS} i supravodljivo, T_{SV} stanje. Aktivacijska energija u VGS stanju Δ_{SDW}, asimptotski otpori, R_∞ te volumni udjeli metalne faze c (vol%) dok je uzorak u području koegzistencije faza dobiveni su iz prilagodbe R *vs.* T rezultata na prilagođeni Arrheniusov zakon, Jed. S.12. I_c su kritične struje za potiskivanje SV faze.

istovremenu pojavu dviju faza nazivamo područjem koegzistencije. Ovisno o temperaturi, javlja se ili VGS/Metal ili VGS/SV koegzistencija. U području $T_{\mathrm{SV}} \lesssim T \lesssim T_{\mathrm{VGS}}$ uočeno je snažno histeretično ponašanje između otpornih krivulja u hlađenju i grijanju. Pretpostavljamo da je histereza uzrokovana VGS/Metal segregacijom faza u zasebne domene čija je veličina i oblik temperaturno ovisan. Slični oblici histeretičnog ponašanja termostruje uočeni su u VGN stanju $(NbSe_4)_{10}I_3$ [146]. U području gdje su metal-VGS prijelazi i dalje dobro definirani, R *vs.* T krivulje su karakterizirane oštrim padom otpora na $T = 1.2 \pm 0.01$ K. Razumno je pretpostaviti da je time uočena kondenzacija prije spomenutih metalnih (M) domena u SV

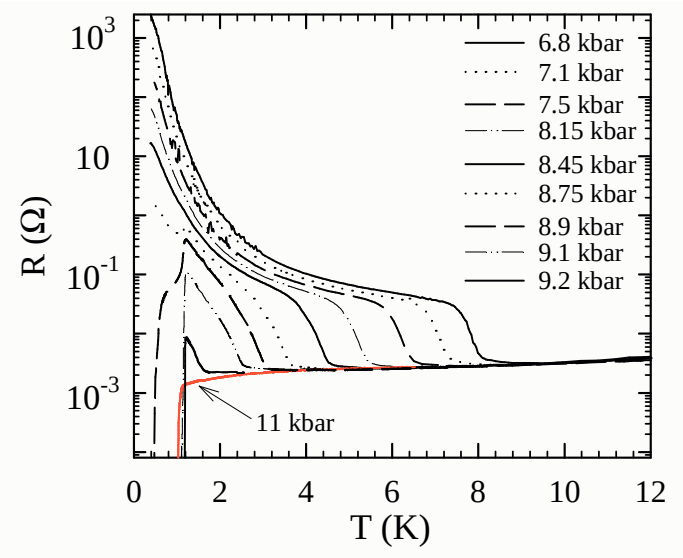

Slika S.12: (a) Logaritam otpora *vs.* temperatura u hlađenju pri različitim tlakovima. Iznad VGS prijelaza otpor opada kao u metalima. (b) Ispod VGS prijelaza otpor eksponencijalno raste, kao za izolator. Za tlakove $p > 8.65$ kbar primjećuje se blaži ili jači gubitak otpora, koji za tlakove $p \geq 9.1$ kbar prelazi u stanje nultog otpora, kao u supravodičima.

domene (dok VGS domene ostaju nepromijenjene). SV domene mogu ili perkolirati i stvarati makroskopske domene, ili se pak mogu povezivati preko dovoljno tankih VGS međupodručja, koja dopuštaju Josephsonov efekt. Oba bi mehanizma vodila na nulti otpor. Detaljnije razmatranje eksperimentalnih rezultata potvrdit će te pretpostavke.

Pri $p = 8.65$ kbar, ispod $T = 1.2 \pm 0.01$ K, otpor mjeren minimalnom strujom od 1μA opadne na samo 30% vrijednosti mjerene strujom od 100μA. Zapravo, u mjerenju jakom strujom ne uočava se nikakav pad otpora, tj. Arrhenius ponašanje otpora nastavlja se kontinuirano do najnižih temperatura. Pri $p = 8.9$ kbar, za najniže struje 1-10μA otpor opada na nulu snižavanjem temperature ispod $T = 1.2 \pm 0.01$ K. Za struje veće od 123μA nulti otpor potpuno nestaje i na najnižoj temperaturi 0.35 K, no niti za najveću primijenjenu struju od 1 mA nije uočeno ponovno uspostavljanje Arrhenius ponašanja karakterističnog za VGS fazu.

Daljnjim povišenjem tlaka do 9.1-9.3 kbar uočava se oštar pad otpora sve do nule unutar područja 30-40 mK od početka opadanja na oko $T = 1.2 \pm 0.01$ K. U ovom području tlakova koristi se istosmjerna pulsna tehnika budući su potrebne velike struje za potiskivanje supravodljivog stanja. Pri 9.1 kbar, na najnižoj temperaturi 0.4 K, kritična struja je $I_c = 7$ mA. Pri 9.3 kbar I_c

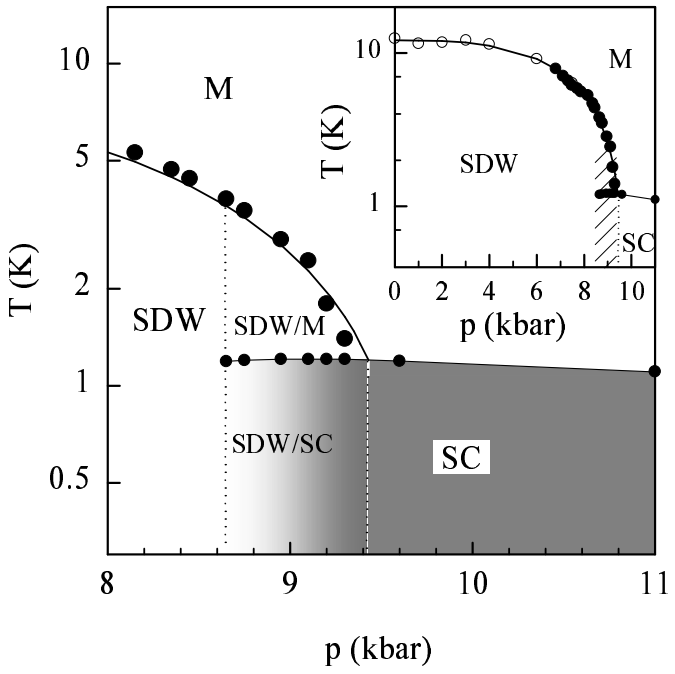

Slika S.13: Fazni dijagram $(TMTSF)_2PF_6$ u području visokih tlakova i niskih temperatura. SDW/M označava područje nehomogene koegzistencije metalne, M, i VGS faze (SDW-*spin-density wave*), ispod T_{VGS} linije (crne, veće, točke). Ispod $T_{SV} = 1.20 \pm 0.01$ K linije (crne, manje, točke), Ta se koegzistencija pretvara u koegzistenciju VGS i supravodljive faze, SC-*superconducting*. Pojačano zasjenjenje (SDW/SC područje) ispod T_{SV} označava povećanje volumnog udjela SV faze. Manja slika: Naš je dijagram dopunjen točkama Biškup *et al.* (otvoreni kružići). Puna linija jest rezultat prilagodbe na teorijski izraz za T_{VGS} *vs.* p; Jed. S.11).

poraste na 35 mA, istu vrijednost koja se mjeri i u čistom SV stanju pri 11 kbar.

Precizno određivanje temperatura prijelaza metal-VGS, metal-SV, kao i VGS-SV, te precizna mjerenje tlaka omogućilo nam je izradu p, T faznog dijagrama, Sl. S.13. Korišteni su i podaci iz ref. [12] za tlakove do 7.5 kbar. Podatke smo uspješno prilagodili na empirijsku formulu

$$T_{\mathrm{VGS}}(p) = T_1 - [(T_1 - T_{\mathrm{SV}}) * (p/p_c)^3] \tag{S.11}$$

gdje su $T_1 = T_{\mathrm{VGS}}(1bar)$ i p_c slobodni parametri a $T_{\mathrm{SV}} = 1.2$ K je eksperimentalni rezultat. Prilagodba daje $T_1 = 12.0 \pm 0.15$ K i $p_c = 9.43 \pm 0.04$ kbar, koji se odlično poklapaju s eksperimentalnim vrijednostima.

S.4.2 Određivanje udjela domena u području koegzistencije 8.65 – 9.43 kbar - model segregacije faza

Za temperature $T < T_{\mathrm{SV}} = 1.2$ K pretpostavili smo da u uzorku postoje SV i VGS domene koje pokazuju svojstva iz područja gdje su te faze nemiješane, tj. kao na 11 i 6.8 kbar. Radi jednostavnosti pretpostavili smo da se domene paralelno protežu od jednog kraja uzorka do drugog te primjena tlaka, dakle, mijenja udio pojedinih domena, tj. poprečni presjek. Kritičnu struju pri pojedinom tlaku p povezali smo sa udjelom SV faze c u poprečnom presjeku: $c = I_c(p)/I_c(11\mathrm{kbar})$. Vrijednosti I_c dane su u Tablici S.1.

Za temperature $T_{\mathrm{SV}} < T < T_{\mathrm{VGS}}$ pretpostavili smo analognu sliku, s time da se miješaju VGS i metalne domene. Prema modelu paralelnih domena dobivamo

$$1/R(T) = c/R_m + (1-c)/R_{\mathrm{VGS}} \tag{S.12}$$

gdje je R_m otpor 100% metalnog uzorka i $R_{\mathrm{VGS}} = R_\infty exp(\Delta_{\mathrm{VGS}}/T)$. Prilagodbom eksperimentalnih rezultata dobiva se udio c metalnih domena kao i Δ_{VGS}, R_∞ dani u tablici S.1.

Dakle u području tlakova 8.65 kbar–9.43 kbar izveli smo dvije nezavisne procjene udjela ne-VGS faza. Uz prije iznesenu pretpostavku kako na 1.2 K samo metalne domene prelaze u SV domene, možemo korelirati dvije procjene, c i $I_c/(35$ mA), Sl. S.14. Pokazuje se da u području 9.1–9.43 kbar, postoji proporcionalnost dviju procjena. To vodi na zaključak kako se uistinu domene paralelno protežu od kraja do kraja uzorka. U području 8.65–9.1 kbar, Josephsonovi spojevi postoje duž vodljivih kanala u VGS/SV području. Stoga je kritična struja snižena neproporcionalno volumnom udjelu SV domena.

M. Héritier iz Laboratoire de Physique des Solides, Orsay, Francuska, [135] predložio je model kojim bi se diskutirala uočena koegzistencija. Studira se relativna stabilnost faza: metalne, VGS, SV, kao i područja koegzistencije, ili VGS/M ili pak VGS/SV. Ključan je parametar nesavršenost ugnježđenja $t_b^{'} = t_b^2/t_a$ Jed. S.2. Primjena tlaka opisuje se povećanjem toga parametra. M. Héritier argumentira kako je uspostava prostorno *heterogene* faze energetski povoljnija od opstanka prostorno *homogene* VGS faze:

- Ako se zanemari mogućnost koegzistencije može se odrediti kritična linija $t_b^{'**}(T)$ za uspostavu/nestanak VGS faze. Naime, porastom $t_b^{'}$ raste VGS slobodna energija $F_m\left(t_b^{'}\right)$, do kritične vrijednosti $t_b^{'**}$ gdje homogena VGS faza nestaje.

- Stabilnost VGSa naglo opada u blizini $t_b^{'**}$. Nagib kritične linije je vrlo

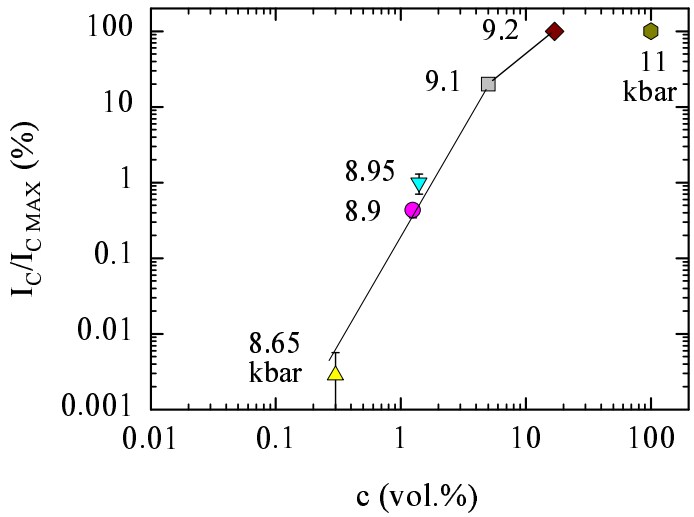

Slika S.14: Korelacija kritične struje I_c na 0.4 K, u VGS/SV području i volumnog udjela c (vol.%) metalne faze u području VGS/M, $T_{\mathrm{SV}} < T < T_{\mathrm{VGS}}$. Vrijednosti I_c i c nalaze se u tablici S.1.

velik.

- Relevantna veličina za stabilizaciju $t_b^{'**}$ jest b-parametar jedinične ćelije. Zaista, porastom b jako opada $t_b^{'}$, pa, shodno, opada i $F_m\left(t_b^{'}\right)$.

- Heterogena faza je uvijek povoljnija: magnetski dio $(1-c)\,\Omega$, ima parametar ćelije $b+\delta b_1$, a magnetska mu je energija snižena zbog povećanog b; drugi dio $c\Omega$, jest metalan, parametra je $b-\delta b_2$, (Ω je ukupni volumen). Znači $\delta b_2/\delta b_1 = (1-c)/c$. U modelu je pretpostavljen konstantni volumen. Gubitak na elastičnoj energiji ovakve deformacije je proporcionalan $(\delta b)^2$ dok je dobitak u magnetskoj energiji proporcionalan $\left(\frac{\partial F_m}{\partial t_b^{'}}\right)\left(\frac{\partial t_b^{'}}{\partial b}\right)\delta b$. Što je viši nagib $\left(\frac{\partial F_m}{\partial t_b^{'}}\right)$, to je veći dobitak u energiji.

Minimiziranjem tih dvaju doprinosa slobodnoj energiji po δb_1 i c, potvrđuje se pretpostavka o stabilnosti heterogene faze. U području parametra $t_b^{'} = t_{b1}^{'} < t_b^{'**} < t_b^{'} = t_{b2}^{'}$ u okolici kritične linije, energetski je povoljnija uspostava heterogene faze, Sl. S.15.

Nadalje, na nižim temperaturama metalne će domene prijeći u SV stanje. Tako da treba ispitati i energijske dobitke formiranja heterogene faze VGS/SV. Sve što se čini jest uključivanje SV slobodne energije, F_s. Nije potrebno činiti nikakve pretpostavke o mehanizmu formiranja SV faze,

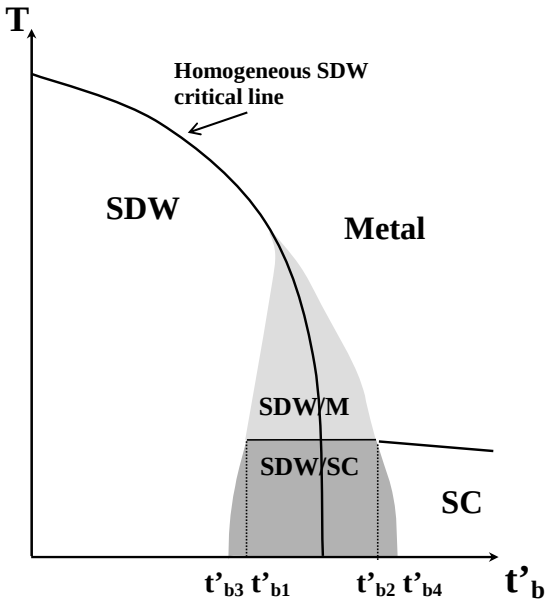

Slika S.15: Shematski fazni dijagram koji prikazuje nehomogene VGS/M i VGS/SV faze u blizini kritične linije. Parametar nesavršenosti ugnježđenja $t_b^{'}$ korespondira eksperimentalno primijenjenom tlaku.

niti o simetriji parametra uređenja. Već zbog same činjenice da je slobodna energija snižena s obadvije strane kritične linije biti će dovoljna da se ukaže na proširenje područja heterogenosti $t_{b3}^{'} < t_{b1}^{'} < t_b^{\prime **} < t_{b2}^{\prime} < t_{b4}^{'}$, kao što je i prikazano na slici S.15.

Unutar ovakvog modela ne očekuje se ovisnost T_{SV} o tlaku. Najveća širina područja stabilnosti je ostvarena na $T = 0$ K. Na kraju, zaključimo kako su eksperimentalno poznate veličine, na kojima se gradi ovaj model: $t_b^{'} = 10K$ [149, 150], $\frac{\partial t_b^{'}}{\partial p} = 1\mathrm{K/kbar}$ [22, 151], $\frac{1}{b}\frac{\partial b}{\partial p} = 3\ 10^{-3}\ \mathrm{kbar}^{-1}$[152]. Uz ove vrijednosti dobiva se širina područja koegzistencije od 1 kbar. Slaganje s našim eksperimentom , gdje je to područje širine 0.8 kbar je više nego dobro, pogotovo ako uzmemo u obzir relativnu grubost analize.

S.4.3 Diskusija

Ovim novim istraživanjem p, T faznog dijagrama $(\mathrm{TMTSF})_2\mathrm{PF}_6$ sugerirano je 0.8 kbar široko područje koegzistencije SV i VGS makroskopskih domena. Zanimljivo je da je neovisno o tlaku, i shodno tome promjenjivom udjelu domena, temperatura prijelaza u SV fazu ostajala ista. Model koji je razvio M. Héritier, na osnovi vrlo općenitih argumenata kao što su promjene

volumena i energije domena, predviđa formiranje heterogene faze u kojoj koegzistiraju metalne (SV) i magnetske domene. Time je ponudio plauzibilnu interpretaciju naših rezultata, ali s obzirom na općenitost argumenata, moguća je primjena i na druge faze u međusobnoj kompeticiji.

Kako je granica SV/VGS zapravo karakteristika općenitog faznog dijagrama Bechgaard-Fabre soli, to je fenomen koegzistencije nedavno pokazan i za druge materijale iz porodice: $(TMTTF)_2PF_6$, u području 4.73 -5.26 GPa, [7] kao i $(TMTTF)_2BF_4$, u području 33.5-37.5 kbar, [153]. Za posljednji materijal uočeno je i, o tlaku neovisno, gornje kritično magnetsko polje $H_{c2} = 2$ T, što se može smatrati izravnom posljedicom postojanja magnetskih makroskopskih domena u SV fazi.

Osim ovih eksperimenata koji potvrđuju ispravnost tvrdnji (naših, kao i M. Héritiera) o postojanju makroskopske koegzistencije faza, nalazimo i teorijske radove čiji rezultati dodatno ukazuju na tu mogućnost. Duprat i Bourbonnais [157] su nedavno računali interferenciju SV i VGS kanala u prisustvu snažnog odstupanja od idealnog ugnjžđenja. Osim općenito važnog ukazivanja na mogućnost pojave SV faze ispod VGS faze u blizini kritičnog tlaka i jedan detalj iz njihovog rada se povezuje s našim rezultatima: devijacija Δ/T_{VGS} od BCS omjera zbog neuniformnog karaktera VGS procjepa. Dok je ova Disertacija bila završavana, pojavio se i rad direktno motiviran našim rezultatima, Podolsky *et al.* , [159]. Autori su ujedinili AF(VGS) i SV faze u sklopu SO(4) simetrije, istovremeno pokazujući postojanje takve simetrije u Luttinger tekućinama. Zahtjevi koje SO(4) simetrija postavlja na prirodu faznih prijelaza objašnjavaju pojavu područja koegzistencije kakva su uočena na $(TMTSF)_2PF_6$ i drugim TM_2X materijalima.

S.5 Istraživanje faznog dijagrama $(La, Sr, Ca)_{14}Cu_{24}O_{41}$

Slijedi prikaz naših istraživanja električnog transporta, na $Sr_{14-x}Ca_x$-$Cu_{24}O_{41}$ materijalima, a u usporedbi sa $La_ySr_{14-y-x}Ca_xCu_{24}O_{41}$ materijalima. Rezultati koji su integralni dio ovog rada objavljeni su u sklopu četiri publikacije u APS časopisima, [78, 171, 160, 161].

S.5.1 Eksperimentalna tehnika

Uzorke kvazi-1D kuprata sintetizirala je grupa J. Akimitsu, T. Sasaki i T. Nagata sa Department of Physics, Aoyama-Gakuin University, Kanagawa, Japan. Monokristali su rekristalizirani iz kalciniranih, sinteriranih polikristala zonskim pretaljivanjem u infracrvenoj peći. Iz velikih monokristala ispiljeni su uzorci duljine 3-5 mm i presjeka 0.2-0.4 cm^2. Preciznost rezanja potvrđena je difraktometrijom X-zrakama. Radi mjerenja istosmjerne otpornosti na uzorke se montiraju 4 anularna kontakta, dok se za mjerenja kompleksne vodljivosti montiraju dva kontakta na krajeve uzorka. Dobri kontakti se postižu pečenjem u atmosferi kisika uzorka premazanog srebrnom pastom DuPont6828 na 750 K tokom 1 sata. U slučaju neuspješne pripreme kontakata mogući su artefakti: previsoka otpornost na sobi, previsoke aktivacijske energije, jaki nelinearni efekti. U mjerenjim kompleksne vodljivosti može se pojaviti previsoki kapacitet u područjima gdje bi inače trebao biti zanemariv. Mjerenja istosmjerne otpornosti vršena su u Helij-kriostatu u području 300-2 K, visokotemperaturnoj peći, 300-750 K, kao i u He-kriostatu u kojem je nosač uzoraka imao mogućnost grijanja do 400 K. Ovaj posljednji postav smo koristili kada je trebalo pažljivo izmjeriti La supstituirane uzorke upravo u okolini 300 K. U rasponu temperatura 2-700 K mjereni otpori pokrivaju 14-15 redova veličine. Stoga su korištena 4 različita postava. Osnovni postav su *lock-in* pojačala za 4kontaktna mjerenja otpora 1 mΩ-1 kΩ. Istosmjerna tehnika, sa strujnim izvorom i nanovoltmetrom do otpora 100 MΩ. Za više otpore korišten je elektrometar u V/I modu (primjenjuje se napon i mjeri struja). To je pak dvokontaktno mjerenje, kao i mjerenje najviših otpora do 2 TΩ gdje se niskofrekventni napon primjenjuje direktno na uzorak, a dobivena struja se u strujnom pretpojačalu pojačava i pretvara u napon, te očitava na lock-in pojačalu. Ta je tehnika korištena i u mjerenjima kompleksne vodljivosti, na najnižim frekvencijama, 0.01 - 10000Hz. Na višim frekvencijama koristi se analiator impendancija, 20-10 MHz. Radi tih mjerenja nosač uzoraka opremljen je tankim mjernim koaksijalnim kablovima, kako bi se

minimizirali parazitski kapaciteti. Mjerenjima pozadine, tj. mjerenjima nosača uzoraka bez montiranog uzorka, te oduzimanjem tih vrijednosti, $Y(\omega)_{open} = G(\omega)_{open} + iB(\omega)_{open}$, od rezultata za uzorke $Y(\omega) = G(\omega) + iB(\omega)$, osigurali smo da parazitni kapaciteti ne utječu na rezultate. Nakon oduzimanja pozadine se komponente kompleksne vodljivosti transformiraju u komponente kompleksne dielektrične funkcije prema:

$$\varepsilon_0\varepsilon'(\omega) = \frac{l}{S}\frac{B(\omega)}{\omega} \tag{S.13}$$

$$\varepsilon_0\varepsilon''(\omega) = \frac{l}{S}\frac{G(\omega) - G_0}{\omega} \tag{S.14}$$

gdje je ε_0 permitivnost vakuuma, 8.858 pF/m. G_0 je istosmjerna vodljivost. $\frac{l}{S}$ je omjer duljine i presjeka uzoraka, tzv. konstanta oblika uzorka. Na eksperimentalno dobiveni dielektrični odziv prilagođava se Havriliak-Negami (HN) funkcija [140]. To je poopćeni oblik Debye funkcije, često upotrebljavane za opis relaksacije u neuređenim sistemima.

$$\varepsilon(\omega) - \varepsilon_{\mathrm{HF}} = \frac{\Delta\varepsilon}{1 + (i\omega\tau_0)^{1-\alpha}} \tag{S.15}$$

$\Delta\varepsilon = \varepsilon_0 - \varepsilon_{\mathrm{HF}}$ je dielektrična jakost odziva, a ε_0 i $\varepsilon_{\mathrm{HF}}$ su statička i visokofrekventna dielektrična konstanta. τ_0 i $1 - \alpha$ su središnje relaksacijsko vrijeme i parametar oblika koji opisuje simetrično širenje distribucije relaksacijskih vremena. Rezultati mjerenja su prilagođavani metodom najmanjih kvadrata u kompleksnoj ravnini, što omogućava razlučivanje moda većeg od 0.5 pF. S obzirom na konstante oblika istraživanih uzoraka minimalna opservabilna dielektrična jakost je 400-1500 s rezolucijom čak i ± 10. Naše rezultate do 10 MHz kombiniramo sa kvazi-optičkim mikrovalnim mjerenjima, 5 to 25 cm^{-1} (150-750 GHz) , kao i sa infracrvenim mjerenjima, do 10 000 cm^{-1}, prof. M. Dressela i suradnika B. Gorshunov, P. Haas i T. Rõõm sa Sveučilišta u Stuttgartu, Njemačka.

S.5.2 Pojava VGNa duž ljestvica $Sr_{14}Cu_{24}O_{41}$

Kod izovalentno supstituiranih materijala $Sr_{14-x}Ca_xCu_{24}O_{41}$ od ukupnog broja šupljina, $\delta_h = 6$ jedna je šupljina prebačena na ljestvice, barem na višim temperaturama, i mobilna je za razliku od vrlo lokaliziranih šupljina što preostaju na lancima. Smatramo da je ta šupljina odgovorna za električni transport. Početni prikaz za temu ima osnovni materijal cijele (La, Sr, Ca)$_{14}$-$Cu_{24}O_{41}$ porodice materijala - $Sr_{14}Cu_{24}O_{41}$. Kako u ovom materijalu nema supstitucije, tako je i nered sveden na minimum. Početni prikaz rezultata

na Sl. S.16 za $Sr_{14}Cu_{24}O_{41}$ uključuje prikaz snažne korespondencije rezultata mjerenja istosmjerne i kompleksne vodljivosti (niskofrekventne dielektrične spektroskopije - NFDS). Mjerenja istosmjerne otpornosti, prikazana su u ovisnosti o inverznoj temperaturi. Oznaka $E||c$ znači da je mjereno duž c-smjera, tj. duž ljestvica. Područje temperatura je 750-50 K, vodljivost na sobi je visoka, 500 $\Omega^{-1}cm^{-1}$, potvrđujući postojanje mobilnih šuplljina na ljestvicama. Uočili smo izolator-izolator prijelaz na 210 K, širok 40 K, znatno veće relativne širine u odnosu na prijelaze u $(TMTSF)_2PF_6$, Ref. [27]. Širina prijelaza ukazuje na postojanje intrinsičnog nereda. Različite aktivacijske energije definirane su za visoko-$\Delta_{H.T.} = 900$ K i niskotemperaturnu, $\Delta_{L.T.} = 1300$ K, fazu. Dielektrični modovi dobiveni analizom kompleksne vodljivosti jakosti su $\Delta\varepsilon = 10^4$-10^5. Iznad 110 K nije bilo moguće mjeriti jer je mod napustio frekventni prozor uređaja. Pretpostavljeno ponašanje $\Delta\varepsilon$ za x=0 prikazano je crtkanom linijom, bazirano na rezultatima za $x = 3$ i 9, Ref. [160, 161]. Za te materijale snižavanjem temperature $\Delta\varepsilon$ se naglo javlja i postiže maksimum na, slijedom, $T_c = 140$ K i $T_c = 10$ K. A te temperature savršeno korespondiraju temperaturama izolator-izolator prijelaza uočenim u istosmjernim mjerenjima. Dielektrični je mod karakteriziran sa $1-\alpha = 0.8$ parametrom. Znači da je distribucija relaksacijskih vremena šira od Debyeve, ali se i sužava, sa slabljenjem moda ispod 70 K. Središnje relaksacijsko vrijeme τ_0 i istosmjerna otpornost korespondiraju, jednakom aktivacijskom energijom $\rho_{dc} \propto \tau_0 \propto e^{\Delta_{L.T.}/k_BT}$ ispod T_c. Ekstrapolacijom τ_0 do najviših temperatura dobiva se asimptotsko relaksacijsko vrijeme reda, 10^{-10}-10^{-11} s, puno dulje od uobičajenih vremena za kvazičestice, 10^{-15} s.

Vrlo veliko asimptotsko vrijeme, i jakost dielektričnog moda ukazuju na kolektivni relaksacijski mehanizam – fazonski odgovor VGNa na izmjenična električna polja. Prošireni mod ukazuje na to da je VGN zapet na nasumični potencijal pozadine. Standardna je, za fazonski odgovor, korespondencija aktivacijskih energija za ρ_{dc} i τ_0. Stoga je procjep $\Delta_{L.T.} = 1300$ K identificiran kao VGN procjep, a temperatura prijelaza, $T_c = 210 \pm 20$ K, kao izolator-VGN temperatura prijelaza.

Osim radiofrekeventnog moda fazonski odgovor VGNa je karakteriziran i zapetim (*pinned*) modom koji se očekuje u mikrovalnom području. Zapeti mod su Kitano *et al.* [162, 163] uočili u mikrovalnim mjerenjima, na 1.8 cm^{-1} (60 GHz), Sl. S.17.

Iz temperaturne ovisnosti vodljivosti u širokom frekventnom spektru, od mikrovalova do infracrvenog, nalazimo da opadanje vodljivosti počinje već ispod 240 K, [78]. Ova se temperatura slaže sa $T_{VGN} = 210 \pm 20$ K iz istosmjernih i mjerenja kompleksne vodljivosti. Infracrveni spektar opada s frekvencijom već ispod 2500 cm^{-1}, a VGN procjep se očitava kao rub u infracrvenom spektru, ≈ 900 cm^{-1}.

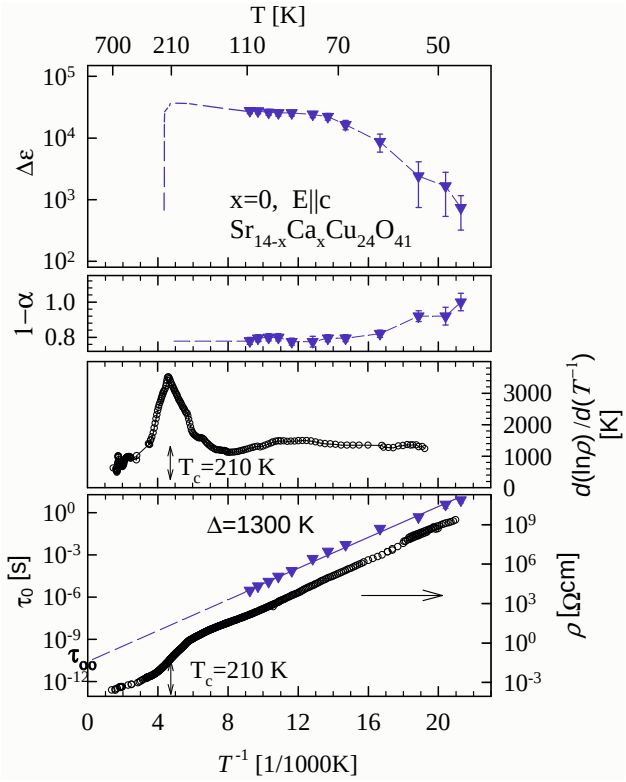

Slika S.16: Istosmjerna i NFDS mjerenja $Sr_{14}Cu_{24}O_{41}$ duž c osi. Dane su ovisnosti otpornosti i NFDS parametara o inverznoj temperaturi $1/T$, Jed. S.15. Gornja slika: Dielektrična jakost $\Delta\varepsilon$. Pretpostavljeno ponašanje $\Delta\varepsilon$ prikazano je crtkanom linijom. Druga slika s vrha: parametar 1-α opisuje simetrično širenje distribucije relaksacijskih vremena. Donja slika: Središnje relaksacijsko vrijeme τ_0 i istosmjerna otpornost su termički aktivirane $\rho_{dc} \propto \tau_0 \propto e^{\Delta_{\mathrm{L.T.}}/k_B T}$ ispod T_c s aktivacijskom energijom $\Delta_{\mathrm{VGN}} \approx 1300$ K. $T_c = 210 \pm 20$ K je dobiven logaritamskom derivacijom otpornosti. Crtkana linija naznačuje ekstrapolaciju τ_0 do asimptotskog vremena τ_∞.

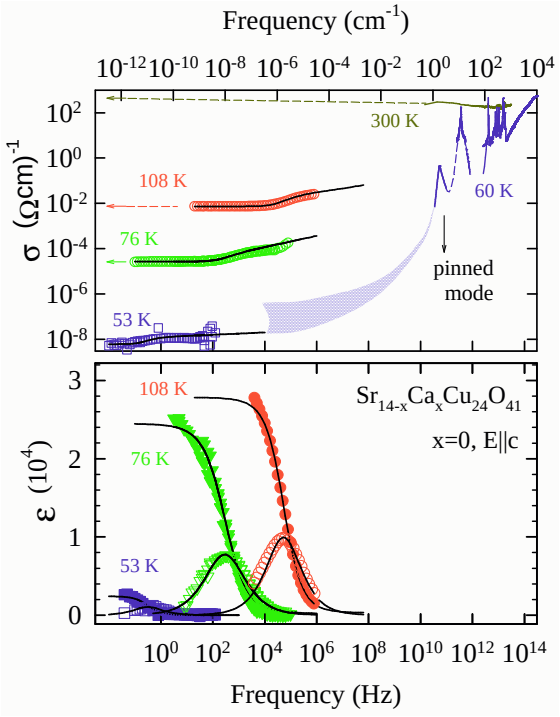

Slika S.17: Široki spektri za $Sr_{14}Cu_{24}O_{41}$, na nekoliko temperatura. Vodljivost je prikazana u gornjoj slici a kompleksna dielektrična funkcija u donjoj (imaginarni ε" i realni ε' dio, otvoreni i puni simboli, tim slijedom). Pune linije su rezulat prilagodbe na generaliziranu Debye funkciju. Mod u mikrovalnom području, na 1.8 cm^{-1}, određen je u [162]. Horizontalne strelice s lijeva označavaju istosmjernu vodljivost. Opadanje infracrvene vodljivosti na nižim temperaturama korespondira otvaranju VGN procjepa.

Standardna svojstva VGN osnovnog stanja u $Sr_{14}Cu_{24}O_{41}$

Gore predstavljeni rezultati potvrđuju kako je u $Sr_{14}Cu_{24}O_{41}$ uočen standardni fazonski odgovor VGNa na izmjenično električno polje. Standardni odgovor na istosmjerno električno polje je pak nelinearna vodljivost, [126]. Ta je vodljivost posljedica kolektivnog doprinosa jednočestičnoj vodljivosti od proklizavanja kondenzata. Model klasične čestice može opisati različite eksperimentalne rezultate povezane s nelinearnom vodljivošću, [164]. Ipak, za potpuno razumijevanje potrebno je razumjeti da faza kondenzata nije uniformna kroz realan materijal. Kondenzat je naime zapet efektivnim potencijalom zapinjanja i faza se prilagođava tom potencijalu. Potencijal zapinjanja mogu generirati nečistoće ili pak kondenzat može biti sumjerljiv s kristalnom rešetkom. Istosmjerno električno polje mora svladati taj potencijal i stoga je nelinearna vodljivost vala gustoće karakterizirana električnim poljem praga E_T iznad kojeg se javlja proklizavanje. Veličina polja praga ovisi o vrsti zapinjanja, kao i o tome je li u pitanju VGS ili VGN materijal. Kako se VGS javlja na red veličine nižim temperaturama od VGNa, to su i energijske skale, pa tako i polje praga red veličine niže. Polje praga na temperaturama 50-100 K (relevantnim za kvazi1D kuprate) doseže i do 30-130 V/cm, kao npr. u slučaju N=3 sumjerljivog VGNa u kvazi1D organskom materijalu Cu(DMe-DCNQI)$_2$, [165, 143].

No, u našim mjerenjima na $Sr_{14}Cu_{24}O_{41}$, nelinearna vodljivost i polje praga nisu uočeni. Također, rezultati Maeda *et al.* [168] mogu se interpretirati konzistentno s našim rezultatima. Svi su ovi rezultati. pak, u kontradikciji sa rezultatima Blumberg *et al.* ,[167], koji su izvjestili o nelinearnoj vodljivosti i polju praga $E_T = 0.2$ V/cm. Inspekcijom njihovih rezultata, našli smo da je nelinearni efekt na dvostrukoj vrijednosti polja praga 50%, a da je već na 1 V/cm vodljivost povećana 100%. Takvu nelinearnost smo u našim rezultatima uočili samo u slučaju loše pripremljenih kontakata na uzorku.

Rezultate mjerenja nelinearnosti moguće je kvantitativno analizirati u sklopu modela klasične čestice za VGN. U tom su modelu za standardne VGN materijale (npr. o-TaS_3, Wu *et al.* , [170]) uspješno povezani jakost dielektričnog odziva $\Delta\varepsilon$ i polje praga E_T - tj. uočena je obrnuta proporcionalnost:

$$\varepsilon_0 \Delta\varepsilon E_T = \frac{M\mathrm{e}}{\pi ab} \tag{S.16}$$

Član s desne strane predstavlja broj lanaca po jedinici poprečnog presjeka. a i b su parametri rešetke, a M je broj nosilaca naboja po jediničnj ćeliji.

e je jedinični naboj elektrona 1.6×10^{-19} C. Na primjeru o-TaS_3 nalazi se da direktna kalkulacija daje red veličine veće polje praga od izmjerenog. Direktna kalkulacija na bazi $\Delta\varepsilon \approx 3 \times 10^4$ za $Sr_{14}Cu_{24}O_{41}$, rezultira sa poljem praga 10^3 V/cm, što po analogiji možemo umanjiti za red veličine, ali će rezultat i dalje biti visoko iznad najvećeg polja primijenjenog u našem eksperimentu. Primijetimo, Blumberg *et al.* su izvjestili o dva reda veličine većem $\Delta\varepsilon$ nego u našim mjerenjima, stoga bi polje praga u mjerenjima na našem uzorku trebalo biti dva reda veličine veće od polja navedenih u njihovom radu. Tako procijenjeno polje bi iznosilo 20 V/cm, što je ponovo iznad granice našeg eksperimenta. Dakle, smatramo da je različita kvaliteta uzoraka onemogućila detekciju nelinearne vodljivosti kao standardne karakteristike fazonskog odgovora VGNa u našim mjerenjima, za razliku od mjerenja Blumberga *et al.*

Kako su u $Sr_{14}Cu_{24}O_{41}$ uočena dvije karakteristike fazonskog odgovora VGNa na izmjenično polje, to je prema Littlewoodovoj analizi moguće procijeniti m^* - efektivnu masu VGN kondenzata. Uočen je zapeti mod na Ω_0 =1.8 cm^{-1}, a relaksacijsko vrijeme niskofrekventnog dielektričnog moda pokazuje aktivacijsko ponašanje do najnižih temperatura. Kako i mjerenja istosmjerne vodljivosti σ_z pokazuju isto aktivacijsko ponašanje kao i τ_0, to se može smatrati da je efektivna masa temperaturno neovisna, (vidi str. 206). Vrijednost efektivne mase m^* ≈100 može se usporediti sa standardnim vrijednostima $m^* = 1$ za VGS [37] ili standardnim $m^* = 10^2 - 10^4$ za VGN [126]. Nadalje, kod standardnih VGN materijala moguće je povezati širinu energijskog procjepa sa efektivnom masom, $m^* \propto \Delta^2_{CDW}$ i vrijednosti m^* ≈100 i $\Delta_{CDW} = 1300$ K situiraju $Sr_{14}Cu_{24}O_{41}$ blizu standardnim VGN materijalima. Odstupanja se mogu pripisati činjenici da je veza ti veličina kontrolirana jačinom elektron-fonon vezanja, vjerojatno smanjenom u kupratima.

Zaključci

U mjerenjima istosmjernog električnog transporta na $Sr_{14}Cu_{24}O_{41}$ uočen je prijelaz u niskotemperaturno izolatorsko stanje s $T_c = 210\ K$ i $\Delta = 1300$ K. To stanje identificiramo kao VGN formiran na podsistemu ljestvica, za koje se pretpostavlja da su odgovorne za električni transport. Dok je zapeti mod uočen u mikrovalnim mjerenjima drugih autora, u našim NFDS mjerenjima uočili smo široki mod aktiviran kao i istosmjerna vodljivost. I mjerenja u blisko infracrvenom spektru potvrđuju ove rezultate, [78, 160]. Proračunali smo efektivnu masu m^* ≈100, koja je bliska standardnim vrijednostima za VGN materijale. Iako nismo uočili nelineranu vodljivost, ukazujemo na rezultate drugih autora gdje je ova uočena. Proturječje se može

objasniti različitom kvalitetom uzoraka. Iznesenim smo potvrdili teorijsku pretpostavku o pojavi VGN stanja u natjecanju sa SV stanjem u kvazi1D kupratnim materijalima.

S.5.3 Lokalizacija šupljina u lancima $La_ySr_{14-y-x}Ca_xCu_{24}O_{41}$

U neizovalentno supstituiranim materijalima broj šupljina je smanjen, $\delta_h \leq 5$, i sve su locirane na podsistemu lanaca. Nema izvješća o uređenjima na podsistemu lanaca. Kako bismo pojasnili mehanizam transporta naboja istražili smo $La_3Sr_3Ca_8Cu_{24}O_{41}$ i $La_{5.2}Ca_{8.8}Cu_{24}O_{41}$ materijale, mjerenjima istosmjernog otpora i NFDS, do 1 MHz i u temperaturnom rasponu od 750 do 35 K.

U oba materijala, $La_{5.2}$ i La_3 uočeno je aktivacijsko ponašanje iznad odgovarajućih $T_c = 330$ K i 300 K, s energijama $2\Delta = 4200$ K i 3200 K, Sl. S.18. Ispod T_c sve do 50-35 K istosmjerna vodljivost ponašala se prema Mottovu zakonu za vođenje preskakanjem nasumičnih udaljenosti (*variable-range hopping*) - VRH vođenje:

$$\sigma_{dc}(T) = \sigma_0 \exp\left[-(T_0/T)^{\frac{1}{1+d}}\right] \tag{S.17}$$

a za dimenzionalnost sistema koji vodi dobivamo $d = 1$. Fizikalni smisao T_c jest da nasumično preskakanje prelazi u preskakanje između najbližih susjeda povišenjem temperature iznad $T_c = \Delta/(2\alpha c)$ (α^{-1} je lokalizacijska duljina, c je parametar lanca), [172, 173]. VRH aktivacijske energije dobivene prilagodbom eksperimenta na Jed. S.17 za $La_{5.2}$ i La_3, $T_0^{exp} = 5 \cdot 10^4$ K i $T_0^{exp} = 2.9 \cdot 10^4$ K odgovaraju teorijskim vrijednostima $T_0^{th} = 8\Delta c\alpha \approx 4.6 \cdot 10^4$ K i $T_0^{th} = 8\Delta c\alpha \approx 3.5 \cdot 10^4$ K. Ovi rezultati direktno pokazuju da je transport naboja u neizovalentno supstituiranim kvazi1D kupratima baziran na mehanizmu vođenja preskakanjem ograničenim u jednoj dimenziji, dakle duž lanaca (gdje se naboj jedino i nalazi).

NFDS mjerenja na oba materijala $La_{5.2}$ i La_3, pokazala su potpunu neovisnost kompleksne vodljivosti o frekvenciji. Dakle, nisu uočeni dielektrični modovi, karakteristični za VGN. Općenito, kod mehanizma transporta preskakanjem očekuje se također frekventna ovisnost, no na višim frekvencijama

$$\sigma(\nu, T) = \sigma_{dc}(T) + A(T) \cdot \nu^s \qquad s \approx 1 \tag{S.18}$$

Odgovarajuće frekventno područje prijelaza u frekventno ovisnu vodljivost (ν_{co}) nalazi se iznad našeg područja, 1MHz, ali i ispod područja, 6-350 cm^{-1},

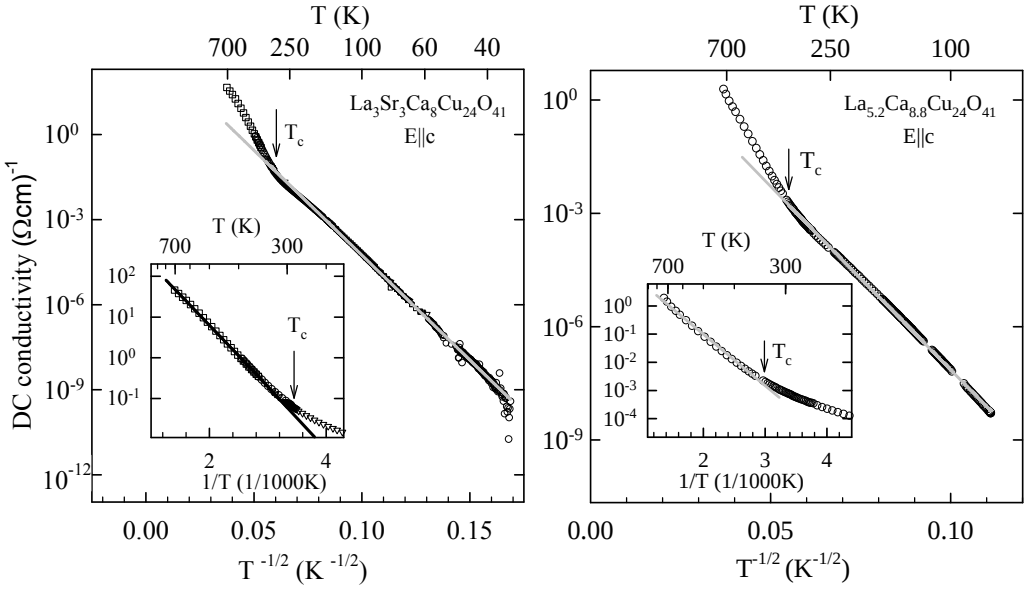

Slika S.18: Istosmjerna vodljivost σ_{dc} $La_3Sr_3Ca_8Cu_{24}O_{41}$ i $La_{5.2}Ca_{8.8}$-$Cu_{24}O_{41}$ duž c-osi *vs.* $T^{-1/2}$. Iznad ogovarajućih T_c = 300 K i 330 K, σ_{dc} slijedi aktivacijsko ponašanje, što indicira mehanizam transporta naboja preskakanjem između najbližih susjeda (pune linije u umetnutoj slici). Ispod T_c ponašanje $\sigma_{dc} \propto \exp(T^{-1/2})$ odgovara režimu vođenja preskakanjem nasumičnih udaljenosti - Mottovom VRH vođenju u jednoj dimenziji (pune linije u glavnoj slici).

u kojem je mjerila grupa iz Stuttgarta, [171]. Ipak, važno je primijetiti da interpolacija izmeu tih dvaju podruja mjerenja daje kvantitativno ispravne vrijednosti ν_{co}, kao frekvencije gdje udaljenost preskakanja pod utjecajem statičkog polja, $R_0 = (\Delta c/2\alpha T)^{1/2}$ postaje veća od udaljenosti preskakanja pod utjecajem izmjenične pobude, $R_\nu = \frac{1}{2}\alpha \ln(\nu_{ph}/\nu_{co})$, [172].

Usporedba $Sr_{14-x}Ca_x$... i $La_ySr_{14-y-x}Ca_x$... materijala

Prvo, svakako treba navesti da u $La_ySr_{14-y-x}Ca_xCu_{24}O_{41}$ materijalima nije uočena niti jedna karakteristika VGN osnovnog stanja, za razliku od Sr_{14}-$Cu_{24}O_{41}$. Drugo, električne vodljivosti (na sobi) materijala La_3 i $La_{5.2}$ su vrlo različite od one za $Sr_{14}Cu_{24}O_{41}$: 1400 i 13 u usporedbi sa 0.002 $(\Omega\text{cm})^{-1}$. Dok se kod neizovalentno supstituiranih materijala vodljivost vrlo jako mijenja sa supstitucijom, dotle kod $Sr_{14-x}Ca_xCu_{24}O_{41}$ materijala izovalentna supstitucija ne utječe bitno na vodljivost na sobi. Istovremeno, kad se

razmotre energijsko-temperaturne skale, ovisnost je obrnuta. Neizovalentna supstitucija slabo utječe na T_{co} ili aktivacijske energije, dok kod izovalentne supstitucije u $Sr_{14-x}Ca_xCu_{24}O_{41}$ od $x = 0$ do $x = 8$ temperatura faznog prijelaza i VGN procjep bivaju snažno potisnuti. Materijal $x = 8$ je važan za usporedbu zato što sadrži jednaki udio Ca kao i uspoređivani La... materijali.

Zaključci

Materijali $La_3Sr_3Ca_8Cu_{24}O_{41}$ i $La_{5.2}Ca_{8.8}Cu_{24}O_{41}$ su izolatori karakterizirani mehanizmom električnog transporta preskakanjem duž lanaca. Mikroskopski, predlažemo opis u kojem snažne lokalne distorzije lanaca stvaraju neperiodički potencijal za šupljine. Tj. lanci bakar-kisik u neizovalentno supstituiranim $La_ySr_{14-y-x}Ca_xCu_{24}O_{41}$ materijalima mogu se promatrati kao sistem u kojem nered, povezan s nasumičnim rasporedom šupljina, uzrokuje Andersonovu lokalizaciju i shodno tome se uočava Mott VRH ponašanje vodljivosti. Pretpostavljamo da to vrijedi za sve neizovalentno supstituirane materijale, gdje je broj šupljina manji od 6. Također i razlikom od tri reda veličine u vodljivosti potvrdili smo pretpostavku iz prethodnog odjeljka S.5.2. da se transport u $Sr_{14-x}Ca_xCu_{24}O_{41}$ materijalima odvija u podsistemu ljestvica. Time je dan i zaključni dokaz kako se VGN u $Sr_{14}Cu_{24}O_{41}$ formira na tom podsistemu, kao što smo predložili [160, 167].

Dok u lancima La... materijala nije uočeno nikakvo uređenje, dotle je na lancima $Sr_{14-x}Ca_xCu_{24}O_{41}$ materijala uočena uređenost naboja (istovremena s VGN uređenjem na ljestvicama). Stoga, predlažemo mogućnost faznog prijelaza u $(La, Sr, Ca)_{14}Cu_{24}O_{41}$ materijalima, gdje neuređeni lanci sa $0 \leq \delta_h < 6$ prelaze u nabojno uređen izolator za $\delta_h = 6$. Kako se pri tome transport prebacuje s lanaca na ljestvice je nerazjašnjeno i stoga ukazujemo na potrebu istraživanja u $5 < \delta_h < 6$ području faznog dijagrama.

S.5.4 Potiskivanje VGNa Ca-supstitucijom u ljestvicama $Sr_{14-x}Ca_xCu_{24}O_{41}$

Istraživani su materijali x=0, 3, 6, 8, 9, 11.5. Mjerenja istosmjerne otpornosti i NFDS vršena su duž sva tri kristalna smjera, u rasponu temperatura 750 - 2 K. Svi materijali pokazuju usporedive vodljivosti na sobi, uz naglašenu anizotropiju, Tablica S.2.

Pri prijelazu iz visokotemperaturne u VGN fazu aktivacijske energije u (c,a) ravnini rastu za $0 \leq x \lesssim 6$, indicirajući otvaranje VGN procjepa, Sl. S.19. Za razliku od standardnih VGN materijala, ovdje je visokotemperaturna (V.T.) faza izolatorska. To objašnjavamo elektronskim međudjelovanjem koje je jako u kupratima i vodi na Mottovo izolatorsko ponašanje u toj fazi. Prijelaz je relativno širok već za osnovni materijal $x = 0$ i Ca-supstitucijom se širi, a što se može pripisati neredu koji je unesen Ca-supstitucijom. VGN procjep je za x = 8,9 snažno potisnut tako da je Δ_{VGN} 2-3 puta manji od $\Delta_{\mathrm{V.T.}}$.

Analogno VGN procjepu opada i temperatura prijelaza, 210 K za $x = 0$ do 7 K za $x = 9$. Za $x = 11.5$ prijelaz se više ne uočava. Potrebno je naglasiti da postoji potpuna analogija (poklapanje karakterističnih vrijednosti, Tablica S.2) između rezultata u c-smjeru (duž ljestvica) i a-smjeru (poprijeko ljestvica). Istovremeno, u b-smjeru, poprečnom na slojeve ljestvica, svojstva istosmjernog električnog transporta su različita. Uočavaju se drugačije aktivacijske energije, a ne registriraju se fazni prijelazi. Tj., za x = 3,9 javlja se samo jedna aktivacijska energija u cijelom temperaturnom području, dok za $x = 0$ postoji promjena u aktivaciji na 170 K. No kako je tu aktivacijska energija na visokim temperaturama viša od bilo koje određene u c- ili a-smjeru, to ova promjena najviše podsjeća na promjenu u transportu preskakanjem kod $La_ySr_{14-y-x}Ca_x$-$Cu_{24}O_{41}$ materijala. Vjerojatno se transport naboja u smjeru poprečnom na slojeve ljestvica odvija putem preskakanja između najbližih susjeda. Treba napomenuti da pojava vrha u logaritamskoj derivaciji $d(\ln\rho)/d(T^{-1})$, Sl. S.19, jasno ukazuje na fazni prijelaz i dugodosežno VGN uređenje u (c,a) ravnini za $x \lesssim 6$. Dotle, za x = 8,9 materijale pojava jedino promjene aktivacije otpornosti, (u oba smjera unutar ravnine ljestvica), naznaka je da se uspostavlja samo VGN uređenje konačnog dosega.

Naglašena dielektrična relaksacija na niskim frekvencijama uočena za sve materijale x=3, 6, 8, 9, kao i za osnovni $x = 0$ (Sl. S.20) pruža dokaze o formiranju VGNa [78, 160]. Glavne karakteristike relaksacije ne mijenjaju se kvalitativno s Ca-supstitucijom $0 \leq x \leq 9$: dielektrična jakost $\Delta\varepsilon = \varepsilon_0 - \varepsilon_{HF} \approx 5 \times 10^4$, simetrično širenje distribucije relaksacijskih vremena $1 - \alpha \approx 0.8$, i centralno relaksacijsko vrijeme τ_0, koje je termički aktivirano,

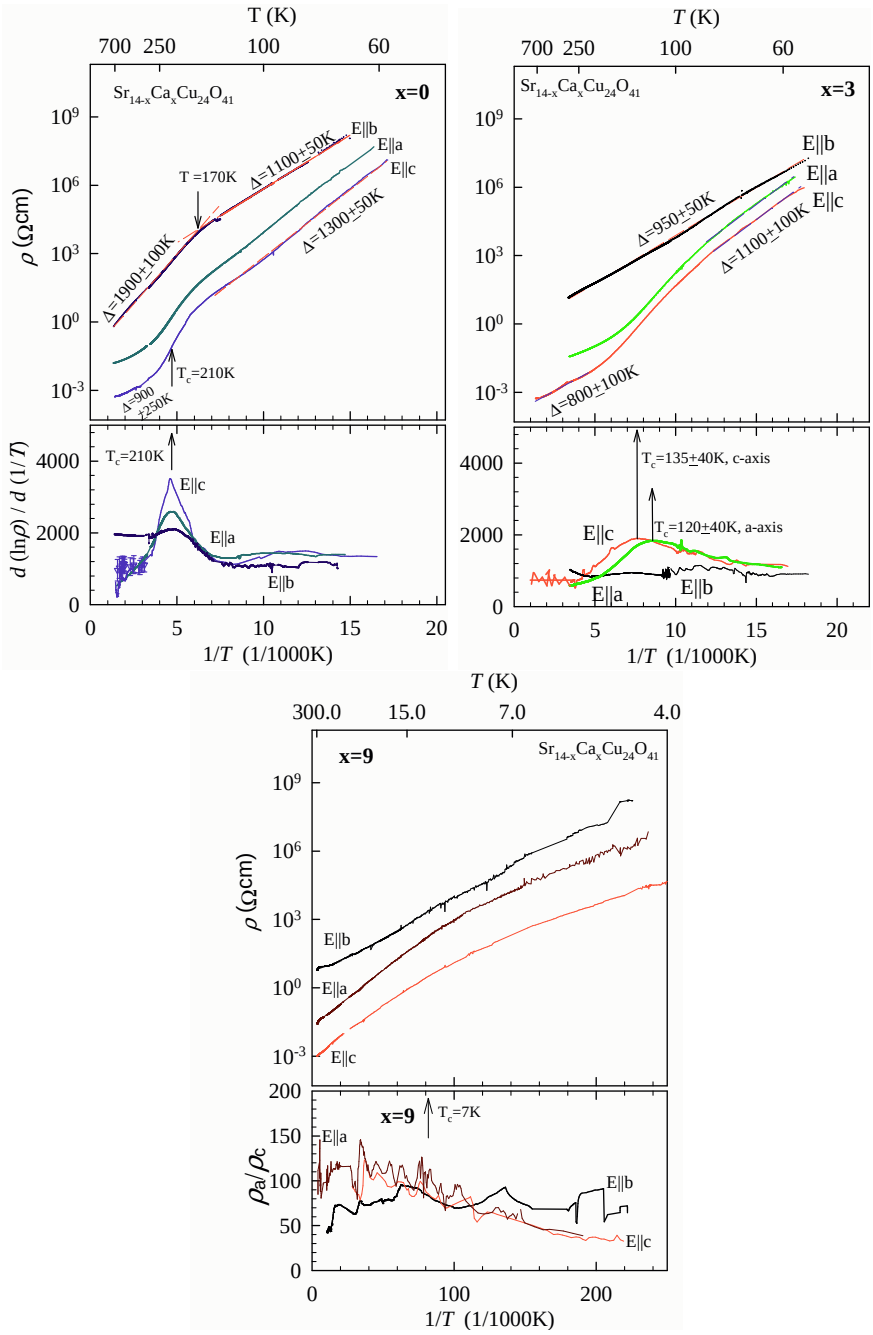

Slika S.19: Rezultati mjerenja istosmjerne otpornosti za tri reprezentativna materijala x=0, 3, 9, duž triju kristalnih osi. Odgovarajuće logaritamske derivacije otpornosti za sva tri smjera su također prikazane. ρ_{dc} je termički aktiviran i aktivacijske energije su naznačene. Dok su unutar (c-a) ravnine izotropne, sasvim su različite u b-smjeru.

analogno istosmjernoj vodljivosti; $\tau_0(T) \propto \rho(T)$ (vidi također Sl. S.16). Naši rezultati demonstriraju kako je fazni prijelaz u VGN stanje snažno potisnut Ca-supstitucijom. Savršena korespondencija između temperatura na kojima se $\Delta\varepsilon$ javlja i postiže maksimum sa temperaturama prijelaza određenim iz istosmjerne otpornosti, postoji za oba smjera u (c-a) ravnini ljestvica.

Analogija između dvaju smjerova unutar ravnine ljestvica postoji samo za x=0, 3, (Sl.S.21) kao i $x = 6$ materijale, dok se za materijale $x = 8$,9 nije javio dielektrični odziv u a-smjeru, duž prečkica. Također treba primijetiti da je dielektrični odziv u poprečnom, a-smjeru red veličine manje jakosti od onoga u c-smjeru. U trećem b-smjeru, poprečnom na ravninu, nisu uočene karakteristike dielektričnog odziva VGNa. Kao i u istosmjernim mjerenjima, može se primijetiti analogija transporta u b-smjeru sa transportom duž neuređenih lanaca $La_ySr_{14-y-x}Ca_xCu_{24}O_{41}$ materijala.

Zaključci

U 1D materijalu očekuje se stvaranje VGNa duž lanaca. Detekcija dielektričnog odziva u radio-frekventnom spektru, karakterističnog za VGN, ali u poprečnom smjeru je neočekivana, [127]. Ipak, kako je zbog vezanja među lancima VGN vektor ugnježđenja $Q(2k_F, \pi/b)$, to Q^{-1} nije paralelan osi lanaca. Tj. kako integrali prekrivanja $t_\perp$ nisu zanemarivi, naboji kondenzirani u VGN imaju i stupanj slobode u smjeru preklapanja orbitala. Shodno tome, fazonski odgovor VGNa bi se mogao pojaviti i u poprečnom smjeru na lance. No, dosada je fazonski odgovor bio uočen samo duž osi najviše vodljivosti, i prema dostupnim saznanjima, nije bilo rezultata za poprečne smjerove. Nadalje Kitano *et al.* , koji su uočili zapeti mod u c-smjeru nisu ga pronašli u a-smjeru, no može se ocijeniti da se taj mod nalazi na višim frekvencijama, iznad granice eksperimenta tih autora.

Naglasimo i da omjer $\Delta\varepsilon$ u c- i a-smjeru možemo povezati i sa anizotropijom u istosmjernoj otpornosti ρ_a/ρ_c, koji su istog reda veličine 10 za $x \leq 8$, dok za $x = 9$ materijal nestaje odziv u poprečnom smjeru, kao što se i anizotropija povećava, do 160, Tablica S.2.

Ukratko, ustanovili smo kako u (c,a) ravnini ljestvica nastaje 2D dugodosežno uređenje VGNa, i postavili 2D model anizotropne fazonske disperzije.

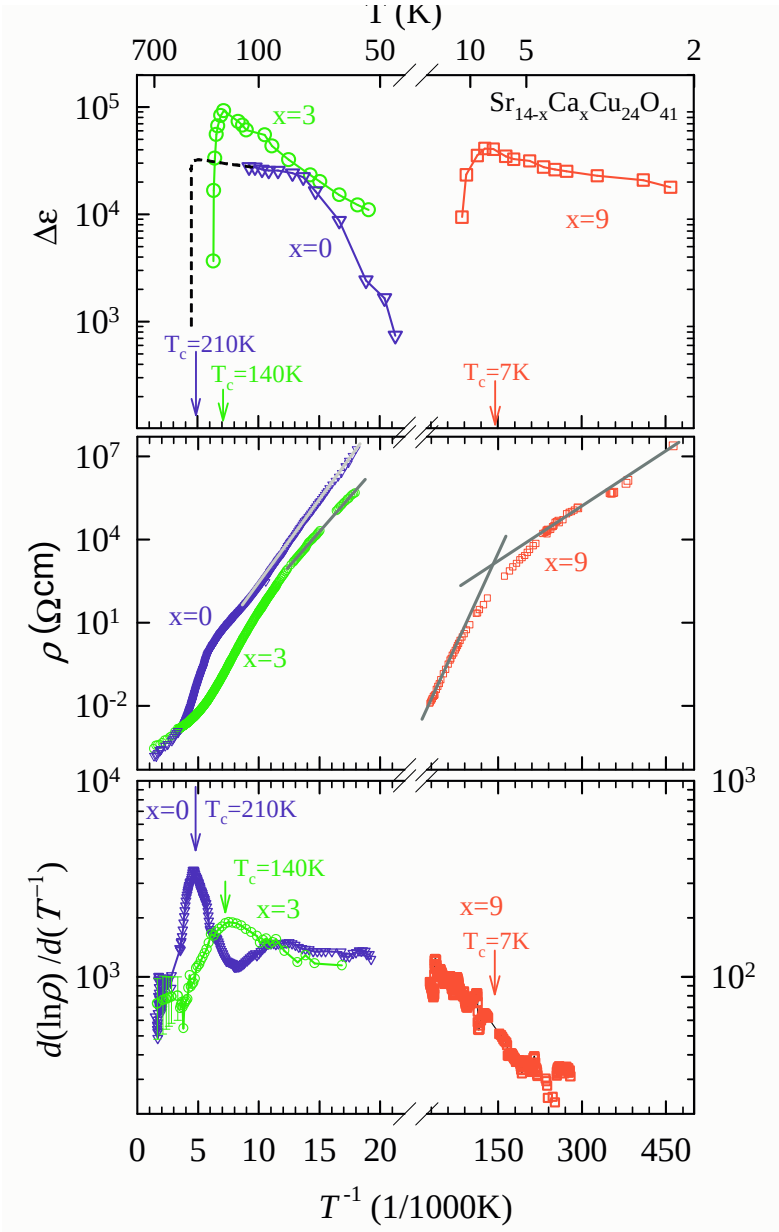

Slika S.20: Temperaturna ovisnost dielektrične jakosti $\Delta\varepsilon$ VGN niskofrekventnog moda (gornja slika) i istosmjerne otpornosti ρ (srednja slika) u $Sr_{14-x}Ca_xCu_{24}O_{41}$ za tri materijala x. Mjerenja su duž smjera ljestvica. Strelice indiciraju VGN temperaturu prijelaza T_c, određenu iz logaritamske derivacije otpornosti. Temperature gdje $\Delta\varepsilon$ postiže maksimum, savršeno odgovarju tim T_c. Pretpostavljeno ponašanje $\Delta\varepsilon$ za $x = 0$, na osnovi uočenog za $x = 3$ i 9, prikazano je crtkanom linijom.

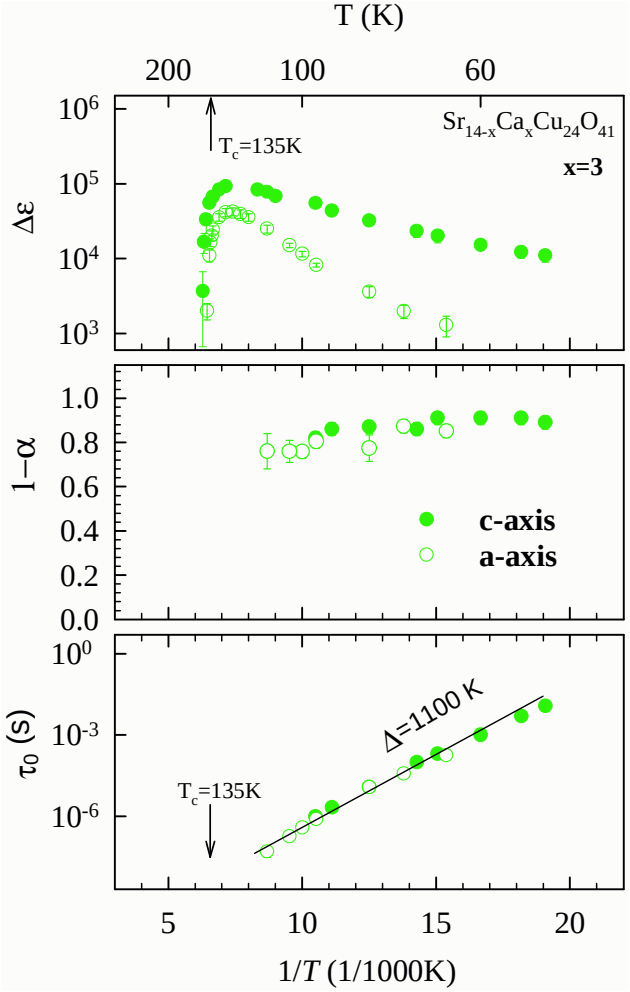

Slika S.21: Parametri dielektričnog odziva za reprezentativni materijal x=3, dobiveni za mjerenja gdje je izmjenično polje primijenjeno duž i poprijeko ljestvica, tj. duž c- i a-smjera. Gornja slika: dielektrična jakost $\Delta\varepsilon$. Maksimum $\Delta\varepsilon$ se nalazi na istoj temperaturi za oba smjera. Ova temperatura koincidira sa T_c određenim iz logaritamske derivacije otpornosti, Fig. S.19. Srednja slika: parametar 1-α opisuje simetrično širenje distribucije relaksacijskih vremena, koje je isto za oba smjera. Donja slika: centralno relaksacijsko vrijeme τ_0 isto je za oba smjera. τ_0 je termički aktiviran; $\tau_0 \propto e^{\Delta_{CDW}/k_BT}$ ispod T_c, s aktivacijskom energijom $\Delta_{CDW} \approx 1100$ K jednakom kao za istosmjernu otpornost.

	σ_{RT} (S/cm)	T_c (K)	Δ_{CDW} (K)	$\Delta_{\mathrm{H.T.}}$ (K)	ρ_i/ρ_j 300K	ρ_i/ρ_j CDW	$\Delta\varepsilon_{max}$ at T_c	$\Delta\varepsilon_c/$ $/\Delta\varepsilon_a$
x=0 c-os	500	210	1300 ± 50	900 ± 250			3×10^4	7.5
a-os	17	210	1300 ± 50	800 ± 300	ρ_a/ρ_c 30	ρ_a/ρ_c 15	4×10^3	
b-os	0.03	T_{co} 170	$\Delta_{\mathrm{L.T.}}$ 1100 ± 50	1900 ± 100	ρ_b/ρ_c 10000	ρ_b/ρ_c 300	no mode	
x=3 c-os	400	140	1100 ± 50	800 ± 100			1×10^5	2.5
a-os	28	120	1100 ± 50	800 ± 300	ρ_a/ρ_c 13	ρ_a/ρ_c 3	4×10^4	
b-os	0.07	—	950 ± 50	950 ± 50	ρ_b/ρ_c 6000	ρ_b/ρ_c 15	no mode	
x=6 c-os	300	55	300 ± 40	280 ± 60			9×10^4	—
a-os	70	55	300 ± 40	360 ± 60	ρ_a/ρ_c 4	ρ_a/ρ_c 5	—	
x=8 c-os	600	11	80 ± 10	160 ± 20			5×10^4	∞
a-os	54	11	80 ± 10	160 ± 20	ρ_a/ρ_c 10	ρ_a/ρ_c 12	no mode	
x=9 c-os	1200	7	30 ± 5	100 ± 20			4×10^4	∞
a-os	40	7	30 ± 5	100 ± 20	ρ_a/ρ_c 30	ρ_a/ρ_c 150	no mode	
b-os	0.15	—	70 ± 10	70 ± 10	ρ_b/ρ_c 10000	ρ_b/ρ_c 30000	no mode	
x=11.5 c-os	1000	T_{co} 6.5	$\Delta_{\mathrm{L.T.}}$ 5	$\Delta_{\mathrm{H.T.}}$ 22 -ispod 50K		ρ_i/ρ_j L.T.	no mode	
a-os	100	6.5	5	22 -ispod 50K	ρ_a/ρ_c 10	ρ_a/ρ_c 50	no mode	

Tablica S.2: Rezultati mjerenja istosmjerne vodljivosti za $Sr_{14-x}Ca_x$-$Cu_{24}O_{41}$ materijale, mjereni duž triju kristalnih osi: vodljivost na sobnoj temperaturi, VGN temperatura prijelaza, VGN aktivacijska energija, aktivacijska energija u visokotemperaturnoj fazi, anizotropija vodljivosti na 300K, anizotropija u VGN fazi. Radi usporedbe dani su i NFDS rezultati, tj. maksimumi jakosti dielektričnog odziva, za c- i a-smjerove, za koje je dielektrični odziv uočen. Omjer maksimuma, $\Delta\varepsilon_c/\Delta\varepsilon_a$, može se povezati s anizotropijom istosmjerne vodljivosti ρ_a/ρ_c.

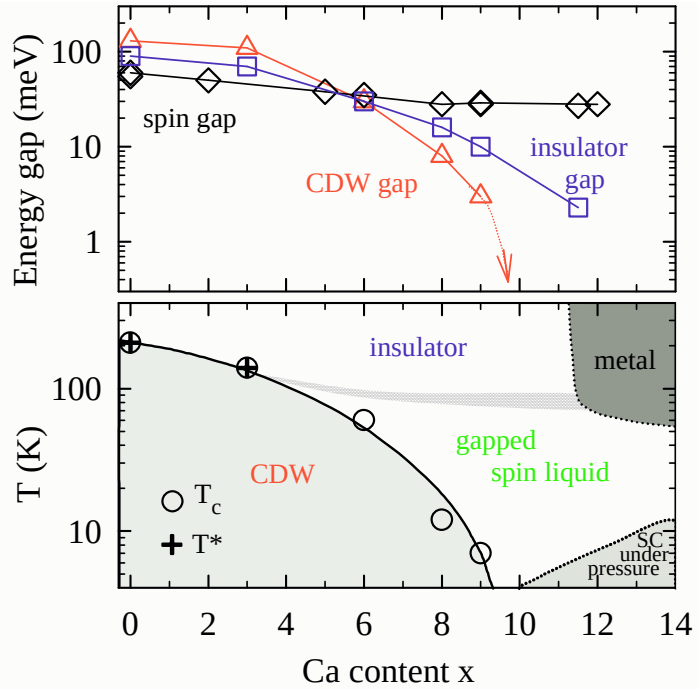

Slika S.22: Gornja slika: Ovisnost energijskih skala u ljestvicama $Sr_{14-x}Ca_x$-$Cu_{24}O_{41}$ u ovisnosti o Ca-udjelu. Donja slika: Kvalitativni fazni dijagram za $Sr_{14-x}Ca_xCu_{24}O_{41}$ u funkciji Ca-udjela.

S.6 Diskusija

S.6.1 Fazni dijagram ljestvica i lanaca

Slika S.22 sažima naše rezultate mjerenja transporta naboja u ljestvicama $Sr_{14-x}Ca_xCu_{24}O_{41}$. Visoko-temperaturno stanje je izolatorsko. Ispod izolator-izolator prijelaza identificirali smo VGN stanje koje je snažno potisnuto Ca-supstitucijom. V.T. stanje opstaje i pri Ca-supstitucijama gdje se javlja supravodljivost, i tek primjena tlaka 3-6 GPa obnavlja metalna svojstva i omogućava pojavu SV na najnižim temperaturama, 12 K ili manje, ovisno o tlaku i udjelu Ca. Naše rezultate treba korelirati s mjerenjima u magnetskom sektoru, gdje je osnovno stanje spinska tekućina, karakterizirana procjepom u spektru spinskih ekscitacija. Spinski procjep za razliku od VGN procjepa opstaje i do $x = 12$, kao što i temperatura prijelaza T^* iz paramagnetskog u stanje spinske tekućine ostaje barem oko 100 K, [104].

Napomenimo da se VGN stanje standardno javlja prilikom metal-izolator prijelaza. Stoga je potrebno pokušati objasniti porijeklo V.T. faze. S obzirom na vodljivost na sobi i dimenzije jedinične ćelije u $Sr_{14-x}Ca_x$-

$Cu_{24}O_{41}$, prema Drude modelu, srednji slobodni put nosilaca naboja je manji od parametra lanca, kao i od vlastite de Broglie valne duljine tih kvazičestica. Time je zadovoljen Ioffe-Regel kriterij, za koji je Mott predložio da naznačava situaciju kad nered u sistemu lokalizira nosioce te dolazi do metal-izolator prijelaza, "Andersonova" prijelaza. Ipak, 1D kuprati su sistem blizak polupopunjenju, a kako je unutaratomska elektronska interakcija jaka $U = 3 - 4eV$ ($U/4t > 1$) i Mottova lokalizacija (Mott izolator, tj. nabojno uređen izolator) je moguće objašnjenje svojstava V.T. faze, ali i pojave VGN stanja.

Na ovom mjestu, prikladno je i razjasniti mehanizam kojim V.T. i VGN faze bivaju potisnute pri Ca-supstituciji. Ca-supstitucija povećava transfer šupljina s lanaca na ljestvice. Time se sistem udaljava od polupopunjenja. Također se pri tome povećavaju i transfer integrali t, tako da opada $U/4t$ omjer. Oba utjecaja ukazuju na slabljenje uvjeta za Mott lokalizaciju. Spomenimo i da je utjecaj tlaka analogan efektu Ca-supstitucije. Kako je VGN snažnije potisnut od V.T. faze dodatni utjecaj moguće je potražiti u povećanju dimenzionalnosti sistema, standardnom mehanizmu u kvazi1D materijalima. No, taj je ovdje isključen, budući se anizotropija transporta u ravnini ljestvica ne mijenja. Najvjerojatnije je nered unesen Ca-supstitucijom (indiciran širenjem VGN prijelaza) odgovoran za pojačano potiskivanje VGN faze. Mikroskopski, deformacije ljestvica se javljaju zbog neregularne koordinacije Sr^{2+} i Ca^{2+} iona [70, 71], kao i zbog smanjenja b parametra, tj. prbliženja podsistema ljestvica i lanaca. Specifično, teorijski rad Tsuchiizu i Suzumura, [120], ukazao je i na mogućnost da smanjenje omjera međuatomske i unutaratomske interakcije U/V utječe na potiskivanje VGNa i eventualnu pojavu SV stanja na visokim x. Promjenu V ti autori su korelirali i sa promjenom popunjenja - tj. retransferom šupljina.

Kako bismo naglasili utjecaj vezanja između podsistema, konstruirali smo fazne dijagrame ljestvica i lanaca, gdje se uočava visok stupanj korelacije, Sl. S.23. 2D dugodosežno VGN uređenje na ljestvicama, kao i 2D uređenje naboja na lancima prelaze u kratkodosežno za $x \gtrsim 6$. I u magnetskom sektoru postoji korelacija. Na podsistemu ljestvica javlja se osnovno stanje spinske tekućine, istovremeno s pojavom uređenog stanja antiferomagnetski dimera na lancima. No, dok ovo posljednje biva zamijenjeno AF uređenjem na $x \gtrsim 11$, dotle spinski procjep na ljestvicama opstaje do najviših x, dapače postoji i pod tlakom, kad se javlja SV.

S.6.2 Priroda VGN i SV faze u ljestvicama

Naši rezultati pokazuju da fazonska disperzija u radio-frekventnom području postoji i duž smjera ljestica i duž poprečnog smjera, prečkica, što je indikacija

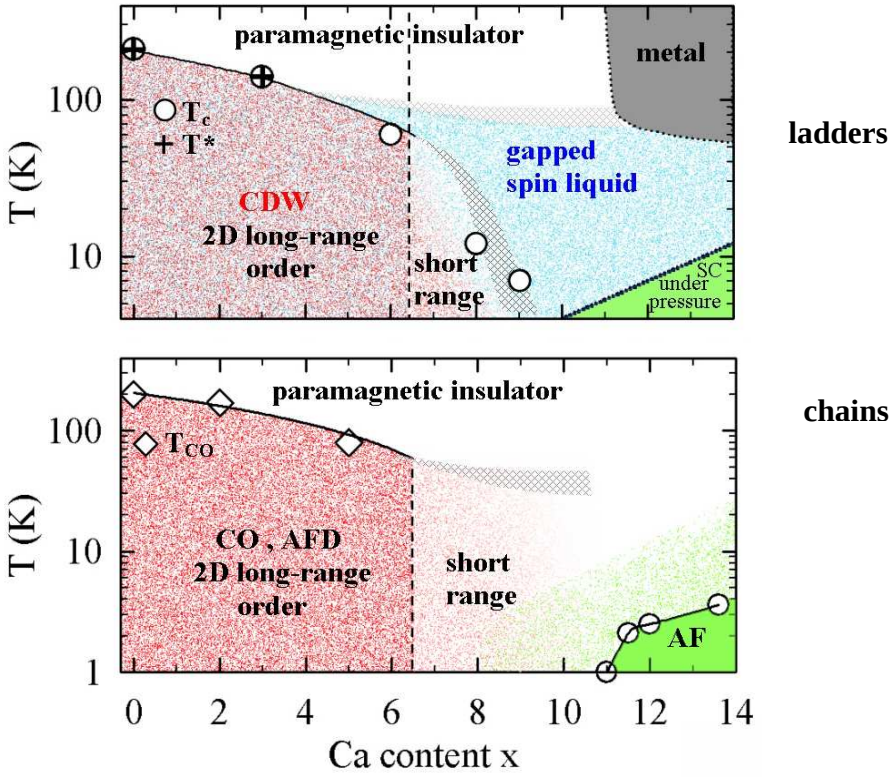

Slika S.23: Korespondencija faznih dijagrama ljestvica i lanaca, prikazani su i nabojni i spinski sektor. Gornja slika predstavlja ljestvice (*ladders*), a donja lance (*chains*).

da VGN u ljestvicama $Sr_{14-x}Ca_xCu_{24}O_{41}$ nije standarnog tipa. Ipak, u principu ne nalazimo razlog, zašto takva observacija ne bi bila objašnjiva proširenjem 1D fazonskog modela na 2D.

Nadalje, $Sr_{14-x}Ca_xCu_{24}O_{41}$ su kvazi1D sistem s jakim elektron-elektron interakcijama, i Mott lokalizacija vjerojatno vodi na nastanak V.T. faze, tako da bi i osnovno stanje moglo biti stanje djelomično uređenog naboja. Vjerojatno VGN na ljestvicama pada između dvije granice: uređenja itinerantnih i lokaliziranih naboja. Ipak, kolektivne ekscitacije su slične onima standardnog VGNa, a i efektivna masa kondenzata $m^* \approx 100$ u granicama je standardnih VGN materijala.

Osnovno stanje u ljestvicama $Sr_{14-x}Ca_xCu_{24}O_{41}$ moglo bi također biti i neko od egzotičnih stanja gdje je angularni moment u Peierlsovom kanalu različit od $s = 0$, tj. $p = 1$ ili $l = 2$. Na razmatranje takvih stanja se nailazi u radu Mazumdar i Campbell [121], koji naglašavaju da standardna slika za valove gustoće, upravljana ugnježđenjem nije primjenjiva na jako interagirajuće sisteme. Nadalje, Tsuchiizu *et al.* , [120] razmatrajući parametre U i V primjenjive za kuprate, ukazuju na pojavu *vezne*-VGN faze (*bond*-CDW) između VGN i VGS faza.

Ipak, standardni primjer pojave uređenosti naboja ($4k_F$ VGN- *Wigner kristal*) u Fabre soli $TMTTF_2AsF_6$ [185], pokazuje kako se to osnovno stanje ne može eksperimentalno usporediti s VGN na ljestvicama. Divergencija dielektrične jakosti koja prati pojavu uređenosti naboja u $TMTTF_2AsF_6$, sasvim je različita od nagle pojave dielektrične jakosti na prijelazu u VGN stanje u $Sr_{14-x}Ca_xCu_{24}O_{41}$. Disproporcionacija naboja, uočena u NMR rezultatima za $TMTTF_2AsF_6$, svakako nije uočena u $Sr_{14-x}Ca_x$-$Cu_{24}O_{41}$, [186, 98].

Nakratko, osvrćemo se i na SV stanje koje se javlja u $10 \leq x \leq 13.6$, pod visokim tlakom 3-6 GPa, ispod 12 K. U Dagottovu modelu spinski procjep neohodan je element u mehanizmu nastanka SV. Taj procjep uistinu i opstaje i uočen je iznad SV prijelaza u NMR mjerenjima pod tlakom [104, 108]. Intrigantna je ovdje odsutnost pojave SV stanja u $x = 0$ materijalu, gdje tlak također uklanja izolatorsku fazu, i gdje također opstaje spinski procjep. Korelirano je to s pojavom niskoležećih stanja unutar procjepa, koja se ne javljaju kod $x = 0$, ali postoje u supravodljivom $x = 12$. Tj. SV se javlja tek ako postoji dovoljno velika gustoća nosilaca na Fermi površini, što je kontradiktorno Dagottovu modelu. I pojava Hebel-Slichter vrha ukazuje na konačan procjep u svim smjerovima, nesukladan d-simetriji predloženoj od Dagotta. Radi interpretacije tih rezultat, Fujiwara *et al.* predložili su kako SV stanje nije uspostavljeno sparivanjem na jednoj prečkici, već izeđu susjednih.

Na kraju prikaza naših rezultata i pripadajuće diskusije, uočimo da je

priroda VGN faze blisko povezana s prirodom supravodljivosti u $Sr_{14-x}Ca_x$-$Cu_{24}O_{41}$ materijalima. Jesu li ova stanja nekonvencionalna, karakterizirana simetrijom različitom od $s = 0$, nije još razjašnjeno. Svakako su potrebna daljnja istraživanja radi razjašnjenja tih pitanja.

S.7 Završni zaključci

Ova studija kvazi-jednodimenzionalnih materijala usmjerila se na razumijevanje i unaprijeđenje eksperimentalnih faznih dijagrama. Posebno, natjecanje i/ili koegzistencija supravodljivosti i stanja valova gustoće bilo je razmotreno kroz istraživanja transporta naboja. Istraživani su kvazi1D materijali: jednostavni lančasti $(TMTSF)_2PF_6$ iz 25 godina poznate porodice Bechgaard-Fabre soli s prijenosom naboja i noviji (La, Sr, Ca)$_{14}$Cu$_{24}$O$_{41}$, kompozitni lanac/ljestvice kuprati. Svako je istraživanje novih kvazi1D materijala (kao što su ovi kuprati) instruktivnije u usporedbi s rezultatima na reprezentativnom materijalu $(TMTSF)_2PF_6$.

Izvedena je detaljna studija istosmjerne otpornosti i kritičnih struja u području 6.8–11 kbar faznog dijagrama $(TMTSF)_2PF_6$, s dosad nepostignutom kontrolom tlaka. Pronađeno je usko područje 8.65–9.43 kbar, gdje koegzistiraju VGS/metal i VGS/SV, tj., ispod metal/VGS prijelaza, dijelovi uzorka ostajali su metalni. Daljnjim sniženjem temperature ispod 1.2 K metalni bi dijelovi prešli u SV stanje. Volumni udio VGS faze je opadao s porastom tlaka u području koegzistencije. Dva su različita određenja volumnog udjela ukazala na dva režima. U području 9.1–9.43 kbar domene se protežu cijelom duljinom uzorka. U području 8.65–9.1 kbar Josephsonovi spojevi (ili centri proklizavanja faze), prisutni su duž vodljivih kanala u VGS/SV regiji.

Predložen je jednostavan model koegzistencije, baziran na varijacionoj teoriji. Indicirao je kako je moguća pojava nehomogene faze, čija je slobodna energija manja od energije homogene faze (VGS ili metalne). Time se kvalitativno, pa i kvantitativno objašnjavaju naši rezultati. Istovremeno, mikroskopski modeli, objašnjavaju naše rezultate samo kvalitativno.

Za razliku od $(TMTSF)_2PF_6$ gdje su interakcije slabe, u kvazi 1D kupratima vrijede modeli jakog vezanja. Kad se diskutira natjecanje/koegzistencija faza vala gustoće i SV unutar faznog dijagrama spojeva $A_{14}Cu_{24}O_{41}$ (A=Sr, Ca, La, Y...) teorijski pristup je teži i još nedovoljno razvijen.

Studirali smo dvije porodice materijala te smo u $La_ySr_{14-y-x}Ca_x$-$Cu_{24}O_{41}$ materijalima ustanovili da je mehanizam transporta naboja preskakivanje šupljina duž podsistema lanaca i da se taj podsistem ponaša kao 1D izolator s neredom kao pokretačem lokalizacije.

U $Sr_{14-x}Ca_xCu_{24}O_{41}$materijalima, na podsistemu lanaca javlja se dugodosežno uređenje naboja povezano sa spinskim uređenjem. No, tu postoje šupljine transferirane u podsistem ljestvica, koje su mobilne i zaslužne za električni transport. Otvoreno je pitanje kako se transport naboja prebacuje s lanaca na ljestvice kad broj šupljina raste od manje od 5 kod neizovalentno dopiranih $La_ySr_{14-y-x}Ca_xCu_{24}O_{41}$ do 6 šupljina (s barem

jednom transferiranom u ljestvice) u izovalentno supstituiranim $Sr_{14-x}Ca_x$-$Cu_{24}O_{41}$. Moguće postojanje faznog prijelaza u području broja šupljina $\lesssim 6$ trebalo bi razriješiti daljnjim istraživanjima.

Transport naboja (u podsistemu ljestvica) studiran je u materijalima x=0, 3, 6, 8, 9, 11.5. Ispod T_c = 210 K za x=0 do 7 K za x=9 uočen je prijelaz u izolatorsko, VGN stanje. VGN procjep je potisnut naglo, kao i T_c od 1300 K do 30 K. VGN je identificiran mjerenjima niskofrekventne dielektrične spektroskopije, gdje je uočen termalno aktivirani široki fazonski odgovor. Dielektrični odziv se pojavljivao točno na T_c iz istosmjernih mjerenja. Također je prethodno objavljeno da je uočen zapeti mod, kao još jedna tipična karakteristika fazonskog odgovora VGNa. Koristeći te rezultate, proračunali smo efektivnu masu m^* ≈100 kondenzata, u granicama za standardne VGN materijale. Nelinearna vodljivost, proklizavanjem VGN kondenzata nije uočena (iako je objavljena od drugih autora), vjerojatno zbog različite kvalitete uzoraka koja je podigla polje praga za naše uzorke iznad nama eksperimentalno dostupnih električnih polja.

Istraživanja anizotropije unutar ravnine ljestvica (c,a) za $Sr_{14-x}Ca_x$-$Cu_{24}O_{41}$, $0 \leq x \leq 9$ ukazala su na skup svojstava sličan za oba smjera. Dok je sama anizotropija otpornosti ρ_a/ρ_c reda veličine 10, temperature prijelaza u VGN stanje i sam VGN procjep bili su isti. Najinteresantnije je što je u oba smjera uočena i VGN fazonska relaksacija, slabija za red veličine u poprečnom, a-smjeru. Nije uočena samo za x=8,9 što korelira sa pojačanjem anizotropije otpornosti koja za x=9 doseže i 160 u VGN stanju. Dakle, naši rezultati impliciraju da se u ljestvicama uspostavlja dugodosežno 2D uređenje VGNa. Važno je napomenuti, da je to praćeno i 2D uređenošću naboja na podsistemu lanaca. Oba uređenja prelaze u kratkodosežno za $x \geq 6$ i za $x \leq 11.5$ nestaju. Ova koreliranost naglašava povezanost podsistema.

Visokotemperaturna (V.T.) faza znakovito je izolatorska, unatoč visokoj vodljivosti na sobi (jednakoj onoj $(TMTSF)_2PF_6$-metala). V.T. faza robusnija je od VGNa i opstaje do najviših x. V.T. aktivacijska energija je za $x \lesssim 6$ usporediva s VGN procjepom, no na višim x postaje barem 2-3 puta veća.

Kompleksnosti doprinosi i ponašanje spinskog procjepa koji je skoro neovisan o Ca-supstituciji, i opstaje do najviših x=12, za razliku od VGN procjepa.

Iznad 3 GPa u $Sr_{14-x}Ca_xCu_{24}O_{41}$, $10 \leq x \leq 13.6$ tlak potiskuje izolatorsku V.T. fazu i uspostavlja metalno ponašanje prije prijelaza u supravodljivo stanje. Pri tome spinski procjep opstaje, što je predviđeno i teorijski. Ali, niskoležeća pobuđenja su uočena unutar spinskog procjepa, što dovodi u pitanje prirodu SV faze, ukazujući na s-tip simetrije, iako teorijska razmatranja vode na d-tip.

Nije poznato opstaje li AF stanje na lancima za $x > 11$ pod tlakom, istovremeno sa SV stanjem. Ta mogućnost povlači pitanja o mogućnosti koegzistencije SV i magnetizma, ali na različitim podsistemima kompozitnog materijala.

Naposlijetku, iznesimo pretpostavku da je porijeklo V.T. i VGN faza u ljestvicama i mehanizam njihovog potiskivanja blisko povezan. Kako je V.T. faza podložna potiskivanju tlakom to je Andersonova lokalizacija isključena kao uzrok izolatorskog ponašanja. No kako su kuprati blizu polupopunjenja i kako je unutaratomska Coulombska repulzija jaka $U = 3 - 4eV$ $(U/4t > 1)$, Mottova je lokalizacija prihvatljivija kao uzrok nastanka V.T. faze. Odstupanje od polupopunjenja (transferom šupljina u ljestvice) ili povećanje integrala t pri Ca-supstituciji/tlaku (ekvivalentnog su učinka), mogu ukloniti V.T. fazu. No kako pri tome anizotropija u ravnini ljestvica nije promijenjena, slabljenje ugnježđenja nije moguć mehanizam za objašnjenje snažnog potiskivanja VGN faze u odnosu na V.T. Najplauzibilniji je utjecaj nereda, unesenog u podsistem ljestvica Ca/Sr zamjenom, ali i povećanjem vezanja s podsistemom lanaca.

VGN u ljestvicama vjerojatno nije standardnog tipa. To je indicirano uočenom pojavom anizotropnog fazonskog odgovora, kao i time što su kuprati sistem s jakim elektron-elektron interakcijama. Posebno je daljnje istraživanje potrebno kako bi se ustanovilo je li 2D fazonski odgovor specifičan uređenju na ljestvicama, ili je zajednički kvazi-2D sistemima s uređenošću naboja. VGN u ljestvicama vjerojatno pada između uređenja itinerantnih i lokaliziranih naboja. Osnovno stanje ljestvica bi također moglo biti jedna od egzotičnih, nabojno uređenih faza, karakteriziranih sparivanjem koje nije s-tipa, no kolektivne ekscitacije i odziv na vanjska pobuđenja nisu teorijski opisani za te faze.

Na kraju, priroda i potiskivanje VGNa u ravnini ljestvica blisko je povezana sa scenariom pojave supravodljivosti. Ostaje pitanje o (ne)konvencionalnosti prirode tih stanja, uz potrebu daljnjeg istraživanja kako bi se ta pitanja pojasnila.

Bibliography

[1] D. Jérome, in *Organic Conductors:Fundamentals and Applications*, ed. by J. P. Farges, (Marcel Dekker, Inc., New York, 1994).

[2] S. Lefebvre, P. Wzietek, S. Brown, C. Bourbonnais, D. Jérome, C. Méziere, M. Fourmigué and P. Batail, Phys. Rev. Lett. **85**, 5420 (2000).

[3] N. D. Mathur *et al.* , Nature **394**, 39 (1998).

[4] J. Orenstein and A. J. Millis, Science **288**, 468 (2000); M. Maple, Journal of Magnetism and Magnetic Materials **177**, 18 (1998).

[5] V. J. Emery, Synthetic Metals **13**, 21 (1986).

[6] H. Ito, T. Ishiguro, M. Kubota and G. Saito, J. Phys. Soc. Jpn. **65**, 2987 (1996).

[7] H. Wilhelm, D. Jaccard, R. Duprat, C. Bourbonnais, D. Jérome, J. Moser, C. Carcel, and J. M. Fabre, Eur. Phys. J. B **21**, 175 (2001).

[8] S.-C. Zhang, Science **275**, 1089 (1997).

[9] S. Nagaosa, Science **275**, 1078 (1997).

[10] D. Jérome, Science **252**, 1509 (1991).

[11] T. Vuletić, C. Pasquier, P. Auban-Senzier, S. Tomić, D. Jérome, K. Maki and K. Bechgaard, Eur. Phys. J. B **21**, 53 (2001).

[12] N. Biškup, S. Tomić and D. Jérome, Phys. Rev. B **51**, 17972 (1995).

[13] A. Hinchliffe and H. J. Soscún Machado, Int. J. Mol. Sci. , **1**, 39 (2000).

[14] K. Bechgaard, JACS **103**, 2440 (1981).; K. Bechgaard, C. S. Jacobsen, K. Mortensen, H. J. Pedersen and N. Thorup, Solid State Commun. **33**, 1119 (1980).

[15] N. Thorup, G. Ringdorf, H. Soling and K. Bechgaard, Acta Cryst. B **37**, 1236 (1981).

[16] J. F. Kwak, J. E. Schirber, P. M. Chaikin, J. M. Williams, H.-H. Wang, L. Y. Chiang, Phys. Rev. Lett. **56**, 972 (1986).

[17] T. Ishiguro, K. Yamaji and G. Saito, *Organic Superconductors* (Springer Berlin, 1998).

[18] P. M. Chaikin, J. Phys. I France **6**, 1875 (1996).

[19] C. Bourbonnais and D. Jérome, in *Advances in Synthetic Metals, page 206*, edited by P. Bernier, S. Lefrant and G. Bidan (Elsevier, 1999).

[20] C. Bourbonnais and D. Jérome, cond-mat/9903101.

[21] D. Jérome, A. Mazaud, M. Ribault and K. Bechgaard, J. Physique Lettres **41**, L-95 (1980).

[22] P. M. Grant, J. Physique Colloque **44**, C3-847 (1983).

[23] C. S. Jacobsen *et al.* , Phys. Rev. Lett. **53** 194 (1984).

[24] T. Takahashi, Y. Maniwa, H. Kawamura and G. Saito, J. Phys. Soc. Jpn. **55**, 1364 (1986).

[25] D. Jérome and H. J. Schulz, Adv. Phys. **31**, 299 (1982).

[26] O. Traetteberg, G. Kriza, C. Lenoir, Y.-S. Huang, P. Batail and D. Jérome, Phys. Rev. B **49**, 409 (1994).

[27] S. Tomić, J. R. Cooper, W. Kang, D. Jérome and K. Maki, J. Phys. I France **1**, 1603 (1991).

[28] K. Mortensen, Y. Tomkiewicz and K. Bechgaard, Phys. Rev. B **25**, 3319 (1982).

[29] J. M. Delrieu, M. Roger, Z. Toffano, A. Moradpour and K. Bechgaard, J. Physique (France) **47**, 839 (1986).

[30] J. B. Torrance, H. J. Pedersen and K. Bechgaard, Phys. Rev. Lett. **49** 881 (1982).

[31] L. P. Le *et al.* , Europhys. Lett. **15**, 547 (1991); and Phys. Rev. B **48**, 7284 (1993).

[32] A. W. Overhauser, Phys. Rev. **167**, 691 (1968).

[33] J. P. Pouget and S. Ravy, J. Phys. I France **6**, 1501 (1996).

[34] J. P. Pouget and S. Ravy, Synthetic Metals **85**, 1523 (1997).

[35] K. Ichimura, M. Kobayashi, K. Nomura, T. Hanajiri, J. Yamada, S. Nakatsuji and H. Anzai, Synthetic Metals **120**, 897 (2001).

[36] S. Kagoshima, Y. Saso, M. Maesato, R. Kondo, T. Hasegawa, Solid State Commun. **110**, 479 (1999).

[37] G. Grüner, *Density Waves in Solids* (Addison-Wesley, Reading, MA, 1994).

[38] S. Tomić, J. R. Cooper, D. Jérome and K. Bechgaard, Phys. Rev. Lett. **62**, 462 (1989).

[39] G. Kriza, G. Quirion, O. Traetteberg, W. Kang and D. Jérome, Phys. Rev. Lett. **66**, 1922 (1991); E. Barthel, G. Kriza, G. Quiron, P. Wzietek, D. Jérome, J. B. Christensen, M. Joergensen and K. Bechgaard, Phys. Rev. Lett. **71**, 2825 (1993).

[40] T. Takahashi, Y. Maniwa, H. Kawamura, K. Murata and G. Saito, Synth. Metals **19**, 225 (1987).

[41] J. C. Lasjaunias, K. Biljaković, F. Nad', P. Monceau and K. Bechgaard, Phys. Rev. B **72**, 1283 (1994).

[42] M. Basletic, B. Korin-Hamzic and K. Maki, Phys. Rev. B **65**, 235117 (2002).

[43] B. Korin-Hamzic, M. Basletic and K. Maki, Europhys. Lett. **59**, 298 (2002).

[44] T. Vuletić, D. Herman, N. Biškup, M. Pinterić, A. Omerzu, S. Tomić and M. Nagasawa, J. Phys. IV **9**, Pr10–275 (1999).

[45] G. Mihaly, Y. Kim and G. Grüner, Phys. Rev. Lett. **66**, 2806 (1991); **67**, 2713 (1991).

[46] L. J. Azevedo, J. E. Schirber, J. M. Williams, M. Beno and D. Stephens, Phys. Rev. B **30**, 1570 (1984).

[47] R. Brusetti, M. Ribault, D. Jérome and K. Bechgaard, J. Physique **43**, 801 (1982).

[48] M. Nagasawa, T. Sambongi, K. Nomura and H. Anzai, J. Phys. (Paris) Colloq. **3**, C2-49 (1993).

[49] G. Montambaux, in *Low-Dimensional Conductors and Superconductors , page 233*, edited by D. Jérome and L. G. Caron (Plenum Press, New York, 1987).

[50] J. Sólyom, Adv. Phys. **28**, 201 (1979).

[51] H. J. Schulz, D. Jérome, M. Ribault, A. Mazaud and K. Bechgaard, J.Physique Lettres **279**, L51 (1981).

[52] R. L. Green *et al.* , Mol. Cryst. Liq. Cryst. **79**, 173 (1982); M. Y. Choi *et al.* , Phys. Rev. B **25**, 6208 (1982); S. Bouffard *et al.* , J. Phys. C **15**, 2951 (1982).

[53] L. C. Hebel and C. P. Slichter, Phys. Rev. **113**, 1504 (1959).

[54] K. Andres *et al.* , Phys. Rev. Lett. **45**, 1449 (1980).

[55] P. Garoche, R. Brusetti, D. Jérome and K. Bechgaard, J. Physique Lettres **43**, L-147 (1980).

[56] S. Belin and K. Behnia, Phys. Rev. Lett. **79**, 2125 (1997).

[57] I. J. Lee, M. J. Naughton, G. M. Danner, and P. M. Chaikin, Phys. Rev. Lett. **78**, 3555 (1997); I. J. Lee, P. M. Chaikin, and M. J. Naughton, Phys. Rev. B **62**, R14669 (2000).

[58] A. M. Clogston, Phys. Rev. Lett. **9**, 266 (1962).

[59] M. Takigawa, H. Yasuoka and G. Saito, J. Phys. Soc. Jpn. **56**, 873 (1987).

[60] I. J. Lee, S. E. Brown, W. G. Clark, M. J. Strouse, M. J. Naughton, W. Kang and P. M. Chaikin, Phys. Rev. Lett. **88**, 017004 (2002).

[61] R. L. Green and E. M. Engler, Phys. Rev. Lett. **45**, 1587 (1980).

[62] S. Tomić, D. Jérome, P. Monod and K. Bechgaard, J.Physique Lettres **43**, L839 (1982).

[63] K. Yamaji, J. Phys. Soc. Jpn. **51**, 2787 (1982).

[64] K. Yamaji, J. Phys. Soc. Jpn. **56**, 1841 (1987).

[65] Y. Hasegawa and H. Fukuyama, J. Phys. Soc. Jpn. **55**, 3978 (1986).

[66] K. Yamaji, J. Phys. Soc. Jpn. **52**, 1361 (1983).

[67] K. Machida and T. Matsubara, J. Phys. Soc. Jpn. **50**, 3231 (1981).

[68] E. Dagotto, Rep. Prog. Phys. **62**, 1525 (1999).

[69] M. Uehara, T. Nagata, J. Akimitsu, H. Takahashi, N. Mori and K. Kinoshita, J. Phys. Soc. Jpn. **65**, 2764 (1996).

[70] T. Siegrist, L. F. Schneemeyer, S. A. Sunshine, J. V. Waszczak and R. S. Roth, Mat. Res. Bull. **23**, 1429 (1988).

[71] E. M. McCarron, M. A. Subramanian, J. C. Calabrese and R. L. Harlow, Mat. Res. Bull. **23**, 1355 (1988).

[72] T. M. Rice, S. Gopalan and M. Sigrist, Europhys. Lett. **23**, 445 (1993).

[73] E. Dagotto and T. M. Rice, Science **271**, 618 (1996).

[74] S.-C. Zhang and T. M. Rice, Phys. Rev. B **37**, R3759 (1988).

[75] T. Osafune, N. Motoyama, H. Eisaki and S. Uchida, Phys. Rev. Lett. **78**, 1980 (1997).

[76] N. Nücker, M .Merz, C. A. Kuntscher, S. Gerhold, S. Schuppler, R. Neudert, M. S .Golden, J. Fink, D. Schild, S. Stadler, V. Chakarian, J. Freeland, Y. U. Idzerda, K. Conder, M. Uehara, T. Nagata, J. Goto, J. Akimitsu, N. Motoyama, H. Eisaki, S. Uchida, U. Ammerahl and A. Revcolevschi, Phys. Rev. B **62**, 384 (2000).

[77] E. Dagotto, J. Rieira, and D. Scalapino, Phys. Rev. B **45**, 5744 (1992).

[78] B. Gorshunov, P. Haas, T. Rõõm, M. Dressel, T. Vuletić, B. Korin-Hamzić, S. Tomić, J. Akimitsu and T. Nagata, Phys. Rev. B **66**, 060508(R) (2002).

[79] K. Ishida, K. Kitaoka, Y. Tokunaga, S. Matsumoto, K. Asayama, M. Azuma, Z. Hiroi and M. Takano, Phys. Rev. B **53**, 2827 (1996).

[80] V. J. Emery, *Highly Conducting One-Dimensional Solids, page 247*, edited by J. Devreese, R. Evrard, and V. van Doren (Plenum, New York, 1979).

[81] Z. Hiroi, J. Solid State Chem. **123**, 223 (1996).

[82] O. Milat, G. Van Tendeloo, S. Amelinckx, M. Mehbod and R. Deltour, Acta Cryst. B **48**, 618 (1992); T. Fukuda, J. Mizuki and M. Matsuda, Phys. Rev. B **67**, 012104 (2003); Comment by: S. van Smaalen, Phys. Rev. B **67**, 026101 (2003).

[83] M. Arai and H. Tsunetsugu, Phys. Rev. B **56**, R4305 (1997).

[84] N. Motoyama, T. Osafune, T. Kakeshita, H. Eisaki and S. Uchida, Phys. Rev. B **55**, R3386 (1997).

[85] Y. Mizuno, T. Tohyama and S. Maekawa, J. Phys. Soc. Jpn. **66**, 937 (1997).

[86] M. Kato, K. Shiota and Y. Koike, Physica C **258**, 284 (1996).

[87] S. Uchida, T. Ido, H. Takagi, T. Arima, Y. Tokura and S. Tajima, Phys. Rev. B **43**, 7942 (1991).

[88] M. Matsuda and K. Katsumata, Phys. Rev. B **53**, 12201 (1996).

[89] S. A. Carter, B. Batlogg, R. J. Cava, J. J. Krajewski, W. F. Peck, Jr., and T. M. Rice, Phys. Rev. Lett. **77**, 1378 (1996).

[90] L. P. Regnault, J. P. Boucher, H. Moudden, J. E. Lorenzo, A. Hiess, U. Ammerahl, G. Dhalenne, and A. Revcolevschi, Phys. Rev. B **59**, 1055 (1999).

[91] R. S. Eccleston, M. Uehara, J. Akimitsu, H. Eisaki, N. Motoyama, and S. Uchida, Phys. Rev. Lett. **81**, 1702 (1998).

[92] M. Matsuda, K. Katsumata, H. Eisaki, N. Motoyama, S. Uchida, S. M. Shapiro and G. Shirane, Phys. Rev. B **54**, 12199 (1996).

[93] O. Milat, private communication

[94] D. E. Cox, T. Iglesias, K. Hirota, G. Shirane, M. Matsuda, N. Motoyama, H. Eisaki and S. Uchida, Phys. Rev. B **57**, 10750 (1998).

[95] K. Kumagai, S. Tsuji, M. Kato, and Y. Koike, Phys. Rev. Lett. **78**, 1992 (1997).

[96] T. Imai, K. R. Thurber, K. M. Shen, A. W. Hunt and F. C. Chou, Phys. Rev. Lett. **81**, 220 (1998).

[97] R. S. Eccleston, M. Azuma and M. Takano, Phys. Rev. B **53**, R14721 (1996).

[98] M. Takigawa, N. Motoyama, H. Eisaki and S. Uchida, Phys. Rev. B **57**, 1124 (1998).

[99] V. Kataev, K.-Y. Choi, M. Grüninger, U. Ammerahl, B. Büchner, A. Freimuth and A. Revcolevschi, Phys. Rev. B **64**, 104422 (2001).

[100] S. Ohsugi, K. Magishi, S. Matsumoto, Y. Kitaoka, T. Nagata and J. Akimitsu, Phys. Rev. Lett. **82**, 4715 (1999).

[101] T. Nagata, H. Fujino, J. Akimitsu, M. Nishi, K. Kakurai, S. Katano, M. Hiroi, M. Sera and N. Kobayashi, J. Phys. Soc. Jpn. **68**, 2206 (1999).

[102] M. Isobe, M. Onoda, T. Ohta, F. Izumi, K. Kimoto, E. Takayama-Muromachi, A. W. Hewat and K. Ohoyama, Phys. Rev. B **62**, 11667 (2000).

[103] K. Magishi, S. Matsumoto, Y. Kitaoka, K. Ishida, K. Asayama, M. Uehara, T. Nagata and J. Akimitsu, Phys. Rev. B **57**, 11533 (1998).

[104] Y. Piskunov, D. Jérome, P. Auban-Senzier, P. Wzietek and A. Yakubovsky, Phys. Rev. B **69**, 014510 (2004).

[105] S. Katano, T. Nagata, J. Akimitsu, M. Nishi and K. Kakurai, Phys. Rev. Lett. **82**, 636 (1999).

[106] N. Motoyama, H. Eisaki, S. Uchida, N. Takeshita, N. M.ori, T. Nakanishi and H. Takahashi, Europhys. Lett. **58**, 758 (2002).

[107] T. Nagata, M. Uehara, J. Goto, N. Komiya, J. Akimitsu, N. Motoyama, H. Eisaki, S. Uchida, H. Takahashi, T. Nakanishi and N. Mori, Physica C **282-287**, 153 (1997).

[108] N. Fujiwara, N. Mori, Y. Uwatoko, T. Matsumoto, N. Motoyama and S. Uchida, Phys. Rev. Lett. **90**, 137001 (2003).

[109] S. Barišić and S. Brazovskii, *Recent Developments in Condensed Matter Physics, Vol. 1, p. 327*, ed. by J. T. Devreese (Plenum, New York, 1981).

[110] V. J. Emery, R. Bruinsma and S Barišić, Phys. Rev. Lett. **48**, 1039 (1982).

[111] R. E. Peierls, *Quantum Theory of Solids*, (Oxford University, New York/London, 1955).

[112] A. Virosztek and K. Maki, Phys. Rev. B **37**, 2028 (1988).

[113] J. Hubbard, Proc. R. Soc. A **276**, 238 (1963).

[114] V. J. Emery, Phys. Rev. B **14**, 2989 (1976).

[115] E. H. Lieb and F. Y. Wu, Phys. Rev. Lett. **20**, 1445 (1968).

[116] K. V. Efetov and K. I. Larkin, Soviet Phys. JETP, **42**, 390 (1975).

[117] K. Uzelac, J. Phys. C: Solid State Phys. **19**, L441 (1986).

[118] M. Tsuchiizu and A. Furusaki, Phys. Rev. Lett. **88**, 056402 (2002).

[119] M. Nakamura, J. Phys. Soc. Jpn. **68**, 3123 (1999); Phys. Rev. B **61**, 16 377 (2000).

[120] M. Tsuchiizu and Y. Suzumura, cond-mat/0311534.

[121] S. Mazumdar and D. K. Campbell, Phys. Rev. Lett. **55**, 2067 (1985).

[122] H. Fröhlich, Proc. R. Soc. A **223**, 296 (1954).

[123] P. A. Lee, T. M. Rice and P. W. Anderson, Phys. Rev. B **14**, 703 (1974).

[124] S. Barišić, Mol. Cryst. Liq. Cryst. **119**, 413 (1985); S. Barišić, *Electronic properties of inorganic materials with quasi-one-dimensional structures, Part 1, page 1*, edited by P. Monceau (Reidel, Dordrecht/Boston/Lancaster, 1986).

[125] A. Bjeliš, in *Applications of Statistical and Field Theory Methods to Condensed Matter*, edited by D. Baeriswyl *et al.* (Plenum Press, New York, 1990).

[126] G. Grüner, Rev. Mod. Phys. **60**, 1129 (1988).

[127] P. B. Littlewood, Phys. Rev. B **36**, 3108 (1987).

[128] H. Fukuyama, P. A. Lee, Phys. Rev. B **17**, 535 (1978); P. A. Lee, T. M. Rice, Phys. Rev. B **19**, 3970 (1979).

[129] R. J. Cava, R. M. Fleming, P. Littlewood, E. A. Rietman, L. F. Schneemeyer and R. G. Dunn, Phys. Rev. B **30**, 3228 (1984).

[130] R. J. Cava, R. M. Fleming, R. G. Dunn and E. A. Rietman, Phys. Rev. B **31**, 8325 (1985).

[131] R. J. Cava, P. Littlewood, R. M. Fleming, R. G. Dunn and E. A. Rietman, Phys. Rev. B **31**, 2439 (1986).

[132] R. M. Fleming, R. J. Cava, L. F. Schneemeyer, E. A. Rietman and R. G. Dunn, Phys. Rev. B **33**, 5450 (1986).

[133] D. Reagor, S. Sridhar, M. Maki and G. Gr$\acute{}$uner, Phys. Rev. B **32**, 8445 (1985).

[134] M. Kończykowski, M. Baj, E. Szafarkiewicz, L. Kończewicz and S. Porowski, *High Pressure and Low Temperature Physics, page 523*, edited by C. W. Chu and I. A. Woollam (Plenum Press, New York, 1978).

[135] T. Vuletić, P. Auban-Senzier, C. Pasquier, S. Tomić, D. Jérome, M. Héritier and K. Bechgaard, Eur. Phys. J. B **25**, 319 (2002).

[136] O. Milat, unpublished.

[137] I. Tanaka and H. Kojima, Nature, **337**, 21 (1989).

[138] M. Prester and I. Živković, unpublished.

[139] M. Pinterić, T. Vuletić, S. Tomić and J. U. von Schütz, Eur. Phys. J. B **22**, 335 (2001).

[140] S. Havriliak and S. Negami, J. Polym. Sci. C **14**, 99 (1966).

[141] S. Tomić, N. Biškup, M. Pinterić, J. U. von Schütz, H. Schmitt and R. Moret, Europhys. Lett. **38**, 219 (1997).

[142] M. Pinterić, M. Miljak, N. Biškup, O. Milat, I. Aviani, S. Tomić, D. Schweitzer, W. Strunz and I. Heinen, Eur. Phys. J. B **11**, 217 (1999).

[143] M. Pinterić, T. Vuletić, M. Lončarić, S. Tomić and J. U. von Schütz, Eur. Phys. J. B **16**, 487 (2000).

[144] G. Kozlov and A. Volkov, *Topics in Applied Physics* **74**, Millimeter and Submillimeter Wave Spectroscopy of Solids, ed. G.Grüner (Springer-Verlag, Berlin, 1998).

[145] L. P. Gor'kov, J. Phys. I France **6**, 1697 (1996).

[146] A. Smontara, K. Biljaković, J. Mazuer, P. Monceau and F. Lévy, J. Phys. Cond. Matt. **4**, 3273 (1992).

[147] M.Tinkham, *Introduction to superconductivity, Chap.11* (McGraw-Hill, New York, 1996).

[148] G. Montambaux, Phys. Rev. B **38**, 4788 (1988).

[149] G. Montambaux, M. Héritier and P. Lederer, J. Phys.: Condens. Matter **19**, L293 (1986).

[150] M. Héritier, G. Montambaux and P. Lederer, J. Physique Lettres **45**, 943 (1984).

[151] L. Ducasse, M. Abderrabba, J. Hoarau, M. Pesquer, B. Gallois and J. Gaultier, J.Physique Colloque **47**, C19-3805 (1986).

[152] B. Gallois *et al.* , Mol. Cryst. Liq. Cryst. **148**, 279 (1987).

[153] C. Pasquier, P. Auban-Senzier, T. Vuletić, S. Tomić, M. Héritier and D. Jérome, J. Phys. IV **12**(9), Pr9-197 (2002).

[154] R. Moret, S. Ravy, J. P. Pouget and R. Comes, Phys. Rev. Lett. **57**, 1915 (1986).

[155] S. Tomić and D. Jérome, J. Phys.: Condens. Matter **1**, 4451 (1989).

[156] L. P. Gor'kov and A. G. Lebed', J. Physique Colloque **44**, C3-1531 (1983).

[157] R. Duprat and C. Bourbonnais, Eur. Phys. J. B **21**, 219 (2001).

[158] V. J. Emery, J. Physique Colloque **44**, C3-977 (1983).

[159] D. Podolsky, E. Altman, T. Rostunov, and E. Demler, cond-mat/0403406.

[160] T. Vuletić, B. Korin-Hamzić, S. Tomić, B. Gorshunov, P. Haas, T. Rõõm, M. Dressel, J. Akimitsu, T. Sasaki and T. Nagata, Phys. Rev. Lett. **90**, 257002 (2003).

[161] T.Vuletić, T. Ivek, B. Korin-Hamzić, S. Tomić, B. Gorshunov, P. Haas, M. Dressel, J. Akimitsu, T. Sasaki and T. Nagata, submitted to Phys. Rev. Lett. (2004).

[162] H. Kitano, R. Isobe, T. Hanaguri, A. Maeda, N. Motoyama, M. Takaba, K. Kojima, H. Eisaki and S. Uchida, Europhys. Lett. **56**, 434 (2001).

[163] H. Kitano, R. Inoue, A. Maeda, N. Motoyama, K. Kojima, H. Eisaki and S. Uchida, Physica C **341-348**, 463 (2000).

[164] G. Grüner, A. Zawadowski and P. M. Chaikin, Phys. Rev. Lett. **46**, 511 (1981).

[165] T. Vuletić, M. Pinterić, M. Lončarić, S. Tomić and J. U. von Schütz, Synth. Metals **120**, 1001 (2001).

[166] R. C. Lacoe, J. R. Cooper, D. Jérome, F. Creuzet, K. Bechgaard and I. Johanssen, Phys. Rev. Lett. **58**, 262 (1987).

[167] G. Blumberg, P. Littlewood, A. Gozar, B. S. Dennis, N. Motoyama, H. Eisaki, and S. Uchida, Science **297**, 584 (2002).

[168] A. Maeda, R. Inoue, H. Kitano, N. Motoyama, H. Eisaki and S. Uchida, Phys. Rev. B **67**, 115115 (2003).

[169] P. B. Littlewood, Solid State Commun. **65**, 1347 (1988).

[170] Wei-yu Wu, L. Mihály and G. Grüner, Solid State Commun. **55**, 663 (1985).

[171] T. Vuletić, B. Korin-Hamzić, S. Tomić, B. Gorshunov, P. Haas, M. Dressel, J. Akimitsu, T. Sasaki and T. Nagata, Phys. Rev. B **67**, 184521 (2003).

[172] N. F. Mott and E. A. Davis, *Electronic Processes in Non-crystalline Solids* (Oxford University, London, 1971).

[173] Z. G. Yu and X. Song, Phys. Rev. Lett. **86**, 6018 (2001).

[174] J. C. Dyre and T. B. Schröder, Rev. Modern Physics **72**, 873 (2000).

[175] F. Ladieu and M. Sanquer, Ann. Phys. (Paris) **21**, 267 (1996).

[176] M. L. Knotek and M. Pollack, Phys. Rev. B **9**, 664 (1974).

[177] V. K. S. Shante and C. M. Varma, Phys. Rev. B **8**, 4885 (1973).

[178] K. R. Thurber, K. M. Shen, A. W. Hunt, T. Imai and F. C. Chou, Phys. Rev. B **67**, 094512 (2003).

[179] S. Pachot, P. Bordet, R. J. Cava, C. Chaillout, C. Darie, M. Hanfland, M. Marezio and H. Takagi, Phys. Rev. B **59**, 12048 (1999).

[180] N.F.Mott *Metal-Insulator Transitions* (Taylor and Francis, London, 1990).

[181] P. W. Anderson, Phys. Rev. **109**, 1492 (1958).

[182] A. F. Ioffe and A. R. Regel, Prog. Semicond. **4**, 237 (1960).

[183] V. J. Emery and S. A. Kivelson, Phys. Rev. Lett. **74**, 3253 (1995).

[184] U. Schollwöck, S. Chakravarty, J. O. Fjaerestad, J. B. Marston and M. Troyer, Phys. Rev. Lett. **90**, 186401 (2003).

[185] F. Nad', P. Monceau, C. Carcel and J. M. Fabre, J. Phys.: Condens. Matter **12**, L435 (2000).

[186] D. S. Chow, F. Zamborszky, B. Alavi, D. J. Tantillo, A. Baur, C. A. Merlic and S. E. Brown, Phys. Rev. Lett. **85**, 1698 (2000).

Abstract

The spin/charge density-wave (SDW/CDW) phases in relation with superconductivity (SC) were studied by linear and non-linear dc resistivity and low-frequency dielectric spectroscopy. Quasi-one-dimensional (q1D) materials from two different families were studied: single chain $(TMTSF)_2PF_6$, an organic Bechgaard-Fabre charge-transfer salt and $(La, Sr, Ca)_{14}Cu_{24}O_{41}$, composite chain/ladder cuprates. Using an improved control of the applied pressure, in the phase diagram of $(TMTSF)_2PF_6$ a 0.8 kbar wide pressure range, featuring an SDW/SC coexistence, was found. The inhomogeneous character is supported by the analysis of the resistivity between T_{SDW} and T_{SC} and the superconducting critical current. $T_{\mathrm{SC}} = 1.2$K is practically constant here and only the SC domain proportion is increasing under pressure. Experimental results are correlated with a model comparing the free energy of a SDW/SC segregated phase and of homogeneous phases. Nonisovalently substituted q1D cuprates $La_ySr_{14-y-x}Ca_xCu_{24}O_{41}$ are insulators with hopping transport along the chains, a 1D disordered system. Disorder is due to random structural distortions of chains induced by irregular coordination of the La/Sr/Ca ions. The transport switches from the chains to ladders in isovalently substituted $Sr_{14-x}Ca_xCu_{24}O_{41}$, due to mobile holes transferred into the ladders. A phase transition is identified below which a 2D long-range CDW order develops in the ladders. That is, in addition to the mode along the ladders, the collective CDW screened mode is observed in the direction of the ladder rungs. The transport perpendicular to the ladder planes is dominated by hopping. Ca-substitution suppresses CDW phase with T_{CDW} decreasing from 210 K (x=0) to 7 K (x=9), and the CDW gap from 1300 K to 30 K, respectively. The suppression is due to the changes in coupling parameters in this strongly coupled system, as well as to disorder introduced at the Sr sites. This ground state falls between the CDW order of itinerant charges and the charge order of localized charges. Its non-standard nature might also be characterized by non-s-wave like pairing. SC is reported to be established in $x > 10$ when CDW is completely removed under pressure. CDW properties speak in favor of also non-s-wave 2D nature of SC.

Sažetak

Valovi gustoće spina/naboja (VGS/VGN) povezani sa supravodljivošću (SV) istraživani su mjerenjima (ne)linearne istosmjerne otpornosti i niskofrekventne dielektrične spektroskopije. Istraživani su kvazi-jednodimenzionalni (kvazi1D) materijali iz dviju različitih porodica: jednostavni lančasti $(TMTSF)_2PF_6$, Bechgaard-Fabre organska sol s prijenosom naboja i $(La, Sr, Ca)_{14}Cu_{24}O_{41}$, kompozitni lanac/ljestvice kuprati. Unaprijeđenom kontrolom tlaka, pronađeno je u faznom dijagramu $(TMTSF)_2PF_6$ područje širine 0.8 kbar, karakterizirano VGS/SV koegzistencijom. Nehomogeni karakter potvrđen je analizom otpornosti između T_{VGS} i T_{SV} te SV kritičnih struja. U tom području $T_{\mathrm{SV}} = 1.2$K je praktično konstantan i jedino udio SV domena raste s tlakom. Eksperimentalni rezultati su korelirani s modelom u kojem se uspoređuju slobodne energije nehomogene VGS/SV i homogenih faza. Neizovalentno supstituirani kvazi1D kuprati $La_ySr_{14-y-x}Ca_xCu_{24}O_{41}$ su izolatori, s transportom preskakanjem duž lanaca, 1D neuređenog sistema. Nered je posljedica nasumičnih strukturnih deformacija lanaca, induciranih neregularnom koordinacijom La/Sr/ca iona. Električni transport se prebacuje s lanaca na ljestvice u izovalentno supstituiranim $Sr_{14-x}Ca_xCu_{24}O_{41}$, sa šupljinama transferiranim u ljestvice. Identificirali smo fazni prijelaz ispod kojeg se uspostavlja 2D dugodosežno uređenje VGNa u ljestvicama. Tj., osim moda duž ljestvica, kolektivni zasjenjeni VGN mod javlja se i u smjeru prečkica ljestvica. Transport poprečno na ravninu ljestvica je dominiran preskakanjem. Ca-supstitucija potiskuje VGN fazu, tj. temperatura prijelaza T_{VGN} opada od 210 K (x=0) do 7 K (x=9), a VGN procjep od 1300 K do 30 K. Potiskivanje je uzrokovano promjenama parametara vezanja, bitnim u kupratima, kao sistemima s jakim vezanjem, ali i neredom unesenim na Sr-mjestima. Uočeno osnovno stanje nalazi se između VGN uređenja itinerantnih naboja i nabojnog uređenja lokaliziranog naboja. Njegova bi nestandardna priroda mogla biti karakterizirana i sparivanjem različitim od s-tipa. SV se javlja za $x > 10$, dok VGN biva potpuno potisnut tlakom. Svojstva VGN stanja govore i u prilog SV stanja ne-s-tipa i 2D prirode.

Biography

Personal data :

I was born in 1971, in Zagreb, Croatia. I was educated through the elementary and high school in the home town.

Academic qualifications :

- 1990: Started the studies of physics on the Faculty of Science, University of Zagreb, Croatia.
- 1994 – 1996: Scholarship of Institute of Physics, Zagreb.
- 1998: B.Sc. in Physics – Thesis: *Nelinearna vodljivost vala gustoće spina u Bechgaardovim solima.*
- 1998: Assistant position at the Institute of Physics, Zagreb, in the research group of dr. S. Tomić.
- 1999 – 2002: Post-graduate studies (Ph.D. student) of Condensed Matter Physics at the Faculty of Science, University of Zagreb, Croatia.
- 2002 – 2004: Doctoral studies directed towards preparation of the Thesis titled: *Collective Electronic States of New Quasi-One-Dimensional Materials.*

Research :

As an experimentalist I primarily use low-frequency dielectric spectroscopy (LFDS) and linear and nonlinear dc transport techniques in the laboratory at the Institute of Physics, Zagreb. My research concentrates on quasi1D materials: SDW phase of Bechgaard salts, Mott-Peierls CDW phase of DCNQI materials, CDW phase of quasi1D cuprates $(La,Sr,Ca)_{14}Cu_{24}O_{41}$.

Visits :

- 1999 & 2000: Laboratoire de Physique des Solides, Orsay, France, group of dr. D. Jérome.
- 2002: Universität Stuttgart, Germany, 1. Physikalisches Institut, group of prof. M. Dressel.

Conferences :

- 1999: Workshop on Electronic Crystals, ECRYS '99, La Colle-sur-Loup, France.
- 1999: GDR522, Matériaux moléculaires du magnétisme aux supraconducteurs organiques, Gif-sur-Yvette, France.
- 2000: International Conference on Science and Technology of Synthetic Metals, Gastein, Austria.
- 2002: From Solid State to Biophysics, Dubrovnik, Croatia.
- 2003: International school of solid state physics, 30th workshop: Symmetry and heterogeneity in high temperature superconductors, Erice, Italy.
- 2004: From Solid State to Biophysics II, Dubrovnik, Croatia.
- 2004: International Conference on Low Energy Electrodynamics in Solids, Kloster Banz, Germany.
- 2004: The 5^{th} International Conference on Biological Physics, Gothenburg, Sweden.

Biografija

Osobni podaci :

Rođen sam 1971., u Zagrebu. Osnovnu i srednju školu pohađao sam u rodnom gradu.

Akademske kvalifikacije :

- 1990: Započeo sam studij fizike na Prirodoslovno-matematičkom fakultetu (PMF) u Zagrebu.
- 1994 – 1996: Stipendist sam Instituta za fiziku, Zagreb.
- 1998: Diplomirao sam (zvanje: dipl. ing. fizike) s radom naslova: *Nelinearna vodljivost vala gustoće spina u Bechgaardovim solima.*
- 1998: Primljen sam u statusu znanstvenog novaka na Institut za fiziku, u znanstveno-istraživačku grupu dr. S. Tomić.
- 1999 – 2002: Poslijediplomski studij fizike čvrstog stanja na PMF-u u Zagrebu.
- 2002 – 2004: Doktorski studij, usmjeren ka izradi Disertacije naslovljene: *Kolektivna elektronska stanja novih kvazijednodimenzionalnih materijala.*

Znanstveno-istraživački rad :

Kao eksperimentalnom fizičaru primaran mi je rad s tehnikom niskofrekventne dielektrične spektroskopije (NFDS) i tehnikama mjerenja istosmjernog, linearnog i nelinearnog, električnog transporta, u laboratorijima grupe dr. S. Tomić, na Institutu za fiziku. Moje istraživanje usredotočeno je na kvazi1D materijale: VGS fazu Bechgaardovih soli, Mott-Peierls VGN fazu DCNQI materijala, VGN fazu kvazi1D kuprata $(La,Sr,Ca)_{14}Cu_{24}O_{41}$.

Rad u inozemnim laboratorijima :

- 1999 & 2000: Laboratoire de Physique des Solides, Orsay, France, grupa dr. D. Jéromea.
- 2002: Universität Stuttgart, Germany, 1. Physikalisches Institut, grupa prof. M. Dressela.

Znanstveni skupovi :

- 1999: Workshop on Electronic Crystals, ECRYS '99, La Colle-sur-Loup, France.
- 1999: GDR522, Matériaux moléculaires du magnétisme aux supraconducteurs organiques, Gif-sur-Yvette, France.
- 2000: International Conference on Science and Technology of Synthetic Metals, Gastein, Austria.
- 2002: From Solid State to Biophysics, Dubrovnik, Croatia.
- 2003: International school of solid state physics, 30th workshop: Symmetry and heterogeneity in high temperature superconductors, Erice, Italy.
- 2004: From Solid State to Biophysics II, Dubrovnik, Croatia.
- 2004: International Conference on Low Energy Electrodynamics in Solids, Kloster Banz, Germany.
- 2004: The 5^{th} International Conference on Biological Physics, Gothenburg, Sweden.

List of publications

1 N. Biškup, **T. Vuletić**, D. Herman, S. Tomić, M. Nagasawa and K. Bechgaard. Low Frequency Dielectric Response in Spin Density Wave Phase of Bechgaard Salts. Synth. Metals **103**, 2052 – 2053 (1999).

2 **T. Vuletić**, D. Herman, N. Biškup, M. Pinterić, A. Omerzu, S. Tomić and M. Nagasawa. Single-particle and spin-density wave charge dynamics in $(TMTSF)_2PF_6$ and $(TMTSF)_2AsF_6$: A comparative overview. J. Phys. IV **9**(10), Pr10–275–Pr10–277 (1999).

3 M. Pinterić, **T. Vuletić**, M. Lončarić, S. Tomić and J. U. von Schütz. Low frequency dielectric spectroscopy of the Peierls-Mott insulating state in the deuterated copper-DCNQI systems. Eur. Phys. J. B **16**(3), 487–493 (2000).

4 S. Tomić, M. Pinterić, **T. Vuletić**, J. U. von Schütz and Dieter Schweitzer. Low-frequency dielectric spectroscopy of commensurate density waves. Synth. Met. **120**, 695–698 (2001).

5 **T. Vuletić**, M. Pinterić, M. Lončarić, S. Tomić and J. U. von Schütz. Non-ohmic electrical transport in the Peierls-Mott state of deuterated copper-DCNQI systems. Synth. Met. **120**, 1001–1002 (2001).

6 **T. Vuletić**, C. Pasquier, P. Auban-Senzier, S. Tomić, D. Jérome, K. Maki and K. Bechgaard. Influence of quantum Hall effect on linear and nonlinear conductivity in the FISDW states of the organic conductor $(TMTSF)_2PF_6$. Eur. Phys. J. B **21**, 53 – 60 (2001).

7 M. Pinterić, **T. Vuletić**, S. Tomić and J. U. von Schütz. Complex low-frequency dielectric relaxation of the charge-density wave state in the $(2,5(OCH_3)_2DCNQI)_2Li$. Eur. Phys. J. B **22**, 335–341 (2001).

8 **T. Vuletić**, P. Auban-Senzier, C. Pasquier, S. Tomić, D. Jérome, M. Héritier and K. Bechgaard. Coexistence of Superconductiv-

ity and Spin Density Wave orderings in the organic superconductor $(TMTSF)_2PF_6$. Eur. Phys. J. B **25**, 319–331 (2002).

9 B. Gorshunov, P. Haas, T. Rõõm, M. Dressel, **T. Vuletić**, B. Korin-Hamzić, S. Tomić, J. Akimitsu and T. Nagata. Charge Density Wave formation in $Sr_{14}Cu_{24}O_{41}$. , Phys. Rev. B **66**, 060508(R) (2002).

10 S. Tomić, **T. Vuletić**, M. Pinterić and B. Korin-Hamzić. Modalities of self-organized charge response in low dimensional systems. J. Phys. IV **12**(9), Pr9–211–214 (2002).

11 C. Pasquier, P. Auban-Senzier, **T. Vuletić**, S. Tomić, M. Héritier and D. Jérome. Coexistence of superconductivity and spin density wave orderings in Bechgaard and Fabre salts. J. Phys. IV **12**(9), Pr9–197–200 (2002).

12 **T. Vuletić**, B. Korin-Hamzić, S. Tomić, B. Gorshunov, P. Haas, M. Dressel, J. Akimitsu, T. Sasaki and T. Nagata. Variable-range hopping conductivity in the copper-oxygen chains of $La_3Sr_3Ca_8Cu_{24}O_{41}$. Phys. Rev. B **67**, 184521 (2003).

13 **T. Vuletić**, B. Korin-Hamzić, S. Tomić, B. Gorshunov, P. Haas, T. Rõõm, M. Dressel, J. Akimitsu and T. Nagata. Suppression of the charge-density wave state in $Sr_{14}Cu_{24}O_{41}$ by calcium doping. Phys. Rev. Lett. **90**, 257002 (2003).

14 M. Pinterić, **T. Vuletić** and S. Tomić. Properties of Mott-Peierls insulating phase in deuterated copper-DCNQI systems. Proceedings of 39th international conference on microeletronics, devices and materials, MIDEM 2003, 231–236 (2003).

15 M. Pinterić, **T. Vuletić**, M. Lončarić, K. Petukhov, B. Gorshunov, J. U. von Schütz, S. Tomić and M. Dressel. MottPeierls phase in deuterated copper-DCNQI systems: a comprehensive study of longitudinal and transverse conductivity and ageing effects. J. Phys.: Condens. Matter **15**, 7351–7364 (2003).

16 **T. Vuletić**, T. Ivek, B. Korin-Hamzić, S. Tomić, B. Gorshunov, P. Haas, M. Dressel, J. Akimitsu, T. Sasaki and T. Nagata. Anisotropic charge modulation in ladder planes of $Sr_{14-x}Ca_xCu_{24}O_{41}$. submitted to Phys. Rev. Lett. (2004); cond-mat/0403611